Study of the multi-length scale structure of metallic glasses using synchrotron X-rays and phase-field crystal modelling

Wei Zhang

School of Engineering

University of Hull

This thesis is submitted for the degree of

Doctor of Philosophy

April 2016

I would like to dedicate this thesis to my lovely wife, sisters and parents, without their love, support and encouragement, there would never be success to my life.

Declaration

I hereby declare that except where specific references are made to the work of others, the contents of this dissertation are original and have not been submitted in whole or in part for consideration for any other degree or qualification in this, or any other university. This dissertation is my own work and contains nothing which is the outcome of work done in collaboration with others, except as specified in the text and acknowledgements.

<div align="right">

Wei Zhang

April 2016

</div>

Acknowledgements

Firstly I would like to thank my supervisor Dr Jiawei Mi. It has been an honour to work with him. I really appreciated all the opportunities, resources and especially some stimulating ideas he brought to me. The enthusiasm he has for research also strongly motivates me when carrying on my research and for future career development in research.

I was so grateful for the *UoH–CSC* joint PhD studentship awarded from the university of Hull and Chinese Scholarship Council. Without the financial support, I would be not possible to pursuit a PhD degree in UK.

Also, I want to thank all members in the Advanced Material groups for their friendship during my time in Hull. The tough times we experienced together in national labs left me unforgettable memories. All past and present group members including my friends whom I have worked with are: PhD students Theerapatt Manuwong, Dongyue Tan, Jiachuan Khong, Tunglik Lee and Wenjia Du; the joint student, Tian'en Yang and research fellow Dr yongjiang Huang, Dr Liang Zheng and Dr Chuangnan Wang.

I would also like to thank the technical support from the workshops and Labs in the university, Tony Sinclair (SEM), Garry Robinson (SEM), Craig Stephenson (ICT), just name a few.

All alloys, ribbons and ingots of metallic glasses and composites used in this work, were prepared by Dr Yongjiang Huang and his colleagues of Harbin Institute of Technology, China. I really appreciated these. In addition, I would also like to thank Dr Liang Zheng from Beijing Institute of Aeronautical Materials, China for the Gleeble thermal shock experiments.

Also special thanks are given to Dr Tan Sui, and professor Alexander M. Korsunsky from Department of Engineering Science, University of Oxford, UK for their contribution on the FIB–SEM sectioning tomography.

It is a pleasure to give a great acknowledgement to Diamond Light Source (DLS), ISIS spallation neutron source, Swiss Light Source (SLS) for the beamtimes awarded to my research (as summarised in Table 1 below), and also to the beamline scientists, Dr Andrew Boedy from the beamline I13, Dr Thomas Connolley from I12 in DLS, Dr Winfreied kockelmann from GEM, ISIS, and Dr Julie Fife from Tomcat, PSI for most valuable advices on data analyses.

My time at Hull was very enjoyable in large part due to the many friends and groups that became a part of my life. I am grateful for time spent with housemates, friends and others in memories.

Lastly, I would like to thank my family for all their love and encouragement.

Table 1 The syncrotron X-ray and neutron beamtimes awarded during my research

Proposal No.	Title	Beamline	Date	duration
MT9252–1	Tomography study of 3-D dendritic crystalline microstructure in bulk metallic glass matrix composites	I13	11/10/2013	72 hrs
EE9902–1	In-situ study of the evolution of atomic structure of metallic glasses under extreme pressure	I15	18/04/2014	72 hrs
MT9974–2	Tomography study of 3-D dendritic crystalline microstructure in bulk metallic glass matrix composites	I13	09/10/2014	96 hrs
EE10440-1	Time-resolved studies of the atomic structure evolution of metallic glass and composites during solidification	I12	04/02/2015	72 hrs
20140233	In-situ tomography studies of the microstructural evolution of metallic glass composites during isothermal heating and solidification	Tomcat	31/10/2014	8 hrs
70009	Phase identification of the thermally shocked bulk metallic glass composite	GEM	31/07/2014	8 hrs

Publications

W. Zhang. *et al*. Multi-scale Characterisation of the 3D Microstructure of a Thermally-Shocked Bulk Metallic Glass Matrix Composite. Sci. Rep. 5, 18545; doi: 10.1038/srep185 45 (2015).

T. Manuwong, **W. Zhang**, *et al*. "Solidification of Al Alloys Under Electromagnetic Pulses and Characterisation of the 3D Microstructures Using Synchrotron X-ray Tomography." Metallurgical and Materials Transactions A 46.7 (2015): 2908-2915.

C. Wang, D. Tang, **W. Zhang**, W. Du, T. Connolley, J. Mi. (2015). High speed synchrotron X-ray imaging of ultrasonic bubble cloud in liquid metal. In Journal of Physics: Conference Series (Vol. 656, No. 1, p. 012178). IOP Publishing.

W. Zhang, J. Mi. Phase-Field-Crystal Modelling of the Order-to-Disordered Atomistic Structure Transition of Metallic Glasses. Proceedings of 4th international Conference on Advances in Solidification Processes. Beaumont Estates, Old Winsor, UK, on 8th to 11th, July 2014.

W. Zhang, J.C. Khong, J. Mi. Study of Local Ordering in Zr-Ti Based Bulk Metallic Glass Matrix Composite Using HRTEM Based Image Processing and Synchrotron X-ray Total Scattering. (under review).

W. Zhang, J.C. Khong, T. Connolley, J. Mi. Synchrotron X-ray *in-situ* Studies of the Evolution of Atomic Structures of Bulk Metallic Glass. (under review).

Abstract

Metallic glasses and composites are a new class of metal alloys which have unique mechanical and functional properties. The structure of metallic glasses and composites are key to understand the glass formation ability and also their unique properties. However it is often very challenging to determine the structure of such amorphous materials using conventional experiment methods.

The research studies the multi-length scale structures of metallic glasses and composites with different composition and processing conditions. A novel experimental apparatus were designed made, and commissioned for in-situ PDFs studies.

The composition dependent atomic structure of binary and ternary metallic glasses were characterised using synchrotron X-ray pair distribution functions. And a binary vacancy phase-field crystal model and a ternary model developed based on it, were successfully used to interpret the atomic structure changes with composition for the binary alloys, CuZr and NiTi, and also the ternary alloys, CuZrAl and TiCuNi.

Systematic in-situ experiments were conducted using this novel apparatus at the synchrotron X-ray diffraction beamline, I12, Diamond light source. A large amount of real-time diffraction patterns of Vit1 ($Zr_{41.2}Ti_{13.8}Cu_{12.5}Ni_{10}Be_{22.5}$) with different thermal conditions, were acquired in this research. A highly thorough procedure of data reduction, processing and analysis enables to get high quality in-situ PDFs and extract the key information for understanding the local structure evolution during the crystallisation from supercooled liquid and annealed amorphous state, and also that during the glass formation with different cooling conditions at atomic scale.

The significant advantage of bulk metallic glass matrix composites (BMGMC) is the strong atomic bond across the amorphous–crystalline interface which is formed in-situ during solidification. The transition from an ordered to disordered atomic structure plays a critical role in determining the mechanical properties in atomic scale. Several HRTEM image based methods, fast Fourier transformation, auto correlation function, and 2D pair distribution function, *etc*, were used to characterise the local ordering from short range to long inter-atomic range.

Furthermore, the mechanical properties of such BMGMCs are often strongly related to the complex crystalline dendrites, and a well-understanding of 3D morphologies of the dendrites is also very important. However, the 3D structures and their morphologies of such composite at nano and micrometre scale have never been reported before. The high density electric currents were used to thermally shock a Zr-Ti based BMGMC (DH3) to different temperatures, and used X-ray micro-tomography, FIB-SEM nanotomography and neutron diffraction to reveal the morphologies, compositions, and volume fractions of the nano and microstructures of the thermally-shocked composites and their thermal stabilities under rapid heating by electric currents.

The key research findings are:

- A binary vacancy phase-field crystal model and a ternary model have been developed and successfully used to interpret the atomic structure changes with composition for the binary alloys, CuZr and NiTi, and also the ternary alloys, CuZrAl and TiCuNi. As the concentration of Cu and Ti increases, the populations of Cu-Cu atomic pairs / Ti-Ti atomic pairs increase, which leads to increasing peak intensity of the first / second peak. The atomic size ratio significantly affects the peak positions and peak shape of PDFs for binary and ternary alloys. The peak separation of the first PDF peak for $Zr_{55}Cu_{40}Al_5$ is mainly due to the increasing population of Zr-Cu and Zr-Al pairs.

- An dedicated experimental apparatus were designed, made, and commissioned for the total scattering experiments using Synchrotron X-rays, which can be used to thoroughly acquire high-quality X-ray scattering data for real time studies of atomic structure using pair distribution functions.

- The crystallisation of Vit1 during heating is very different to those found during slow cooling. The crystallisation induced by heating is very rapid, and the crystalline structure is formed in 6 s, while that occurred in cooling is fairly slow ($\sim$ 21 s), and the atomic structure are largely determined by the cooling rates. During the crystallisation induced by heating at 1.5 K/s, Zr_2Cu is formed at 270 °C and $ZrBe_2$ is formed 457 °C. While Zr_2Cu and $ZrBe_2$ are formed together during the crystallisation induced by slow cooling.

- A novel 2D HRTEM image based pair distribution function method was proposed to characterise the local structure transition within amorphous-crystalline interface at atomic level. The 2D PDFs, which are very sensitive to ordered and disordered structure, can provide an alternative approach to characterise the local ordering using HRTEM.

- The 3D nano and microstructures of the DH3 at different thermal shock conditions were studied and characterised using X-ray microtomography and FIB-SEM nanotomgraphy. It is found that the ductile β-Zr crystalline dendrites are interlocked 3D structures with complex morphology of a few hundreds of micrometres. They are not the "globular" particles of a few to tens of microns in length, as previously inferred from 2D imaging. The amorphous to crystalline transition at the interface under thermal shock by applying electric current is very different to that occurred in isothermal heating conditions. The large difference in electric resistivities between the amorphous matrix and the crystalline dendrites resulted in differential heating across the amorphous-crystalline interface, which led to the nucleation of new crystalline phases (Zr_2Cu and $ZrBe_2$) preferably at the interface, rather than within the

amorphous matrix. They grew concurrently to form 3D eutectic network as revealed by using the FIB-SEM nanotomography.

Table of contents

List of figures

List of tables

Chapter 1

Introduction

1.1 Background of the research

Most naturally occurred metals and man-made metallic alloys have long-range ordered atomic structures, *i.e.* crystalline structures [1]. However, most natural materials do not have such perfect long-range ordered atomic structures, and they are generally called disordered materials [2]. For example, naturally occurred SiO_2 glasses and polymer-based materials are the typical disordered materials. Natural metals and glasses are very common materials on earth, and have been used, exploited and developed independently and separately for many thousand years by human beings until 1959 when the first metallic glass was discovered in Caltech by Duwez *et.al* [3] through the rapid quenching of a binary $Au_{75}Si_{25}$ alloy with a cooling rate of 10^7 K/s.

Since then, intensive research activities have been devoted on developing many hundreds of new metallic glass alloy systems, and to solve the fundamental and applied scientific issues in structure, properties, design and fabrication, and applications of metallic glasses [4–6].

Currently the following issues are subject to intensive research [7]:

- **Atomic structure** is one of the central topics of metallic glasses. Since amorphous materials often do not have any translational and rotational symmetry in long range, it

is very challenging to characterise the atomic structure by conventional experimental methods, such as diffraction, imaging, *etc*. Therefore, it is essential to exploit advanced experimental techniques, or develop novel modelling methods to effectively characterise a given amorphous structure and extract the key structural information relevant to glass formation and structure related properties.

- It is well known that the **properties of materials** are determined by the structure of materials. For the amorphous materials, especially the MGs, it is very difficult to determine the correlations of structure to properties, since the structure of metallic glasses is still an unsolved puzzle, which is far from being well understood. Therefore, the predictions of the macroscopic properties of MGs are still in progress.

- Although there are several **alloy design principles** being proposed to fabricate the BMGs, however, there is still a huge difficulty in the component design of new BMGs. Up to date, The development of the new BMGs is still based on trial and error methods [7]. The precisely design of the multi-component BMG systems is still very challenging due to lack of effective alloy design principles.

In this work, we only focus on studying the atomic structure of metallic glasses and composites using experimental and modelling methods.

1.2   Objectives of the research

- Atomic structure of metallic glasses, and the transition from amorphous structure to crystalline structure.

- Using advanced experimental methods to study the relationship between structure and alloy composition and processing conditions.

- Develop numerical model to assist the understanding of atomic structures and the relationship between alloy composition and processing conditions.

- Study in-situ the evolution of atomic structures of metallic glasses in conventional solidification conditions.

- Characterise the multi-length scale, 2D and 3D structures in an unconventional thermal shock process.

1.3   Structure of the thesis

The thesis consists of 8 chapters, and each is briefly described below.

Chapter 1 is a brief introduction of the research background, the objectives and the structure of the thesis.

Chapter 2 reviews the literatures that are directly relevant to the research, and they are grouped into five sections, including a brief review and discussion on (1) the structure of ordered and disordered materials, (2) metallic glasses and metallic glasses composites, (3) electron, X-ray and neutron based structural characterisation techniques and the associated fundamental theories and data analysis methods, (4) Phase-field crystal (PFC) model and the numerical methods.

Chapter 3 describes, in details, the design, making and commissioning of a novel apparatus for high temperature in-situ X-ray diffraction studies, the samples used and the setup of the in-situ X-ray diffraction experiments, followed by the relevant data processing and analysis methods used in the experiments. The Gleeble thermal shock experiments, and the high resolution transmission electron microscopy, synchrotron X-ray micro-tomography and focus ion beam plus scanning electron microscopy nano-tomography methods used to characterise the atomic, nano and microstructures of the thermally shocked bulk metallic glass composites are also included in this chapter.

Chapter 4 presents detailed studies on the local atomic structures of CuZr and NiTi binary metallic glass alloys using pair distribution function; and in-situ studies of the

evolution of atomic structures of the Vitreloy 1 (Vit1) bulk metallic glass alloy during different heating and cooling conditions.

Chapter 5 presents a comprehensive structural characterisation result for DH3 alloy (a ZrTi based metallic glass composite), and then the thermally shocked by using a Gleeble 3500 thermomechanical simulator. The local atomic structure in as-cast condition, and the structural transition across the amorphous-crystalline interface is presented together with the compositions, volume fractions and 3D morphologies of the nano and microstructures formed during thermal shock processing.

Chapter 6 describes the 2D binary vacancy phase-field crystal model, the numerical and parallel computing scheme used in the research, and the simulation results to show the effects of composition, atomic size ratio, and thermal conditions on local atomic structures. The development of a ternary vacancy phase-field crystal model based on the binary model and simulation results for different cases are described in this chapter as well.

Chapter 7 discusses, in details, the significance of key experimental and modelling results from this work, with particular emphases on how to use the combined in-situ experimental studies and phase-field crystal modelling to quantify and understand the atomic structures of metallic glasses and their correlations with alloys compositions and processing conditions.

Chapter 8 summarises the major scientific findings and contributions of the research to this important research field. Possible future directions to continue this work are also briefly discussed.

Chapter 2

Literature review

2.1 Ordered and disordered materials

All natural or man-made solid materials are made of atoms located in three dimensional
(3D) space. Dependent on whether there is symmetry or correlation in the 3D arrangement
(structure) of the atoms, solid materials can be generally classified as either ordered or
disordered materials [8]. The degree of freedom that is ordered or disordered can be
translational (crystalline ordering), rotational (ferroelectric ordering), a spin state (magnetic
ordering) or compositional ordering [8]. In the context of structural order of atoms, the
order can be in a full crystalline space group symmetry, or in a correlation. The strictest
form of structural order in a solid is lattice periodicity where a certain pattern of atoms (the
arrangement of atoms in a unit cell) is repeated again and again to form a translationally
invariant tiling of space, *i.e*, a long-range ordered atomic structure [9]. The possible
symmetries have been classified in 14 Bravais lattices and 230 space groups [9]. Most
naturally occurred metals and man-made metallic alloys have such crystalline periodic
symmetries and often called crystalline materials [2, 9].

However, a large group of natural materials do not have such long-range ordered atomic
structures, and they are generally called non-crystalline, disordered, amorphous or glassy
materials. For example, naturally occurred SiO_2 glasses and polymer-based materials

are typical disordered materials. The terminology varies in different contexts, which sometimes causes confusion. Generally, non-crystalline, disordered, and amorphous are often used without significant difference when referring to materials without long-range atomic structure order, while glass is mostly used to describe a disordered solid obtained from quenching a liquid.

Although lack of long-range atomic order (> 10 Å), most of disordered or amorphous materials contain short-range (0–5 Å) and medium range (5–10 Å) ordered atomic structures formed by the chemical bonding in a range of a few to a few tens of angstrom (Å), *i.e*, several bond lengths [10].

2.1.1 Thermodynamic description of state of disorder

Generally, materials can be viewed as a thermodynamic system containing a huge number of atoms, and two competing driving forces are responsible for driving the change of its state. As illustrated in Fig. 2.1a, any system that is not in equilibrium with its local environment tends to move to a lower energy state by decreasing its internal energy to a local minimum state. While, on the other hand, any thermodynamic system has the tendency to become a more disordered state by increasing its entropy as much as possible according to the second law of thermodynamics [11]. For any process the thermodynamic system experienced, the two driving forces compete each other until an equilibrium state is reached.

When the thermodynamic system is a material containing a large number of atoms, decreasing its internal energy means to move the atoms to distances where the minimum energy state is achieved for the materials [11]. Such minimum energy state can be, in principle, calculated based on the inter-atomic potentials and distances of the atoms inside the materials. Fig. 2.1b shows a general type inter-atomic potential as a function of atomic distance [12]. Many different types of such potentials have been proposed and used in the past [12], especially in the field of molecular mechanics, molecular dynamics modelling, for example the bond order potential [13], the Lennard-Jones potential [12] and embedded

atom model [14], *etc*. Apparently, the minimum energy is reached at the distance of bond length, and this energy is often called the bonding energy of atoms [11].
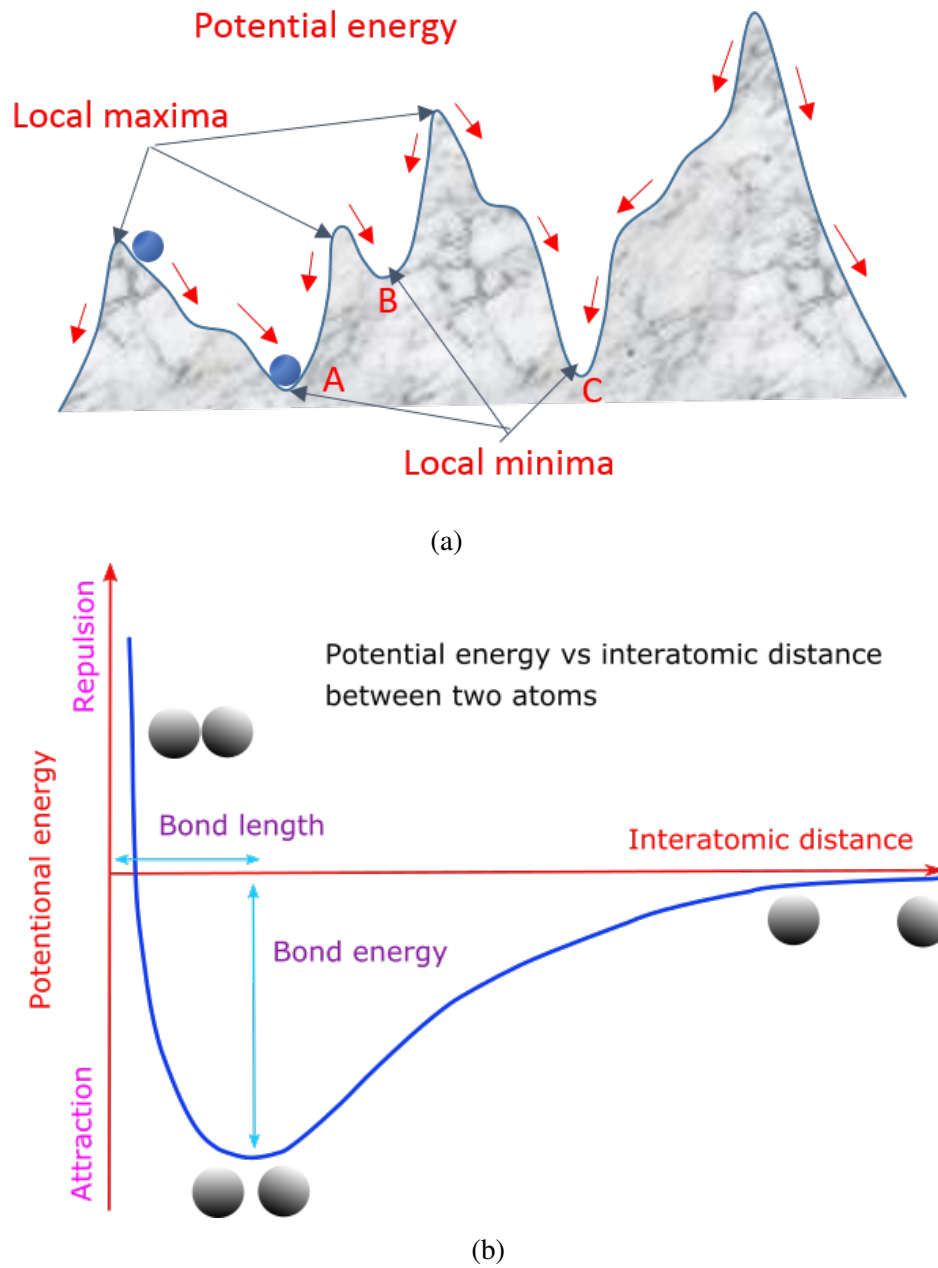
Fig. 2.1 (a) A schematic illustration, showing a potential energy curve with local maxima and minima, and (b) a general type atomic potential.

The concept of entropy is developed further in the context of statistical mechanics where a dynamic system can be considered to have a large number of microstates (*i.e*, microscopic configurations of individual atoms and molecules).

Entropy is defined to be proportional to the natural logarithm of the number of microstates, which can give rise to the observed macrostate of the system [15]. Mathematically, entropy in statistical mechanics is described as [15]:

$$S = -k_B \sum_i p_i \ln p_i \qquad (2.1)$$

Where, k_B is the Boltzmann constant; the summation is over all possible microstates of the system, and p_i is the probability that the system is in the i_{th} microstate [15].

Apparently, a macrostate with the largest number of microstates is more likely to be realised in a thermal equilibrium condition. Therefore, the final state of a given dynamic system (a material system) is determined by the tendency of realising the minimum internal energy with the maximum entropy.

Glass formation from liquid to solid can be viewed as the evolution of one specific thermodynamic system over temperature. The competing driving forces are the tendency of nucleating crystalline grains versus the slowing down of motion of atoms (*i.e.* increasing of viscosity) in an undercooled liquid as temperature decreases to below the melting temperature.

The grain nucleation rate of an undercooled liquid is often described by the classical nucleation theory [16] below:

$$R = N_s \cdot Z \cdot j \cdot \exp\left(\frac{-\Delta G^*}{k_B T}\right) \qquad (2.2)$$

Where, R is the nucleation rate; N_s is number of nucleation site; Z is Zeldovich factor. Essentially the Zeldovich factor is the probability of a cluster at the critical nucleus size to grow out to form a stable crystal. j is the rate at which molecules attach to the nucleus causing it to grow. $\Delta G^* = \left(\frac{16\pi(\gamma^{SL})^3 T_m^2}{3(\Delta H_m)^2}\right)\frac{1}{(\Delta T)^2}$ is free energy barrier of nuclei in which γ^{SL}
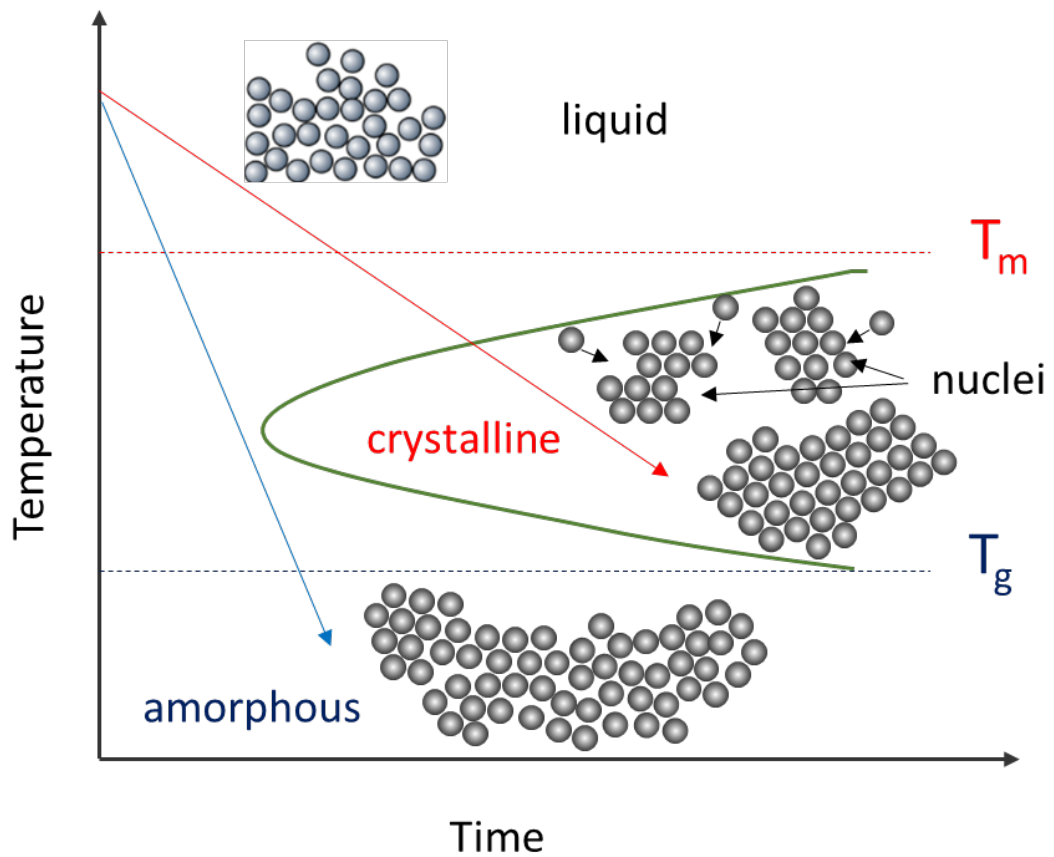
Fig. 2.2 A typical time–temperature–transformation (TTT) diagram.

is the interfacial energy of liquid and solid interface, ΔH_m is latent heat of melting, and ΔT is undercooling; T is absolute temperature and k_B is the Boltzmann constant.

Eq. 2.2 indicates that nucleation rate increases with the increasing of undercooling (ΔT), however the increase is countered by the slowing down of motion of atoms in the undercooled liquid, and eventually by configurational freezing [17] of the atoms in the undercooled liquid, leading to the formation of an amorphous state.

Viscosity, η, is a kinetic parameter [18] often used to measure the slowing down of motion of atoms and configurational freezing; and η increases exponentially with the decreasing of temperature T [18]:

$$\eta = \eta_0 \cdot \exp\left(W/kT\right) \tag{2.3}$$

Where η_0 is the high temperature limit of η, k is the Boltzmann constant, and W is an effective activation energy of viscous flow. For natural glasses, W is independent of temperature, therefore, $\log(\eta)$ and $1/T$ has a linear relationship.

The atomic structure of a metal alloy formed from a supercooled liquid is determined by the competition between the tendency of crystalline nucleation and increasing in viscosity, which can be summarised by the time–temperature–transformation (TTT) diagram as typically presented in Fig. 2.2. A nose-like boundary (the green curve in Fig. 2.2) separates the amorphous and crystalline regions [19]. A higher cooling rate (the blue line) leads to glass formation, while a lower rate (the red line) results in crystallisation. Apparently, alloys with good glass forming ability have a nose-like boundary shifted to the right. In addition, a narrow supercooled temperature region, *i.e.* a smaller $(T_m - T_g)$ coupled with a higher reduced glass transition temperature, $T_{rg} = T_g/T_m$ can also facilitate glass formation [19].

2.1.2 Mathematical description of geometrical configuration of atoms

For ordered materials, the atomic structure can be well described by crystallographic lattice periodicity, *i.e*, the equilibrium positions of all atoms can be regarded as a periodic extension of the building block - the unit cell, in which the position of the constituent atoms are well defined [20]. However, an exact determination of the positions of all atoms in an amorphous or disordered material is mathematically impossible, due to the lack of long range translational order. In practice, the atoms in an amorphous sample of a macroscopic size can be described, in principle, by a huge number of different configurations without any alterations in the physical properties of the bulk sample [21]. As such, the atomic structure of amorphous solids is normally described in terms of statistical distributions [21].

(a) H_2O [25]

(b) SiO_2 [25]

(c) $Cu_{64}Zr_{36}$ [26]

(d) Vit1 ($Zr_{41.2}Ti_{13.8}Cu_{12.5}Ni_{10}Be_{22.5}$) [27]
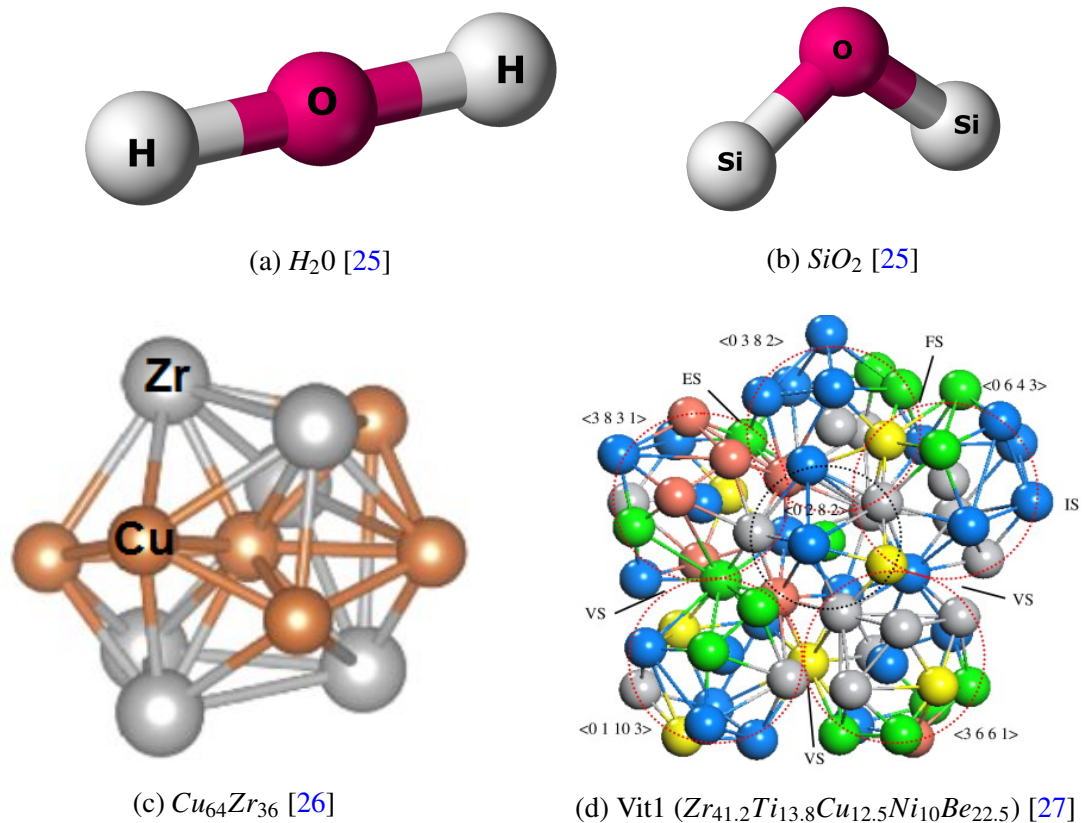
Fig. 2.3 The bond angles and structures for four cases, where the balls represent the nuclei and sticks represent the bonds.

For example, bond angle distribution, pair distribution function are often used in metallic glasses to describe the atomic structure [22].

2.1.2.1   Bond between atoms and their bond angles

Atoms are bonded together with chemical bonds, *i.e,* covalent bond, ionic bond, metallic bond, *etc*, to form molecules or atomic clusters [23].

Bond length and bond angles are two important parameters to describe the configuration of molecules and atomic clusters [24]. The bond length is defined as the average distance between the nuclei of two atoms that are bonded together in any given molecules or atomic clusters. Bond angle is the angle formed between two atomic bonds with a common atom linking the two bonds together [24].

Fig. 2.3 presents several examples of the bond angle for different molecules in 3D. H_2O in Fig. 2.3a has an ideal bond angle of 180 ° between the two O-H bonds, and SiO_2 in Fig. 2.3b has an ideal bond angle of 120 ° between the two Si-O bonds. Fig. 2.3c shows the simulated atomic configuration of $Cu_{64}Zr_{36}$, which is a typical binary alloy of metallic glasses. Fig. 2.3d shows the simulated atomic configuration of Vit1 alloy ($Zr_{41.2}Ti_{13.8}Cu_{12.5}Ni_{10}Be_{22.5}$). Clearly, metallic glasses, even the simplest binary alloys such as $Cu_{64}Zr_{36}$, have various bond angle for different atomic pairs.

For any atomic cluster, if a reference atom is chosen, any other atoms in the nearest neighbourhood bonded directly to the reference atom will have, in general, different bond angles. Statistically, the distribution of such bond angles can be used to describe the spatial relationships of such neighbouring atoms, *i.e*, the spatial arrangement of bonded atoms in the nearest neighbour atomic shell in a statistic way. For amorphous or disordered materials, the distribution of bond angles is one of the important parameters for characterising the atomic structures [22].

2.1.2.2 Pair distribution function and atom coordination number

Pair distribution function (PDF) describes the distribution of distances between pairs of particles in a given particle system, such as atoms, molecules, colloids, *etc.* [28]. Mathematically, PDF is the probability of a specific particle at a distance r from a reference particle [28]. The pair distribution function is a standard method used for describing the atomic structures of glasses, polymers and liquids [28].

As shown in Fig. 2.4, PDF in a particles system represents the changes of number density with distance r from a reference point. In other words, it is a probability measurement of finding a particle at a distance r away from a reference particle provided. The general algorithm to calculate PDF involves determining how many particles are located in a distance of r away from the reference particle.

The mathematical definition of the PDF g(r) is,
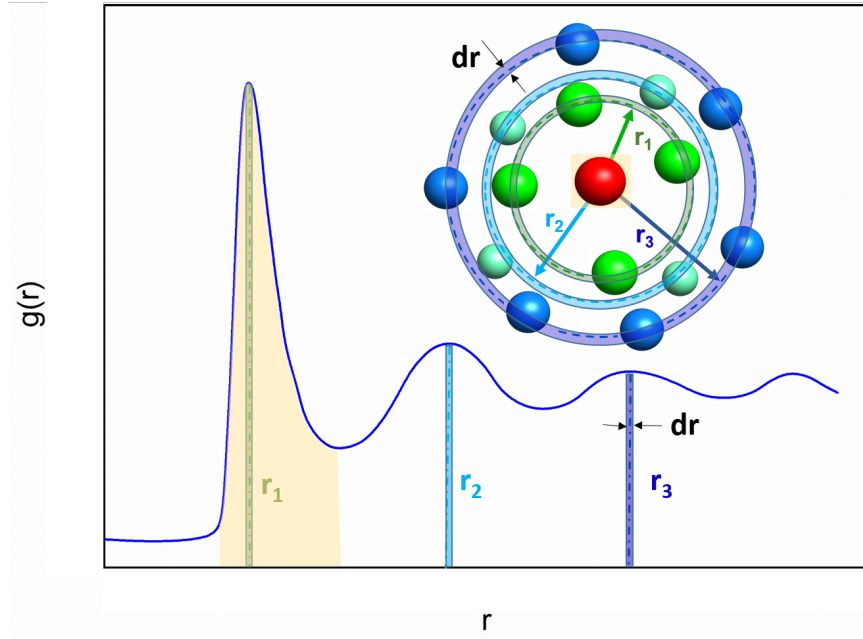
Fig. 2.4 A typical pair distribution function, $g(r)$, local maxima in the $g(r)$ is obtained at different atomic distances, $\mathbf{r_i}$ (i=1, 2, 3...) from the reference atom (the red atom). The areas covered by the $g(r)$ peaks are the number of nearest neighbouring atoms. For example, the nearest atom coordination number can be obtained by integrating the area (the shaded area in yellow) under the first peak [21].

.

$$g(r) = \frac{1}{4\pi\rho_0 N r^2} \sum_{v}\sum_{\mu} \delta\left(r - r_{v\mu}\right) \qquad (2.4)$$

where, ρ_0 is the averaged number density of atoms in the system of N atoms. δ is a Dirac delta function [29]. PDF is a one-dimensional function which has peaks at distances, $r_{v\mu} = \left|\mathbf{r}_v - \mathbf{r}_\mu\right|$, the distance between the v_{th} and μ_{th} atoms.

Another extensively used correlation function is the reduced pair distribution function, $G(r)$ [28]:

$$G(r) = 4\pi\rho_0\left(g(r) - 1\right) \qquad (2.5)$$

$G(r)$ converges to zero at a large r. Although less physically intuitive than $g(r)$, it is widely used in X-ray or neutron scattering studies [21]. The advantage of using $G(r)$ is that it can be directly calculated via Fourier transform of the structure functions obtained from diffraction experiments. Structure functions of materials can be calculated based on the total scattering intensity of X-rays or neutrons. The procedure will be explained in details in section 2.3.

With a well-defined PDF peak, the number of neighbour atoms in the atomic shell, *i.e*, the coordination number N_C around a reference atom, can be calculated by integrating the area under that peak (*e.g.* the shaded area in Fig. 2.4):

$$N_C = \int_{r_1}^{r_2} 4\pi r^2 \rho_0 g(r) dr \tag{2.6}$$

Where, r_1 and r_2 define the left bound and right bound of the first PDF peak, *i.e*, the first coordination shell. The peak height is inversely proportional to the peak width of PDF [30]. The width of peak contains information about thermal motion of the atoms, or static disorder [21], and for amorphous or disordered materials, peak width often gives information about the degree of disorder in the structure [21]. Sharp and intensive PDF peaks often indicates more ordered structure, and *vice versa*.

The position of peaks give atomic pair distance of that particular atomic shell, and any apparent split or separation of a peak indicates changes of atomic structure in that particular shell directly [28, 31]. Such characteristics are very common in disordered systems such as gases, liquids, and glasses. For long range ordered crystals, all neighbours at all lengths are well defined, which are characterised by sharp PDF peaks in short to long range radial distance.

Fig. 2.5 shows typical PDFs for gas, liquid, and crystalline solid, respectively together with the corresponding spatial arrangement of atoms for each case. For an ideal gas without interactions of atoms, its PDF should be unity at all atomic distance. However, most real

(a) Gas
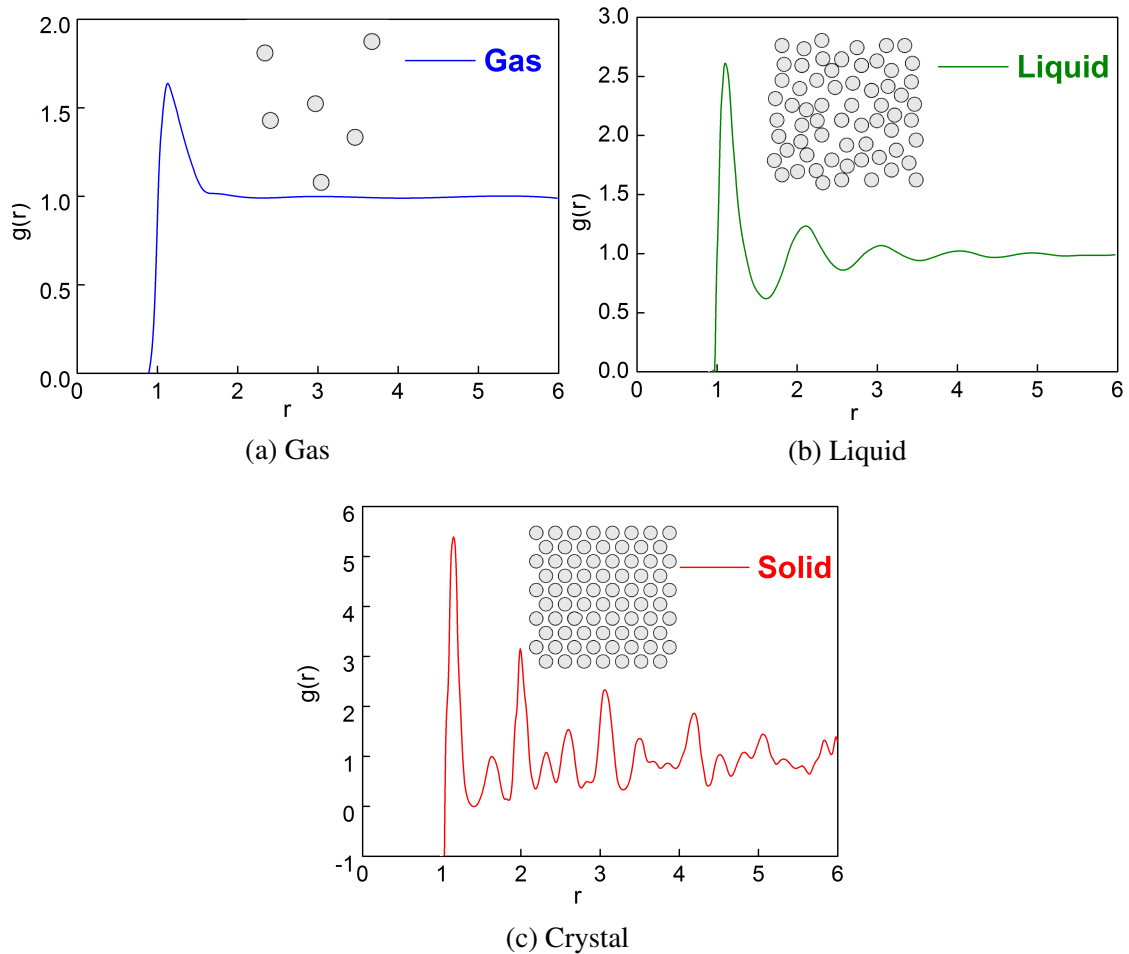
(b) Liquid

(c) Crystal

Fig. 2.5 Typical pair distribution functions for (a) gas, (b) liquid, and (c) crystalline solids.

gas systems still have atoms that are interacting with each other within the first nearest neighbourhood. Such reactions are reflected in the first PDF peak in the short atomic range in Fig. 2.5a [32]. In liquid, more atoms beyond the first nearest neighbour are interacting and strongly correlated, leading to a modulation of g(r) extending over a few more neighbour shells [32] as indicated by Fig. 2.5b. The oscillations of PDF are rapidly damped, indicating a gradual smearing out of the short-range order [32] until g(r) reaches unity at a relative long range.

For a full crystalline structure, Fig. 2.5c illustrates the well defined sharp PDF peaks. Since crystal is anisotropic, the PDF involves an average over all orientations of the lattice.

The structures of liquids and amorphous solids are quite similar, hence their PDFs are generally difficult to be distinguished from each other [32]. There is short range order at

short atomic distance but the long-range order is lost. The main difference is of course that amorphous materials are rigid. Hence on the microscopic level, atoms in amorphous solids just vibrate around their equilibrium position. In liquids, time plays a more important role and various time dependent correlations functions can be defined [32].

A comparison between the structural properties of amorphous and liquid metals shows that the general features in the structure of the amorphous phase, are similar to those of the liquid state, except that a shoulder in the second peak was observed in both structure function and PDF [33]. In addition, the intensity of the first PDF peak of amorphous solids is higher than that of liquid, since the nearest neighbouring atoms of amorphous solid is more dense–packed.

The PDF can be calculated directly by extracting particle positions from microscopy images of atoms or particles [34], but most often it is calculated by Fourier transformation of the diffraction patterns of materials obtained from X-rays, neutrons or electrons diffraction experiments. In those cases, significant space and time averaging occur [35].

2.1.2.3 Voronoi tessellation and Delaunay triangulation

In mathematics, a Voronoi tessellation [37] is a partitioning of a plane into regions based on distance to points in a specific subset of the plane. The set of points (called seeds, sites, or generators) is defined beforehand (the black points in Fig. 2.6), and for each seed there is a corresponding region consisting of all points closer to that seed than to any other (the red convex polygon in Fig. 2.6c). These regions are called Voronoi cells.

The Voronoi tessellation of a set of points is dual to its Delaunay triangulation (the black triangle in Fig. 2.6b). In other words, it is a diagram created by taking pairs of points that are close together and drawing a line that is equidistant between them and perpendicular to the line connecting them. That is, all points on the lines in the diagram are equidistant to the nearest two (or more) source points. This technique is often used to unambiguously determine the neighbouring atoms, *i.e*, coordination number without the need for a cutoff
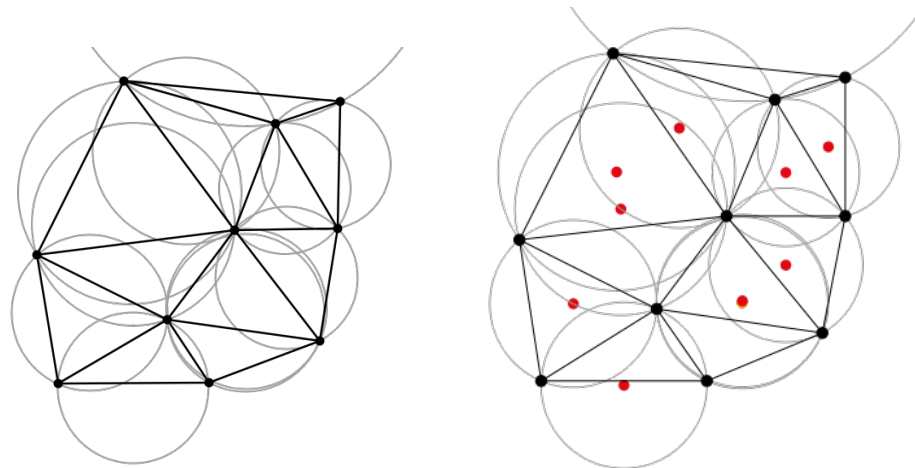
(a) The Delaunay triangulation in the plane with circumcircles.

(b) The Delaunay triangulation with all the circumcircles and their centres (in red).
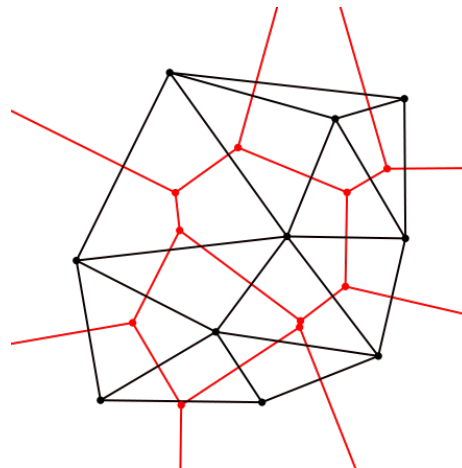
(c) Connecting the centres of the circumcircles produces the Voronoi diagram (in red).

Fig. 2.6 Schematic illustrations, showing the procedures for Delaunay triangulation and Voronoi tessellation [36].

[35]. Only the atoms sharing a common cell boundary/surface are regarded as nearest neighbours.

Voronoi tessellations of regular lattices of points in two or three dimensions give rise to many familiar tessellations. A 2D lattice gives an irregular honeycomb tessellation, with equal hexagons with point symmetry; in the case of a regular triangular lattice, the honeycomb tessellation is regular; in the case of a rectangular lattice, the hexagons reduce

to rectangles in rows and columns; a square lattice gives the regular tessellation of squares [37].

2.1.2.4 Crystallographic description

Crystallography [38] is a well established methodology to describe atom arrangement in 3D space for ordered materials. X-rays, neutron and electron diffractions are the commonly used experimental techniques to obtain crystallographic information from crystalline materials [39, 40].

Fig. 2.7a illustrates the principle of X-ray crystallography. When an incident X-ray beam passes through a crystalline material, such as a single crystal, the constructive interference of the diffracted X-ray beam forms diffraction patterns in the area detector. Diffraction patterns vary due to differences in the structures of materials, and diffraction spots are formed for single crystals, sharp concentric rings for polycrystalline materials, and diffuse halo for amorphous materials [38].

By integrating azimuthally the 2D diffraction patterns, 1D diffraction spectra can be obtained. Fig. 2.7b presents the typical diffraction spectrum from single crystal of α-Fe. Different crystalline plane gives rise to Bragg peaks at different reflection position, if the index of reflections satisfies the Bragg' law [43]:

$$2d \sin \theta = n\lambda \tag{2.7}$$

Where, θ is the diffraction angle; λ is the wavelength of incident X-ray beam; n is a positive integer, accounting for the multiple layers of lattice plane; $d = \frac{a}{\sqrt{h^2+k^2+l^2}}$ is the inter-planar distance, in which a is the lattice spacing, h, k, l is the Miller indices [43] of the lattice plane.

By Fourier transform of the scattered X-ray intensity, the structure factor (a mathematical function describing the amplitude and phase of a wave diffracted from crystal lattice planes
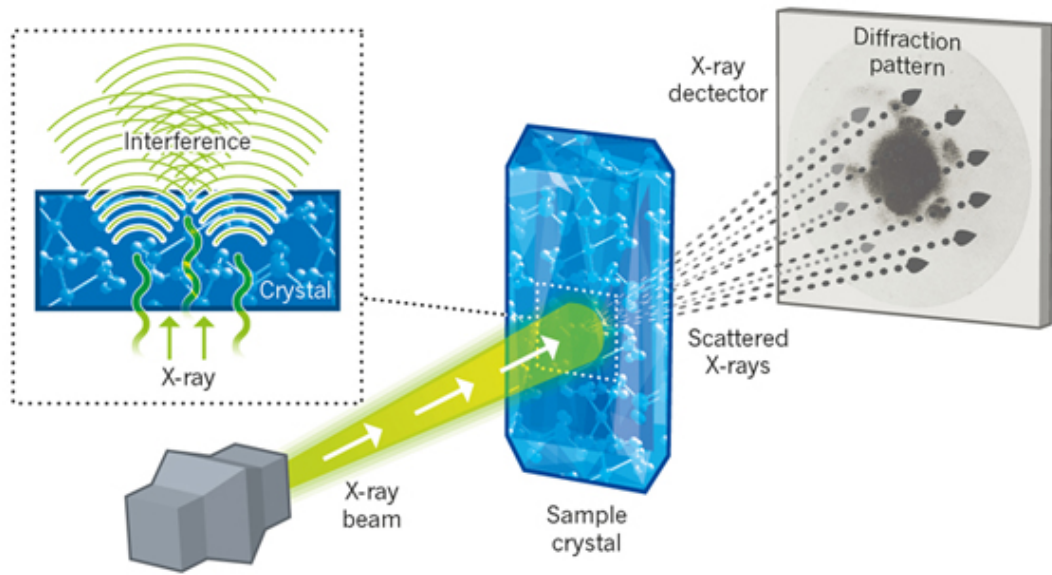
(a) A schematic presentation of an X-ray diffraction experiment [41].
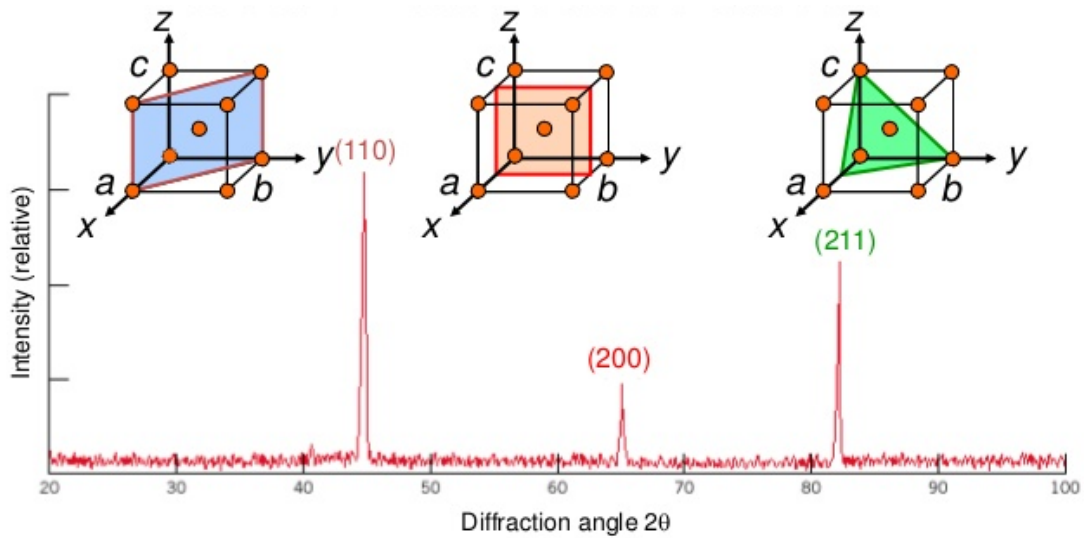
(b) 1D diffraction spectrum of α-Fe [42].

Fig. 2.7 (a) A sketch, showing an X-ray diffraction experiment; (b) the diffraction spectrum of single crystal of α-Fe.

characterised by Miller indices h, k, l) of the materials can be calculated. Finally, the crystal structure can be determined by the structure factor. Giving a known crystal structure of an unit cell [44], structure refinement can be used to determine the structure of unknown phases, or to measure the displacement of lattice planes.

2.2   A brief review of metallic glasses and composites

Metallic glasses (MGs) were firstly discovered in $Au_{75}Si_{25}$ binary alloy in 1959 at Caltech, USA by Klement, Willens and Duwez [3]. Unlike conventional silicon oxide glasses, MGs primarily consist of metallic elements boned together via metallic bonds to form amorphous rather than crystalline structure. The combination of "metallic" and "glass", gives a lot of unique structure related properties that do not exist in conventional metal alloys. For example, higher tensile yield strengths, higher elastic strain limits [45], excellent resistance to wear and corrosion [46]. In addition, metallic glasses in supercooled liquid region possess a good thermoplastic processing capability. Some MGs, *e.g*, Vitreloy alloys, have been already commercialised for sports goods, medical devices, electronic appliance, *etc.* [5].

2.2.1   The development of metallic glass alloys

Metallic glasses are actually the "frozen liquids" that are made by quenching their liquid melts. Since most molten alloys tend to crystallise when they cool down below the melting or liqudus temperature. Therefore, in order to retain amorphous structure, the heat needs to be extracted sufficiently fast so that the liquid alloys are frozen via the so-called glass formation process.

In the early years of metallic glass research and development, rapid quenching with an extremely high cooling rate of $10^5 - 10^7$ K/s [47] was often used to suppress the nucleation and crystal growth of the competing crystalline phases and freeze the liquid atomic configuration [47]. Since the splat quenching method used in the discovery of the first metallic glass $Au_{75}Si_{25}$, more rapid quenching techniques had been developed and used in 1970s -1980s [48]. One of the most successful continuous rapid quenching techniques is melt spinning, which is able to produce metallic glasses in the forms of line, ribbon, and sheet [48]. Until now, the making of metallic glasses are still restricted to 1D lines or 2D ribbons rather than bulk forms if such high cooling rate is needed.

Dependant on the alloy elements used, metallic glasses are classified into four categories by Cheng and Ma [22]: (1) late transition metal-noble metal (LTM–NM), (2) simple metal-rare earth metal (SM–RE), (3) early transition metal-late transition metal (ETM–LTM), and (4) alkali metal-late transition metal (AM–LTM). However, almost all alloys with good glass formation ability (GFA) found so far belong to ETM–LTM.

ZrCu binary alloys belong to ETM-LTM, and are good glass formers [48, 49] with a wide range of tuneable compositions for glass formation. Many multi-component bulk metallic glass (BMG) systems have been developed based on CuZr binary systems. However, NiTi binary alloys [50, 51] are quite different, their structures are very sensitive to composition, and a small change on composition can lead to changes from amorphous to crystalline state.

NiTi alloys not only possess unique properties (shape memory effect) that make them promising candidates for practical applications in high technology, but are also glass-formers. A crystal-to-amorphous (C-A) transition can be achieved in a NiTi based alloy system through tuning the composition.

Because of the above characteristics, ZrCu and NiTi binary systems are chosen as the model alloy systems in this research to study the changes of atomic structures as functions of chemical compositions as detailed in Chapter 4.

From application perspective, enormous number of research and publications ($\sim$ 17,522 up to now) have been devoted to develop new alloy systems that can be made in bulk form using low cooling rate techniques, such as conventional copper mould casting [52]. In 1974, it was found that adding Pd into several metallic glass alloy systems can significantly increase their glass forming ability. For example, Chen [53] produced the first bulk metallic glass (BMG) rods ($\sim$0.5 mm) with the composition of Pd-T-P (T= Ni, Co, Fe), such as $Pd_{77.5}Cu_6Si_{16.5}$ using suction casting with a cooling rate of 10^3 K/s. A further improvement was achieved in 1982 by Turnbull and his co-workers, and they produced $Pd_{40}Ni_{40}P_{20}$ glassy ingots with a diameter of 5 mm using surface etching followed by heating and cooling cycles [54]. However, Pd based BMGs are too expensive to be commercialised, and research interest on them soon faded out.

Since 1980s, research group led by Akihisa Inoue in Tohoku University, and that by William L. Johnson of Caltech have made breakthrough in discovering La [55], Mg [56], and Zr [57, 58] based multi-component alloys with large undercooling and low critical cooling rates (1 K/s to 100 K/s) for glass transition. Their glass forming abilities are very similar to natural oxide glasses [48]. Using conventional copper mould casting, bulk glassy samples with the thickness of 1 cm can be produced.

In 1992, Johnson and Peker developed a quinary alloy based on Zr-Ti-Cu-Ni-Be, *i.e,* $Zr_{41.2}Ti_{13.8}Cu_{12.5}Ni_{10.0}Be_{22.5}$ [58]. With critical casting thickness of up to 10 cm possible in silica containers, the alloy became the first commercially successful BMG, which is known as Vitreloy1 (Vit1). Several variants were also developed based on this quinary alloy system, including Vit2 ($Zr_{46.75}Ti_{8.25}Cu_{7.5}Ni_{10}Be_{27.5}$), Vit4 ($Zr_{46.75}Be_{27.5}Ti_{8.25}Cu_{7.5}Ni_{10}$), *etc.*

Compared to conventional structural materials, such as steel, Vitreloy alloys have similar densities but high Young's modulus, elastic strain-to-failure limit, and high tensile yield strength. Vitreloy contains a large number of different sized atoms, which lead to high viscosity [58]. Above T_g in the supercooled liquid regime, Vitreloy remains stable against crystallisation. Hence, Vitreloy is a good model material system to investigate the structure evolution during the heating and cooling process.

Despite of many exciting mechanical properties [48, 63], most of bulk metallic glasses have not been used as structural material due to their poor ductility. In order to obtain a good combination of strength and ductility, many types of BMG based composite were developed. Fig. 2.8 shows four different cases of bulk metallic glass matrix composites (BMGMC). Fig. 2.8a and b show the BMGMC reinforced by introducing external phases into the BMG matrix, such as carbon fibre and WC particles. Such composites have a sharp phase interface between the BMG matrix and reinforced phases.

There is another type of BMG based composites, in which ductile crystalline phase nucleates and grows in-situ from the super-cooled liquid when the liquid is continuously cooled down to form metallic glass [64, 65]. A strong phase interface between ductile
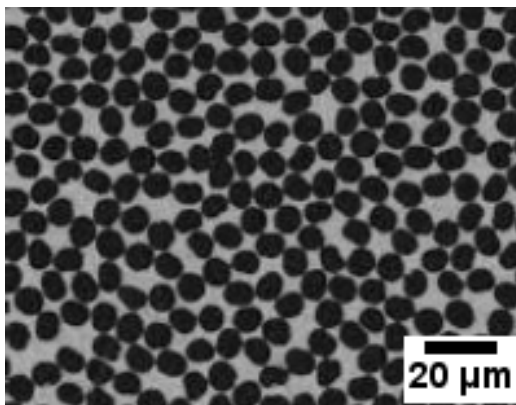
(a) Carbon fibre reinforced BMGMG [59].
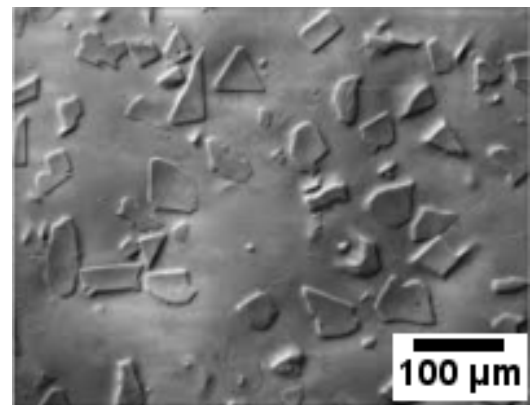
(b) WC reinforced V106 BMGMC [60].
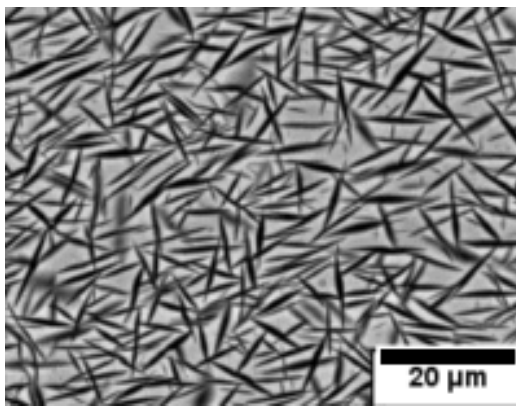
(c) Mg-based BMGMC [61].
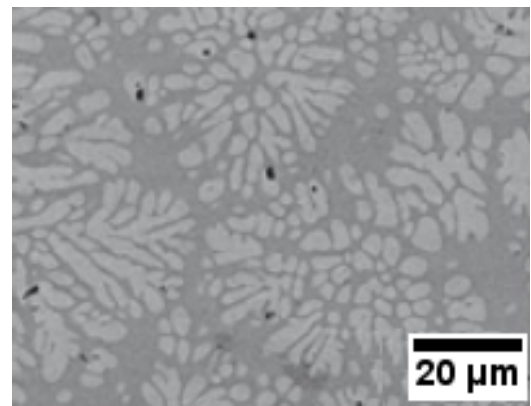
(d) DH1, Zr-based BMGMC [62].

Fig. 2.8 The typical SEM microstructure of bulk metallic glass matrix composites.

crystalline phase and amorphous matrix is formed *in-situ* via metallic bonding. Fig. 2.8c shows that needle-shaped intermetallic phases are formed in-situ within the Mg–based amorphous matrix [61]. Fig. 2.8d shows that crystalline phases with dendrite morphology are formed from a Z–based alloy, DH3 ($Zr_{39.6}Ti_{33.9}Nb_{7.6}Cu_{6.4}Be_{12.5}$). In addition to the strong interface as one of the most important strengthening elements for the composite, the morphology, size, volume fraction and distribution of the crystalline phases are also very important parameters to control the mechanical properties of the composites [62, 66, 67, 60].

In this research, the DH3 alloy is used to study the effect of thermal shock on the changes of nano and micro–structure of BMGMC as described in chapter 5.

2.2.2   The atomic structures of metallic glasses

Unlike crystalline alloys, metallic glasses lack long range atom translational periodicity, and it is impossible to determine their atomic structures using conventional crystallographic method. Since the discovery of metallic glasses, studying and characterising the atomic structures have been the centre of metallic glass researches [68, 22].

Bernal's dense random packing model [69] is amongst the generally accepted structural model, where metallic glasses are considered as frozen metallic liquids with an atomic arrangement controlled by mainly geometrical sphere packing. Bernal's concept [69] is able to successfully model the structures of pure metals together with alloys with constituent species of comparable atomic sizes. Nevertheless, it is not suitable to describe the short- and medium-range order [68] discovered in existing multicomponent metallic glass alloy systems with much lower critical cooling rates.

Generally, in most metallic glass systems, the disordered atom arrangement can only be maintained in a particular length scale [22]. Atoms intend to constitute a short-range order where the local nearest-neighbour surroundings of every atom are similar to any other equivalent atoms.

Most good glass formers often have a slightly higher density compared to those amorphous alloys discovered in the early years of metallic glass researches, which need higher critical cooling rates. This observation indicates that higher packing density is critical to attaining high glass forming ability. Consequently, densely packed icosahedral clusters have been identified as the possible structural model of BMGs. Numerous simulations and experimental studies have indicated that icosahedra are an energetically favourable atomic structure in metal–metal-based metallic glasses [57, 58, 70].

Actually, the atomic configurations of multi-component BMGs are quite diverse because of the differences in interatomic interactions among the constituent elements. Structural/-chemical heterogeneity is also a general phenomenon in multi-component BMGs [71], as

proved by the previous studies of structure and property variations at different length scales in a number of metallic glass systems, such as Zr, Al–based BMGs [72–74].

Currently, how to determine the atomic structure of metallic glasses are still a very active research. Many experiment techniques, such as X-ray absorption fine structure (XAFS) [22], pair distribution function, TEM, *etc*, have been used to extract statistical information about the average glass structure [68]. These experimental data are very valuable for validating the proposed structural models.

In addition, computational models are alternative choices for studying the structure of metallic glasses [22], especially powerful for constructing atomic structure in 3D and providing deep understanding on the interactions among atoms [22]. The widely used modelling methods are reverse Monte Carlo method [75, 76], molecular dynamics simulations [22], dynamic density function theory [77], phase-field crystal model [78], *etc.* In this research, phase-field crystal models were used extensively to study the glass formation of binary and ternary alloys. The detailed theory and models developed and their applications to the interpretations of the atomic structures in binary and ternary alloys are described in Chapter 6.

2.3   Experimental methods for structural characterisation

In this section, the relevant and complementary structural characterisation techniques used in this research are reviewed to provide the scientific background for the experiments and data analyses.

2.3.1   Synchrotron X-rays

X-rays are electromagnetic waves with wavelengths ranging from ultraviolet light to gamma rays as illustrated in Fig. 2.9. The hard X-rays with the wavelength in between 0.1 and

1 Å are often used as radiation probes to measure interatomic distances and study atomic structure [43, 21].
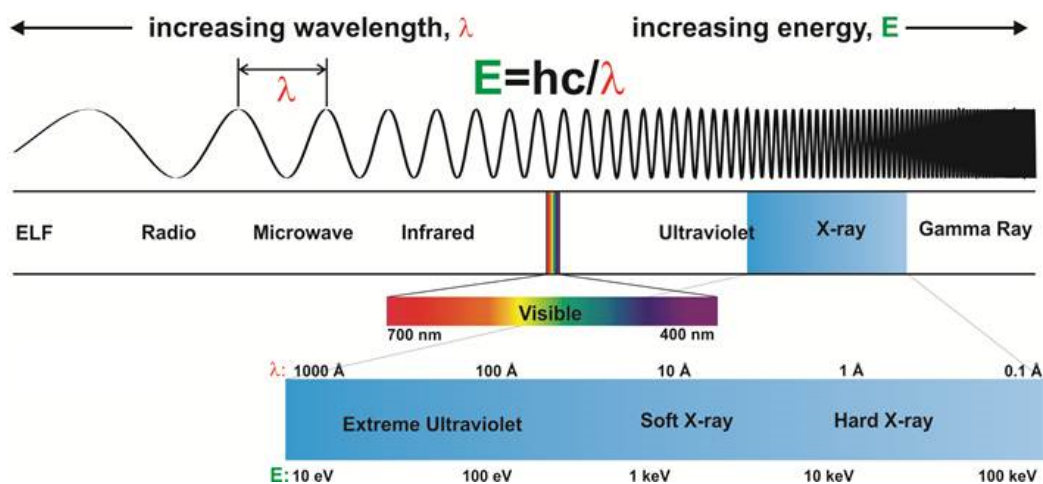
Fig. 2.9 The electromagnetic spectrum that spans the range from radio waves at long wavelengths to gamma rays at short wavelength [79].

Laboratory based X-rays and synchrotron X-rays are two commonly used X-ray sources. Lab based X-rays are produced by X-ray tubes, or rotating anodes [80].
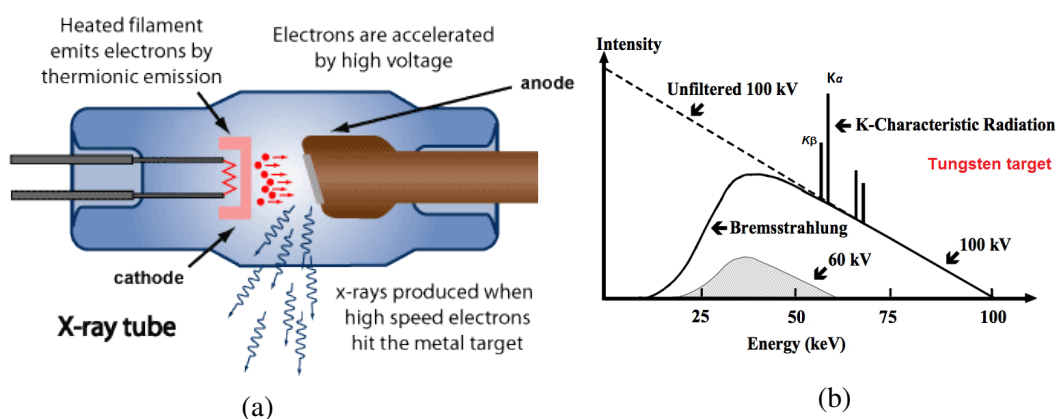
Fig. 2.10 (a) A schematic representation of X-ray tube [81]. (b) The X-ray energy spectrum generated by an X-ray tube with a tungsten target [82].

Fig. 2.10a show a typical X-ray tube with the key parts for generating X-rays. Electrons are emitted from a heating filament (the cathode) and they are accelerated towards the

anode (metal targets made by W, Cu, Cr or Mo) under the applied high voltage of typically a few to a few hundred kVs in a vacuum environment. Upon colliding with anode, the deceleration of electrons by the metal targets produce X-rays with a continuous spectrum, called Bremsstrahlung spectrum [83]. In addition, incident electrons that have sufficient energy can knock electrons out of the inner shells of the target metal atoms and create vacancies. When electrons from higher states drop down to fill those vacancies, X-ray photons (characteristic X-rays) are emitted with the precise energies determined by the difference between the electron energy levels. These characteristic X-rays have fixed wavelengths with brilliance of several orders of magnitude higher than the bremsstrahlung X-rays [83], for example, K_α and K_β in Fig 2.10b. These characteristic X-rays are used for characterisation of crystalline structures.

The wavelengths of the characteristic X-rays generated from X-ray tubes are determined by the metal target materials, and are not tunable. While electron synchrotrons can produce tunable X-rays with much higher brilliance.

At first, the X-rays generated by the bending magnets in an electron synchrotron was considered as a nuisance in parasitic mode due to the undesired energy loss in the context of particles physics in General Electric in US [84]. However very soon after, it was found that synchrotron X-ray is far superior to the conventional X-rays generated by X-ray tube with very broad spectrum, extreme high brilliance and flux, and tenable energies (wavelength) [85].

To make a better use of synchrotron X-rays, a number of the 2nd generation synchrotron facilities were built around the world and solely dedicated to the production of synchrotron light using the bending magnets [86]. With an extreme wide field of research and applications found for synchrotron X-rays, the 3rd generation synchrotrons facilities have been built around the world since the late of 1980s, including European Synchrotron Radiation Facility [87] in Grenoble, France, the Advanced Photon Source [88] in USA, the SPring-8 in Japan [89], and the Diamond Light Source (DLS) in UK [90]. Currently there are ~ 50 syncrotron X-ray facilities operating around the world. In addition to bending magnets,

special arrays of magnets called insertion devices, such as wigglers and undulators [91] are used routinely in the 3rd generation of synchrotron source to produce much brilliant and tunable X-rays that serve for almost all disciplines of scientific research and technology development [92].

Fig. 2.11 shows the typical layout of the 3rd generation of synchrotron X-ray facilities. Firstly, free electrons are created in an electron gun and then these electrons are bundled and linearly accelerated to certain energy level by using a linear accelerator [93] before being injected into the pre-accelerator, *i.e*, booster synchrotron [94]. The electrons are accelerated further in the booster ring to reach 99.99999% of the speed of light [94], and then injected into the storage ring. The electrons circulate inside the storage ring have a speed approximately to the speed of light [87]. Insertion devices, *i.e*, wigglers and/or undulators are installed at certain sectors of the storage ring to generate X-rays for different uses.
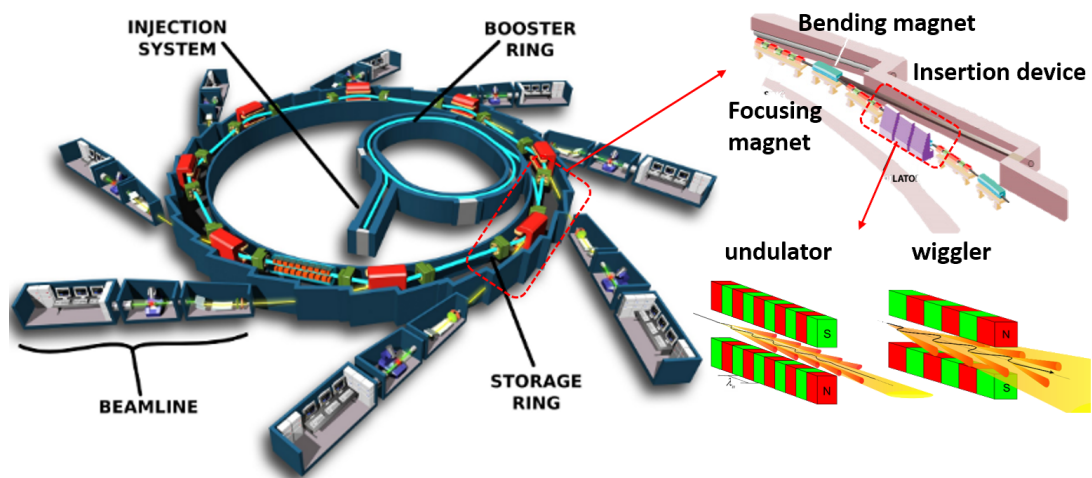
Fig. 2.11 General layout of the 3rd synchrotron radiation source facility. (Copyright EP-SIM 3D/JF Santarelli, Synchrotron Soleil); Magnets and insertion devices in storage ring (Copyright ESRF); undulator and wiggler (Copyright Deutsches Elektronen-Synchrotron).

The most important characteristic of synchrotron X-ray is the extreme brilliance which is defined as [80]:

$$brilliance = \frac{photons}{second \cdot mrad^2 \cdot mm^2 \cdot 0.1\%bandwidth} \tag{2.8}$$

where, *photons* is number of photons produced; $mrad^2$ is the angular divergence of the photons, or how fast the beam spreads out; mm^2 is the cross-sectional area of the beam; $0.1\%bandwidth$ is defined as $0.1\%bandwidth = \frac{\Delta\lambda}{\lambda} = 10^{-3}$ [80]. The greater the brilliance, the more photons of a given wavelength and direction are concentrated on a unit area per second [95].

For example, the X-rays produced by DLS [90] is 10^{11} times more brilliant than that produced by an X-ray tube. In addition, Synchrotron X-rays are tunable in energy and coherence [85], and can be focused into focused beam using X-ray optics for high spatial resolution structural characterisations, for example nano-tomography characterisation with a spatial resolution of 158 nm [96]. The unique radio frequency control of the circulating electrons inside the storage ring can be also utilised to create synchronised very short pulses in the range of nano seconds [97] for the studies of dynamic process with very high temporal resolution during the relevant in-situ experiments, such as ultrasound cavitation [98], *etc*.

2.3.2 X-rays interaction with matters and total scattering

Materials characterisations using X-rays are based on detecting and measuring the signals obtained from the interactions between X-rays and matters. X-rays interact with matters through the oscillating electromagnetic field, which strongly stimulates the electron resonance in atoms [99]. Fig. 2.12 illustrates all possible interactions [100], and they can be generally categorised into two main scattering processes, *i.e.* Rayleigh scattering and Compton scattering; and two absorption processes, *i.e.* photoelectric absorption and pair production.

Apparently, photoelectric absorption is the most dominant mechanism for X-ray attenuation [101, 99]. The actual process is that, after an incident X-ray photon (**B** in Fig. 2.12)
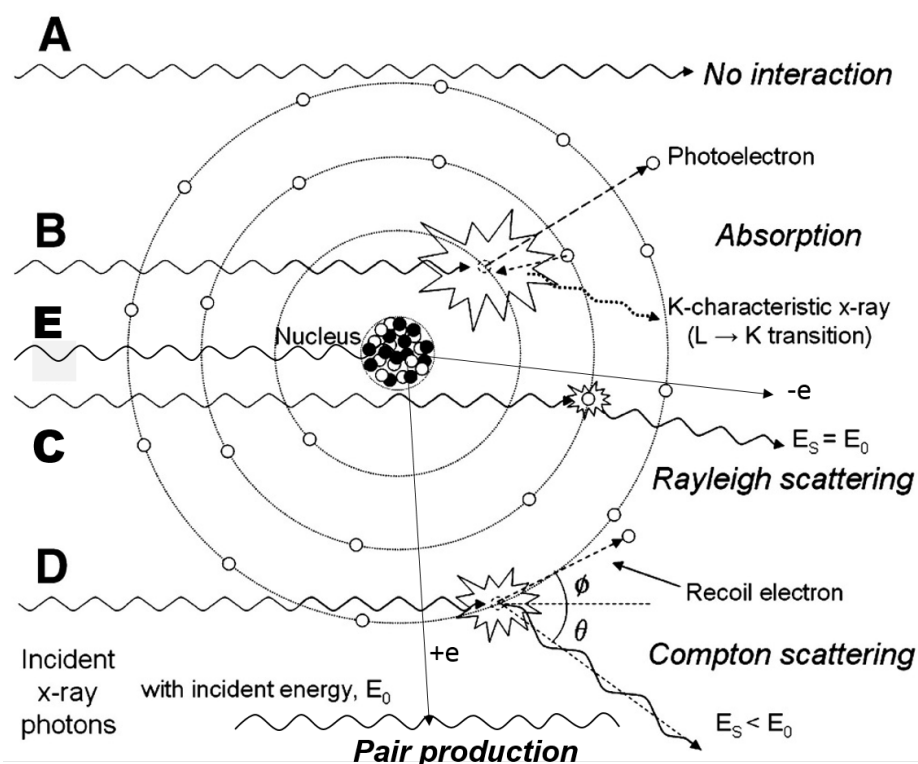
Fig. 2.12 An illustrative description of X-ray interactions with matters: (A) Transmitted X-ray beam without any interaction. (B) Photoelectric absorption. (C) Rayleigh scattering. (D) Compton scattering. (E) pair production [100].

with higher energy "hits" on an electron within the materials, the electron is knocked off from its energy shell with a kinetic energy equal to the energy difference between the incident X-ray photon and binding energy of the electron shell. Then, an electron from an outer shell with less binding energy will leap and refill the vacancy in the inner shell, producing a characteristic X-ray with the energy equal to the binding energy difference between the original outer electron shell and final inner electron shell.

The photoelectric interaction [102] may only occur on the condition that the incident X-ray photon energy is the same as or higher than the binding energy of the electron [102]. Once the X-ray energy is equal to the electronic binding energy, the photoelectric effect tends to be energetically feasible and a significant increase in attenuation happens [102]. As the incident X-ray photon energy increases beyond that of the electron shell binding energy, the possibility of photoelectric absorption decreases proportionally with $1/E^3$ where E is

the X-ray photon energy. The dramatic increase in the possibility of photoelectric absorption occurring at the energy shell binding energy leads to an absorption edge in X-ray attenuation curve as illustrated later in Fig. 2.16. After photoelectric interaction, the majority of the incident X-ray photon energy is absorbed because of the further electron-electron ionization stimulated by kinetic motions of the free photoelectron [103].

Furthermore, the probability of photoelectric absorption occurrence is governed strongly by the atomic number (Z) of the materials and the photon energy (E) of the incident X-rays and is proportional to Z^3/E^3 [102].

Rayleigh scattering is actually an elastic scattering where an incident X-ray photon (C in Fig. 2.12) interacts with an electron and then be scattered with no loss in energy [102]. When Rayleigh scattering occurs, the energy of interacted electrons temporarily increases, but not enough to remove them from the atom. Then an X-ray photon is emitted with the same energy as incident beam but with a slightly different direction after the energetic electrons return to original energy level without any loss of photon energy. Without knocking off the electron, the atom does not have significant recoil, hence most of Rayleigh scattering are forward scattering with a small angle [102]. The possibility of Rayleigh scattering increases with atomic number density of the species of atom and decreases with the energy of the incident X-ray photon [102].

Unlike the Rayleigh scattering, Compton scattering is an inelastic interaction between an electron and incident X-ray photon (D in Fig. 2.12), the energy of which is much higher than the binding energy of the interacted electron. During the Compton scattering, part of the X-ray photon energy is transferred to an electron, which causes a recoil and removal of the electron from energy shell of the atom with a certain angle. While the rest of the incident X-ray photon energy is transferred to a scattered X-ray photon with a trajectory of angle relative to that of the incident photon. The scattered X-ray photons may travel at any angle *theta* relative to the incident beam from 0° to 180°, the recoiled electron however may only be directed forward relatively at an angle *theta* from 0° to 90°.

Pair production, as illustrated in case E of Fig. 2.12, is the interaction of an incident X-ray photon with nucleus to produce an electron and a positron when the incident X-ray photon energy is above the sum of the rest of mass energies of an electron and positron (2×0.511 MeV = 1.022 MeV) [102]. Pair production is the dominant mode of photon interaction with matter when the incident photon energy is in MeV scale or higher [102], but rarely being considered in the X-ray energy range below a few hundreds of KeV [102].

X-ray total scattering is a method [35] of measuring all X-ray photons scattered from a sample by all interactions with the incident X-ray as described above. The actual measured total intensity, $I_T(Q)$, of the scattered X-ray (similar if neutron is used) is composed of several parts:

$$I_T(Q) = I_C(Q) + I_{IC(Q)} + I_{MC}(Q) + I_{BC}(Q) \qquad (2.9)$$

Where, $I_C(Q)$ is the coherent scattering intensity (Raleigh scattering intensity for X-ray); $I_{IC}(Q)$ is the incoherent scattering intensity (Compton scattering); $I_{MC}(Q)$ is the multiple-scattering intensity; and $I_{BC}(Q)$ is the background intensity from sample environment, such as the sample holder and/or container. Among those, only $I_C(Q)$, contains atomic structure information. Therefore, experimentally, other intensities need to be carefully measured and then corrected in order to obtain a "pure" $I_C(Q)$ from Eq. 2.9. Theoretically, $I_C(Q)$ is defined as [35]:

$$I_C(Q) = \frac{1}{N} \sum_{\nu,\mu} b_\nu b_\mu e^{iQ(\mathbf{R}_{\mu\nu})} \qquad (2.10)$$

Where, b_ν is the ν atom scattering amplitude (for X-rays, it is the atomic form factor of the atom ν). $I_C(Q)$ is the scattering intensity per atom. $\mathbf{R}_{\mu\nu} = \mathbf{R}_\mu - \mathbf{R}_\nu$, and $\mathbf{R}_\mu$ is position of the μth atom, $\mathbf{R}_\nu$ is position of the νth atom. Here Q is defined,

$$Q = |\mathbf{Q}| = \left| \frac{4\pi \sin\theta}{\lambda} \right| \tag{2.11}$$

After obtaining $I_C(Q)$, the total-scattering structure function $S(Q)$ which is the normalised scattering intensity by the incident flux per atom in the sample, can be calculated by [35]:

$$S(Q) - 1 = \frac{I_C(Q) - \sum c_i |f_i(Q)|^2}{\sum c_i |f_i(Q)|^2} \tag{2.12}$$

Where, c_i and f_i represent the atomic concentration and X-ray atomic form factor respectively for the atomic species i. However in the case of neutron diffraction, the f_i is replaced by Q-independent neutron scattering lengths, b respectively.

It is convenient to regard $S(Q)$ as a powder diffraction spectrum, which however has been corrected for experimental artifacts and also properly normalised.

2.3.3 Pair distribution function and analyses

The connection between the total scattering intensity of a collection of atoms and the pair distribution function of those atoms is based on the fact [35] that Fourier transformation of the scattering intensity, in the form of structure function $S(Q)$ for isotropic structures, such as liquid and amorphous materials, gives reduced atomic pair distribution function, $G(r)$ as below:

$$G(r) = (2/\pi) \int_{Q=0}^{Q_{\max}} Q \left[S(Q) - 1 \right] \sin(Qr) \, dQ \tag{2.13}$$

where, $S(Q)$ as defined in Eq. 2.12, is the total scattering structure function for isotropic structures, and Q_{max} is the cutoff value of Q for Fourier transformation.

Experimentally, total scattering measurement is very similar to powder diffraction experiments. However some special cares need to be taken to obtain high quality total scattering data, such as high Q range, sufficient counting statistics and low background scattering. Since a high real space resolution of PDF only can be achieved with a large enough Q-cutoff as implied in Eq. 2.13 and also Fig. 3.10. To achieve a high Q range, a X-ray with short wavelength λ is really necessary according to the definition of Q.

Total scattering experiments are routinely carried out using high energy synchrotron X-ray sources and pulsed neutron sources with wavelength of one order of magnitude lower than that generated from the conventional laboratory X-ray sources such as Cu target. Especially for some time resolved studies, such as local structure evolution during phase transition [104]. Rapid acquisition PDF using a 2D image detector coupled with synchrotron X-rays, is extremely useful [105].

From data processing perspective, to obtain a relatively accurate structure function $S(Q)$, the total scattering data has to be corrected for several unwanted experimental scattering information, noise or artefacts, such as background scattering, sample absorption, Compton scattering, multiple scattering [35]. Imperfect corrections result in distortions to $S(Q)$, Normally, these distortions vary much more slowly than the real signals from the structures, and are manifested as sharp peaks at very low in the PDF in a region ($\sim< 1.0$ Å) where no structural information exists [35]. A number of data processing programs are available for corrections and normalisations needed to obtain PDFs from raw data. Commonly used open-source programs are PDFgetX2 [106], PDFgetX3 [107] for X-ray data. All corrections are implemented explicitly in PDFgetX2, however PDFgetX3 adapts an ad-hoc method that can be used to batch process the diffraction data without much human inputs or interaction during the processing.

In this research, PDFgetX3 is used extensively to process the time-resolved total scattering dataset. Hence, the algorithm and procedures used in PDFgetX3 are described in details

here. It generally makes use of the fact that structure function $S(\mathbf{Q})$ should oscillate around and then approach unity as Q goes to infinity [108, 107].

Firstly, the scattering intensity from the "pure" sample is obtained by subtracting the rescaled background intensities:

$$I_m(Q) = I_{raw}(Q) - C_{bg} \cdot I_{bg}(Q) \tag{2.14}$$

Where, $I_m(Q)$ is the scattering intensity from sample without any normalisation, $I_{raw}(Q)$ is raw scattering intensity, $I_{bg}(Q)$ is the scattering intensity from sample holder, and C_{bg} is the background scale factor, which can be tuned to get an optimal background subtraction as illustrated in Fig. 3.9. Eq. 2.14 gives $I_m(Q)$, but it has not been normalised against the incident intensity yet.

Secondly, a reduced structure function $F_m(Q)$ is calculated using the following procedure. The PDFgetX3 algorithm is based on the assumption that the experimental structure function $S_m(Q)$ deviates from its real value by a slowly changing additive factor $\beta_S(Q)$ [108]:

$$S_m(Q) - 1 = S(Q) - 1 + \beta_S(Q) \tag{2.15}$$

Hence, the reduced structure function $F_m(Q)$ can be derived as,

$$F_m(Q) = Q \cdot [S(Q) - 1 + \beta_S(Q)] = F(Q) + Q \cdot \beta_S(Q) \tag{2.16}$$

Now, $F(Q)$ is the ideal reduced structure function which oscillates around zero, and $\beta_S(Q)$ is the error term that produces slowly changing, Q-increasingly dependant background in $F_m(Q)$. In PDFgetX3, the background is estimated by modelling $\beta_S(Q)$ function as an

n^{th} degree polynomial $P_n(Q)$, which is then fitted as $QP_n(Q)$ to the $F_m(Q)$ function. The finally corrected reduced structure function $F_C(Q)$ is obtained by subtracting the $QP_n(Q)$.

$$F_C(Q) = F_m(Q) - QP_n(Q) \qquad (2.17)$$

$F_C(Q)$ shows the correct asymptotic behaviour with $F \to 0$ for large Q value. Finally, $F_C(Q)$ is converted to G(r) using fast Fourier transformation.

Some structure information can be directly obtained from analysing the PDF peaks, such as the peak position, peak width, peak intensity and peak shape [35]. In practice, more quantitative structural information, can be obtained by full profile refinement of the experimental PDF based on a well known structural model. The real space refinement of PDF is very similar to the Rietveld refinement method [109] used in powder diffraction, which is based on a structural model using the least-square regression as implemented in the program PDFFIT [110] and its replacement, *i.e*, PDFfit2 and PDFgui [111].

The full profile refinement needs parameters related to the structural model, and other experiment-dependent parameters. The structure related parameters consist of unit cell parameters (unit cell lengths and angles), atomic fractional coordinates, anisotropic atomic displacement for each atom and the average atomic occupancy of each site [112]. The experiment-dependent parameters includes the overall scale factor, phase scale factors.

Fitting the PDF in PDFfit is straightforward because it can be calculated directly from a structural model using Eq. 2.18,

$$G_c(r) = (1/r) \sum_i \sum_j \left[\left(b_i b_j / \langle b \rangle^2 \right) \delta \left(r - r_{ij} \right) \right] - 4\pi r \rho_0 \qquad (2.18)$$

where $G_c(r)$ is the calculated PDF; the sum runs over all pairs of atoms i and j within the model crystal separated by r_{ij}. The scattering amplitude of atom i is b_i and $\langle b \rangle$ is the

average scattering amplitude of the sample. In the case of X-rays, b_i is the atomic form factor evaluated at a user-defined value of Q. The default value of Q is obtained when b_i is simply the number of electrons of atom i [110].

Apart from the full profile refinement of total PDF, PDFFIT also allows to calculate the partial PDFs by selecting a particular atom pair in the sum over i and j in Eq. 2.18. However, the real space refinement based on a well-known structure model is only valid for fitting the PDF for crystalline phase. Syncrotron X-ray total scattering and PDF method were extensively used to study the evolution of atomic structure of bulk metallic glass during heating and cooling as described in chapter 4.

2.3.4   Neutron diffraction

Neutron diffraction [113, 114] similar to X-ray diffraction, is a kind of elastic scattering of neutron with matter. It is a standard method for determining the atomic structure of materials no matter they are crystals, glasses, or liquid [114]. Normally, a sample to be examined is placed in a beam of thermal or cold neutrons and the scattered intensity by the sample provides structure information of the material.
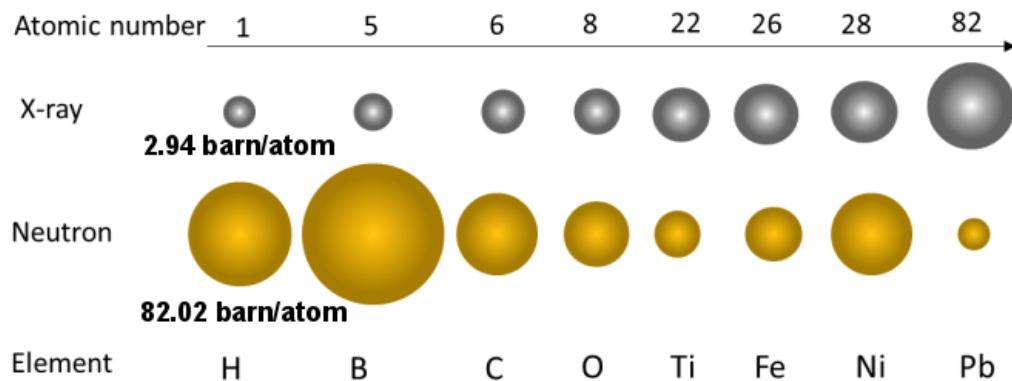
Fig. 2.13 The schematic representation of total scattering cross section of X-ray [115] and neutron [116] for different elements. The diameter of sphere represents the total atomic scattering cross section of atom. 1 barn=1 E-24 cm^2. The exact total scattering cross section of Hydrogen is given as an example.

The interaction of neutrons with matters is different to that of X-rays [114] because neutrons interact directly with the nuclei of atoms, and the scattering intensity is different for different isotopes. As illustrated by Fig. 2.13, it is often that atoms with low atomic number, *e.g.* H and B, cause stronger scattering compared to atoms with large atomic number. Neutron scattering length is different from isotope to isotope, and do not have a linear relationship with the increase of atomic number [114]. In addition, the scattering amplitude of atom does not reduce with the increase of scattering angle or Q as it does for X-rays. Therefore, neutron diffraction spectra often shows strong diffraction peaks even at high angles or Q [114]. The excellent diffraction information obtained at high diffraction angle can be used for characterising the atomic structures of materials more precisely [114].

The neutrons used for diffraction experiments are usually produced by a nuclear reactor [117] or spallation source [118]. For example, ISIS at the Rutherford Appleton Laboratory is a pulsed spallation neutron and muon source in UK, and Fig. 2.14 shows the layout of the source and its first target station [119].

It starts with an ion source, which can produce negative hydrogen ions consisting of two electrons orbiting each proton. These negative ions are introduced into a linear accelerator (linac), in which the ions are accelerated to about 35% of the speed of light over a distance of about 50 m. From then on, the ion becomes proton after the two electrons being stripped off. After that, only these protons are injected into the circular synchrotron consisting of 10 sections arranged along its 163 m circumference. Each section in the circular synchrotron consists of an electric field to accelerate the protons, and also magnetic fields to drive and collimate the pulsed beam. During the acceleration, the intensity of the bending magnets has to be increased in synchronicity with the increasing speed of the protons, in order to keep the protons in the same tight trajectory [121]. After 10,000 circles around the synchrotron, the speed of protons is accelerated to about 84% of the speed of light [121]. They can then be extracted using three fast kicker magnets.

The extracted protons are then be transmitted through a thin graphite target, and 2-3% of the protons is used to produce muons (heavy electrons). The rest of them strike a tantalum
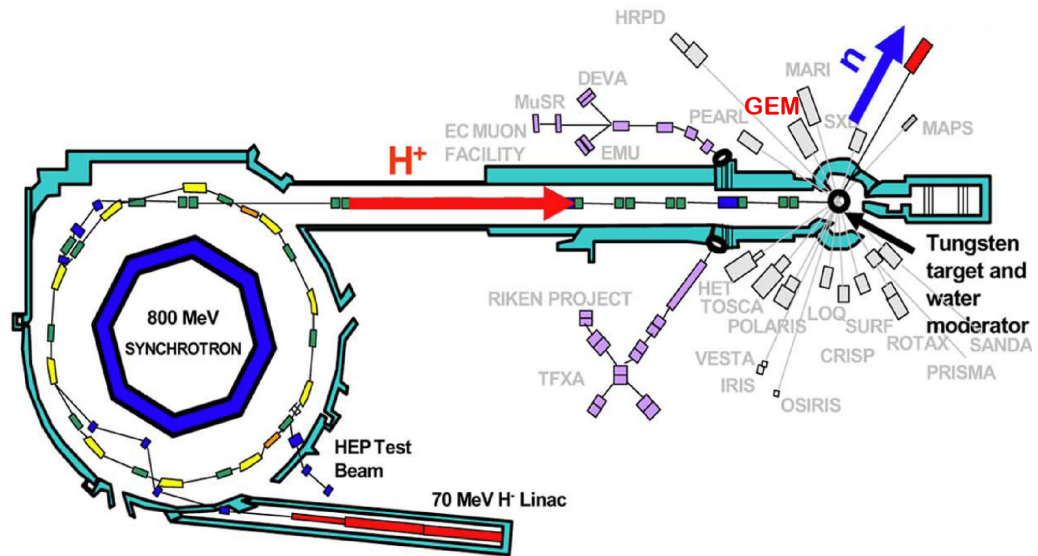
Fig. 2.14 The layout of ISIS pulsed spallation neutron source and its target station 1 [120].

clad tungsten spallation target, where each proton can knock out about 20 neutrons. The target is cooled by the circulation of water to prevent the overheat caused by the 160 kW proton beam. The neutrons are then slowed down or moderated to increase their de Broglie wavelength before they are channelled by beamlines to about 20 instruments, which is optimised individually for different types of research [120].

The General Materials Diffractometer (GEM) beamline [122] houses a good resolution, high-flux powder diffractometer, which are used to study crystalline powder samples. It also has a wide-angular-range, high-flux, low-background instrument for the studies of disordered materials, especially useful for studying the structures of bulk metallic glass composites, inside which crystalline phase and amorphous matrix coexist [123]. In this research, GEM was used for characterising the phases of the bulk metallic glass composites processed under different thermal shock conditions as detailed in Chapter 5.

2.3.5   Imaging based methods

Imaging methods often provide intuitive information for the structures of materials, and electron microscopy is a standard 2D imaging method routinely used in the characterisation of materials. For example, scanning electron microscopy (SEM) is employed to examine bulk sample surface from nano to micrometre scale, and transmission electron microscopy (TEM), especially high resolution transmission electron microscopy (HRTEM) is the standard tool for characterising the structures of materials at atomic and nanometre scale using thin foil samples [124]. However for materials consisting of complex 3D microstructures, these 2D imaging methods cannot obtain the 3rd dimensional structural information. 3D methods, *e.g*, X-ray computed tomography and FIB-SEM serial sectioning tomography need to be used to obtain information on the 3rd dimension. The relevant 2D and 3D imaging characterisation methods used in this research are briefly reviewed here.

2.3.5.1   Electron microscopy

SEM is one of extensively used electron microscopy techniques. In SEM, an electron beam scans across a sample's surface, and the interactions between the incident electrons and the atoms on the sample surface produce a variety of signals that carry the information about the sample's surface topography and composition. Consequently, images and spectra can be converted from those signals to reveal the structural, topological and composition information about the sample.

Three most informative signals generated in SEM are (1) secondary electrons (SE), (2) backscattered electrons (BSE), and (3) X-rays [125]. Secondary electrons are often used to generate the topology of sample top surface because they are released from the atoms on the top surface excited by the electron beam. Therefore, the imaging contrast of second electrons mainly depends on the sample morphology.

Backscattered electrons are the primary beam electrons that are back-scattered from atoms in the sample by elastic scattering. The image contrast generated by BSE is highly

related to the atomic number (Z) of the elements in the sample [125]. The BSE imaging can exhibit phase distribution in the sample thanks to the chemical composition contrast in the sample. BSE imaging usually requires the sample surface to be smoothly ground and polished. Since high atomic number elements backscatter electrons more strongly than low ones, therefore they appear more bright in the micrographs.

X-rays excited by an incident electron beam can be used to perform elemental analysis or chemical characterisation of the specimen because each element in the specimen has a unique electronic structure, which is characterised by a unique set of peaks on its X-ray emission spectrum [126]. The relevant technique is known as energy-dispersive X-ray spectroscopy (EDX) and wave length disperse X-ray spectroscopy (WDX).

The transmission electron microscopy [127] is commonly used in material characterisation because it can obtain high magnification structural information not only in real space by imaging, but also in reciprocal space by electron diffraction almost simultaneously [127].

In TEM, a beam of electrons is transmitted through and interacting with an ultra-thin sample (normally a hundreds of nm thick). An image is formed from the interaction of the electrons transmitted through the specimen, and then magnified and focused onto an imaging device, *i.e*, fluorescent screen or a CCD camera. TEM is capable of imaging at a relatively higher resolution thanks to the small de Broglie wavelength of electrons (in nm). This enables to examine fine structure — even as small as a single column of atoms [128]. At lower magnifications, the image contrast is mainly due to the absorption of electrons in the material. However at higher resolution, especially the HRTEM images [128] are phase-contrast images originated from the complex wave interactions of the transmitted and diffracted electron beams [128]. High quality HRTEM samples usually should have a sample thickness comparable to the mean free path of the electrons [129] travelling through the samples, normally just a few tens of nm [129].

HRTEM [128] is extensively used to study atomic structures. Using a field emission electron source [130] and a uniform-thickness specimen, in many cases, the atomic structure of a specimen can be directly investigated by HRTEM [128].

It is difficult to get the real atomic configurations directly for a local region even with the best HRTEM, because electron micrographs are approximately 2D projections of 3D atom arrays [131] and the 3D local ordering is lost in the 2D projection although some small order features of amorphous material, such as fringes and atom arrays can be still observed using HRTEM [73]. It is desirable to have a quantitative method to examine or retrieve the local ordering information. Correlation technique is a statistical method and mathematical tool to find any repeating patterns for images in real space [132]. A standard method for measuring correlations is the autocorrelation function (ACF) [133, 134]. For any function $f(r)$, the ACF $P(r)$ can be defined as:

$$P(r) = f(r) * f(-r) = \int f(R)f(r+R)dR \tag{2.19}$$

Where the $*$ sign denotes a convolution integral, and $P(r)$ is also a 2D Patterson function [135]. This can be applied to the 2D intensity distribution of an electron micrograph [134].

For an electron micrograph recorded in a digital format, the autocorrelation function of the image intensity can be calculated directly by the equation below:

$$P(r) = \mathscr{F}^{-1}|\mathscr{F}(f(r))|^2 \tag{2.20}$$

Where, $\mathscr{F}$ denotes Fourier transform operation. The practical procedure [133] is that, firstly, the intensity of the graycale image is Fourier transformed, then the fast Fourier transformed image is multiplied by its complex conjugate, and finally the real space ACF pattern can be obtained by Fourier transforming the resulting product of FFT image and its complex conjugate.

HRTEM micrographs are phase-contrast images generated from the interference of the transmitted and diffracted electron beam [128]. The Fourier transformed HRTEM image
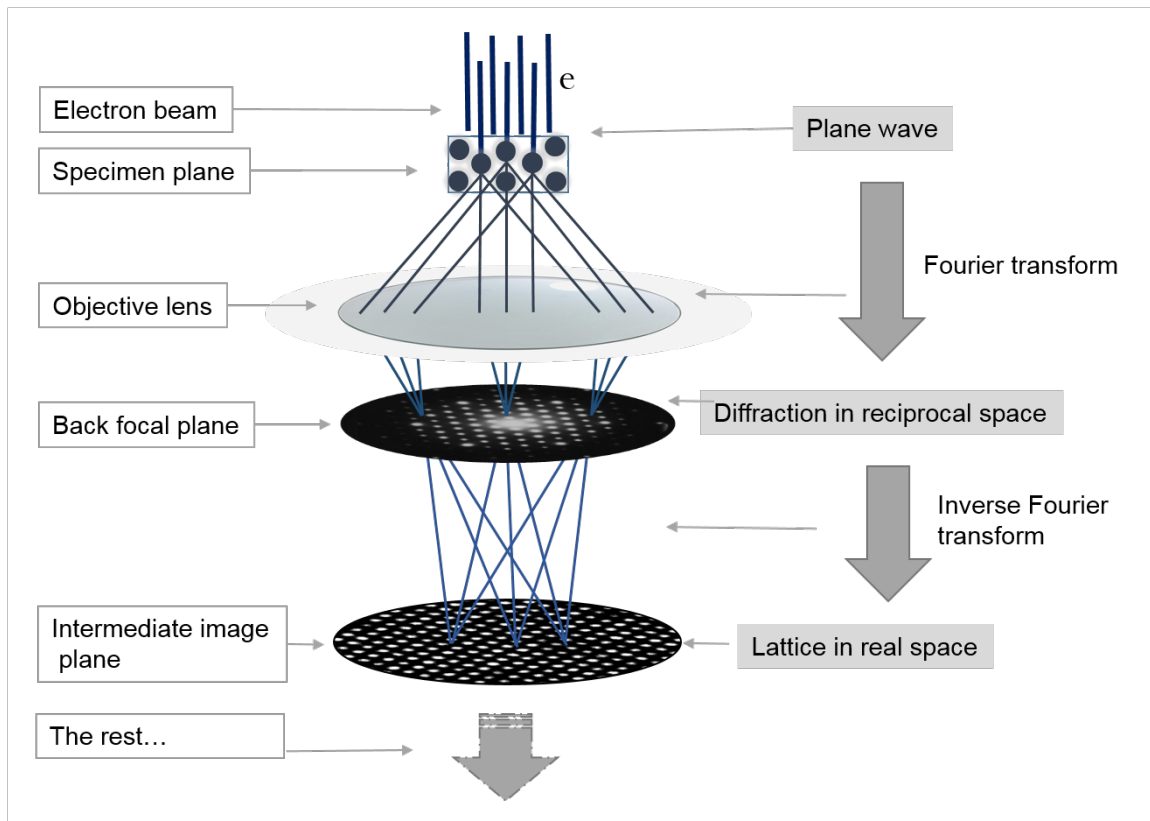
Fig. 2.15 The analogy between Fourier transform and TEM imaging and diffraction mode.

is analogous to diffraction pattern generated in a simplified TEM [136]. By considering the primary electrons in a simplified TEM as shown in Fig. 2.15, there are three planes in the TEM: the intermediate image plane, the back focal plane of the objective lens, and the specimen plane (specimen exit surface). When an electron beam transmits through the specimen exit surface and onto the objective lens, the transmitted and the diffracted beams satisfying the Bragg condition are focused at the back focal plane of the objective lens and form an electron diffraction pattern. Within this plane, the space in which the electron diffraction pattern can be detected is named the reciprocal space, which is mathematically equivalent to the Fourier transform of the real space [136].

When the interference of the transmitted and the diffracted electron beam occurs on the intermediate image plane, it is analogous to the fact that the diffraction pattern in reciprocal space is mathematically converted into the real space to form a magnified image of atomic structure by inverse fast Fourier transform (IFFT). Hence the real space image

and the diffraction pattern in reciprocal space can be converted to each other by using the FFT/IFFT operation [136]. Therefore, for a given real space image obtained by HRTEM, it is straightforward to obtain the corresponding diffraction patterns by applying FFT, although it is spatially limited to tens of nm due to the nature of high resolution TEM.

2.3.5.2   FIB-SEM serial sectioning tomography

FIB-SEM tomography is an important structural characterisation technique for studying materials at μm and nm scale. Such technique often can provide better understanding of volumetric 3D structure rather than 2D cross section. FIB-SEM tomography is a method specific to FIB-SEM dual beam systems [137]. 3D structure is generated by reconstructing a serial of SEM images of 2D cross section prepared by FIB milling. FIB tomography often starts with the selection of a region of interest (ROI) within the sample, then a series of cross-section layers are produced by milling through the ROI using FIB. Different imaging mode of SEM can be used to image the surface of the cross-section layers generated in the milling process.

The acquired 2D image sequences are often not convenient for direct visualisation without post-processing. Various visualisation methods are available, in which a series of grayscale image sequence is imported into the visualisation software as described in section 2.3.5.3. By 3D rendering, different objects can be easily differentiated and presented in different colours and level of transparencies.

2.3.5.3   X-ray radiography and tomography

X-ray radiography is a non-destructive 2D imaging technique, and it uses X-rays to examine the internal structure of an object having different densities and compositions. The image contrast is primarily generated by different X-ray attenuation of the constituent materials of different chemical compositions within the object.

X-ray tomography is a natural extension of X-ray radiography in 3D, and a series of 2D images is obtained and reconstructed to produce a 3D image where each voxel represents the X-ray attenuation for this specific local region. The mechanism for image formation is based on X-ray absorption contrast and phase contrast as detailed below.
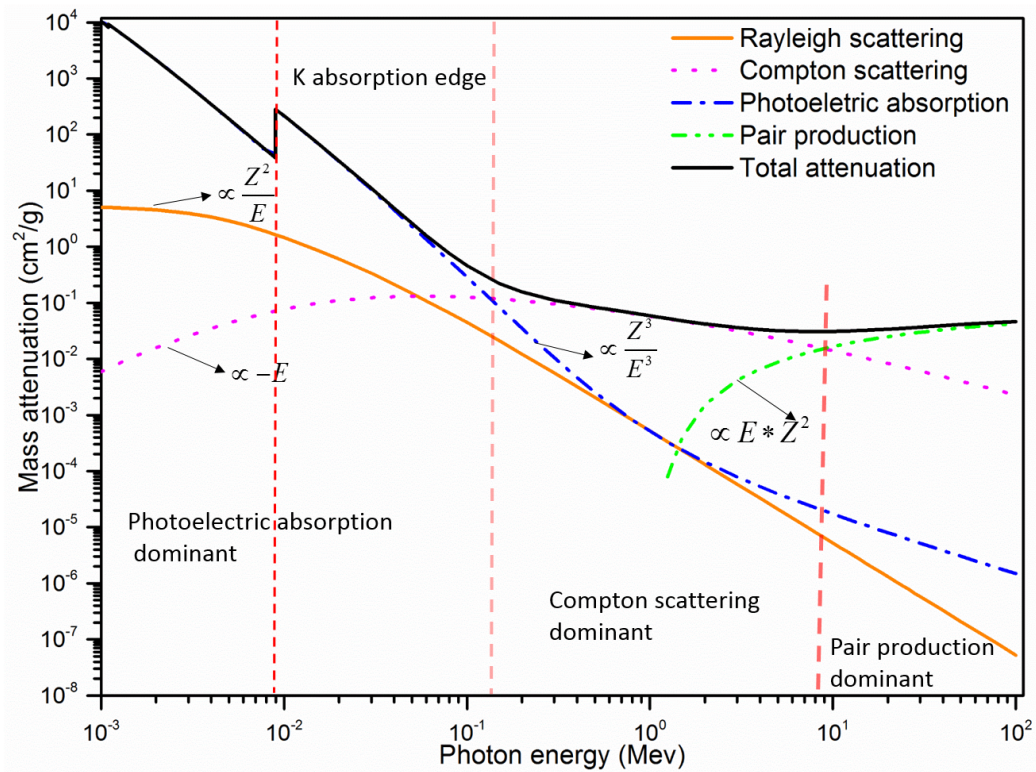
Fig. 2.16 The attenuation of X-ray by Copper due to different mechanisms.

$$I = I_0 \exp(-\mu x)$$

$$I = I_0 \exp\left[\sum_i -\mu_i x_i\right]$$

$$I = \int I_0(E) \exp\left[\sum_i -\mu_i(E) x_i\right] dE$$

Single material
Monochromatic X-ray

Multiple material
Monochromatic X-ray

Multiple material
Polychromatic X-ray
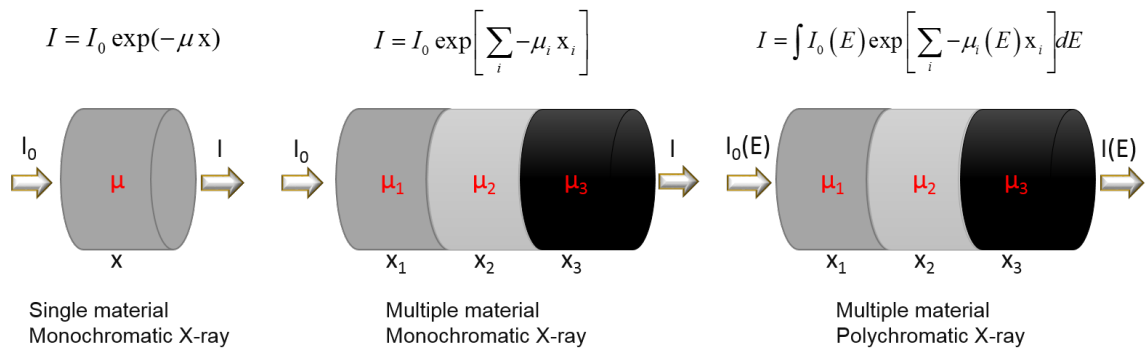
Fig. 2.17 The attenuation of X-ray by objects of different attenuation coefficients and expressed by Lambert Beer's law.

Fig. 2.16 shows, the X-ray mass attenuation for Copper [138] being transmitted through by a monochromatic X-ray beam. Fig. 2.17 shows that the attenuation of X-ray beam intensity through an object can be expressed by Lambert Beer's law. The simple form of Lambert Beer's law [138] is given by:

$$I = I_0 \exp(-\mu x) \tag{2.21}$$

Where I_0 and I are the intensity of incident and transmitted X-rays; μ is the linear attenuation coefficient (1 / length) for the object material and x is the path length of the X-ray passing through the object. If the object is made of multiple materials rather than a single material, the equation becomes:

$$I = I_0 \exp\left[\sum_i -\mu_i x_i\right] \tag{2.22}$$

Where i represents a single material with the attenuation coefficient of μ_i, together with the X-ray path length x_i.

If a polychromatic X-ray is used, since linear coefficient is a function of X-ray energy over the whole range of the X-ray energy (E) spectrum, the Lambert Beer's law has the form as below [139]:

$$I = \int I_0(E) \exp\left[\sum_i -\mu_i(E) x_i\right] dE \tag{2.23}$$

The incident X-ray intensity I_0 and transmitted X-ray intensity I can be measured experimentally. To measure the incident X-ray intensity I_0, the sample is moved out of the field of view and the so-called flat field images are acquired repeatedly. The flat field images not only record the spatial distribution of the incident X-ray intensity I_0, but also show the

variations in the detector due to the fact that the X-ray detector may have a baseline charge independent of the incident X-ray beam [139]. In practice, a baseline image, *i.e*, a dark field taken without X-ray and sample, *i.e*, only contain the characteristic information of the detector. I_d is usually taken and subtracted from the incident I_0 and transmitted images I. Consequently, the corrected X-ray absorption at a single pixel in 2D projections is calculated by [139]:

$$\tau = \ln\left(\frac{I_0 - I_d}{I - I_d}\right) \qquad (2.24)$$

As illustrated in Fig. 2.16, for most materials, there are always sharp discontinuities, the so-called attenuation edges appearing at some particular X-ray energies if the attenuation coefficient μ of a signal material is plotted as a function of X-ray energy. The X-ray attenuation edges predominately are caused by photoelectric absorption, and are often utilised to achieve a better contrast between different chemical phases within the object [139].

In experiment, the optimal X-ray photon energy is often chosen based on a good estimate of the X-ray attenuation contrast among the different phases within the object to be examined. There are a few online X-ray attenuation coefficient database and calculators [140] for such calculations.

X-ray phase-contrast is generated by the difference in refraction of X-rays through materials of different refraction indexes [141]. Fig. 2.18 shows the basic principle to have sufficient phase contrast in X-ray imaging. At a certain sample to detector distance, the phase contrast can be created by interference pattern of refracted and transmitted X-rays.

In-line or propagation-based phase-contrast imaging [142–144] has nearly the same experimental setup as attenuation contrast imaging (Fig. 2.19). Compared to the pure attenuation contrast imaging setup, the only difference is that the detector is placed in some distance away from sample rather than right behind it. Therefore, the refracted X-ray by the
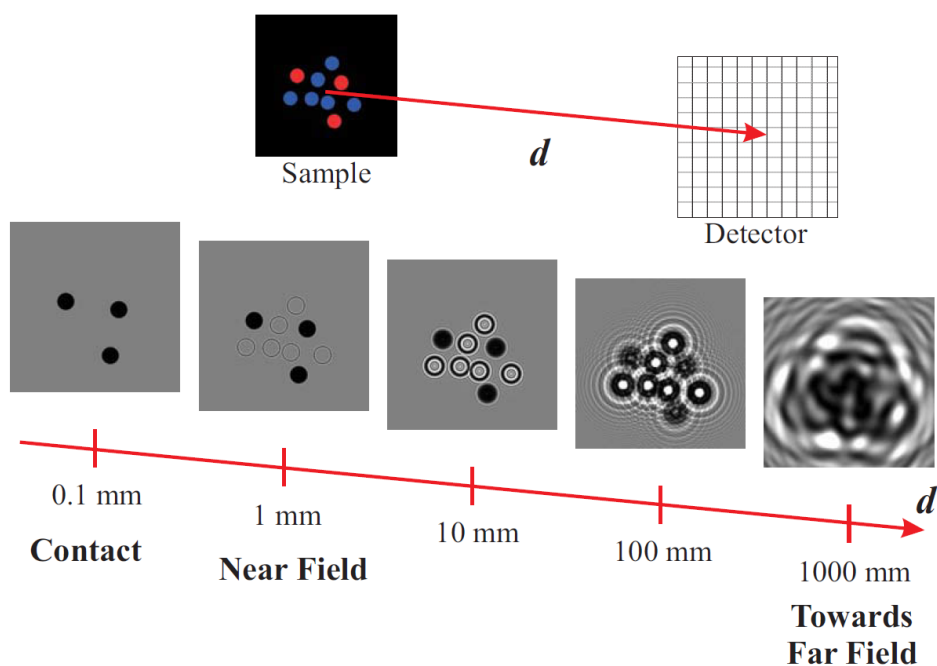
Fig. 2.18 X-ray radiographs simulated to illustrate the transition from pure absorption contrast (in the contact regime) via edge enhancing in-line phase contrast (near field) to stronger phase contrast (Fresnel region) and towards the far-field regime [80].

sample is able to interfere with the transmitted X-ray [143]. Since the X-ray refractive index is very close to unity, these refractive effects is very weak compared to the refraction of light. Consequently, two basic requirements should be satisfied to create sufficient phase-contrast in imaging. The primary one is to have an X-ray source with high spatial coherence, and the second one is to maintain an intermediate sample to detector distance, allowing an interference pattern with Fresnel fringes [145] created. However it has been demonstrated that both requirements for the in-line phase contrast can be easily achieved in Synchrotron X-ray facilities [142, 143, 146].

A very unique advantage of phase contrast in practice is that there is not any strict requirement for chromatic coherence because when imaging in the near-field, the Fresnel fringes [145] are nearly coincident for various energies, allowing polychromatic X-rays to be used. Since differences of image intensity in in-line phase contrast imaging are proportional to the second derivative of the phase image, the technique is more sensitive to high spatial frequencies of phases - abrupt changes in the decrement of the refractive
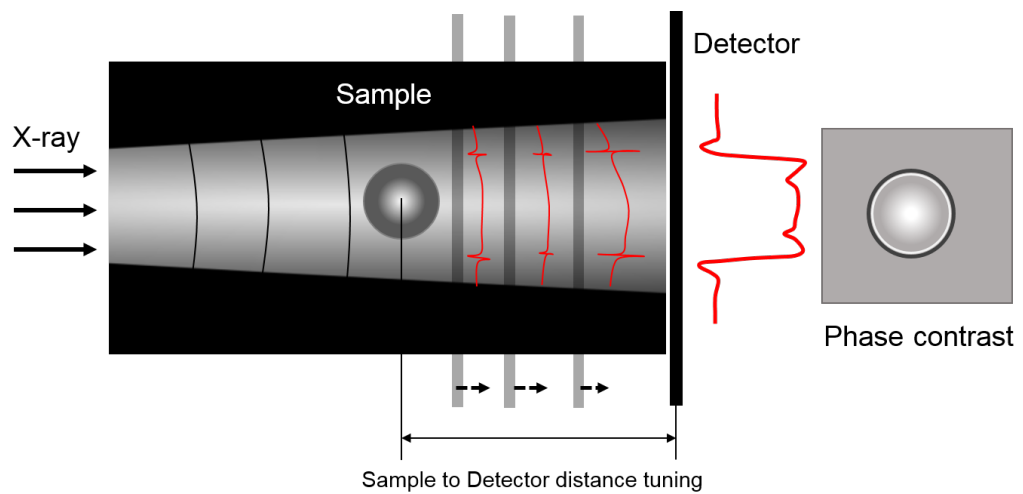
Fig. 2.19 Schematic of the in-line phase-contrast imaging setup, including an X-ray source, sample and a detector.

index [139, 141]. This can generate greater contrast which is able to outline the surfaces

and structural boundaries of the sample compared to a classic absorption contrast [139].
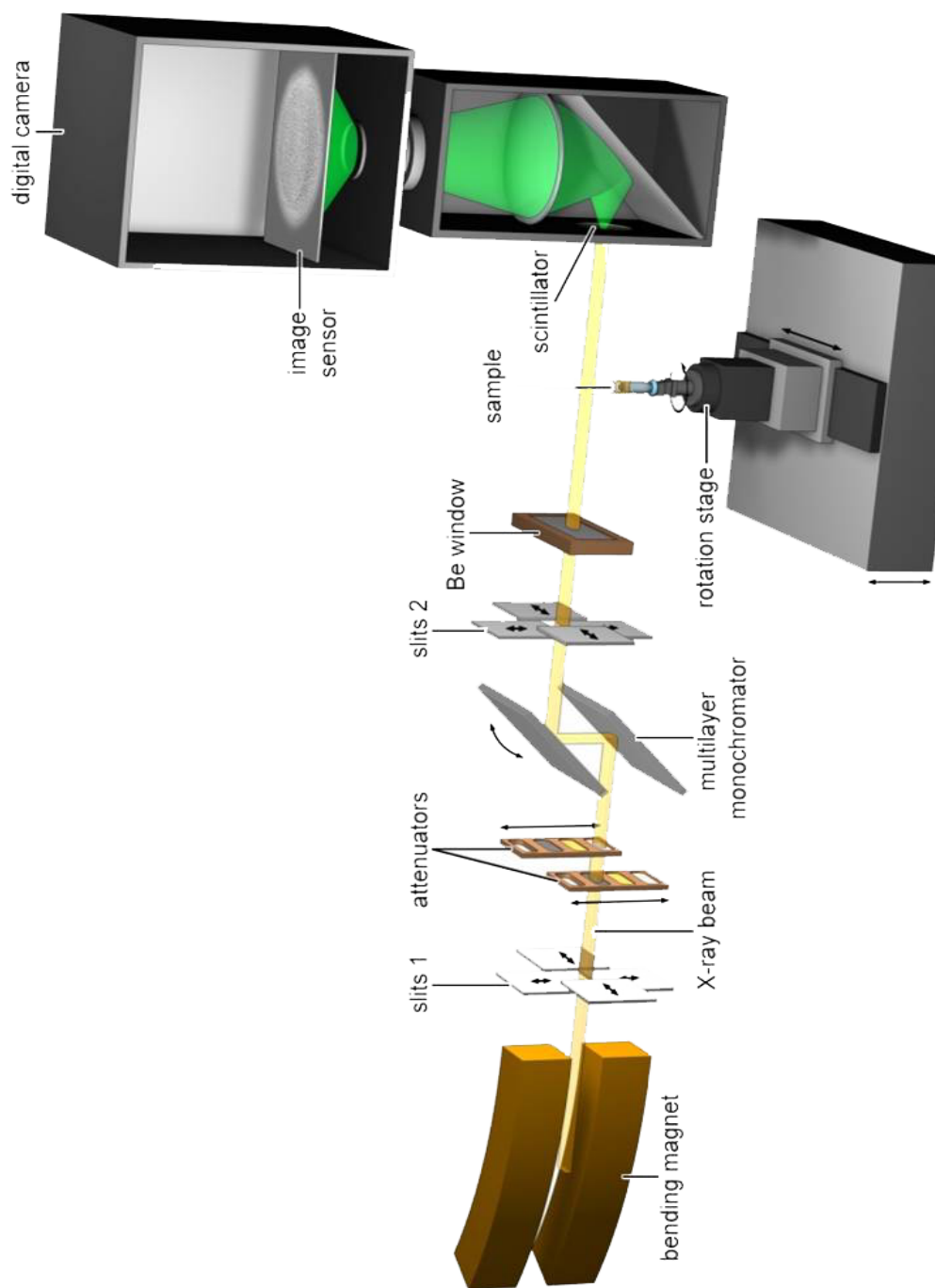
Fig. 2.20 A schematic, showing the general setup for tomography experiment [147].

When parallel beam such as the synchrotron X-ray is used, the intensity of Fresnel fringes caused by the phase-contrast, increases with the propagation distance from sample to detector, so that the edges and boundaries of the sample are enhanced. However if the sample to detector distance continues to increase, these Fresnel fringes will get broader and fade out, and eventually the imaging regime will be replaced by intermediate regime characterised by diffraction fringes [144].

Fig. 2.20 shows the basic setup for a synchrotron tomography experiments. A monochromatic X-ray beam is illuminated onto the sample, which is rotated incrementally on a high precision rotation stage from 0° to 180°, and a series of 2D radiographic projections (radiographs) are recorded in scintillator integrated detector at each rotation step [139].

For 3D reconstruction, the 2D projections are converted into so called sinogram, in which a single horizontal row of grayscale is extracted from each projection, and then stacked from the bottom to top as the increment of sample rotation angle.

The sinograms converted from 2D projections are then reconstructed into 2D tomographic slices (tomograms). As illustrated in Fig. 2.21, each tomogram corresponds to a 2D cross section view of the object being scanned if it were cut through by a horizontal plane. Finally a complete volumetric representation of the object can be obtained by visualising a continuous set of tomograms by object segmentation and 3D rendering.

Once a series of flat field corrected radiographic projections are obtained from a sample, the general procedure described below can be used to do the tomographic reconstruction, which is based on the Random transform [139].

As shown in Fig. 2.21, a radiographic projection is simply a collection of projection functions $L_2(x', \theta_n)$ at the horizontal row of Z_n for a specific rotation angle θ_n. In reconstruction process, these projection functions are normally collected over all rotation increments for a particular row of Z_n, which is known as a sinogram because of the sine shape of the path created by collections of relatively bright pixels over all the projection angles.
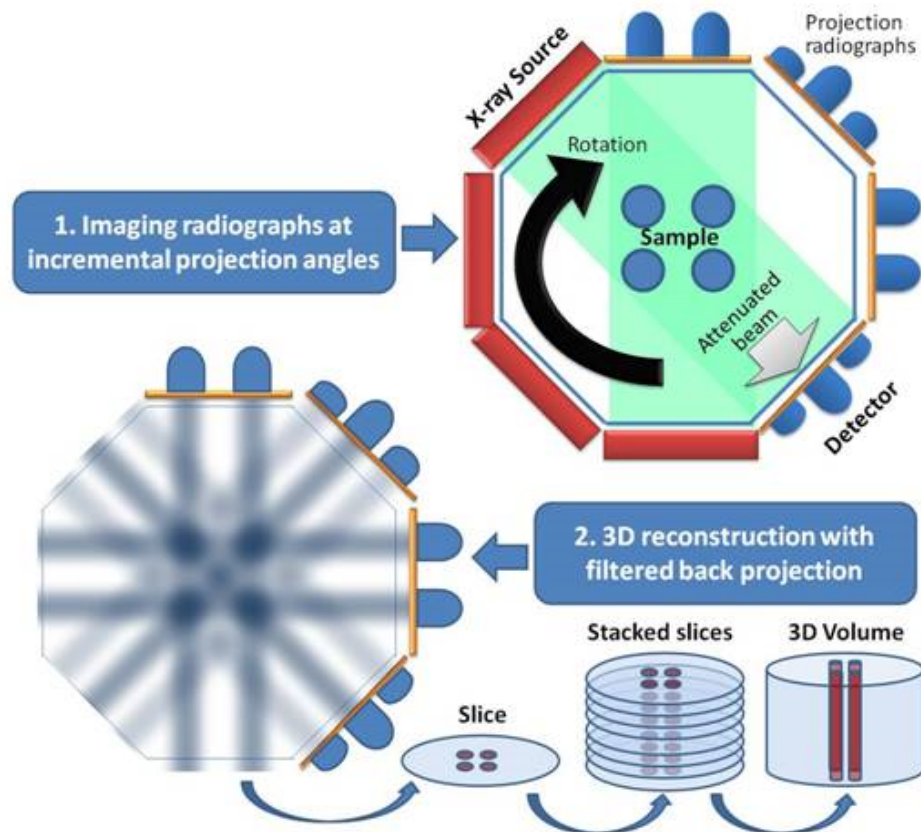
Fig. 2.21 The principle of X-ray tomogrpahy and procedure for 3D reconstruction [148].

In reconstruction, the 2D slice $f(x, y)$ for a particular row of Z_n, has to be determined from the sinogram for the same horizontal row. Mathematically, this problem was solved by Radon in 1917 [139].

Although a unique solution can be established for a continuous $f(x, y)$, practical limitations make the solution process more complicate. Errors are introduced throughout both the discrete nature of data acquisition, and also the inadequate measurement. There are several reconstruction algorithms being developed based on the "Fourier Slice Theorem" [149]. The most extensively used approach is the so-called filtered back projection [150], in which the linear data acquired at each angular orientation are convolved with a specially designed filter and then back projected across a pixel field at the same angle, as illustrated in Fig. 2.21.

Based on the tomograms reconstructed, 3D visualization of the tomographic data provides more qualitative and quantitative structure information compared the conventional 2D images. 3D visualization in general includes image processing, phase segmentation, and 3D volume rendering. A wide range of both commercial and open source software are available for such purpose, such as the commercial software FEI Avizo and its upper stream Amira, and also some open source software, VTK [151], ITK [152], 3D slicer [153], *etc.*.

The spatial resolution of traditional Computed Tomography (CT) systems is often limited by the X-ray beam geometry and also the performance of the detector. A significant improvement in X-ray tomography can be achieved using synchrotron X-rays that have many orders of magnitude higher in brilliance compared to the conventional tube X-rays. High flux is another unique advantage of synchrotron X-rays, which allow fine internal structures to be imaged in a very short exposure time, especially useful for in-situ studies.

Synchrotron X-rays as a parallel beam have a high collimation, which simplifies the tomographic reconstruction algorithm. In addition, a monochromatic synchrotron X-ray beam improves the accuracy of tomograms by eliminating the energy dependence on X-ray absorption [154].

Besides, the photon energy of synchrotron X-rays can be easily selected and tuned for enhancing contrast of different materials. Currently, increasing number of synchrotron radiation facilities have been established around the world. Most of these national facilities have beamline dedicated to imaging and tomographic studies, such as I13 of Diamond light source, UK [155]; TOMCAT of Swiss Light Source, Switzerland [156]; and ID19 in ESRF, France [157], *etc*.

Syncrotron X-ray tomography was used to study the 3D morphology of the crystalline phases of the thermally shocked bulk metallic glass composite as described in chapter 5.

2.4   Modelling of the structures of materials

An accurate and comprehensive description of the structures of materials and those phe-nomena occurring during solidification and crystallisation need to be tackled at atomic level, accounting for particles interactions and their correlations. A very brief review is given in this section to discuss the models developed and used so far for atomic and nano, and microstructure modelling, and the advantages of the phase-field crystal (PFC) models that are extensively used in this research in terms of bridging the length and time scale for structure modelling at atomic level and above.

2.4.1   A brief review of the structure models and methods

There are several modelling methods extensively used in physics, chemistry and material science communities for atomic, nano and microstructure modelling and simulations, which cover different temporal and spatial scales, as shown in Fig. 2.22. Phase field (PF) method [158] is one of the most computationally effective phenomenological models for simulating the microstructural evolution at mesoscale length and diffusive time scales. PF has been proven as an exceptionally powerful computational tool to simulate complex microstructures and phase transformation patterns without any front tracking [159]. Although PF can be extended to simulate different microstructural phenomena by introducing auxiliary phase field order parameters [160], the phenomenological nature of PF and the many arbitrary model parameters used in the PF model make it still major challenges in accurately predicting microstructures.

Another widely used modelling method is molecular dynamics (MD) [161]. It is a powerful tool to study mechanical systems statistically. Precise information about each atom can be determined by postulating the interaction between atoms and solving the resulting equations of motion. However one of the drawbacks of MD is the far too short time scale because too much information of atom oscillations needs to be captured. For example, atomic motions in MD simulations are resolved on time scale of ps to ns, whereas in many
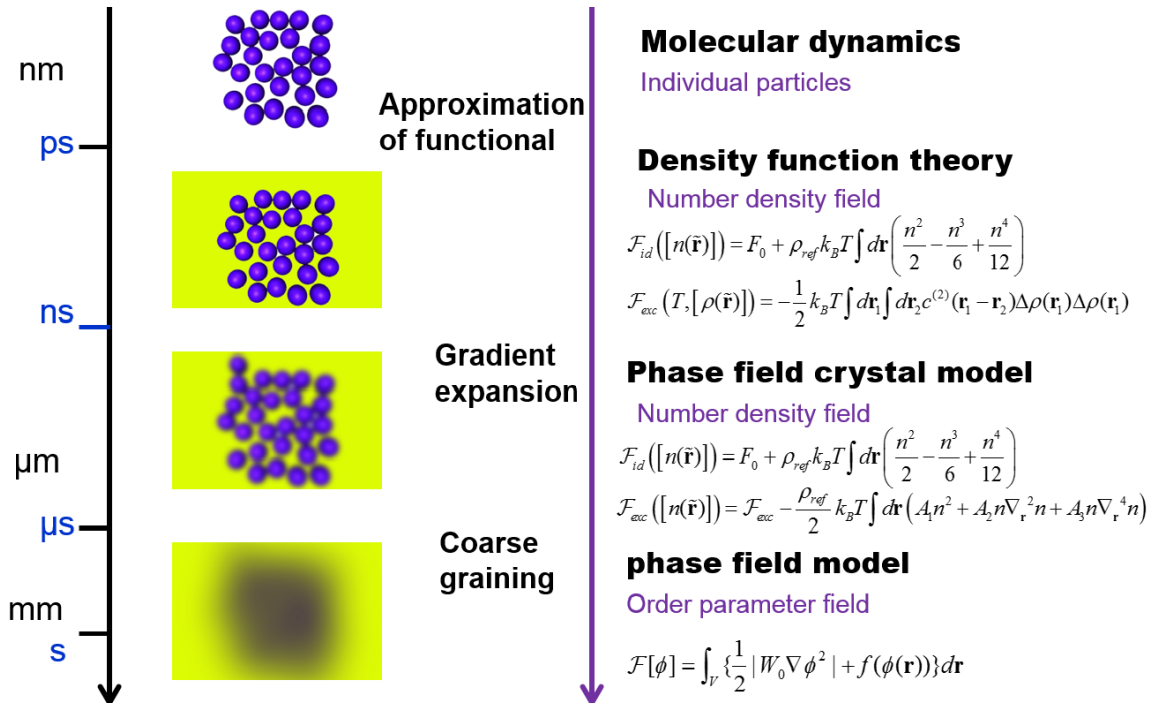
Fig. 2.22 Comparison of different modelling methods at atomic and micrometre scale.

systems the relevant time scales are diffusive (*e.g*, ms in metallic glass [162]). This makes MD method extremely computationally demanding, if not completely inapplicable, for simulation cases that need to understand long time scale events.

Density function theory (DFT) method was historically used for the studies of crystallization of liquids, colloids and metals [163, 164] by modelling them as classical many-body systems. DFT simulates the interparticle interactions and predicts the free energy and the static many-body correlations [164]. DFT operates on atomic length scale and diffusive time scale, and provides extremely high accuracy for the calculation of physical properties [164]. But it is usually very computing demanding especially for a large system, due to the fact that an extremely fine spatial grid is needed to resolve very sharp density peaks [165].

As shown in Fig. 2.23, The phase-field crystal (PFC) approach initially motivated by Swift-Hohenberg model [165], can be derived from the density function theory (DFT) [166] as detailed in the next sections. The density field in PFC model is either a constant for liquid or periodic function for crystalline solid [165].

1977
Roll pattern in convection

phenomelogically

Swift-Hohenberg model:

$$\mathcal{F} = \int d\vec{r}\left(\frac{\psi}{2}(-\beta + (k_0^2 + \nabla_{\vec{r}}^2)^2)\psi + \frac{\psi^4}{4}\right)$$

$$\frac{\partial \psi}{\partial \tau} = \nabla \frac{\delta \mathcal{F}}{\delta \psi}$$

2002
crystalline phase

Phase field crystal model:

$$\mathcal{F} = \int d\vec{r}\left(\frac{\psi}{2}(-\beta + (k_0^2 + \nabla_{\vec{r}}^2)^2)\psi + \frac{\psi^4}{4}\right)$$

$$\frac{\partial \psi}{\partial \tau} = \nabla^2 \frac{\delta \mathcal{F}}{\delta \psi}$$

2002–2006
PFC applications

**Elasticity,
plasticity,
Dislocation,
Grain-boundary
dynamics**

1991
Density function theory

$$\mathcal{F} = \mathcal{F}_{id} + \mathcal{F}_{exc} + \mathcal{F}_{ext} \qquad \frac{\partial \psi}{\partial \tau} = \nabla^2 \frac{\delta \mathcal{F}}{\delta n}$$

**Gradient
Expansion:** $F_{id} = -\frac{\psi^3}{6} + \frac{\psi^4}{12}$

$$F_{exc} = A_1\psi^2 + A_2\psi\nabla_{\vec{r}}^2\psi + A_3\psi\nabla_{\vec{r}}^4\psi$$

2007
PFC derived from DFT

$$\frac{\partial \psi}{\partial \tau} = \nabla^2 \frac{\delta \mathcal{F}}{\delta \psi}$$

2009

**Dynamic density
function theory**

**More
microscopic**

Until now

**Binary PFC,
Modified PFC,
Vacancy PFC,
Amplitude equation of PFC…**

Fig. 2.23 Phase-field crystal and its relations to Swift-Hohenburg and density function theory.

Compared to DFT, the standard PFC model describes the dissipative dynamics as shown in Eq. 2.32 and it only resolves the diffusive processes at long time scale from ns to ms, rather than the collective oscillations of atoms in ps. Furthermore, more diffuse PFC density peaks allow for more efficient numerical computation, and coarser spatial grids which can be used.

In addition, since it is derived from DFT, the PFC model naturally incorporates elasticity, plasticity, and many solid–liquid properties such as surface energies and anisotropy, grain boundary, and dislocations [167]. Besides, several common crystals systems [167] can be handled in PFC, such as body-centred cubic (BCC), face-centred cubic (FCC), and hexagonal close packed (HCP) crystals.

In summary, PFC is a simplified DFT method, and much more computationally efficient for a large system, especially for modelling the evolution of atomic structure in diffusive time scale [165].

2.4.2 Monatomic phase-field crystal model

DFT has established a well-known basis to determine the equilibrium one-particle density field $\rho(\mathbf{r})$ for any classical many-body system. However, the exact form of the grand canonical free-energy density functional $\Omega(T, \mu, [\rho(\mathbf{r})])$ does not exist [167], and has to be derived by approximations [167]. where μ is the chemical potential, and $\rho(\mathbf{r})$ is the atomic number density. Through a legendre transform, the grand canonical functional can be expressed by an equivalent Helmholtz free-energy functional $\mathscr{F}(T, [\rho(\mathbf{r})])$, which is used to derive the PFC model as well [167]. The Helmholtz free energy functional $\mathscr{F}(T, [\rho(\mathbf{r})])$ can be further split into three parts:

$$\mathscr{F}(T, [\rho(\mathbf{r})]) = \mathscr{F}_{id}(T, [\rho(\mathbf{r})]) + \mathscr{F}_{exc}(T, [\rho(\mathbf{r})]) + \mathscr{F}_{ext}(T, [\rho(\mathbf{r})]) \qquad (2.25)$$

Where, $\mathscr{F}_{id}(T,[\rho(\mathbf{r})])$ is the local ideal gas free energy functional, $\mathscr{F}_{exc}(T,[\rho(\mathbf{r})])$ is the excess free energy functional, $\mathscr{F}_{ext}(T,[\rho(\mathbf{r})])$ is the external free energy functional. For simplicity, the temperature dependant free energy is rewritten as $\mathscr{F}([\rho(\mathbf{r})])$.

For the local ideal gas free energy functional, it yields,

$$\mathscr{F}_{id}([\rho(\mathbf{r})]) = \mathscr{F}_0 + \rho_{ref}k_BT \int d\mathbf{r}\left(\rho + \frac{\rho^2}{2} - \frac{\rho^3}{6} + \frac{\rho^4}{12}\right) \qquad (2.26)$$

Where, $\mathscr{F}_0$ is the reference free energy functional, ρ_{ref} is the reference liquid number density, k_B is the Boltzmann constant. For simplicity, the $\rho(\mathbf{r})$ is replaced by ρ here.

Normally the external energy part is neglected in most PFC calculations [166], hence,

$$\mathscr{F}_{ext} = \rho_{ref}\int d\mathbf{r}U_1(\mathbf{r}) = 0 \qquad (2.27)$$

The second part is the excess free energy functional, $\mathscr{F}_{exc}(T,[\rho(\mathbf{r})])$, which describes the excess free energy over the exactly known ideal-gas functional. It consists of all correlations caused by the pair interactions between the particles. However, it is not known explicitly and therefore needs to be approximated appropriately. A classical approximation is known as the Ramakrishnan-Yussouff theory [163]:

$$\mathscr{F}_{exc}(T,[\rho(\mathbf{r})]) = -\frac{1}{2}k_BT \int d\mathbf{r}_1 \int d\mathbf{r}_2 c^{(2)}(\mathbf{r}_1 - \mathbf{r}_2)\Delta\rho(\mathbf{r}_1)\Delta\rho(\mathbf{r}_2) \qquad (2.28)$$

Where, $c^{(2)}(\mathbf{r}_1 - \mathbf{r}_2)$ is the direct pair correlation function of the fluid, and the $\Delta\rho(\mathbf{r}_i)$ is the density difference of the $\rho(\mathbf{r})$ and ρ_{ref} for position i.

For the Ramakrishnan-Yussouff approximation, the direct pair correlation function $c^{(2)}(\mathbf{r}_1 - \mathbf{r}_2)$ is necessarily needed as the main input for the PFC model. Based on the free energy model of DFT, some coarse graining procedure is employed to get the PFC free

energy model. Firstly a scalar dimensionless order-parameter field $n(\mathbf{r})$, the reduced number density given by the relative density deviation $\rho(\mathbf{r}) = \rho_{ref}(1 + n(\mathbf{r}))$ around the prescribed fluid reference density ρ_{ref}, and $c^{(2)}(\mathbf{r}) = c_0^{(2)} - c_2^{(2)}\nabla_{\mathbf{r}}^2 + c_4^{(2)}\nabla_{\mathbf{r}}^4 \mp \cdots$ are inserted into the free energy functional. Then $\mathscr{F}_{id}$ is Taylor expanded up to the 4th order in terms of power of $n(\mathbf{r})$ as,

$$\mathscr{F}_{id}\left([n(\mathbf{r})]\right) = F_0 + \rho_{ref}k_BT \int d\mathbf{r}\left(n + \frac{n^2}{2} - \frac{n^3}{6} + \frac{n^4}{12}\right) \tag{2.29}$$

The nonlocal Ramakrishnan-Yussouff approximation for the excess free-energy functional $\mathscr{F}_{exc}\left([\rho(\mathbf{r})]\right)$ is gradient-expanded to the 4th order:

$$\mathscr{F}_{exc}\left([n(\mathbf{r})]\right) = \mathscr{F}_{exc} - \frac{\rho_{ref}}{2}k_BT \int d\mathbf{r}\left(A_1 n^2 + A_2 n\nabla_{\mathbf{r}}^2 n + A_3 n\nabla_{\mathbf{r}}^4 n\right) \tag{2.30}$$

Where, the constant external free energy is defined as $F_{exc} = F_{exc}\left(\rho_{ref}\right)$, and the coefficients in Eq. 2.30 are $A_1 = 4\pi\rho_{ref}\int_0^\infty dr r^2 c^{(2)}(r)$, $A_2 = \frac{2}{3}\pi\rho_{ref}\int_0^\infty dr r^4 c^{(2)}(r)$, and $A_3 = \frac{1}{30}\pi\rho_{ref}\int_0^\infty dr r^6 c^{(2)}(r)$.

By neglecting the irrelevant constants, all together the PFC free energy functional can be formulated as [167]:

$$\mathscr{F}\left([n(\mathbf{r})]\right) = \rho_{ref}k_BT \int d\mathbf{r}\left(n + A'_1 n^2 + A'_2 n\nabla_{\mathbf{r}}^2 n + A'_3 n\nabla_{\mathbf{r}}^4 n - \frac{n^3}{6} + \frac{n^4}{12}\right) \tag{2.31}$$

Where, $A'_1 = \frac{1}{2}(1 - A_1)$, $A'_2 = -\frac{1}{2}A_2$ and $A'_3 = -\frac{1}{2}A_3$.

The reduced one-particle number density is conserved and its dynamics is assumed to be dissipative via the generalized diffusion equation, therefore, the equation of motion (EOM) can be written as,

$$\frac{\partial n(r,t)}{\partial t} = \frac{D_T}{k_B T} \nabla^2 \left(\frac{\delta F\left(T, [n(r,t)]\right)}{\delta n(r,t)} \right) \tag{2.32}$$

Where, D_T is the diffusion coefficient, and T is temperature. Substituting the free energy function in Eq. 2.31, and the final form of the equation of motion for number density of pure materials in PFC model is formulated as below [167]:

$$\frac{\partial n}{\partial t} = \Gamma \nabla^2 \left(\frac{\delta F}{\delta n} \right) = \Gamma \nabla^2 \left(\left(\Delta B + B^x \left(1 + \nabla^2 \right)^2 \right) n - \frac{n^2}{2} + \frac{n^3}{3} \right) \tag{2.33}$$

Where, $\Delta B = B^l - B^x$, and B^l is the dimensionless bulk modulus of the liquid state, B^x is proportional to the bulk modulus in the crystalline phase.

Since the PFC is derived from DFT, there are several extensions developed for different purposes. The main difference among these extensions comes from the way to establish a free energy functional accounting for particular cases. In the follow sections, more emphasis will be given to the binary PFC model and the vacancy PFC model.

2.4.3   Binary phase-field crystal model

The most extensively used binary generalisation of the monotonic PFC model has been derived from a binary perturbative DFT [166]. For a binary alloy made up of A and B atoms, the free energy functional can be written to lowest order, i.e. the second order, in terms of the direct correlation functions as:

$$
\begin{aligned}
\frac{\mathscr{F}}{k_B T} = \int d\vec{r} & \left[\rho_A \ln \left(\frac{\rho_A}{\rho_l^A} \right) - \delta\rho_A + \rho_B \ln \left(\frac{\rho_B}{\rho_l^B} \right) - \delta\rho_B \right] \\
& - \frac{1}{2} \int \delta\rho_A \left(\vec{r}_1 \right) C^{AA} \left(\vec{r}_1, \vec{r}_2 \right) \delta\rho_A \left(\vec{r}_2 \right) d\vec{r}_1 d\vec{r}_2 \\
& - \frac{1}{2} \int \delta\rho_B \left(\vec{r}_1 \right) C^{BB} \left(\vec{r}_1, \vec{r}_2 \right) \delta\rho_B \left(\vec{r}_2 \right) d\vec{r}_1 d\vec{r}_2 \\
& - \frac{1}{2} \int 2\delta\rho_A \left(\vec{r}_1 \right) C^{AB} \left(\vec{r}_1, \vec{r}_2 \right) \delta\rho_B \left(\vec{r}_2 \right) d\vec{r}_1 d\vec{r}_2
\end{aligned}
\tag{2.34}
$$

where, $\delta\rho_A \equiv \rho_A - \rho_l^A$, and $\delta\rho_B \equiv \rho_B - \rho_l^B$; ρ_l^A and ρ_l^B are the number density of component A and B on the liquid-side of the liquid-solid coexistence region, respectively. It is assumed that all two-point correlation functions are isotropic $C^{ij} \left(\vec{r}_1, \vec{r}_2 \right) = C^{ij} \left(|\vec{r}_1 - \vec{r}_2| \right)$, and all two point direct correlation functions can be Taylor expanded in Fourier space up to the 4th as, $C^{i,j} \left(|\vec{r}_1 - \vec{r}_2| \right) = \left(C_0^{i,j} - C_2^{i,j} \nabla_{r_2}^2 + C_4^{i,j} \nabla_{r_2}^4 \right) \delta \left(\vec{r}_1 - \vec{r}_2 \right)$ in real space.

To make a connection between the alloy free energy and standard phase-field cystal model, it is useful to define the total number density $\rho = \rho_A + \rho_B$, and a local concentration field $c = \rho_A/\rho$. In terms of these fields the atomic densities can be written, $\rho_A = c \cdot \rho$ and $\rho_B = \rho \cdot (1 - c)$. Furthermore it is useful to define $\rho = \rho_l + \delta\rho$ and $\rho_l = \rho_l^A + \rho_l^B$. Substituting these definitions into Eq. 2.34, gives

$$
\begin{aligned}
\frac{\mathscr{F}}{k_B T} = \int & \left(\rho \ln \left(\rho/\rho_l \right) - \delta\rho + \beta\delta c + F_0 \right) d\vec{r} \\
& - \frac{1}{2} \int \delta\rho \left[c C^{AA} + (1 - c) C^{BB} \right] \delta\rho d\vec{r} \\
& + \int \rho \left[c \ln (c) + (1 - c) \ln (1 - c) \right] d\vec{r} \\
& + \int \rho c \left[\left(C^{AA} + C^{BB} \right) / 2 - C^{AB} \right] (1 - c) \rho d\vec{r}
\end{aligned}
\tag{2.35}
$$

where, $\beta \equiv \rho_l \left(C^{AA} - C^{BB} \right) (\rho + \rho_l) / 2 + \rho \ln \left(\rho_l^B / \rho_l^A \right)$, $F_0 \equiv \bar{\rho} \ln[\rho_l \left(\rho_l^A \rho_l^B \right)^{1/2}]$ $- C^{AA}/2 \left[\left(\rho_l^A \right)^2 + \rho_l/2 \left(\rho_l + \bar{\rho} \right) \right] - C^{BB}/2 \left[\left(\rho_l^B \right)^2 + \rho_l/2 \left(\rho_l + \bar{\rho} \right) \right]$.

Based on the simplified free energy in Eq. 2.35, a simple binary model can be established. In order to further develop a numerically simple model, the following dimensionless field is introduced as,

$$\phi_A \equiv (\rho_A - \bar{\rho}_A)/\bar{\rho}$$

$$\phi_B \equiv (\rho_B - \bar{\rho}_B)/\bar{\rho} \tag{2.36}$$

Where, $\bar{\rho}_A$, $\bar{\rho}_B$ and $\bar{\rho}$ are initial number density of A and B and the average number density of the binary alloy, respectively. Also, it is convenient to expand in the following two fields,

$$\phi = \phi_A + \phi_B$$

$$\psi = (\phi_A - \phi_B) + \frac{\bar{\rho}_B - \bar{\rho}_A}{\bar{\rho}} \tag{2.37}$$

Expanding free energy functional formulated in Eq. 2.35 around $\psi = 0$ and $\phi = 0$ gives a free energy functional of the following form:

$$\frac{\mathscr{F}}{\bar{\rho}k_BT} = \int d\vec{r} \left(f_0 + \frac{\phi}{2} \left[B^l + B^s \left(2R^2\nabla^2 + R^4\nabla^4 \right) \right] \phi - s\frac{\phi^3}{3} + v\frac{\phi^4}{4} \right)$$
$$+ \int d\vec{r} \left(\frac{w}{2}\psi^2 + u\frac{\psi^4}{4} + \frac{L^2}{2}|\nabla\psi|^2 + \gamma\psi + \frac{H^4}{2}\psi\nabla^4\psi \right) \tag{2.38}$$

Where, f_0, B^l, B^s, R, s, v, w, u, L, γ, H are PFC parameters related to the $C_0^{i,j}$, $C_2^{i,j}$, $C_4^{i,j}$, $\bar{\rho}$ and ρ_l. The exact expression of all these parameters can be found in [166].

In addition, conserved dynamics is often employed to derive the equation of motions for binary PFC model. In order to decouple the dynamics for the fields ϕ and ψ, the same mobility M is applied for species A and B, assuming a substitutional diffusion between

the two species. Furthermore, if a constant effective mobility is defined as $M_e = \frac{2M}{\bar{\rho}}$ with $M = M_A = M_B$, the evolution equation of binary PFC model has the form of:

$$
\begin{aligned}
\frac{\partial \phi}{\partial t} &= M_e \nabla_{\mathbf{r}}^2 \frac{\delta \mathscr{F}}{\delta \phi} \\
\frac{\partial \psi}{\partial t} &= M_e \nabla_{\mathbf{r}}^2 \frac{\delta \mathscr{F}}{\delta \psi}
\end{aligned}
\tag{2.39}
$$

The equation of motion for binary PFC model can then be formulated by substituting the simplified free energy functional in Eq. 2.38 into the dynamic equation in Eq. 2.39, which gives,

$$
\begin{aligned}
\frac{\partial \phi}{\partial t} =& M_e \nabla_r^2 \left(\phi \left(B_0^l + B_2^l \psi^2 \right) + s\phi^2 + v\phi^3 \right. \\
&+ \frac{B_0^s}{2} \left(2(R_0 + R_1 \psi)^2 \nabla_{\mathbf{r}}^2 + (R_0 + R_1 \psi^4) \nabla_{\mathbf{r}}^4 \right) \phi \\
&\left. + \frac{B_0^s}{2} \left(2\nabla_{\mathbf{r}}^2 \left(\phi (R_0 + R_1 \psi)^2 \right) + \nabla_{\mathbf{r}}^4 \left(\phi (R_0 + R_1 \phi)^4 \right) \right) \right) \\
\frac{\partial \psi}{\partial t} =& M_e \nabla_r^2 \left(B_2^l \psi \phi^2 + \gamma + w\psi + u\psi^3 - L^2 \nabla_r^2 \psi \right. \\
&\left. + 2B_0^s \phi \left((R_0 + R_1 \psi) R_1 \nabla_r^2 + (R_0 + R_1 \psi)^3 R_1 \nabla_{\mathbf{r}}^4 \right) \phi \right)
\end{aligned}
\tag{2.40}
$$

Where, the coefficients B_i^l, B_i^s, R_i with $i = 0, 1, 2, 3..$ are related to the pair correlation function, which can be determined by fitting the pair correlation function obtained either by solving the coupled Ornstein-Zernicke equation [168] or by MD simulations [169]. The binary PFC model has been used for studying a broad range of phase transitions, including the formation of solutal dendrites [166], eutectic structures [166], *etc*.

2.4.4   Vacancy phase-field crystal model

The vacancy PFC (VPFC) model [170] is an important extension of the PFC model that adds a term to the standard free energy density that penalises the negative values of the

particle density, allowing thus for an explicit treatment of vacancies. vacancy PFC (VPFC) model is equivalent to the MD method operating on a diffusive time scale, which has been employed successfully to describe the liquid and crystal structure transition [171], and also to investigate glass formation and structure relaxation of glasses [78, 172]. The free energy functional of such vacancy phase-field crystal model is formulated as:

$$\mathscr{F} = \int d\mathbf{r} \left(\frac{n}{2} \left(-\beta + \left(k_0^2 + \nabla_{\mathbf{r}}^2 \right)^2 \right) n + \frac{n^4}{4} + h \left(\left| n^3 \right| - n^3 \right) \right) \tag{2.41}$$

Here, h in the last term on the right-hand-side is a constant. The new term is a piecewise function that is zero for $n > 0$ and positive for $\phi < 0$. It is then possible to obtain a mixture of density peaks (particles) and vacant areas (where 0), resembling thus to snapshots of liquid configurations or crystalline structures with defects [170, 171]. This allows structural modelling of the disordered and ordered structure transition. The same approach has been used to address the dynamics of glasses [78, 172].

2.4.5 Numerical schemes

In the early stage, the commonly used explicit time marching with finite difference (FD) numerical scheme [173] has been employed to solve the equation of motion for PFC models. However, the explicit time marching proved to suffer severely from the constraints caused by the high order differential operators appearing in the EOM of PFC model, which is up to 12th order. The implicit FD methods have also been developed to obtain a stable solution at a large time step [174]. However, compared to the FD schemes, as a novel alternative, the pseudo-spectral methods soon gain increasing interests in solving the EOM of PFC, because these methods have unconditionally stable time marching scheme while leading to algebraic equations of the diagonal form [175].

More importantly, pseudo-spectral methods provide exponential convergence with the spatial resolution as compared to the polynomial convergence rate of the FD schemes, which

means that comparable simulation results can be obtained with low spatial resolution by pseudo-spectral methods rather than high spatial resolution by the real space methods.

Semi-implicit pseudo-spectral Fourier method [176] is one of the widely used pseudo-spectral scheme. A great advantage of Fourier method is that in frequency space, even powers of gradients become even-powered algebraic expressions of the wave vector (or the inverse wavelength). These methods are thus especially convenient to deal with the differential equations with periodic boundary conditions [176], such as EOM of PFC models, which has several terms of high order even powers of gradients and also the periodic boundary condition.

The paradigm equation can be formulated in a simple form as [177]:

$$\frac{\partial n}{\partial t} = \nabla^2 \left(\frac{F[n]}{\delta n} \right) \tag{2.42}$$

A commonly used form of $F[n]$ in standard monotonic PFC model, for example, can be given as,

$$F[n] = \int \left\{ n \frac{1 - C(\nabla)}{2} n + f(n) \right\} d\mathbf{x} \tag{2.43}$$

Where the operator $C(\nabla)$ is in general a function of gradient operators, that is,

$$C(\nabla) = C_0 + C_2 \nabla^2 + C_4 \nabla^4 \tag{2.44}$$

Where C_0, C_2 and C_4 are the coefficients of the operator $C(\nabla)$. While $f(n)$ represents any nonlinear function of the number density field in PFC model, and $f(n) = -\frac{1}{2}\frac{n^3}{3} + \frac{1}{3}\frac{n^4}{4}$.

Substituting the free energy functional in Eq. 2.43 into the equation of motion in Eq. 2.42, it gives,

$$\frac{\partial n}{\partial t} = \nabla^2 \left[(1 - C(\nabla)) n + N(n) \right] \tag{2.45}$$

Where the nonlinear part is defined as $N(n) = \frac{\partial f(n)}{\partial n}$.

The equation above can be efficiently solved numerically by taking the Fourier transform of both sides, which yields,

$$\frac{\partial \widehat{n}_k}{\partial t} = \nabla_k^2 \left(1 - \widehat{C}(|k|)\right) \widehat{n}_k + \nabla_k^2 \widehat{N}_k[n] \tag{2.46}$$

Where, $N(n) \xrightarrow{\text{FFT}} \widehat{N}_k[n]$, and ∇_k^2 is the discrete Fourier space representation of the ∇^2 (wave vector) for a finite size system (which is algebraic in Fourier space). Finally, $\hat{C}(|k|)\hat{n}_k$ is the Fourier transform of the operator $C(\nabla)n$.

Providing $w_k \equiv \nabla_k^2 \left(1 - \widehat{C}(|k|)\right)$ and $\widehat{n}_k(t) = \nabla_k^2 \widehat{N}_k[n]$, Eq. 2.46 can be reformulated as below,

$$\frac{\partial \widehat{n}_k}{\partial t} = w_k \widehat{n}_k + \widehat{n}_k(t) \tag{2.47}$$

Such an algebraic equation is often in the diagonal form, which can be readily solved if all the relevant Fourier entities, such as w_k and $\widehat{n}_k(t)$ in the equation are evaluated using the existing FFT numerical library [178].

2.5   Summary

A brief description of the order of structure is given followed by a discussion on the thermodynamics and kinetics for ordered to disordered structural transition, and several universal mathematical methods for describing the structures of materials.

The development of metallic glasses and their composites are briefly reviewed. The widely used structural characterisation techniques are also reviewed, including X-ray total scattering and neutron diffraction, X-ray imaging and tomography, and electron microscopy imaging and focus ion beam plus scanning electron microscopy tomography.

The numerical methods for modelling atomic structures and evolution are also reviewed with a focus on the phase-field crystal modelling methods, including the development of free energy functional and three important extensions, monatomic PFC model, binary PFC model, and vacancy PFC model.

Chapter 3

Experimental and data analysis methods

In this chapter, all relevant experimental, image and data analysis methods are described in details, including sample preparation, experimental setup, data acquisition, images and data processing, and data analyses *etc.*

3.1 Alloys and samples

3.1.1 Binary, ternary alloys and ribbon samples

Two typical early transition metal-late transition metal (ETM-LTM) binary alloys, ZrCu and NiTi based binary alloys are chosen for this research and Fig. 3.1 shows their equilibrium binary phase diagrams.

To study and understand the effects of chemical compositions on atomic structures, for each alloy system, three different compositions were chosen, and the selected compositions (in atomic %) are listed in Table. 3.1, and also marked on the respective phase diagrams in Fig. 3.1.

To investigate the effects of atomic size ratio on atomic structures, two typical ternary alloys, $Cu_{55}Zr_{40}Al_5$ and $Ti_{55}Cu_{38}Ni_7$ were chosen. The atomic radii of constituent elements in alloys of $Cu_{55}Zr_{40}Al_5$ and $Ti_{55}Cu_{38}Ni_7$ are: Zr:1.55 Å, Cu:1.35 Å, Al:1.25 Å, Ti:1.4 Å

Table 3.1 The alloys and samples used for studying the changes of atomic structures

Alloy system	Composition	Sample form	Structure	Experimental purpose
CuZr	$Cu_{50}Zr_{50}$	ribbon	amorphous	
	$Cu_{57}Zr_{43}$	ribbon	amorphous	effect of composition
	$Cu_{64.5}Zr_{35.5}$	ribbon	amorphous	
TiNi	$Ti_{65}Ni_{35}$	ribbon	amorphous	
	$Ti_{70}Ni_{30}$	ribbon	composite	effect of composition
	$Ti_{75}Ni_{25}$	ribbon	crystalline	
CuZrAl	$Cu_{55}Zr_{40}Al_5$	ribbon	amorphous	effect of atomic size ratio
TiCuNi	$Ti_{55}Cu_{38}Ni_7$	ribbon	amorphous	
Vit1[1]		ϕ 800 μm needle	amorphous	effect of temperature
DH3[2]		ϕ 70 μm needle	composite	effect of temperature

[1]$Zr_{41.2}Ti_{13.8}Cu_{12.5}Ni_{10}Be_{22.5}$ (atomic.%); [2]$Zr_{39.6}Ti_{33.9}Nb_{7.6}Cu_{6.4}Be_{12.5}$ (atomic. %)

and Ni:1.35 Å. The atomic size ratio for $Cu_{55}Zr_{40}Al_5$ is $R_{Zr} : R_{Cu} : R_{Al}$ = 1.0:0.88:0.78, and for $Ti_{55}Cu_{38}Ni_7$ it is $R_{Ti} : R_{Cu} : R_{Ni}$ = 1.0:0.95:0.95.

Alloy ingots with the designed composition were melt in an arc remelting furnace. The alloys were remelted five times before casting into ribbons of 50 μm thick and about 5 mm wide using melt spinning technique. The ribbons were then cut into 20 mm long small segments for the X-ray diffraction experiments.

3.1.2 Multicomponent alloys and bar/ingot samples

The ZrTi based BMGs (alloy code :Vit1 [58]) was used as a model material to investigate the atomic structure and its evolution during different heating and cooling conditions using in-situ X-ray total scattering and pair distribution function methods.

The alloy which was made by arc melting a mixture of Ti, Zr, Ni, Cu, and Be elements with purities higher than 99.9 wt.% under a Ti-gettered argon atmosphere, was melted using an arc re-melting furnace, then casted into button ingots of 45 mm in diameter. The samples
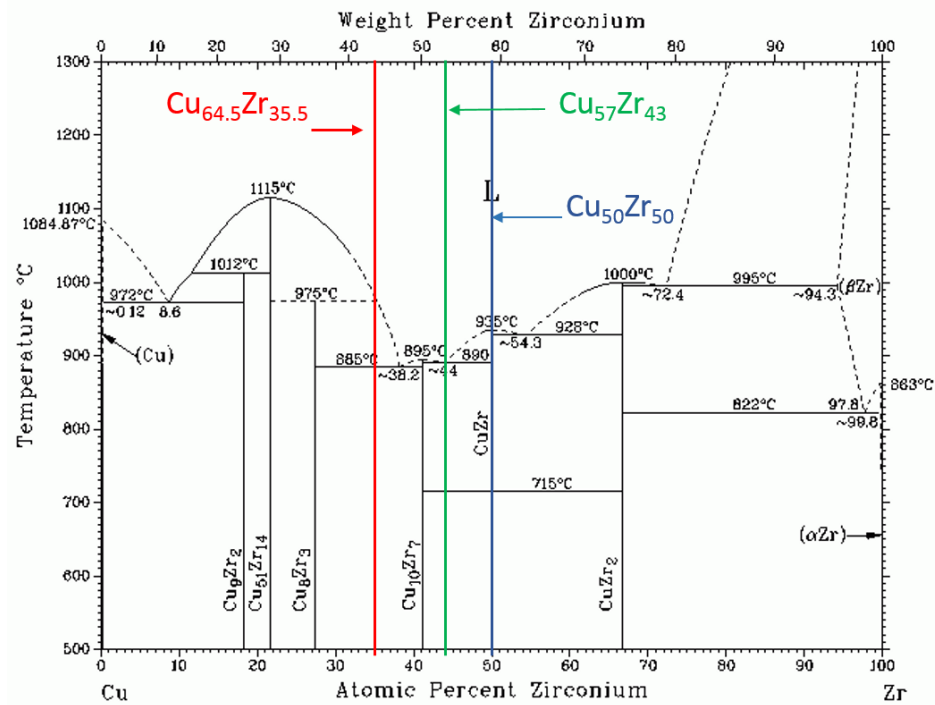
(a)
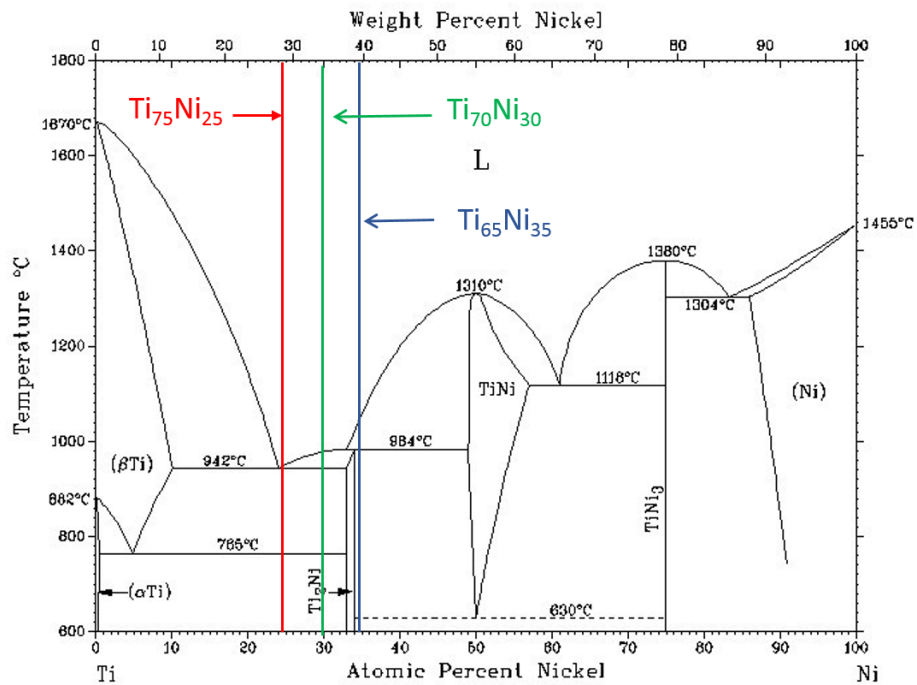
(b)

Fig. 3.1 (a) Phase diagram of (a) ZrCu [179], and (b) that of NiTi binary alloy [180, 181].

were then sectioned into small segments and grounded into 0.7-0.8 mm needle shaped samples before encapsulated into 1 mm diameter quartz capillary tubes.

The Zr-Ti based BMGMC (alloy code : DH3 adapted [62]) was chosen to investigate the atomic structure transition across the amorphous and crystalline phase interface, and also structure changes under thermal shock. This alloy has a well-developed dendritic crystalline structure inside the amorphous matrix, and a combination of tensile strength and excellent ductility can be formed by a metallic bonded phase interface.

The Alloy ingots were made by arc melting a mixture of Ti, Zr, Nb, Cu, and Be elements with purities higher than 99.9 wt.% under a Ti-gettered argon atmosphere. The alloys were remelted at least four times before being casted into a copper mold to form a button ingot of 45 mm in diameter.

All the ribbons, bulk metallic glasses and composites samples were made in the State Key Laboratory of Advanced Welding and Joining, Harbin Institute of Technology, China through the funding and support of a Royal Society K.C. Wong Postdoctoral Fellowship project "Synthesis and in-situ study of the deformation mechanism of ductile Ti-based bulk metallic glasses (£66 K, 03/2012 - 03/2014)".

This is the Royal Society Newton International Fellowship funded by the K. C. Wong Foundation for Dr Yongjiang Huang of Harbin Institute of Technology, China, and my supervisor, Dr Jiawei Mi is the academic host for Dr Huang's Fellowship at University of Hull.

A large number of metallic glass based alloys and samples had been made during this Royal Society project, and a few typical binary and multicomponent metallic glass alloys and composites were selected as the model alloy systems for my PhD project.

3.2 A novel apparatus for high temperature in-situ X-ray diffraction studies

3.2.1 Design of the apparatus

A dedicated experimental apparatus was designed for performing the high temperature in-situ synchrotron X-ray diffraction studies, and the CAD design is presented in Fig.3.2. It primarily consists of three functional units: (1) a heating unit containing a special tube-shape furnace with electric resistance heater, (2) an inert gas circulation system for either protecting the alloys from being oxidised at high temperature or cooling the melt during solidification, and (3) a special sample holder to hold small diameter capillary quartz tubes and metal alloy samples. Fig.3.2 shows the CAD assemblies of the parts that made up the three units. A1 is the 1st CAD assembly, showing all parts assembled together. A2 is the 2nd assembly with the four side walls (P1, P2, P3 and P4) removed from A1 to highlight the tube furnace assembly mounted on a duratec plate (P8) and a metal plate (P9). A3 is the assembly for the special sample holder mounted on a duratec holder (P12) and a metal plate (P13).

The heating unit includes a tube-shape small furnace (P6) with electric resistance heater which is able to reach 920 °C, a duratec insulation base (P8), and four duratec heat insulation side plates (P1, P2, P3 and P4). To allow X-ray beam to pass onto the samples, a 3 mm wide and 35 mm long slot window is cut on side plate P2, and a cone-shaped window with 90.5° outward angle is machined on side plate P1. Similar cone-shaped window with the same outward angle is also made on the tube-shaped furnace (P6). This window opens a sufficient solid angle for acquiring the X-ray diffraction information scattered from the samples, and achieving a higher Q (scattering factor) range measurement.

The gas circulation system consists of a quartz tube (P7, O.D. 18×200 mm, and 1.5 mm wall thickness), a duratec top plug (P5), and a taped sample holder again made of quartz tube (P11) and a duratec holder base (P12). After assembled together, P7, P5, and P12
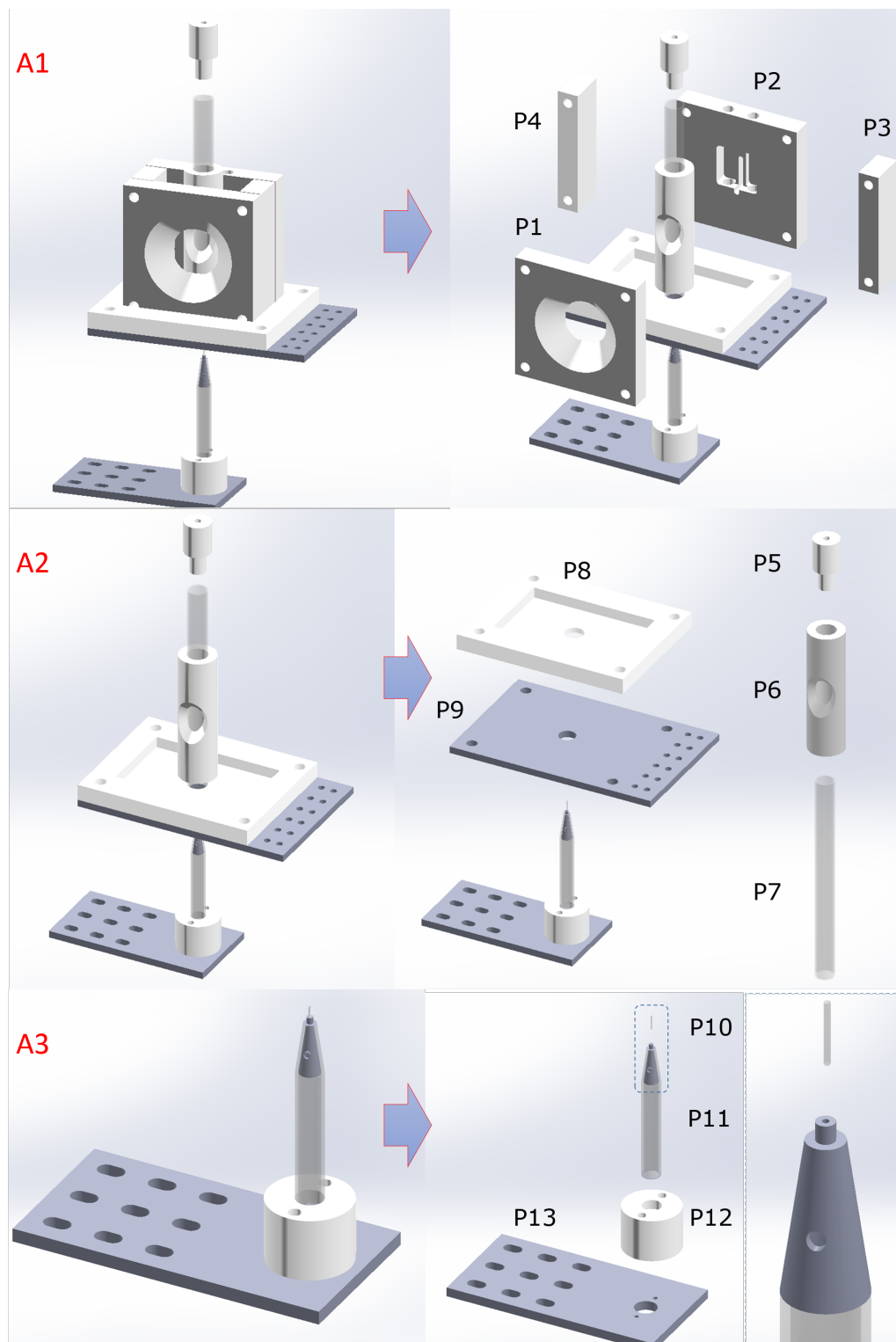
Fig. 3.2 The CAD assemblies of the designed the experimental apparatus for the in-situ high temperature X-ray diffraction studies.

together form an enclosed chamber and inert gases, such as N_2, Ar and He can be introduced into the chamber and the sample holder from the gas inlet hole through P12, circulating inside the enclosed sample chamber, and then flowing out of the chamber through the gas outlet hole through P5. Standard Polytetrafluoroethylene (PTFE) tubes (4.8 mm I. D., and can stand temperature up to 288°C) are used to connect the gas inlet of the apparatus to the pressurised inert gas bottles, and the outlet to the air ventilation system.

The sample holder is made of a small diameter quartz tube (1.2 mm I. D. 10 mm long, 0.5 mm thick) weld on top of a specially-made tapered quartz tube (P11). P11 is set on top of a duratec adaptor which again mounted on a metal base (P13). During the experiment, a metal rod sample with the typical diameter of 0.7 mm and 10 mm long was encapsulated into a standard capillary quartz tube which again inserted into the small diameter quartz tube on top of P11 and sealed tightly using mouldable mastics. P11 was then inserted into P7, allowing the metal rod sample positioned at the centre of the cone-shaped window of P1.

Two holes (∽5 mm diameter) were opened on either side of the top of the tapered section of P11 (just below the welded small quartz tube). The holes allow the inert gas to flow from P11 into P7 to protect the sample during melting and also provide the designed cooling flow by regulating the gas flow rate. Two thermocouples were also threaded through these two holes and the tip was positioned very close to the capillary quartz tube that containing the metal rod sample (less than 0.5 mm away from the capillary quartz tube). The measurement of sample temperature is critical for the in-situ PDF studies.

The material and function of each part of the apparatus are listed in Table. 3.2, and the corresponding CAD drawing for each part is showed in Appendix A.

3.2.2   Making and commission of the apparatus

The electric resistance heater is a key part of the furnace and it is made of the Kanthal wires, a high-resistivity iron-chromium-aluminium alloys for uses of up to 1400°C. The

inner chamber of the furnace is designed as ϕ 18 mm × 120 mm. Based on the calculated resistance for the heating capacity (Appendix B), the diameter and length of the resistance wires is ϕ 0.25 mm × 10 m.

As shown in Fig. 3.3 and also the 2D drawing in Appendix A, the 10 m long ϕ 0.25 mm Kanthal resistance wire is wound into the 50 mm long heating coil with an outer diameter of 4 mm. Then the 50 mm long heating coil is evenly wound around a paper tube (18 mm O. D.) with the two end of heating coil fixed on the paper tube. Before that, a 3D printed cone-shaped insert is penetrated and fixed into the paper tube to form the the 90 ° cone shaped empty for X-ray scattering. Then a mouldable fibre mastic is pasted on the surface of the coil and paper tube layer by layer. For each layer, a hot gun was used to dry the mastic up in order to hold the heating coil firmly onto the paper tube. Approximately 8 mm thick mastic was pasted to cover the heating coil completely. Then the paper tube was removed from the mastic, and the tube furnace was heated in the oven at 200 °C for 8 hours or longer to remove the moisture and built the strength.

Table 3.2 The part, material, and function of the experiment apparatus

Units	Code	Part name	Material	Function
	P1	front plate	duratec	heat insulation
	P2	back plate	duratec	heat insulation
	P3	side plate	duratec	heat insulation
Heating unit	P4	side plate	duratec	heat insulation
	P6	heater	resistance wire and mastic	heating
	P8	heater base	duratec	heater holder
	P9	furnace holder	aluminium alloy	furnace holder
	P5	top plug	duratec	gas outlet
Gas circulation	P7	gas chamber	quartz	gas protection
	P12	bottom adapter	duratec	gas inlet and sample holder positioner
	P10	capillary tube	quartz	sample holder
Sample holder	P11	taped sample holder	quartz	sample holder and gas circulation
	P13	sample holder base	aluminium alloy	base for the sample holder
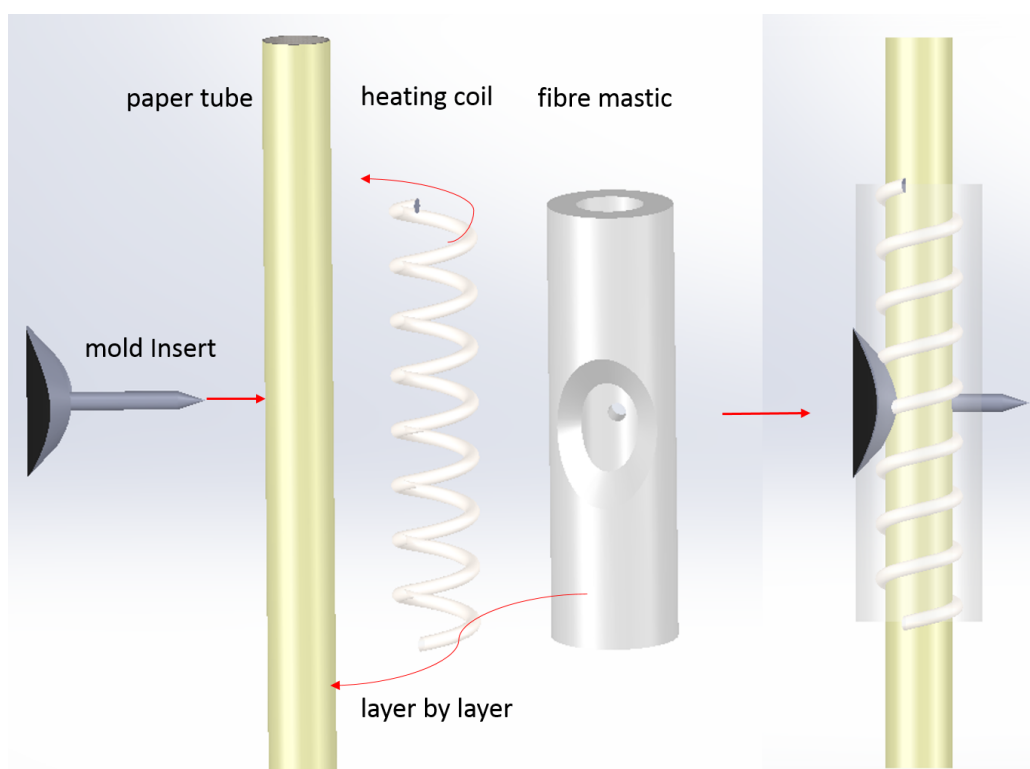
Fig. 3.3 The procedure of making the tube furnace and resistance heating coil.

The other parts of the apparatus, such as the insulation plates, the top and bottom plugs, adaptors were machined using Duratec. The metal bases are made of 6061 aluminium alloy plates. The detailed dimension of those parts can be found in the Appendix A.

In addition to the protection using inert gas, liquid sealing method was also employed to avoid the potential oxidation of the BMG samples during the melting and holding at higher temperature. The BMG sample was first loaded into the capillary tube (P10), then the Pb-60Sn (at.%) sample was loaded on top of the BMG sample. During heating, the Pb-60Sn is completely melted at 200 °C, and it sealed the top space of capillary tube, avoiding the contact of the BMG sample with the remaining air inside enclosed inert gas circulation chamber.

Many rounds of testing and commissioning experiments were carried out at the university laboratory before taking it to the Beamline I12 for the actual experiments. Fig. 3.4 shows the actual set up of the apparatus on Beamline I12. The power sockets and extension cables were connected to the resistance heater with a two way non-fused ceramic terminal block.
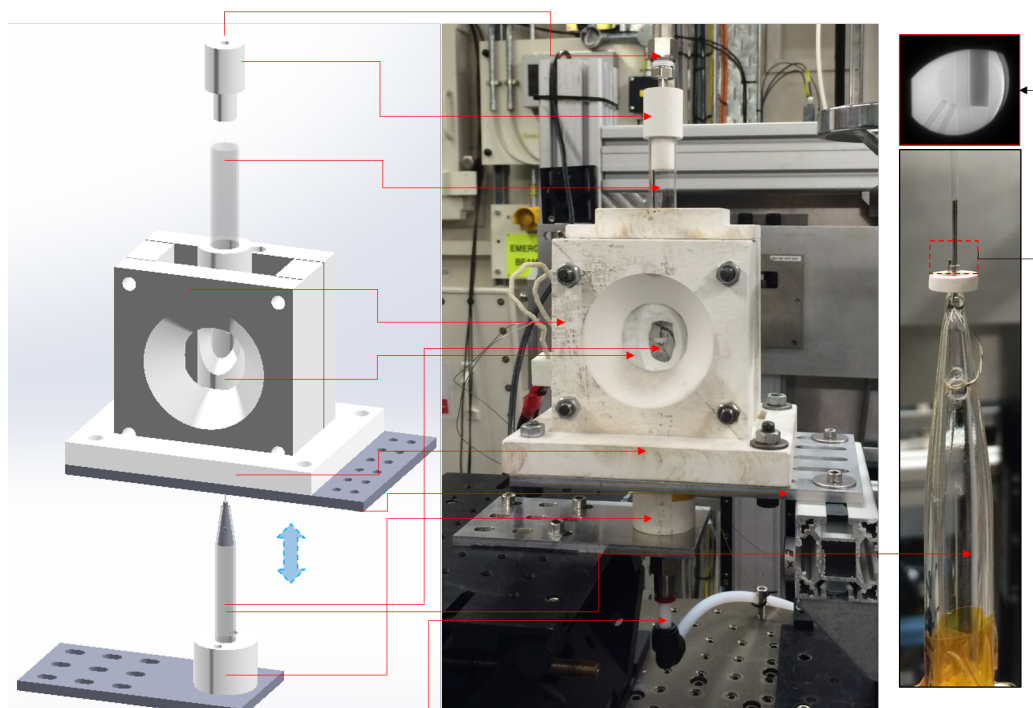
Fig. 3.4 The setup and testing of the experimental apparatus at beamline I12.

The control thermocouples for the heater were positioned very closed to ($\sim$ 0.5 mm) the heating coil in the middle, and were linked to the data acquisition software through a Pico TC08 data logger, and the temperature was controlled by an Omega PID thermal controller.

Before heating, the sample holder unit were lifted until it touches the bottom of the Aluminium furnace holder. A thin layer of fibre mastic was pasted on top surface of the bottom plug before the lifting of the sample holder, it then completely sealed the space between the sample holder and the furnace holder after these two parts sealed tightly. The inlet and outlet of inert gas was connected to the gas tank and gas ventilation system through PTFE pipes, and then inert gas can circulate inside the sample chamber. The flow rate of the inert gas was regulated by the flowmeters. The top plug was tightly fitted in the gas protection tube to seal the top of the apparatus.

3.3   In-situ X-ray diffraction experiments

3.3.1   Sample preparation

The bar ingots were cut into 10 mm long segments and grounded using SiC grinding abrasive papers into needle-shapes sample with a diameter of 0.7 mm before being placed into capillary quartz tubes of 0.9 mm I.D. During grinding, the samples were held by a small chuck mounted on a hand drill.

3.3.2   Experimental setup and X-ray parameters
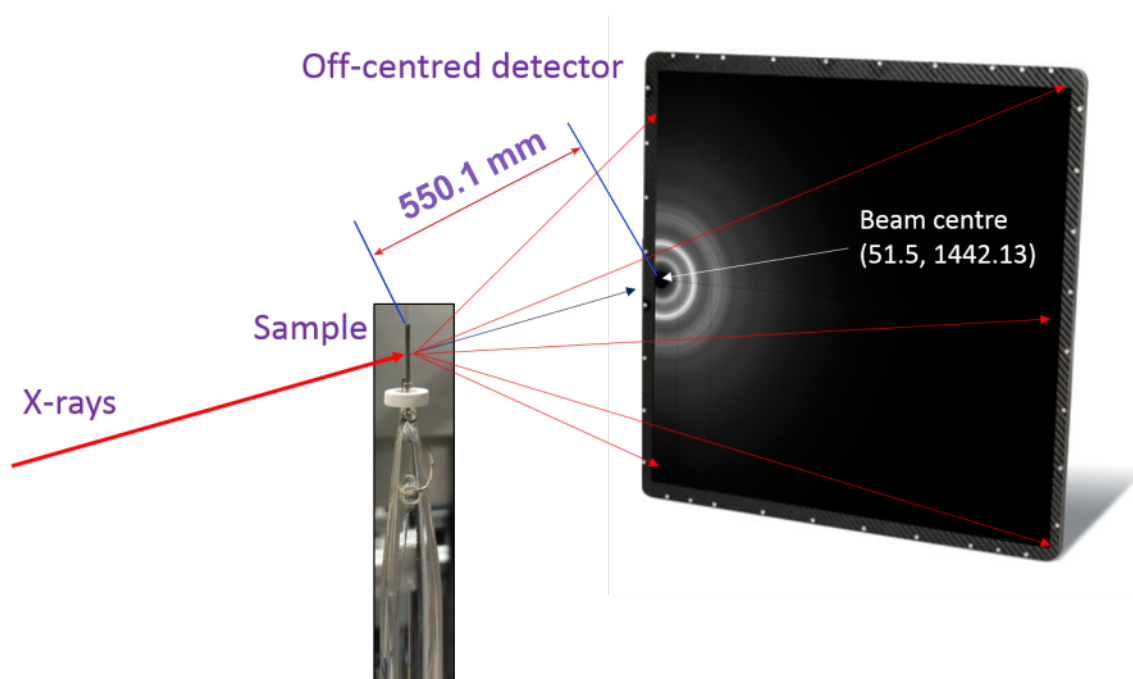
Fig. 3.5 The off centre arrangement of the diffraction detector for the in-situ PDF studies of BMG during heating and cooling processes.

The in-situ total X-ray scattering experiments were conducted at I12 of Diamond light source in 11, Feb 2015. The research is the key part of the proposal "Time-resolved X-ray diffraction in-situ studies of the atomic structure evolution of metallic glass and composites during solidification" (experiment No. EE10440).

Fig. 3.5 shows schematically the off centre arrangement of the diffraction detector, Thales Pixium RF4343. The arrangement ensures that the scattering factor, Q range up to 20 Å^{-1} can be achieved using the monochromatic X-ray energy of 75.37 keV. The beam centre of the off-centred detector was calibrated at (51.5, 1442.13) in pixel. Temperature profile was measured using the I12 data logger at 1 s resolution in addition to the Pico data logger operated at 1 ms resolution. In order to achieve rapid requisition of PDF with a high temporal resolution, the diffraction patterns were continually taken at every second during the in-situ heating and cooling process with the exposure time of 0.5 s. Furthermore, the temperature readings recorded from I12 beamline was synchronised with the diffraction data acquisition, allowing for the study of temperature dependent atomic structure change.

3.3.3 Control of the heating and cooling rates

The furnace is capable of heating samples up to 920 °C at an average heating rate of 1.50 K/s, and under Ar protection. The typical temperature profile is presented in Fig. 3.6a. The cooling was controlled by immediately shutting down the furnace heating and at the same time applying cooling gas, *i.e.* Helium (He) with the Argon (Ar) circulation still on. The cooling rate was tuned by regulating the flow rate of the He and the Ar. Fig. 3.6b shows eight typical average cooling profiles and average cooling rates achieved in the experiments, *i.e*, 14.74, 9.82, 8.75, 8.00, 4.44, 3.35, 0.86, 0.79 K/s, which allow for the study of cooling effects on the phase changes and structure evolution during crystallisation and glass formation. The average heating and cooling rates are calculated by $C_{avr} = \frac{T_{\max} - 200°C}{t_{total}}$, where C_{avr} is average cooling rate, $T_{\max}$ is maximum temperature, and t_{total} is the time for sample to cooled down from $T_{\max}$ to $200°C$.

For each heating or cooling rates, various number of diffraction patterns were obtained. For the average heating rate of 1.5 K/s. the total of 2130 patterns were collected. And for the average cooling rates at 14.7 K/s, the total of 413 diffraction patterns were acquired. The total number of diffraction patterns for the rest of cooling rates are between 413 and 2130.
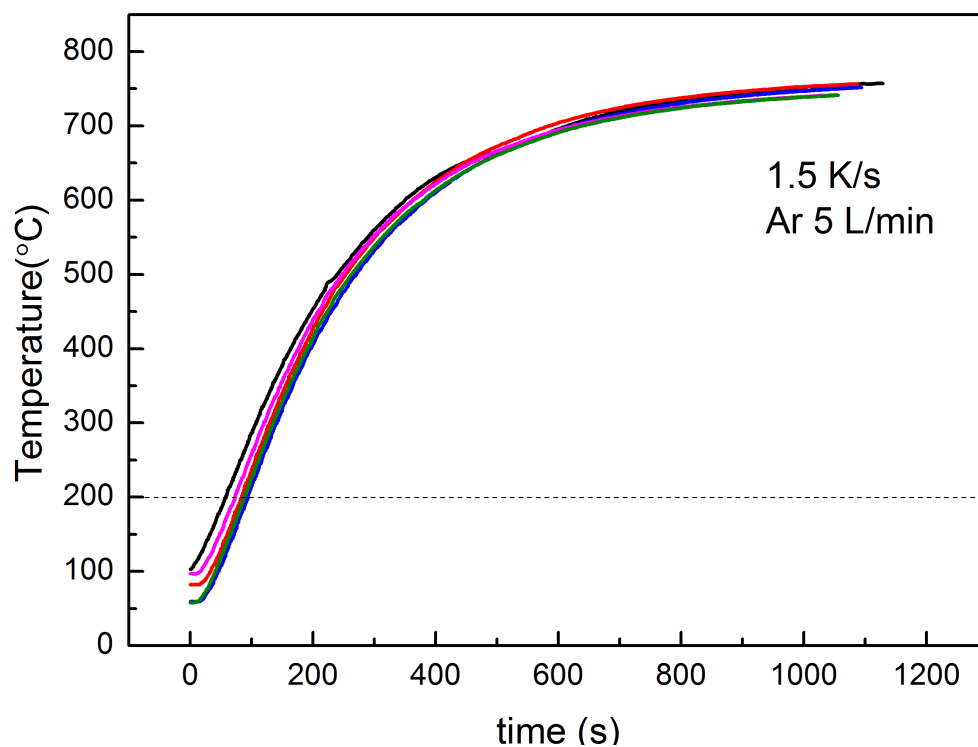
(a) Heating profile and average cooling rates.
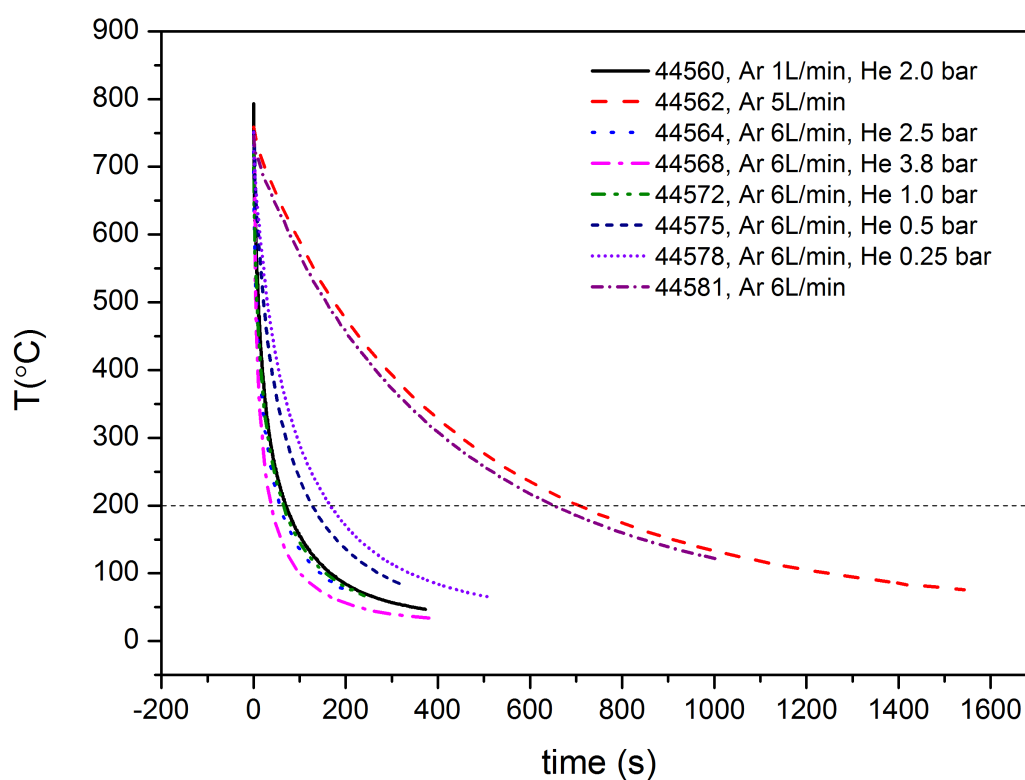
(b) Cooling profile profile and average cooling rates.

Fig. 3.6 The typical temperature profile of the (a) heating and (b) cooling processes in the in-situ X-ray total scattering experiments.

3.3.4 Diffraction data reduction and 1D integration

The diffraction data using the parameters shown in Table. 3.3, were obtained at I15 of DLS through the experiments (EE9902) on 20 April 2014.

The diffraction data reduction for the samples of binary alloys was done using Fit2D. For them, the background correction was carried out in Fit2D before the 1D integration. Before the background subtraction and 1D integration, the undesired pixels caused by the scattering from beam stops and sample surroundings, and also the saturated and dead pixels in the 2D diffraction pattern were masked off.

Fig. 3.7 shows the method for identifying the undesired pixels and the mask generated for all these ex-situ experimental samples. As shown in Fig. 3.7, a copy of the raw diffraction pattern image was rotated 5 ° around the beam centre, then was subtracted from the original image, so that the dead pixels and scattering shadow from beam stop can be readily identified from the difference of the gray value at the same pixel. In addition, the threshold masking was combined to remove dead and saturated pixels. The detector was calibrated using the standard $CeO2$ powder sample, and the calibration parameters was listed in Table 3.3. These parameters were then used to integrate the 2D diffraction patterns into the 1D diffraction spectra.

Table 3.3 Detector parameter calibrated with standard CeO2 sample in Fit2D for the diffraction experiment at I15

Experimental			Detector					
			pixel size (mm)		beam centre (mm)		orientation	
wavelenth	*S-D distance (mm)	expo. time	x	y	x	y	Rotation	Tilt
0.163137 Å	265.383 mm	10s	0.200	0.200	1056.135	1030.989	131.9047	7.739E-02

*S-D distance represents the sample to detector distance.
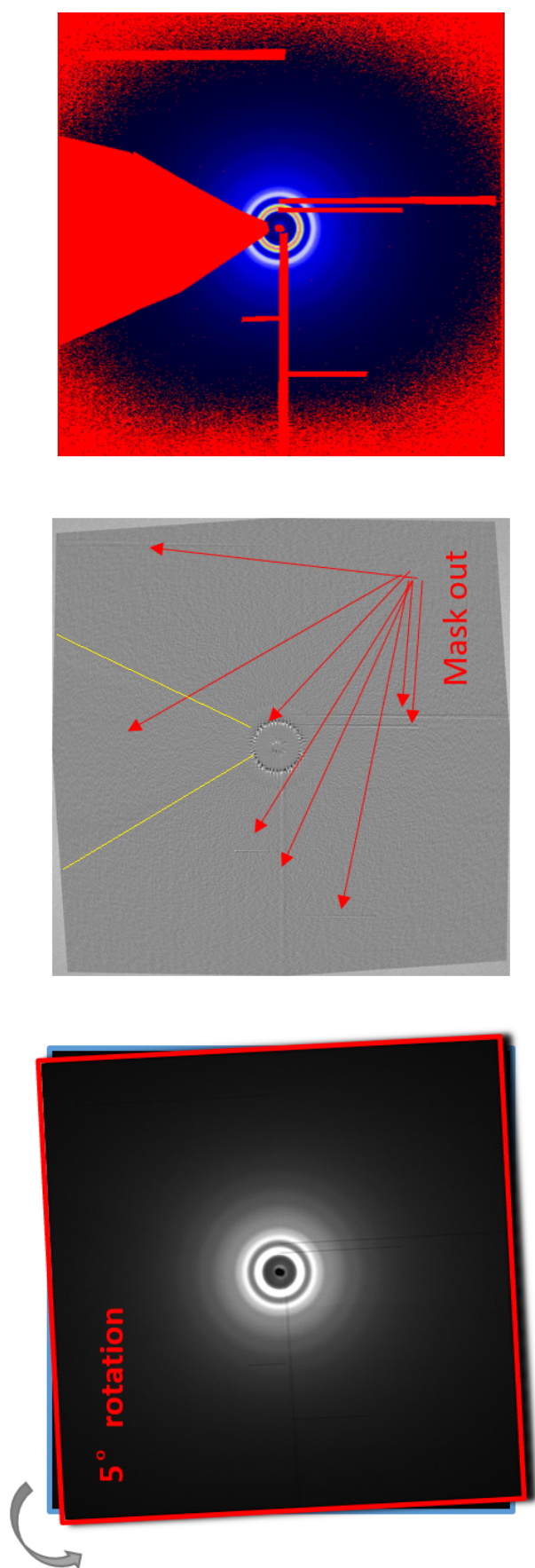
Fig. 3.7 The method to identify the undesired pixels to be masked out, and the mask created in Fit2D.

The data reduction of all the acquired dataset from the in-situ experiments was carried out in a batch mode using the data reduction module of DAWN v1.7 [182]. The same method presented in Fig. 3.7 was used to identify the undesired pixels and generate the mask for the 2D diffraction patterns acquired from the in-situ experiments. The mask generated in Dawn is shown in Fig. 3.8, which includes beam stop, horizontal and vertical strips where the two panels join, dead and saturated pixels. The detector was calibrated with the standard *CeO2* sample in Dawn, and the calibrated parameters are listed in Table 3.4.

Table 3.4 Detector parameter calibrated with standard CeO2 sample in Dawn for the in-situ total scattering experiments at I12

Experimental				Detector						
				pixel size (mm)		beam centre (mm)		orientation		
wavelenth	S-D distance (mm)	type	expo.	x	y	x	y	yaw	pitch	roll
0.1645 Å	550.41 mm	Pixium	1.0s	0.148	0.148	51.5	1442.13	-0.49	0	16.9
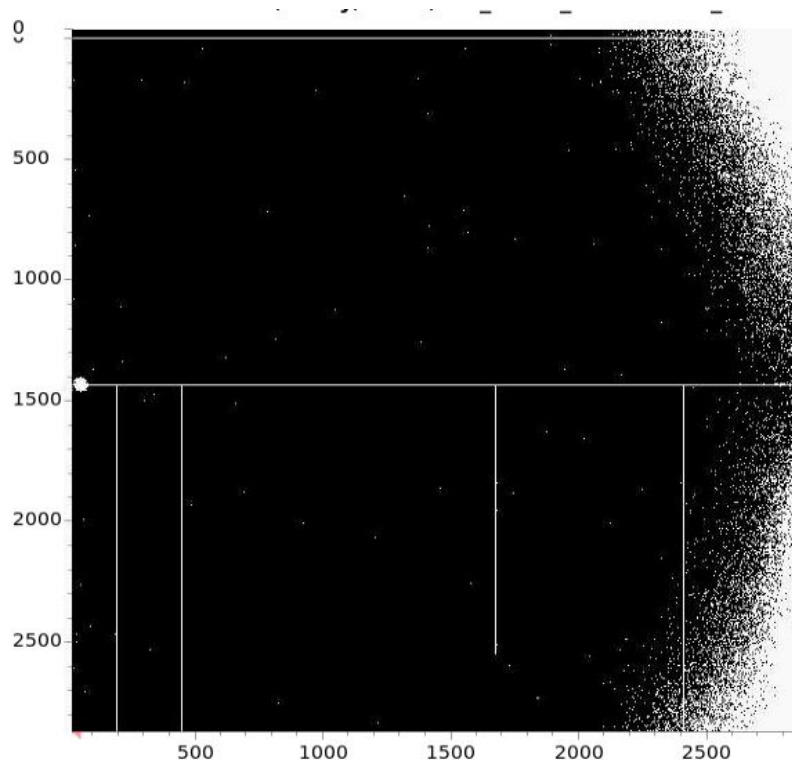
Fig. 3.8 The mask generated for all the dead pixels and beam stops using thresholding masking in Dawn V1.7, the white spots and white lines are areas being masked out.

3.3.5   Conversion from 1D diffraction spectra to pair distribution function

The series of 1D diffraction spectra output from DAWN was further processed to obtain PDF using PDFgetX3 [107]. PDFgetX3 is a scientific program to convert X-ray powder diffraction data to atomic PDFs. It adapts an ad-hoc data correction method capable of computing the pair distribution function in a batch mode, especially useful for a batch data files generated from the in-situ study. It is written in python, and implemented with some scientific-oriented python distribution, such as PythonXY. PDFgetX3 in the interactive mode can be used to tune and obtain optimised conversion parameters by visualising their effect on the resulting PDF.

There is a series of parameters listed in Table. 3.5, which are relevant to the PDF conversion from the X-ray powder diffraction, such as *wavelenth*, *composition*, *r-poly* (r-limit for the maximum frequency in the F(Q) correction polynomial), *bg-scale*, *qmaxinst*, *qmin*, *qmax*, *rmin*, *rmax* and *r-step*, and most of them are tunable parameters as shown in Table 3.5, such as *bg-scale*, *r-poly*, *qmaxinst*, *qmin*, *qmax*, *rmin*, *rmax*. Among these parameters, *bg-scale*, *qmax*, are most sensitive to the profile of PDFs.

Before batch process of the whole data set, it is necessary to tune and optimize these two key factors, *bg-scale* and *qmax*. Fig. 3.9 shows the effect of the different background scale factors on the profiles of PDFs. Based on the comparison of the PDF profiles at the low r range from 0 to 2.5, it was reasonable to choose the *bg-scale* = 0.55 as the optimised background scale parameters since, for the case of 0.55, the deviation of PDF fro zero is the lowest.

Qmax is key to the resulting PDFs, since normally the low *q* cutoff value may lower the structure resolution of PDF, however the pour counting statistics in high *q* caused by the small sample scattering cross-section [28], would generate the termination ripples [183] on the PDF as shown in Fig. 3.10 when qmax is higher than 16. Therefore, the *qmax*=16 is the best choice for the *q* cutoff.

Table 3.5 Parameters used in PDFgetX3 to convert powder diffraction spectra to PDFs

Parameter	value	comments	tuning range
wavelenth	0.1645 (Å)	x-ray wavelength	
composition	ZrTi based	alloy composition	
r-poly	0.9	r-limit for the maximum frequency	0.5–1.0
bg-scale	0.57	background scale factor	0–1.00
qmaxinst	20	q cut-off for structure factor calculation	
qmin	0	minimum q	
qmax	16	maximum q	0–qmaxinst
rmin	0	minimum r	
rmax	20	maximum r	
r-step	0.01	step size to compute PDF	
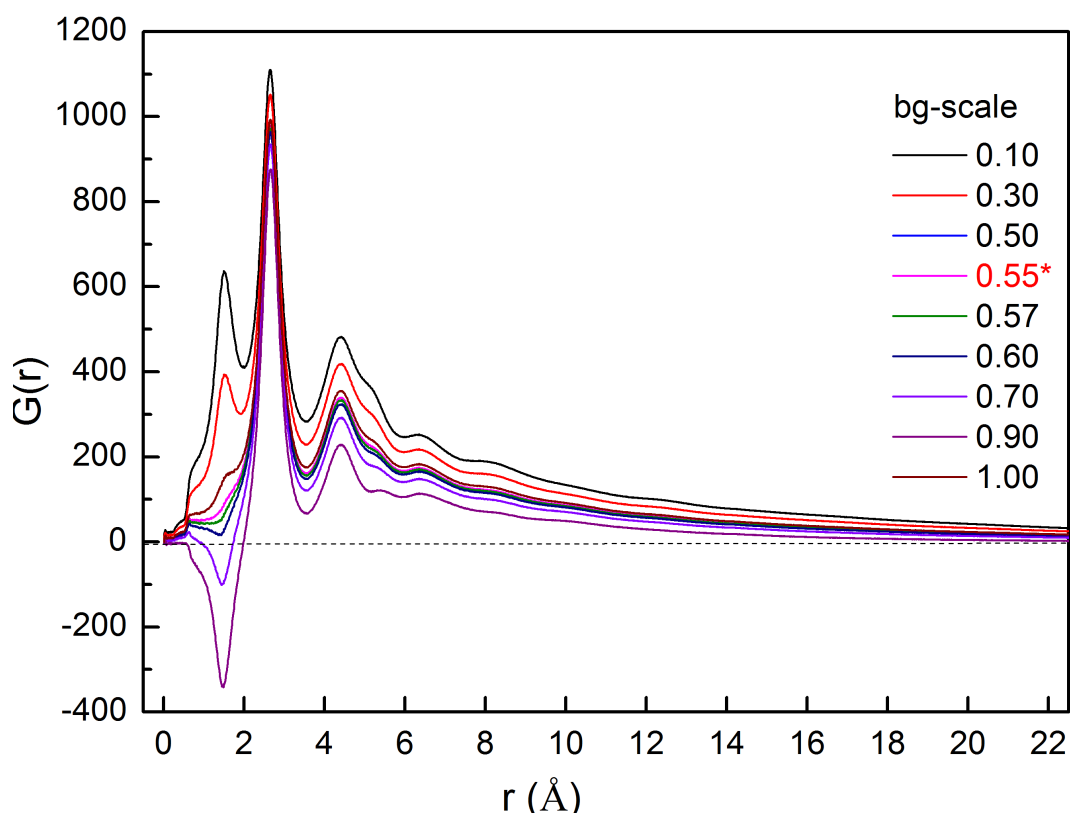
Fig. 3.9 The tuning effect of background scale factor, *bg-scale*.
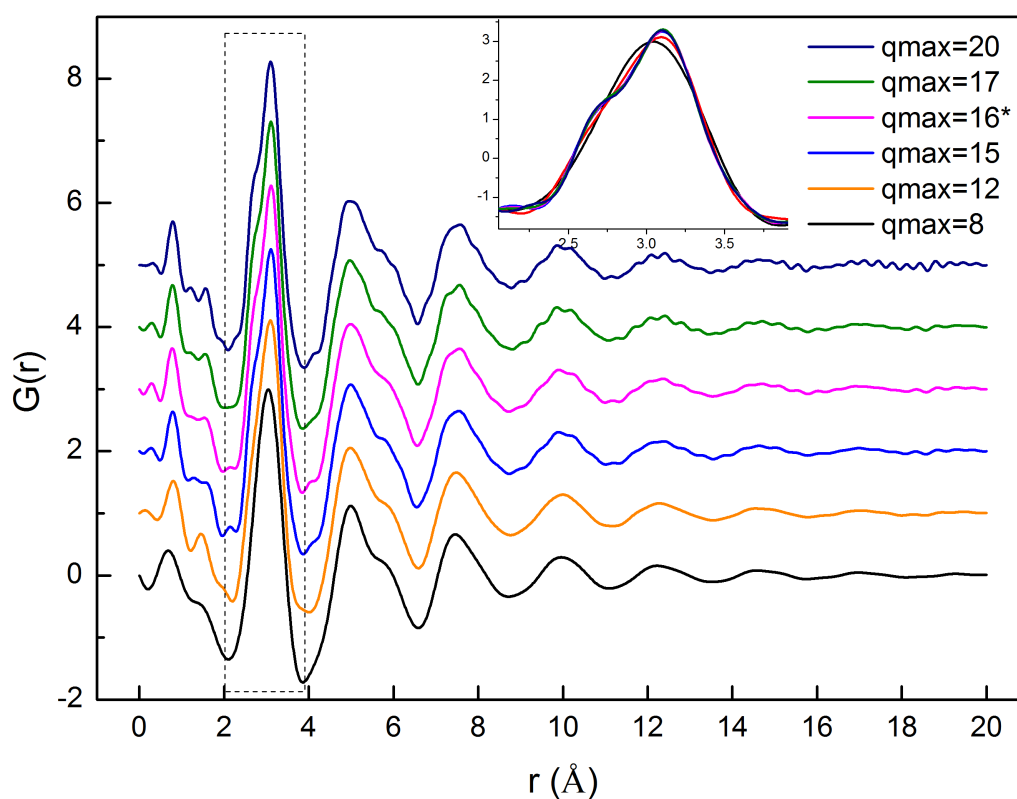
Fig. 3.10 The tuning effect of *qmax*.

3.3.6 Direct analysis and the real space refinement of the PDFs

The structure information can be obtained by direct analysis of the PDFs, such as the evolution of the peak intensities of main PDF peaks, and also the peak shift with the temperature. All peak positions and peak intensity are obtained by detecting all the peaks and hidden peaks in the PDFs in a batch mode in OriginLab. The hidden peaks are detected using the second derivative detection method [184], which searches for local minima within a smoothed second derivative data stream and these local minima often reveal hidden peaks regarded as peak shoulders.

The second derivative can be used to detect hidden peaks in data. The second derivative of the data with hidden peaks is sketched in Fig. 3.11. The adjacent-averaging method [184] is used to smooth the second derivative calculated, in which smoothed value is the average of the data points within the moving window with the size of N data points. The positive values of the second derivative are taken, and 20 points of the window are chosen

to smooth the curve of second derivative using the adjacent averaging method . 15 peaks are selected from all the peaks detected based on the threshold height of 20% of the maxima of the second derivative.
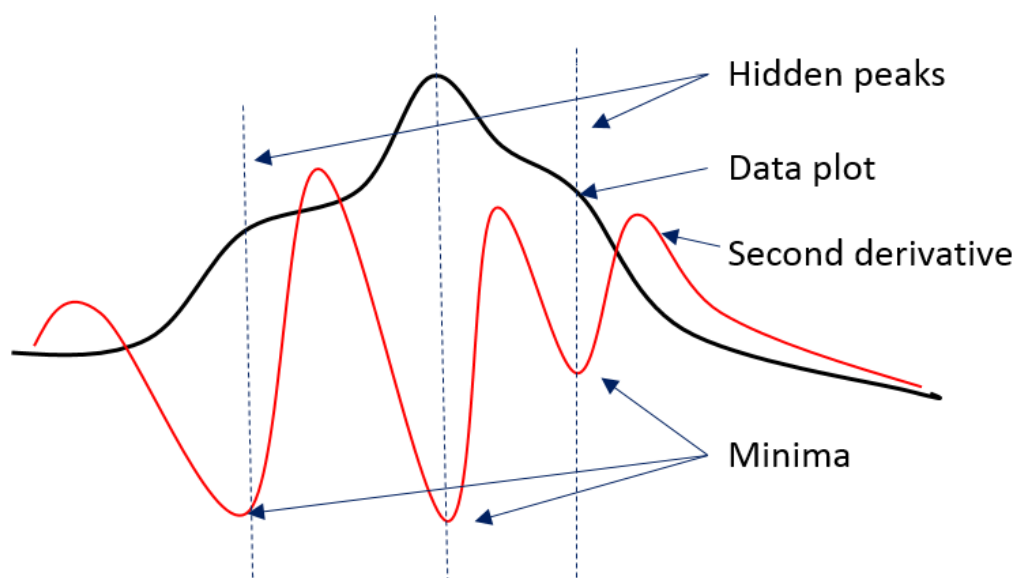
Fig. 3.11 The second derivative detection method for hidden peaks.

In addition, the PDFgui, [111] as an implementation of the full profile real space refinement method, was utilised to fit the acquired PDF of a mixture of crystalline phases to understand how the structure changes in terms of the individual contribution of the atomic pairs during the heating and cooling experiments.

The full profile real space refinement actually refines the parameters for the structural model, and other experiment-dependent parameters until a best-fit between the experimental and the calculated PDF is achieved. The structure parameters are unit cell parameters (unit cell lengths and angles) of crystalline phases, atomic fractional coordinates, anisotropic atomic displacement for each atom and the average atomic occupancy of each site. The experiment-dependent parameters include the overall scale factor, phase scale factors. The two crystalline structure Zr_2Cu and $BeZr_2$ [185, 186] were input as the two dominant phases for the real space refinement.

3.4 Thermal shock experiments using a Gleeble simulator

As an extreme case of heating study, thermal shock treatment was applied to the ZrTi based bulk metallic glass matrix composite to investigate the structure changes of DH3 when subject to a rapid heating rate.

Rod bars of $\phi 9 \times 30$ mm were electrical discharging machined from DH3 composite ingots prepared.

The thermal shock experiment was performed at Beijing Institute of Aeronautical Materials (BIAM) supported by the Royal Academy of Engineering Research Exchange project between Hull University and BIAM. A Gleeble 3500 physical simulator was used to thermally shock these rod bars to the desired temperatures with a high heating rate of $10^2 - 10^3$ K/s. Such a fast heating capability was achieved by taking the advantage of resistance heating generated inside the sample when passing through a high density electric current.
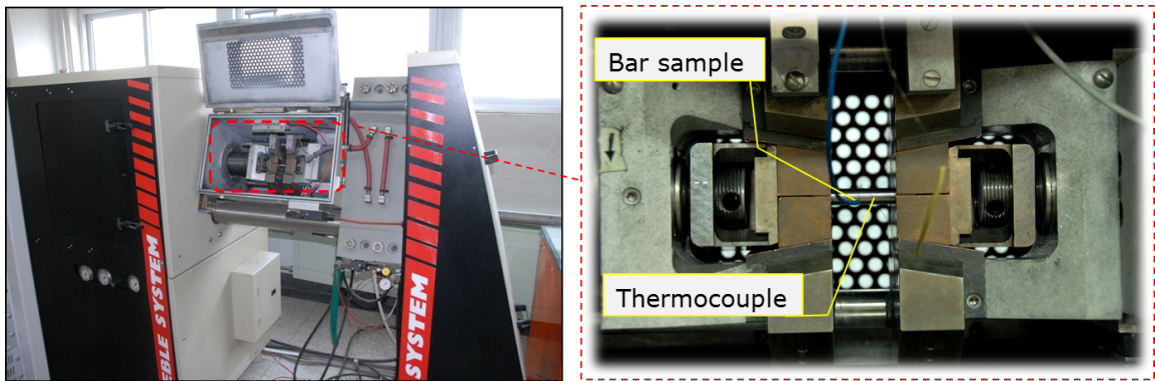
Fig. 3.12 Thermal shock setup of DH3 using a Gleeble 3500 thermomechanical simulator.

As shown in Figure. 3.12, S-type thermocouples of 0.2 mm were spot-welded at the surface in the middle of the rod sample to measure and record the temperature during experiments. A Gleeble 3500 thermo-mechanical simulator and copper (Cu) electrodes were used to clamp the rod samples and thermally shocked them to the preset temperature 550°C, 600°C, 700°C shown in Fig. 3.13a, by Joule heating generated by the high DC current passing through the samples. The measured temperature profiles are presented in

Fig. 3.13b. The peak temperature for the preset 550°C, 600°C cases around 650 °C. The temperature for the case of preset 700 °C failed to be recorded due to heat overshooting and the thermocouple was melted. Fig.3.14 shows the raw samples before thermal shock.

The target temperatures of 550 °C, 600 °C, and 700 °C were chosen, because the glass transition, initial crystallisation and melting temperature of DH3, is reported to be around 347 °C, 447 °C and 800 °C at the heating rate of 0.8 K/s using differential scanning calorimetry [187].

The heating rate was chosen to be $500 °C/s$ and the preset holding time was ~5 s according to the trace of glass transition onset temperature and crystallisation onset temperature upon different heating rate [188, 189].

3.5 Characterisation of the atomic, nano and microstructures of DH3

The 2D structure characterisation was conducted using the electron microscopy, including SEM, and HRTEM. The 3D structure characterisation was carried out using X-ray microtomography, and also the FIB-SEM nano-tomography. The corresponding equipment and experimental methods used are described in this section.

3.5.1 Electron microscopy imaging of 2D structures

SEM samples were cut from the thermally shocked rod samples shown in Fig. 3.14, and specifically the as-cast samples were cut from cold ends and the thermal shocked ones were obtained from the central region of the rod samples. All SEM specimens were ground using SiC abrasive papers and polished down to 1μm diamond suspension. The microstructure were characterized with Zeiss Evo60 SEM operated at 20 kV. At the same time, the chemical composition of each phase was quantified with the energy disperse X-ray spectroscopy (EDX) equipped in the SEM machine.
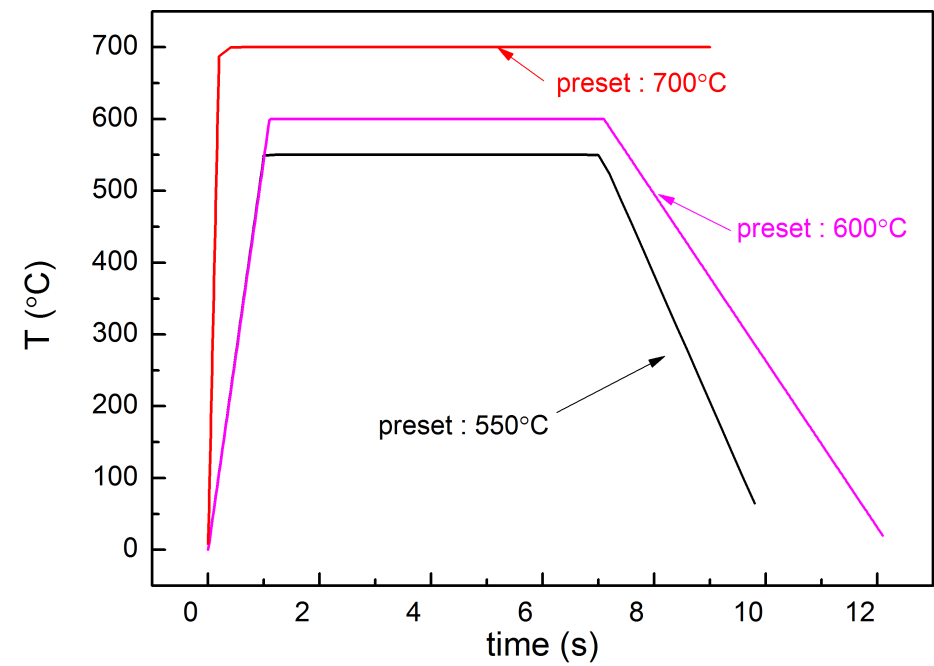
(a)
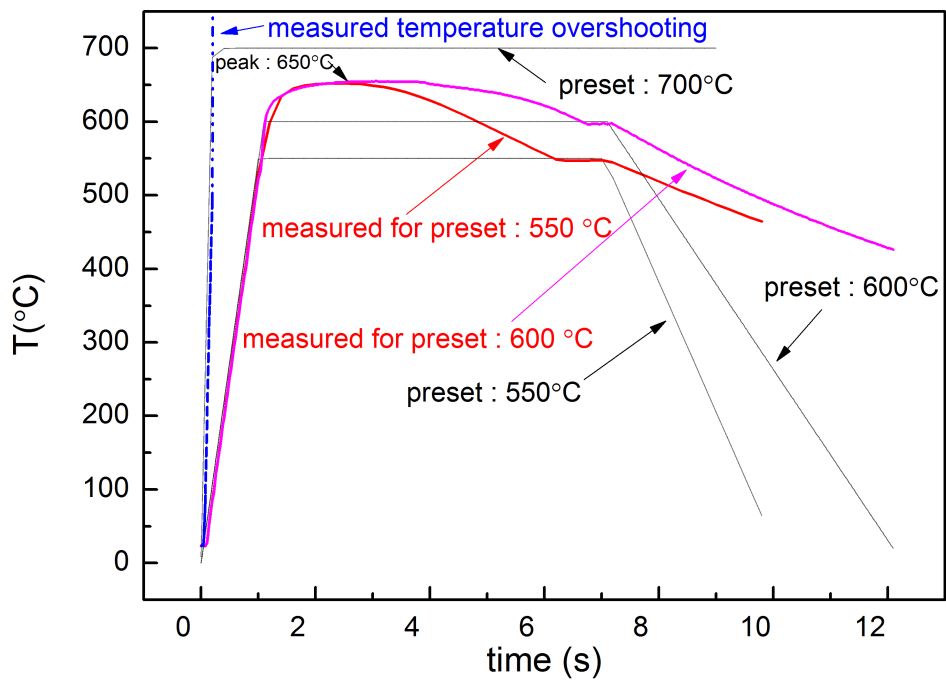
(b)

Fig. 3.13 The (a) preset and (b) measured temperature profiles for the thermal shock experiments.
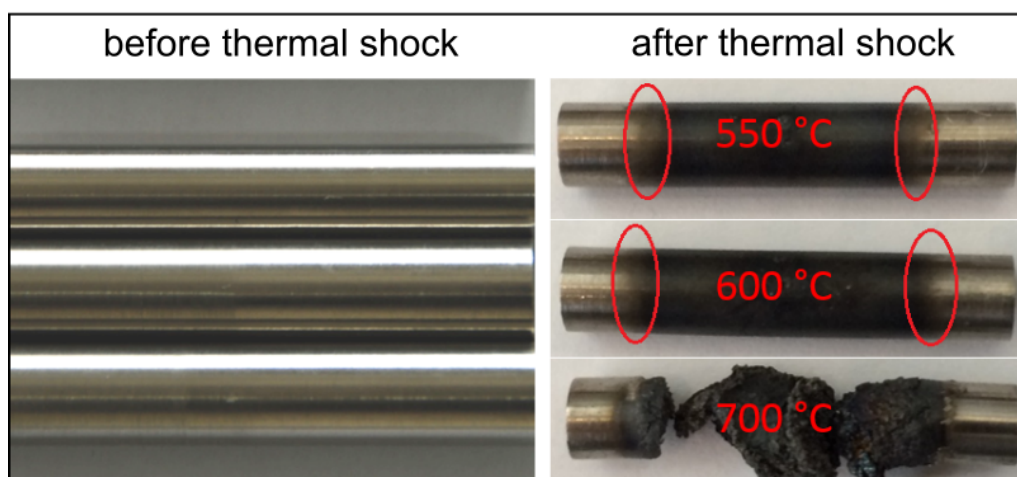
Fig. 3.14 Thermally shocked samples at three different preset temperatures: 550°C, 600°C, 700°C.

The HRTEM experiment of DH3 was carried out in the centre of Beijing electron microscope in the department of Material science, Tsinghua university, Beijing, China by Dr. Hongyu Sun. The thin foils for the HRTEM analysis were prepared by mechanically polishing to a thickness of 80 μm, and then were thinned by twin-jet electropolishing with 4% $HClO_4$+ 96% methanol solution (vol.%) to electron transparent operating at 25V and 30°C. Liquid nitrogen was used to prevent over heating of the thin foils during electropolishing. A high resolution transmission electronic microscope (HRTEM, Philips *Taitan TF30ST*) was operated at 300 kV, with the pixel size: 0.01x0.01 nm.

3.5.2   Image processing and data analysis

3.5.2.1   Two dimensional β-Zr dendrites, intermetallic phases and volume fraction

SEM was used to examine the microstructure changes due to the thermal shock, and to quantify the volume fraction for both as-cast and thermal shocked samples in two dimension. These 2D volume fractions obtained were then compared with 3D volume fraction from X-ray tomography and neutron diffraction, to reveal the thermal stability of different phases of DH3.

The typical back scattered SEM micrographs of as-cast microstructure of DH3 is presented in Fig. 3.15, and the primary dendritic phase (bright region) has the composition of $Ti_{40-44}Zr_{42-45}Nb_{11-14}Cu_{1-3}$ uniformly distributed in the region of glassy matrix with the composition of $Zr_{31-34}Ti_{17-22}Nb_{1-2}Cu_{9-13}Be_{31-38}$ [62] which was crystallised into two secondary phases as shown in Fig. 3.16. These two secondary phases were termed as bright phase and dark phase for present. Furthermore, each secondary phase is determined to possess the different chemical composition using EDX analysis: the dark phase has the composition of $Zr_{52-55}Ti_{27-30}Nb_{4-7}Cu_{9-11}$ and the bright phase has the composition of $(Zr_{46-49}Ti_{24-28}Cu_{19-22}Nb_{3-5})_{100-y}Be_y$, in which the light element Beryllium (Z=10) is not possible to be quantitatively resolved due to the limitation of the EDX detector.
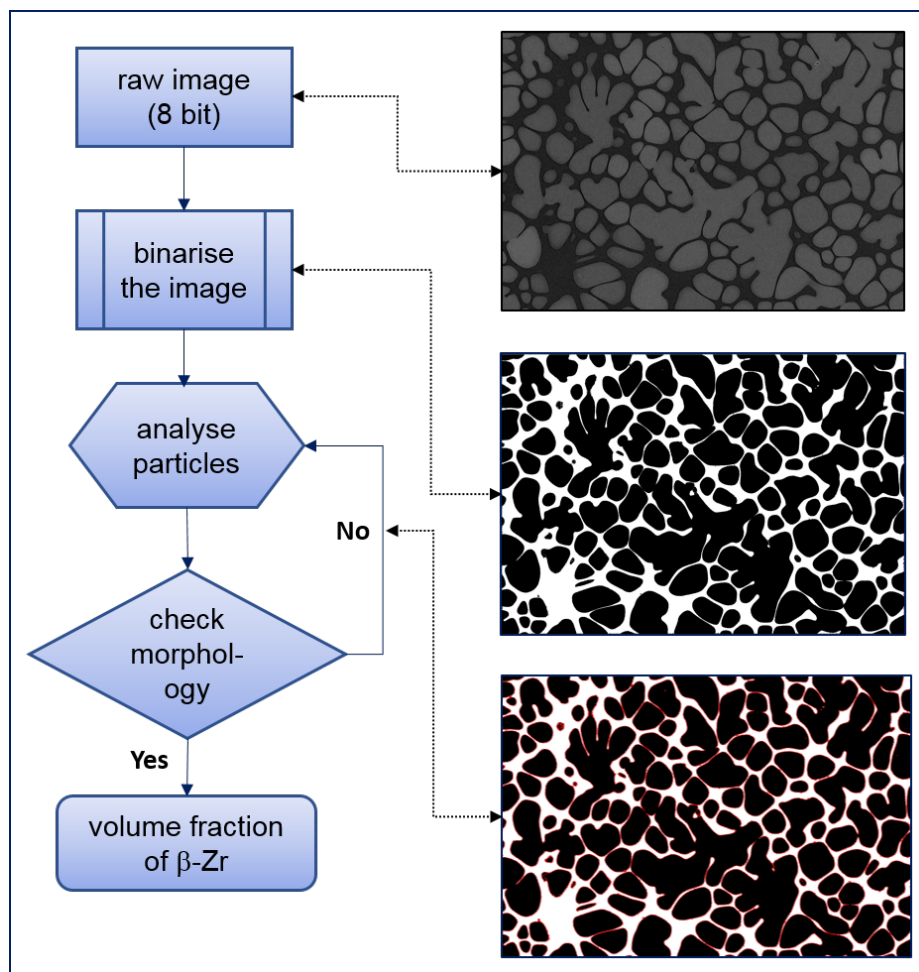
Fig. 3.15 The flow chart for measuring the volume fractions of phases of the as cast DH3.

A conventional approach to quantify the volume fraction is to measure the area percent of each phase in the 2D micrographs by imaging processing. For as-cast DH3, the volume fraction of β-Zr dendrites inside of the amorphous matrix was measured using imageJ [190]. As shown in Fig. 3.15, firstly the 8 bit grayscale raw SEM image was converted into a binary image which separates most of the dendritic phase into dark phase. Then the area percent of the dendritic phases were measured by applying the 'analyse particles', in which the right particle size and roundness needed to be tuned to obtain an optimal results.

For the thermally shocked DH3, there are three crystalline phases in the final state. the volume fraction of each phase can also be obtained by image analysis, but with a more complicated approach. As displayed in Fig. 3.16, initially the $ZrBe_2$ phase can be derived through the procedure as shown in Fig. 3.15. After grayscale inversion, the light phases consists of two phases, β-Zr and Zr_2Cu. Consequently, the microstructure and the area percent of β-Zr can be separated from Zr_2Cu by applying several times 'dilute' and 'erode' function on the image selection of the pre-processed light phases including both the β-Zr and Zr_2Cu phase.

3.5.2.2 The atomic structure across the amorphous–crystalline interface

Four image based methods are used to characterise the atomic local ordering for the HRTEM image, *i.e.*, *autocorrelation function* (*ACF*), *fast Fourier transform* (*FFT*), *Voronoi tessellation* and *2D pair distribution function* (*PDF*) in local region. All image processing was done in ImageJ [190].

Autocorrelation function analysis was used to determine the local ordering of DH3 within the near phase interface based on the HRTEM micrographs. ACF analysis is carried out on templates of 2.13×2.13 nm corresponding to the same order of medium range order (MRO) in metallic glass [191]. As illustrated by the flow chart in Fig. 3.17, the procedure to carry on the ACF analysis can be summarised into several steps: Initially the HRTEM micrograph was split into 12×12 templates of 2.13×2.13 nm; FFT processed image was
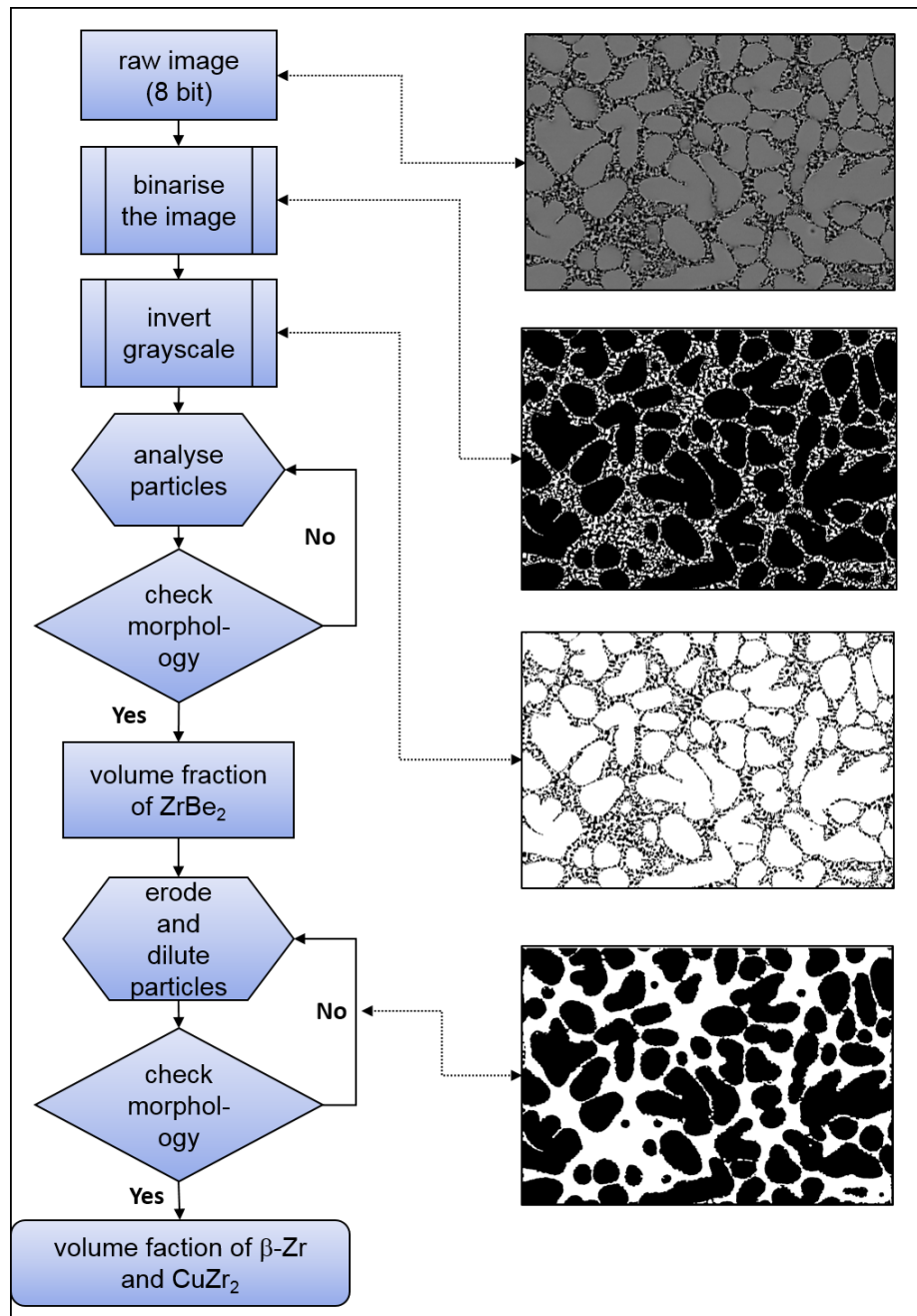
Fig. 3.16 The flow chart for measuring the volume fractions of phases of thermally shocked DH3.

obtained for each of templates via Fourier transform of itself; finally the corresponding real space ACF can be calculated by applying the inverse Fast Fourier transforming (IFFT) of multiplication of real space image with reciprocal FFT image.
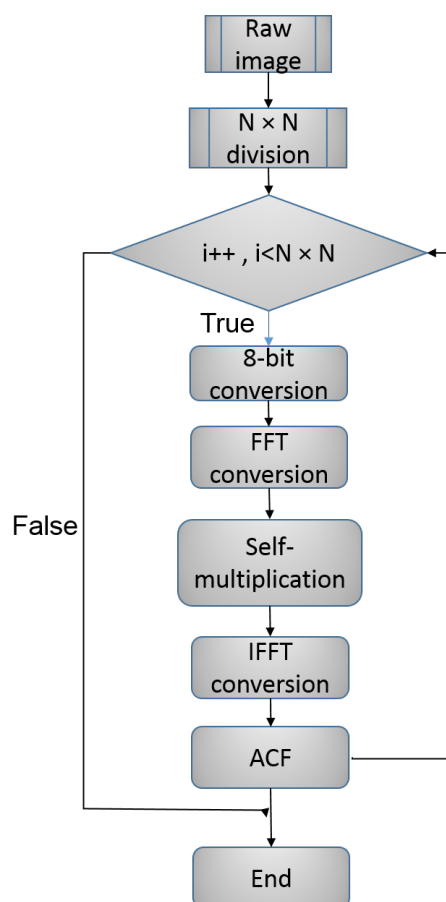
Fig. 3.17 The flow chart to calculate the ACF (left) and PDF (right) using image based methods.

The intermediate image generated in the calculation of ACF by image processing is shown is Fig. 3.18. The diffraction pattern in the reciprocal space can be mathematically reconstructed by fast Fourier transform of itself. Given a HRTEM, the corresponding FFT can be easily calculated by applying "fast Fourier transform" on the raw HRTEM image. Herein, 4×4 templates of 6.4×6.4 nm were split from the raw HRTEM microgrpah, then the FFT processed images can be readily calculated by applying the FFT to all the 16 templates.

| Raw image template | Complex FFT image | Multiplication with itself | ACF image |
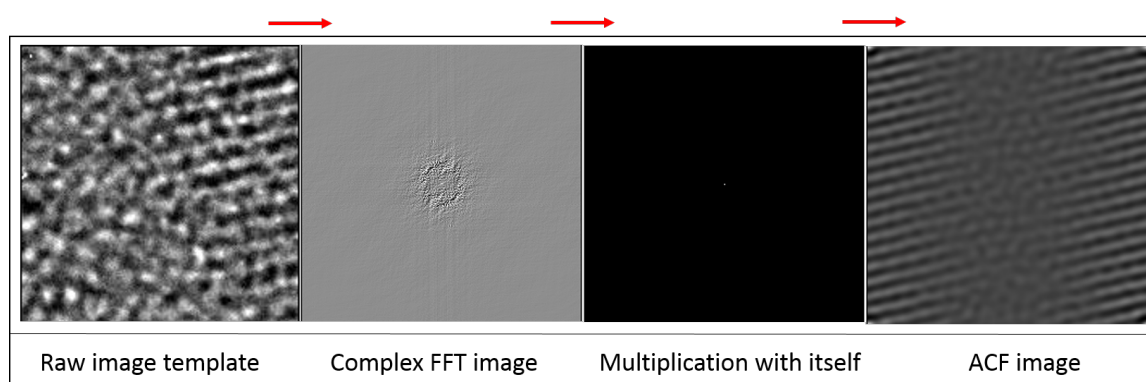
Fig. 3.18 The procedue and intermediate images generated during the calculation of ACF using image based methods.

As illustrated by the flow chart in Fig. 3.17, in order to calculate the 2-D pair distribution function g(r) of DH3 based on HRTEM using image processing, firstly the 2-D spatial "atom" like particles configuration is reproduced from the raw TEM micrograph by applying the "maxima" filter and contrast enhancement for it. Then the centroids of "atom" like particles can be obtained from the 2-D spatial atomic configuration by extracting the maxima points of all the "atom" like particles which are equivalent to the centre of "atom" like particles. Afterwards, the g(r) can be calculated based on all the particle centroids from HRTEM micrographs.

The intermediate images generated in the calculation of g(r) of TEM image is shown in Fig. 3.19. There are several critical steps, and a few of them are quite subjective especially when determining the clear atomic configurations when applying the filters on the micrographs. Furthermore, the local ordering near the phase interface of the crystalline and amorphous matrix can be quantified with Voronoi tessellation of all the particle centroids extracted for PDF analysis.
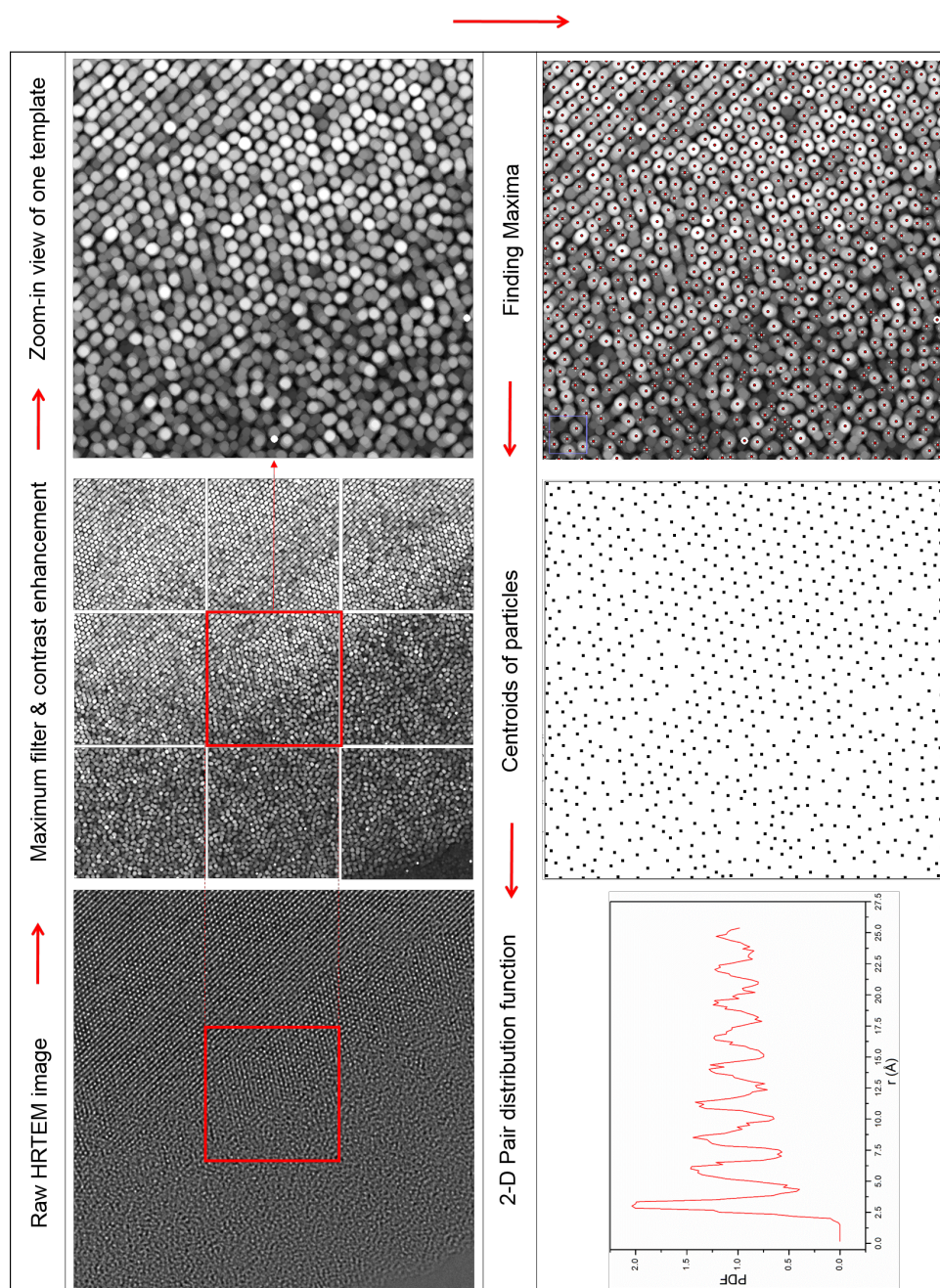
Fig. 3.19 The procedure and intermediate images produced during the calculation of 2D pair distribution function.

3.5.3   Syncrotron X-ray micro-tomography

3.5.3.1   Sample preparation and tomography experiments
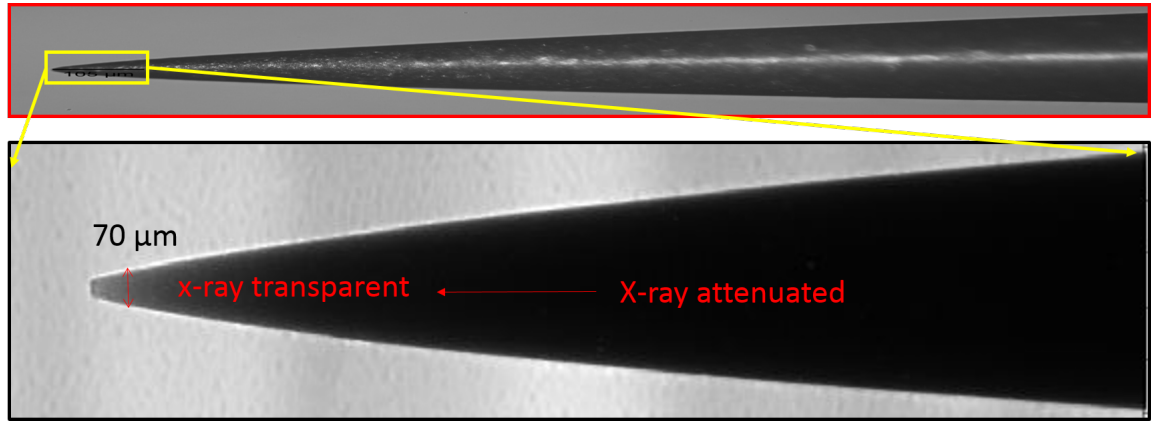
Fig. 3.20 Optical micrograph and X-ray radiographic projection of the tomography sample with a tip diameter of ~70 μm.

Initially, some rod bars with the size of 500 μm were machined from the thermal shocked DH3 samples. The as-cast samples were cut from cold ends and the thermal shocked ones were machined from the central part of the thermally shocked region. These rod bars were then ground and polished to needle-shapes of tip diameters of ~70 μm, which gives good X-ray transparency as shown in the radiographic projection of the needle sample in Fig. 3.20. The microstructure of the samples were deeply etched with Kalling etchant (5 g *CuCl*$_2$ mixed with 100 ml hydrochloric acid and 100 ml ethanol.) [192], and checked by SEM before X-ray tomography scan. Typical SEM microstructure of as-cast and thermally shocked samples are shown in Fig. 3.21.

Synchrotron X-ray micro-tomography experiments were conducted at beamline I13-2 of Diamond Light Source, UK [155] on 14 Oct 2013 and 13 Oct 2014. The experiment is the key part of the proposal titled "Tomography study of 3-D dendritic crystalline microstructure in bulk metallic glass matrix composites" (MT9252 and MT9974).

The Centre for X-ray Optics' X-Ray Interactions With Matter online calculator [140] was used to calculate the X-ray transmission for the two phases. A relatively large difference (10 %) in transmission for the two phases (as shown in Fig. 3.22) was predicted at 17.3
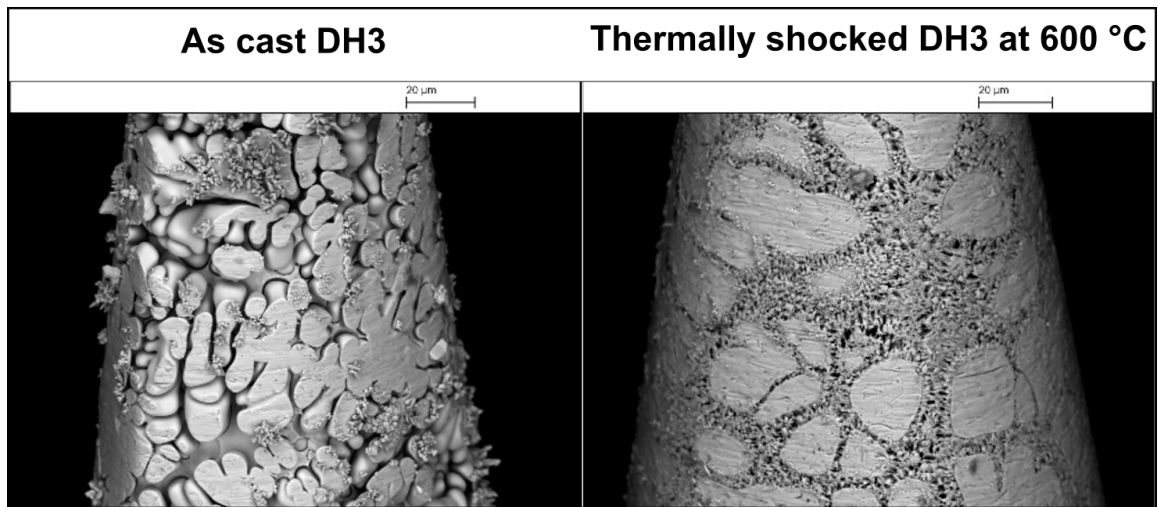
Fig. 3.21 SEM micrographs of as-cast and thermally shocked DH3 after 2 mins chemical etching in Kalling solutions.

keV, and a monochromatic beam of this energy was therefore used to give better contrast than the pink beam as shown in Fig. 3.23. To optimise phase contrast, various propagation (sample-to-scintillator) distances were tested [142], and finally 30 mm was chosen.
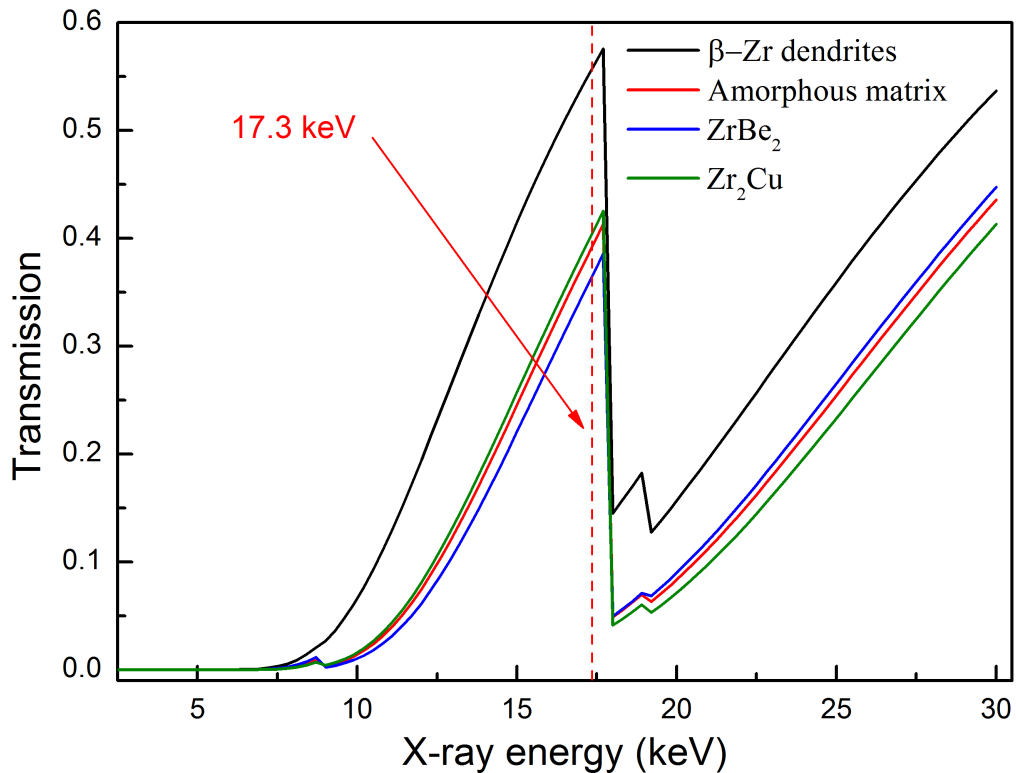
Fig. 3.22 X-ray transmission contrast of all phases inside the thermally shocked DH3.
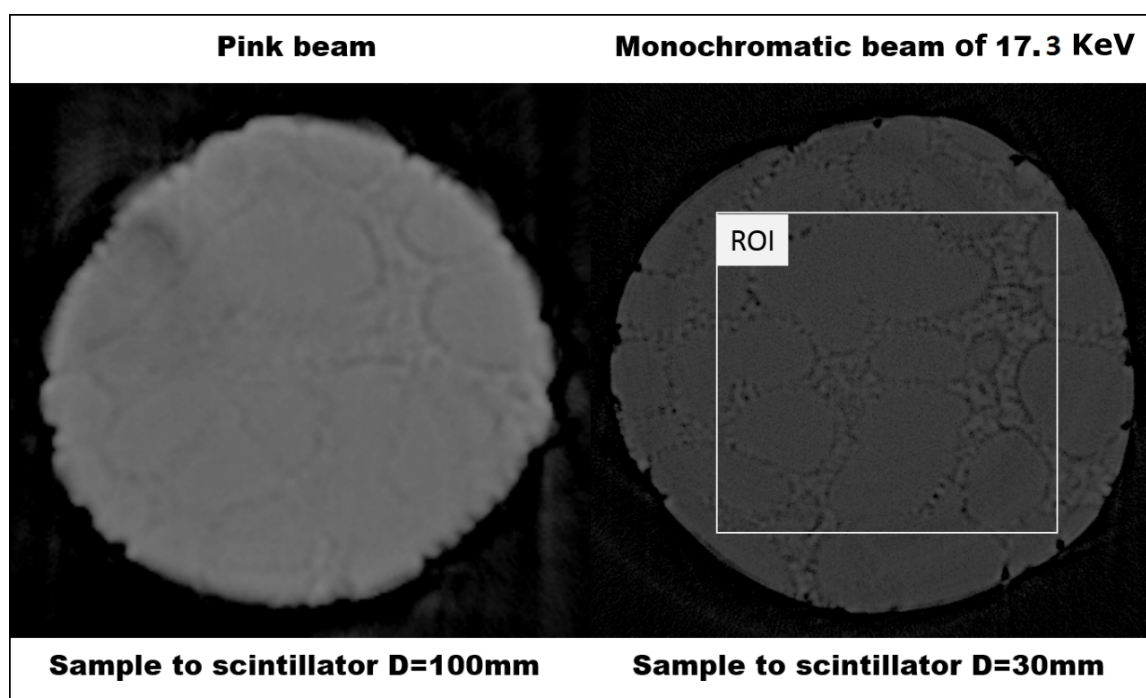
Fig. 3.23 The image contrast obtained respectively by pink beam and monochromatic beam of 17.3 KeV.

Tomography data were acquired using the pco.edge 5.5 detector (PCO AG, Germany) coupled to a 500 μm thick CdWO4 scintillator and optics with 8× magnification. This provided an effective pixel size of 0.81 μm, and a field of view of 2.1 × 1.8 mm. For each tomography scan, 2,001 X-ray projection images were acquired over 180° degrees, with exposure time of 1.90 seconds for each scan. The experimental setup is displayed in Fig. 3.24.

3.5.3.2   Data processing and 3D data rendering

Reconstruction was performed with the tomographic reconstruction module of DAWN v1.7 [182] and the computing cluster at Diamond Light Source. There are two key tunable parameters to achieve an optimal contrast, the *centre of rotation* (*COR*) in pixel, and two ring removal parameters, *ParameterR*, *NumSeries*. During the reconstruction, these three parameters were trailed until an optimal reconstruction was achieved. Fig. 3.25 shows the principle to determine a correct centre of rotation in pixel. There are often some "horse
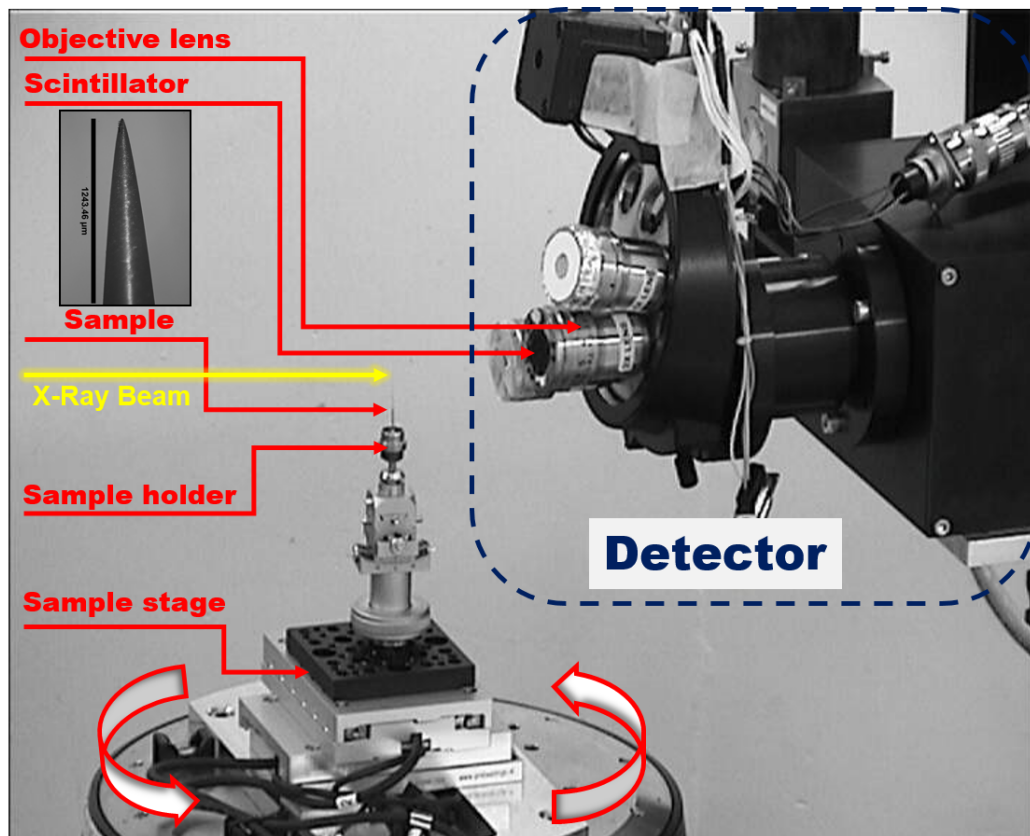
Fig. 3.24 Experimental setup for tomographic scan of DH3 samples.

shoe" patterns surrounding the sample if the wrong *COR* is chosen, therefore, the *COR* was tuned from small number to large number until a turning point of these horse shoe patterns from upwards to downwards was found. Such turning point often implies a right *COR*, e.g, *COR* = 2002 in Fig. 3.25.
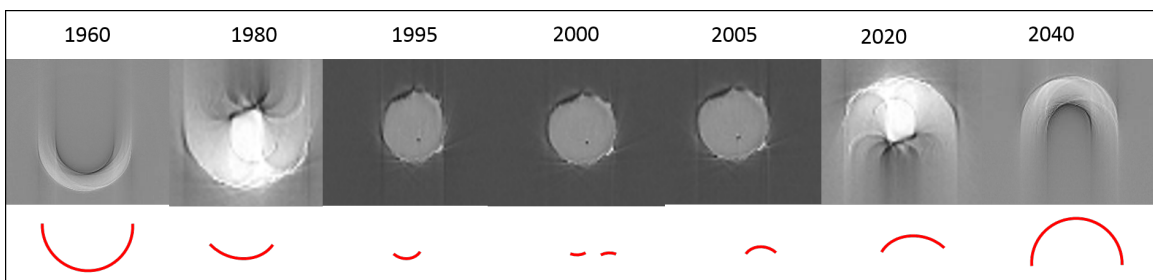
Fig. 3.25 Typical example how to determine the correct centre of rotation for tomographic reconstruction.

The *centre of rotation*, and the two ring removal parameter were then determined as *COR* = 2000.2, *ParameterR* = 10^{-5} and *NumSeries* = 4 for as-cast sample; and *COR* = 2002.2,

ParameterR = 10^{-5} and *NumSeries* = 4 for 600 °C (preset) thermally shocked sample; *COR* = 2006.6, *ParameterR* = 10^{-5} and *NumSeries* = 4 for 700 °C (preset) thermally shocked sample.

Noise removal, tophat-based segmentation and volume fraction measurements were then performed within AVIZO v8.0 (FEI, USA). The secondary dendrites' arm spacing, and tip & root curvature radii were measured using Principal Curvature Plugin (2D/3D) in ImageJ [190] based on the cross section contour line for typical secondary dendrites acquired with AVIZO. In addition, the 3D mean curvature is measured in AVIZO as well.

The procedure of processing the X-ray tomography data is detailed by the flow chart in Fig. 3.26, and the intermediate images produced are shown in Fig. 3.27. Firstly, the whole dataset of tomograms acquired was processed in ImageJ to remove the possbile noise, and also to enhance the contrast; Secondly a region of interest (ROI) was selected and cropped off from the whole tomograms sequence.Thirdly, the cropped image sequence of the ROI was input into AVIZO, in which further noise removal, phase segmentation, and phase quantification, were performed. There are several filters (as shown in flow chart in Fig. 3.26) for removing the various noises. Once a better image quality is achieved, several segmentation tools, such as the *thresholding*, *Blow*, *Top hat*, *Magic wand*, were used to segment the different phases based on their grayscale contrast. At this step, several refinement of segmentation is often needed to further segment the small features with similar grayscale as other phases. Once the phase segmentation is done, the volume fraction of different phases were calculated.

3.5.4 Nano-tomography using FIB+SEM

X-ray micro-tomography was able to resolve the micro-scale structure of DH3, such as the β-Zr dendrites, however, it is very difficult to resolve the nano-scale intermetallic phases, Zr_2Cu and $ZrBe_2$ formed from the amorphous matrix under thermal shock. FIB-SEM nano-
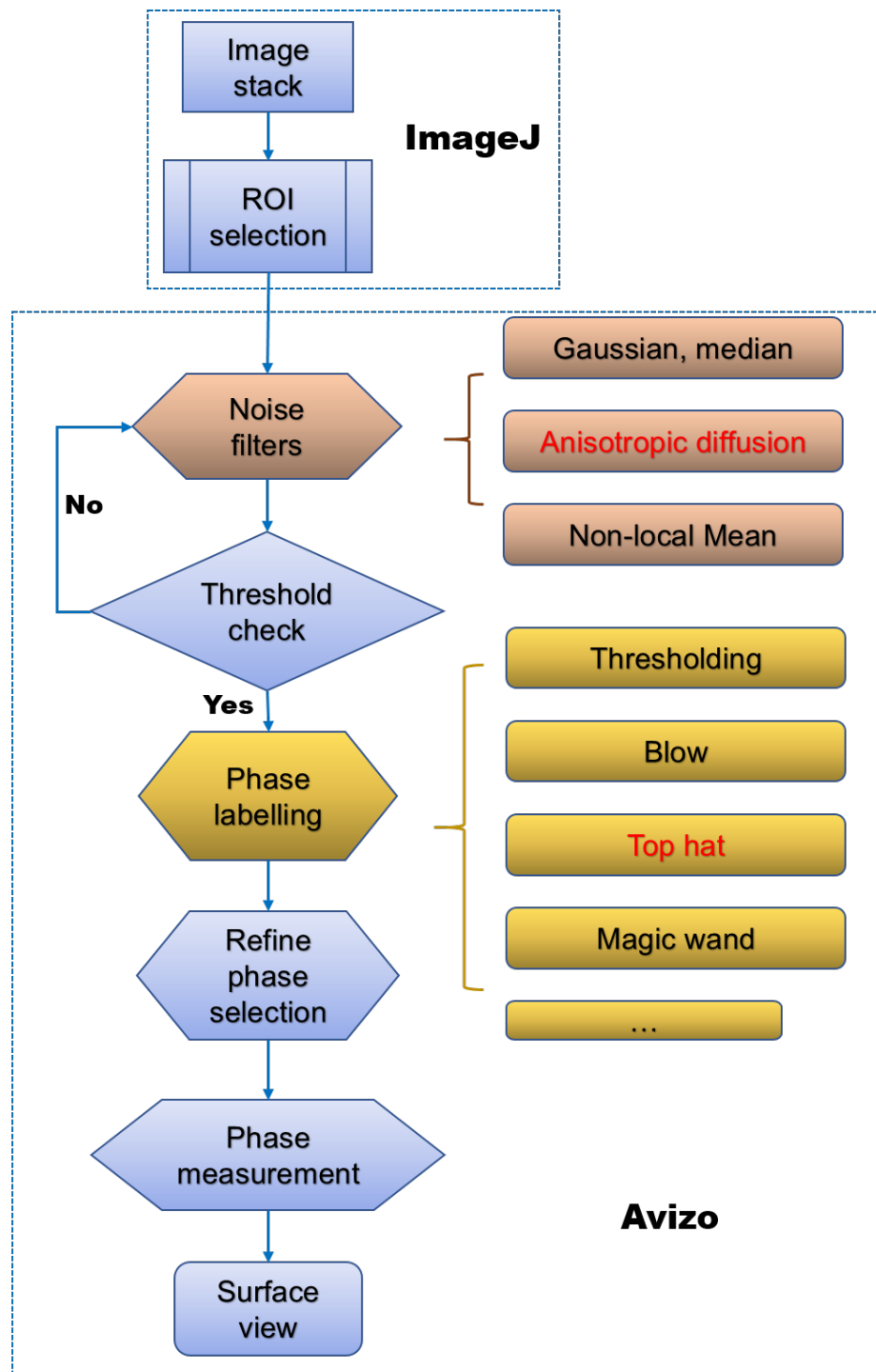
Fig. 3.26 Flow chart of the segmentation procedure for DH3 tomography data. Ana a number of filters that were used for segmentation.
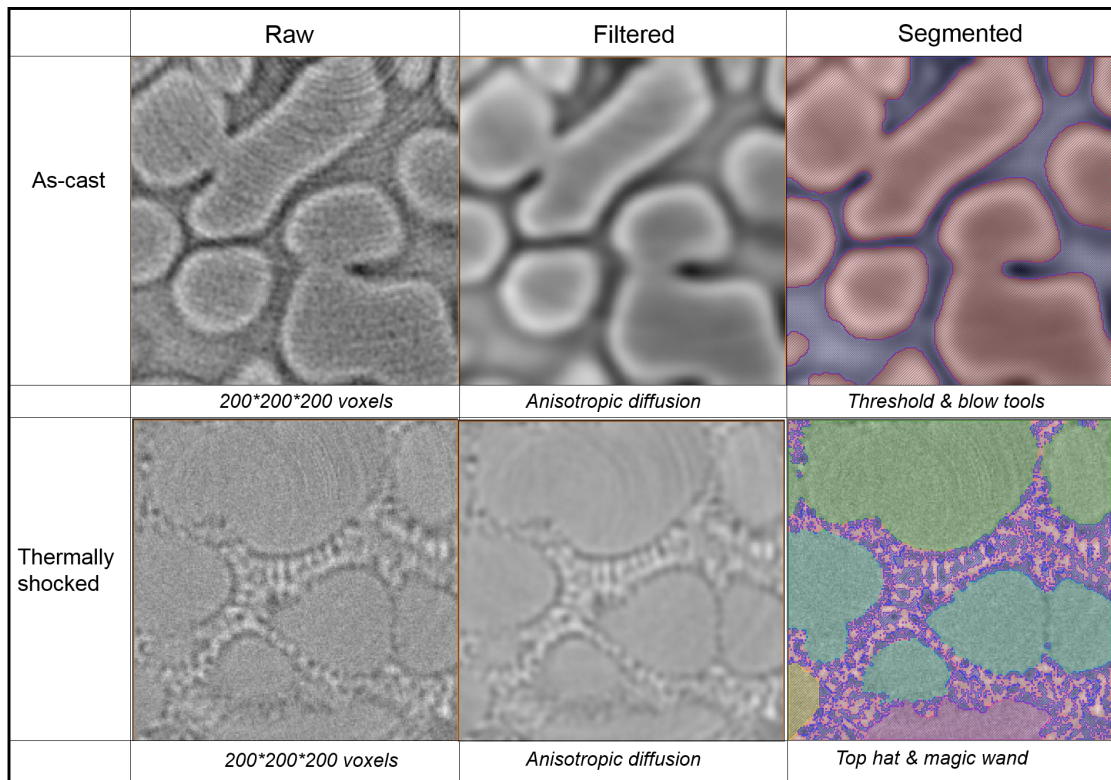
Fig. 3.27 Typical example of raw, filtered and segmented tomogram (from left to right), for as-cast and thermally shocked DH3 sample.

tomography was used as a complementary technique to reveal 3D structure of intermetallic phases.

3.5.4.1 Sample preparation and experiments

FIB-SEM sectioning was carried out by Dr Sui Tan in Multi-Beam Laboratory for Engineering Microscopy (MBLEM), University of Oxford, using an LYRA3 XM (Tescan s.r.o., Brno, Czech Republic). 50 nm layers were removed by FIB, and SEM imaging was performed on each newly exposed surface. The total FIB milling depth was set to 20 μm, the cross-sectional area of 20×20 μm, and 170 sectional images were obtained. This was to ensure that at each milling step, a complete section through the β-Zr, Zr_2Cu and $ZrBe_2$ phases was achieved. Precise alignment of the ion and electron beams was maintained to ensure stable centering of successive images and to avoid electron image drift or "jitter". To study the structure of the Zr_2Cu and $ZrBe_2$ intermetallic phases, higher resolution SEM

imaging was required. For each image frame, the pixel size was set to 25×25nm, and a matrix of 676×468 pixels was used.

3.5.4.2 Data processing and 3D data rendering
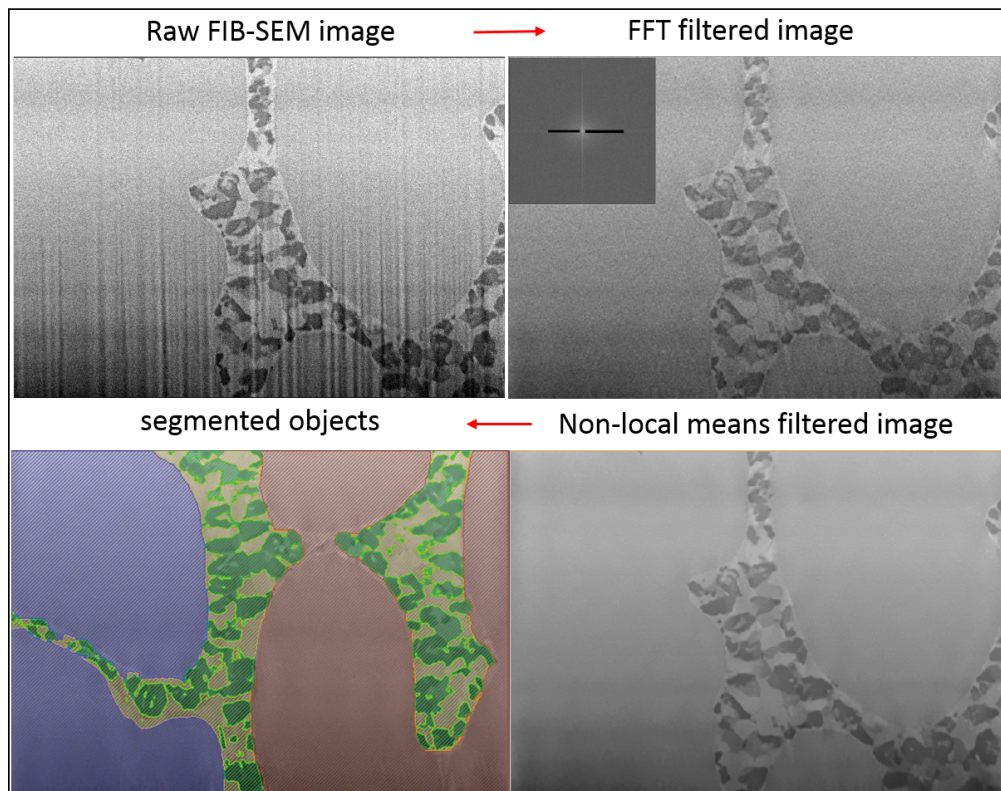
Fig. 3.28 The procedure and the intermediate images of processing the FIB-SEM images and phase segmentation.

Fig. 3.28 shows the procedure and the intermediate images generated during the image processing and rendering of the FIB-SEM image sequences. Periodic noise is the dominant noise for the dataset. A FFT based method was proposed to remove the periodic noise. Firstly, the raw image is FFT transformed, then the random spots with a high frequency in the FFT transformed image are masked off. The FFT image with the mask is then Fourier transformed back to the real space.

The image sequence without the periodic noise were further processed in AVIZO v8.0 (FEI, USA), and further noise removal, phase segmentation with *tophat* method, and 3D rendering is performed.

3.6   Neutron diffraction

For the thermally shocked DH3, in addition to the β-Zr dendrites, there are some new crystalline phases formed from the amorphous matrix during the rapid heating. To identify these newly formed phases, the neutron diffraction was used. Although it is not sensitive to minor phases as X-ray diffraction, it gives more accurate and averaged large-sized bulk phase information due to the lack of micro-absorption [193], furthermore preferred orientation effects that frequently plague X-ray data, but are normally negligible with neutron data.

Neutron diffraction analysis of the as-cast and thermally shocked region of rod bar rapidly heat up to 650°C were carried out using the General Materials Diffractometer (GEM) at ISIS Neutron and Muon Source, UK [194]. The beam size was 15×15 mm; time of flight diffraction patterns were collected in 50 mins to give sufficient counting statistics. The diffractograms were analyzed and fitted by the Rietveld method implemented in the EXPGUI [195] and GSAS programs [196]. Towards the end, the phase fraction and the subsequently derived volume fraction for each phase were determined quantitatively from the fitted diffraction patterns.

3.7   Summary

In this chapter, all the relevant experimental approaches and data processing and analysis methods were described in details. Section 3.1 described the alloy making and sample preparation for all the experiment studies presented in the following chapters.

Section 3.2 presented the design, making and commission of the custom apparatus for in-situ diffraction experiments. It followed the section 3.3, which detailed the experimental setup, data processing and analysis methods used for the in-situ pair distribution function analysis.

Section 3.4 described the experimental setup for the thermal shock studies of DH3. Section 3.5 detailed the characterisation methods used for DH3, which includes the 2D electron microscopy, 3D synchrotron X-ray micro-tomography, and FIB-SEM nano-tomography.

Chapter 4

Experimental result 1- the atomic structure of metallic glass

In this chapter, the composition dependent atomic structure changes, and the processing dependent atomic structure evolution were investigated using synchrotron X-ray total scattering method and pair distribution function. The experiment results are given in the following sections.

4.1 Composition dependent atomic structure

4.1.1 Local atomic structure of CuZr binary alloy

Fig. 4.1 shows 2D diffraction patterns (the 1st column) o the four CuZr alloys, $Cu_{50}Zr_{50}$, $Cu_{57}Zr_{43}$, $Cu_{64.5}Zr_{35.5}$, $Cu_{55}Zr_{40}Al_5$. The corresponding 1D spectrum [called I(Q) hereafter] integrated from each 2D diffraction pattern using Fit2D software for each alloy is shown in the 2nd column. In all cases, two concentric bright rings with diffuse halo are presented in the 2D diffraction patterns, and they are the two dominant scattering peaks in the Q range of $2 \sim 6$ Å^{-1} as can be more clearly seen in the I(Q) curves.These features are the typical diffraction characteristics often found in liquid or amorphous materials.

(a) $Cu_{50}Zr_{50}$

(b)

(c)

(d) $Cu_{57}Zr_{43}$

(e)

(f)

(g) $Cu_{64.5}Zr_{35.5}$

(h)

(i)
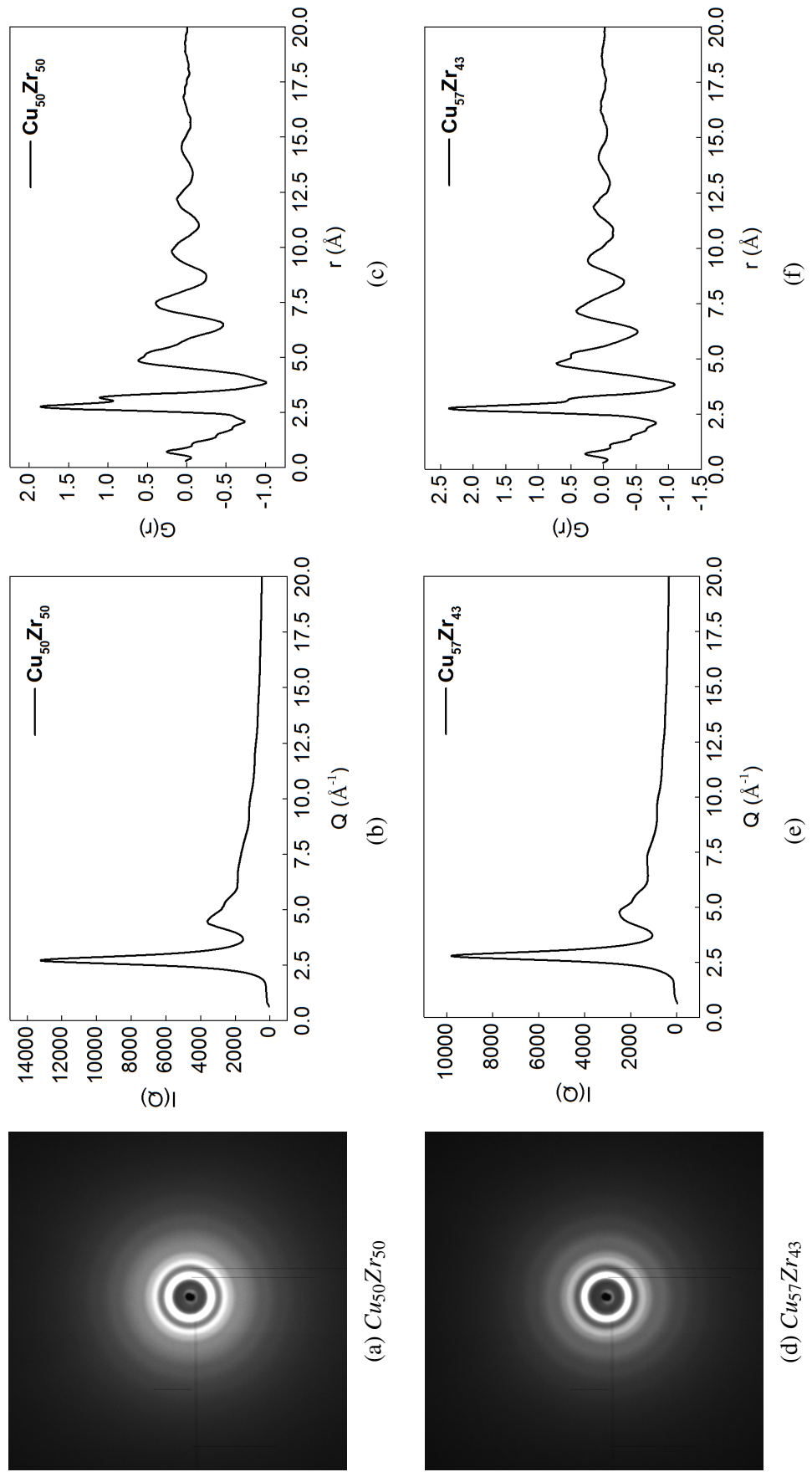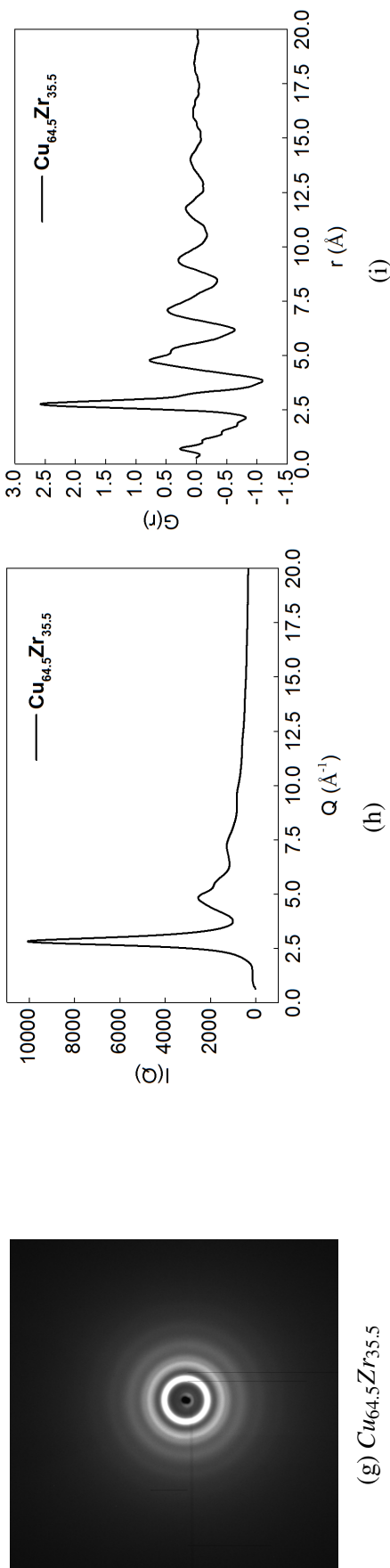
Fig. 4.1 The 2D synchrotron X-ray diffraction patterns (the 1st column), 1D diffraction spectra (the 2nd column), and pair distribution functions (the 3rd column) for the four ZrCu alloys.

Fig. 4.2a shows all I(Q) superimposed together with each I(Q) shifted by an equal distance of 5,000 counts for readability and easy comparison. The regions surround the 1st and 2nd peaks are enlarged and showed in Fig. 4.2b.

Comparing all I(Q), the locations of the 1st peaks of all cases seem to be at the very similar Q, although that of the $Cu_{50}Zr_{50}$ is slightly lower. Similar phenomena are found for the locations of the 2nd peaks for all four cases with minor variation in shape of the curve for the 2nd peaks of $Cu_{50}Zr_{50}$. With such minor variations in all I(Q), it is impossible to quantify the difference, if there is any, in atomic structures for the four alloys.

PDF is used to obtain real space structural information based on the I(Q) of each case, and presented in the 3rd column of Fig. 4.1. Fig. 4.3a also shows the superimposed PDF curves (called G(r) hereafter). Again all G(r) is stacked with an equal spacing of 2.0 for easy comparison. Fig. 4.3b shows the enlarged view of all G(r) in the r range of $2 \sim 10$ Å.

Comparing the G(r) for the three binary alloys, when the concentration of Zr decreases from 50% to 35.5% (from $Cu_{50}Zr_{50}$ to $Cu_{64.5}Zr_{35.5}$), the maxima of the 1st peak increase from 1.85 to 2.58, and the minor peak present on the right-hand side of the 1st peak (at 3.17 Å) for $Cu_{50}Zr_{50}$ gradually disappears as the concentration of Zr decreases. At the same time, on the right-hand side of all 2nd peaks, the minor peaks gradually evolve into shoulder-like features. The maxima of the 1st peak of $Cu_{55}Zr_{40}Al_5$ is between that of $Cu_{50}Zr_{50}$ and $Cu_{64.5}Zr_{35.5}$. It is also interesting to see that, for the 3rd and 4th peaks which are located in the medium atomic range ($6 \sim 10$ Å), their peak locations shift to lower r as the concentration of Cu increases from 50% to 64.5%. For example, the 3rd peak shifts from 7.46 Å to 7.12 Å, while the 4th peaks from 9.78 Å to 9.35 Å, when the alloy composition changes from $Cu_{50}Zr_{50}$ to $Cu_{64.5}Zr_{35.5}$.

4.1.2   Local atomic structure of NiTi binary alloy

Fig. 4.4 presents 2D diffraction patterns (the 1st column) of three TiNi alloys, $Ti_{65}Ni_{35}$, $Ti_{70}Ni_{30}$, $Ti_{75}Ni_{25}$ and the corresponding I(Q) (the 2nd column) integrated from those 2D
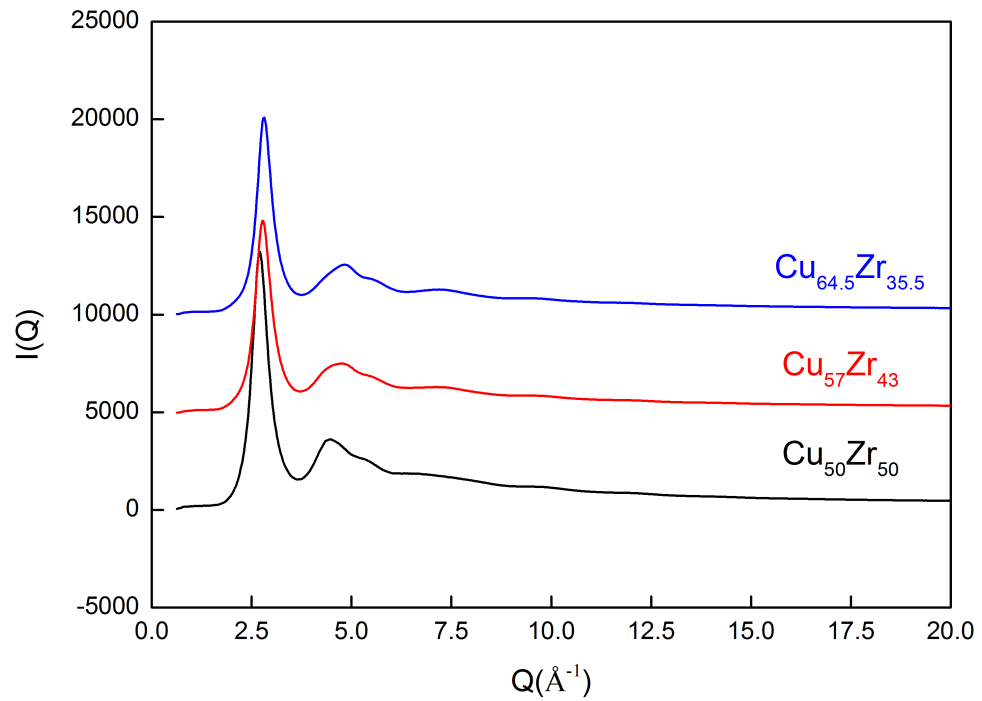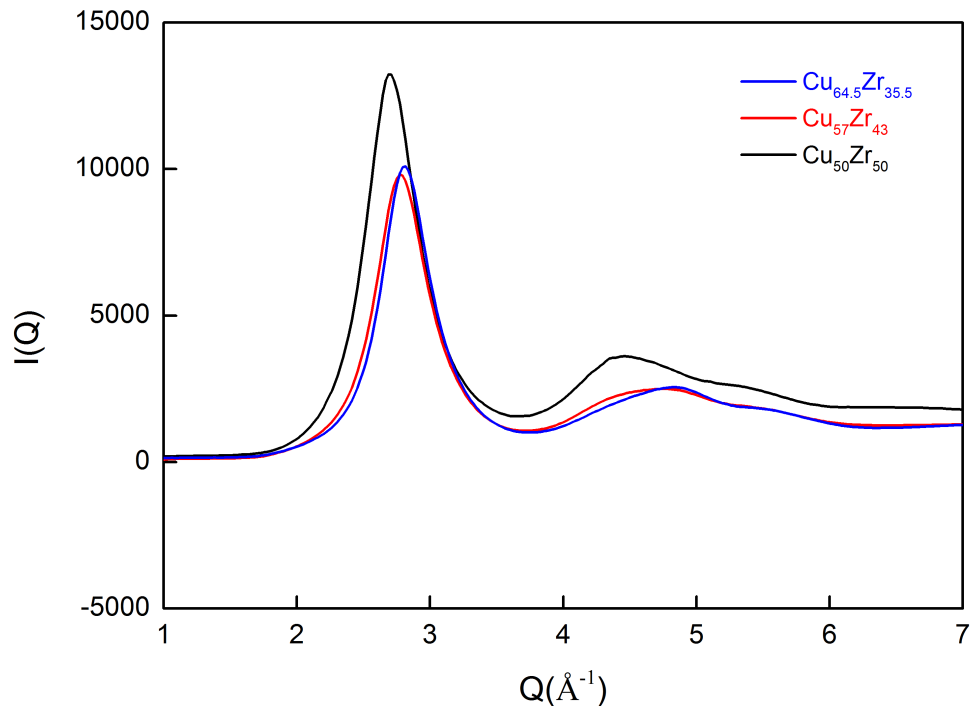
Fig. 4.2 X-ray diffraction spectra obtained for four CuZr alloys. (a) The spectra superimposed with an equal offset spacing of 5,000 counts in y direction. (b) The enlarged view of the diffraction spectra in (a) in the Q range of 1.0 to 7.0 Å^{-1}.
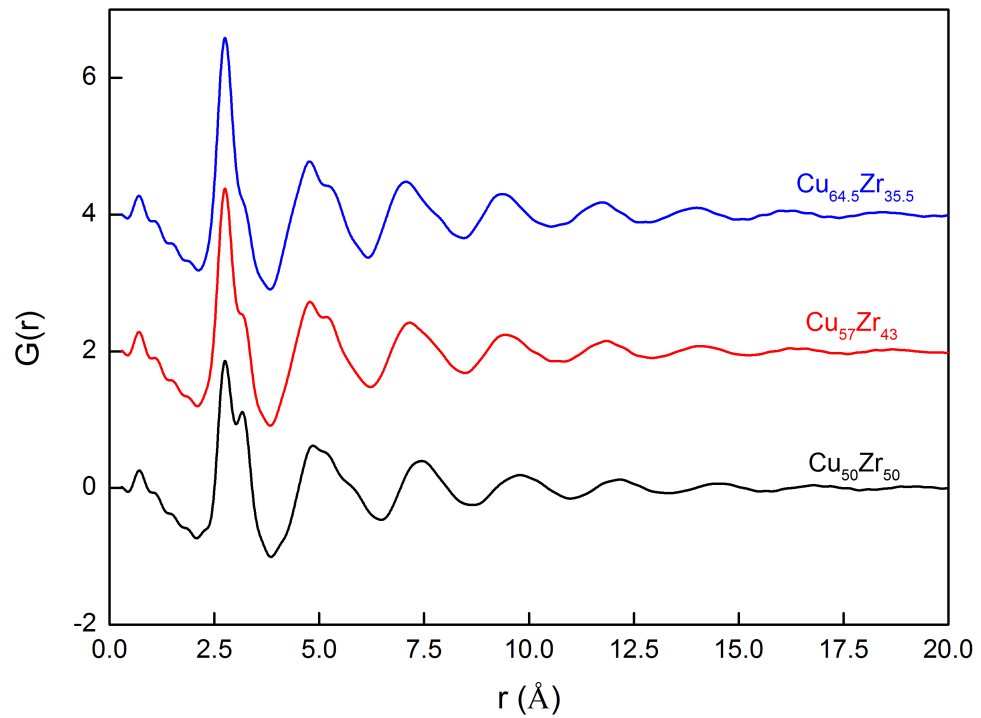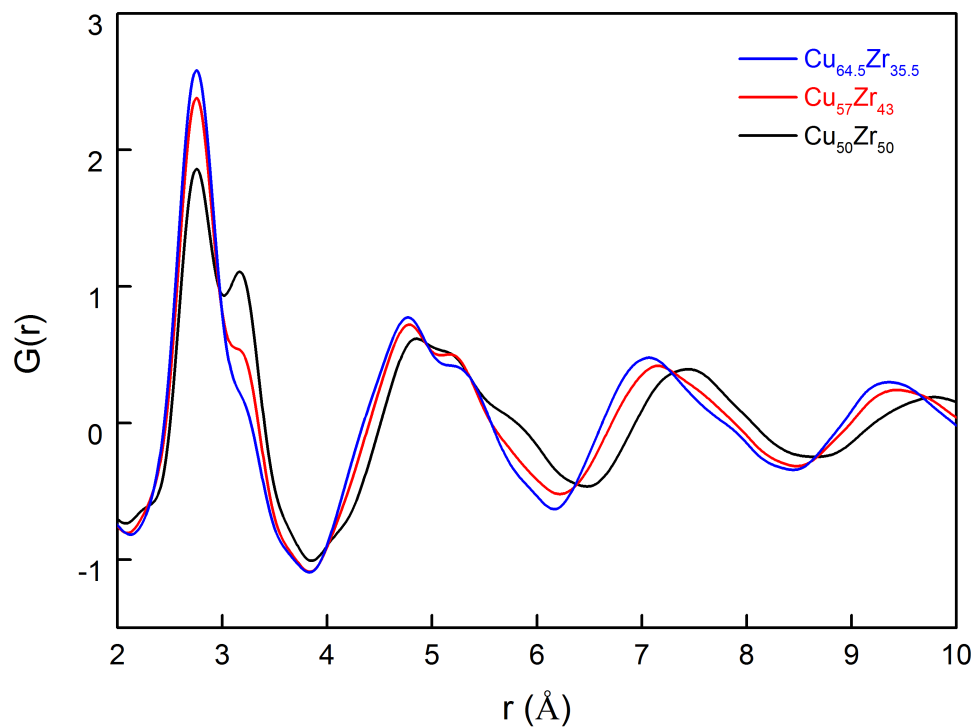
Fig. 4.3 The pair distribution function curves, G(r) for the four CuZr based alloys calculated using the I(Q) showed in Fig. 4.2a. (a) The G(r) superimposed with an equal offset spacing of 2.0 in y direction. (b) The enlarged view of G(r) in the r range of $2 \sim 10$ Å.

patterns, and the G(r) (the 3rd column) calculated based on I(Q). Fig. 4.5a shows all I(Q) superimposed together with each I(Q) shifted by a fixed spacing of 5,000 counts. The regions in the range of $1 \sim 7$ Å^{-1} (corresponding to short and medium atomic range) are enlarged and shown in Fig. 4.5b.

Unlike the diffraction patterns of CuZr alloys, clear structure changes from amorphous to crystalline phases are shown in the 2D diffraction patterns in Fig. 4.4. For $Ti_{65}Ni_{35}$, a diffuse halo due to amorphous structure is present in the diffraction pattern, while for $Ti_{75}Ni_{25}$, the diffraction pattern shows the typical characteristics of crystalline structure, *i.e*, sharp concentric rings superimposed with Brag spots. For the case of $Ti_{70}Ni_{30}$, the diffraction pattern is a mixture of sharp concentric rings and diffuse halo, indicating that a mixture of crystalline and amorphous phases is present in $Ti_{70}Ni_{30}$.

More quantitative structure information is revealed by I(Q) presented in Fig. 4.5. For $Ti_{65}Ni_{35}$, there are only two dominant diffuse scattering peaks (the 1st and the 2nd peaks with the peak maxima of $\sim 3,000$ and ~ 300 respectively) in the Q range of < 5.0 Å^{-1}. However, I(Q) of $Ti_{75}Ni_{25}$ has many sharp diffraction peaks, and the dominant peak has a peak intensity of $\sim 20,000$. For $Ti_{70}Ni_{30}$, there are a few minor peaks overlapping on the diffuse peak as that of $Ti_{65}Ni_{35}$, while the 1st and 2nd peaks become more intense (peak intensity of $\sim 5,300$ and 2,245 respectively), It is interesting to find that, for the three alloys, the positions of the 1st peak stay at the same location, *i.e.* 2.8 Å^{-1}, and do not change as the composition changes. While the 2nd peak shifts from 4.81 to 4.61 Å^{-1} when alloy changes from $Ti_{65}Ni_{35}$ to $Ti_{70}Ni_{30}$.

(a) $Ti_{65}Ni_{35}$

(b)

(c)

(d) $Ti_{70}Ni_{30}$

(e)

(f)

(g) $Ti_{75}Ni_{25}$

(h)

(i)
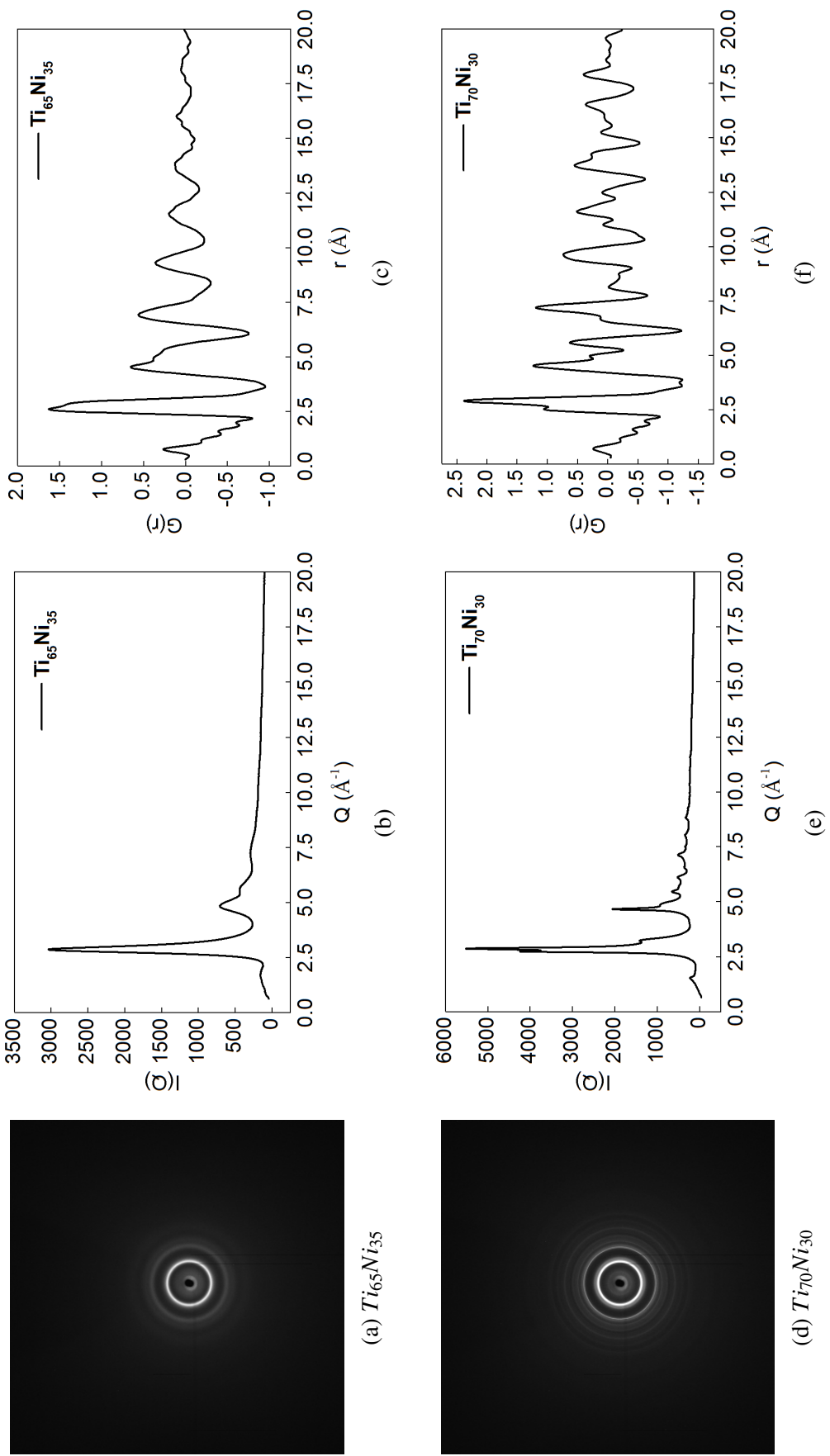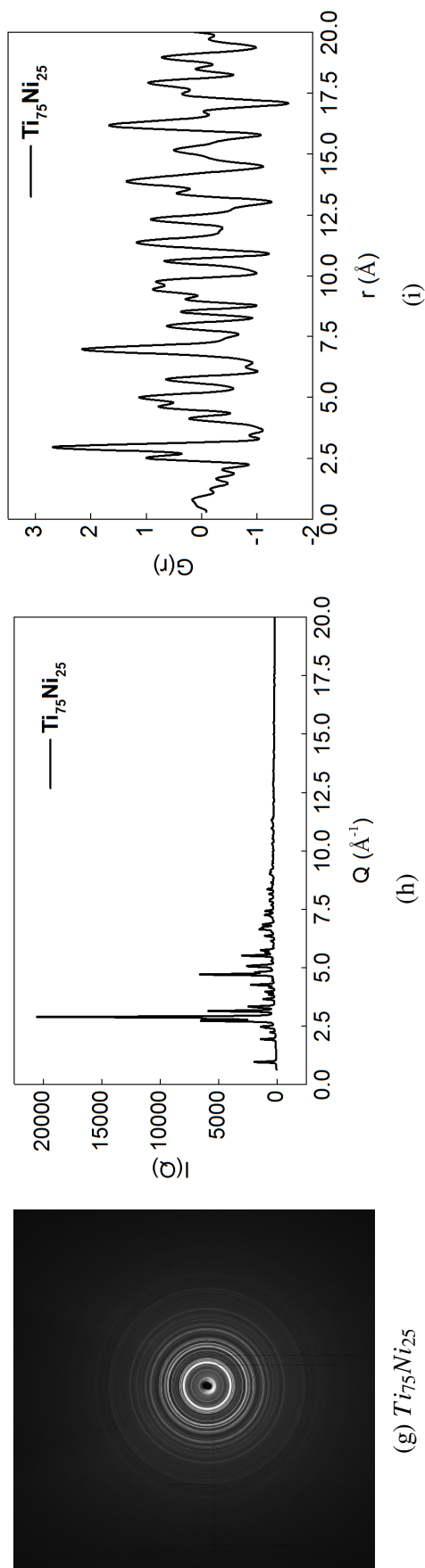
Fig. 4.4 The 2D synchrotron X-ray diffraction patterns (the 1st column), 1D diffraction spectra (the 2nd column), and pair distribution functions (the 3rd column) for three TiNi alloys.
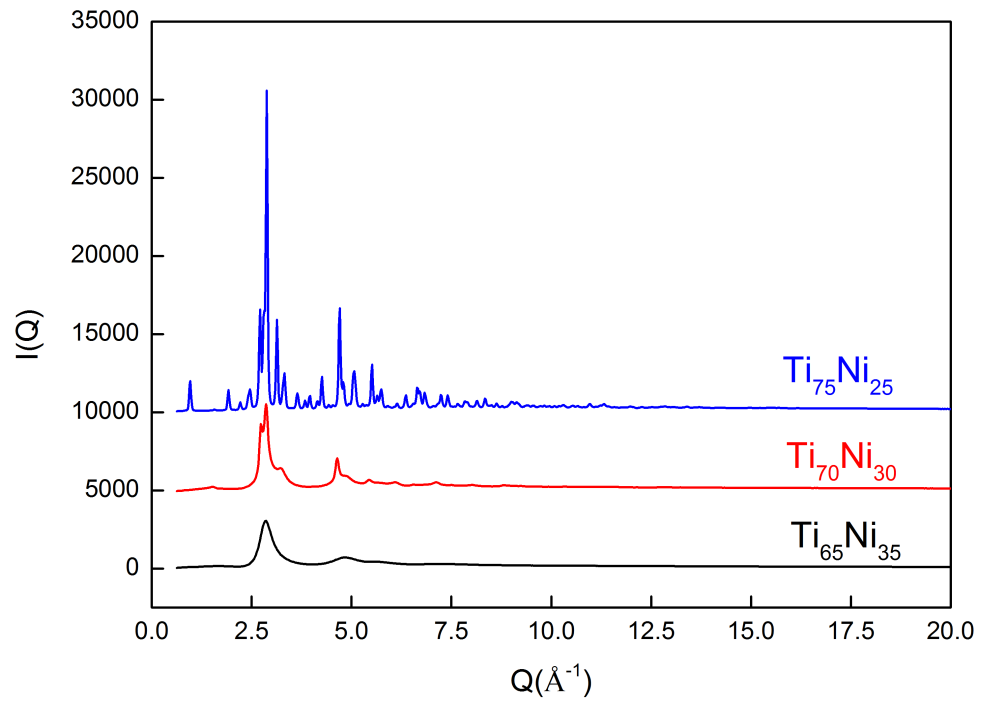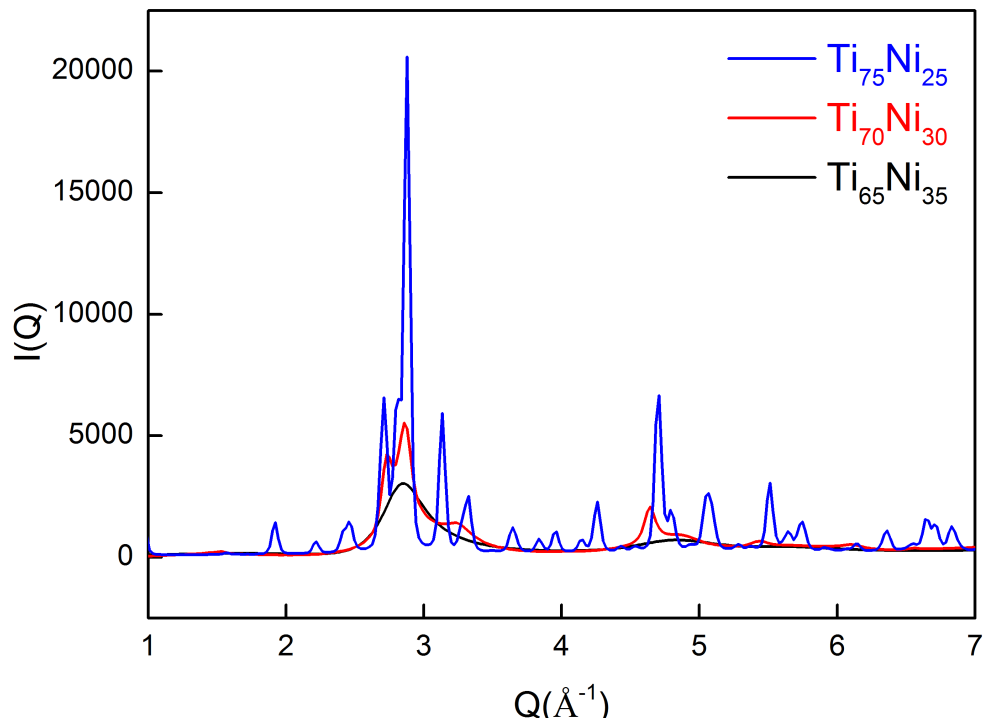
Fig. 4.5 (a) The diffraction spectra of three TiNi alloys, with an offset spacing of 5,000 counts in y direction. (b) The enlarged view of diffraction spectra showed in (a) in the range of 1 to 7 Å^{-1}.
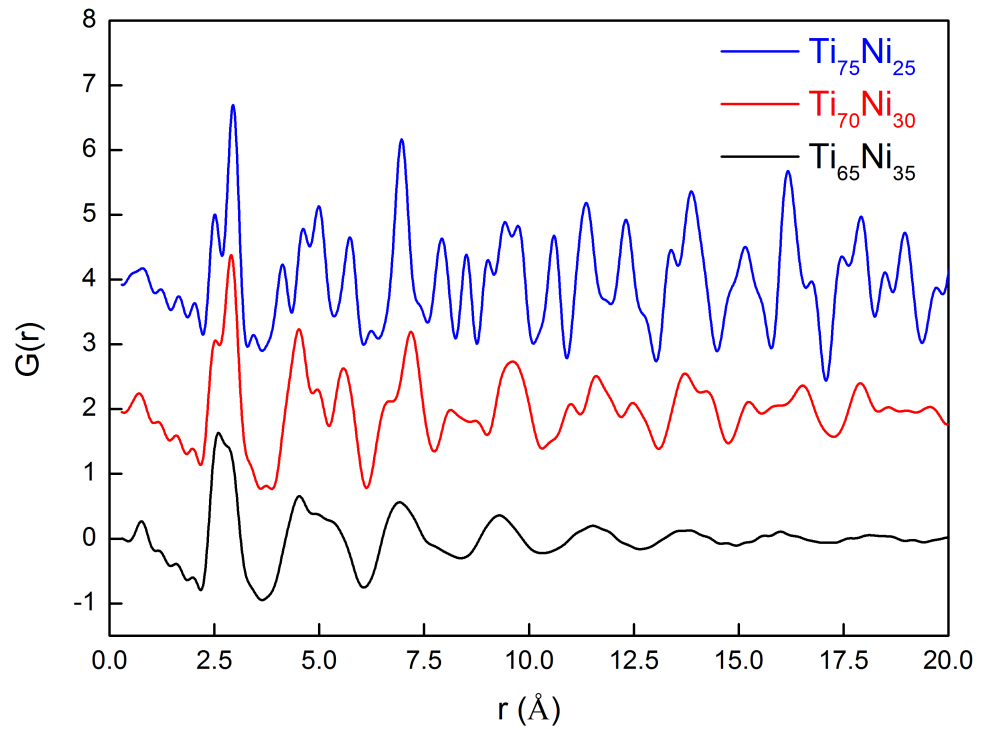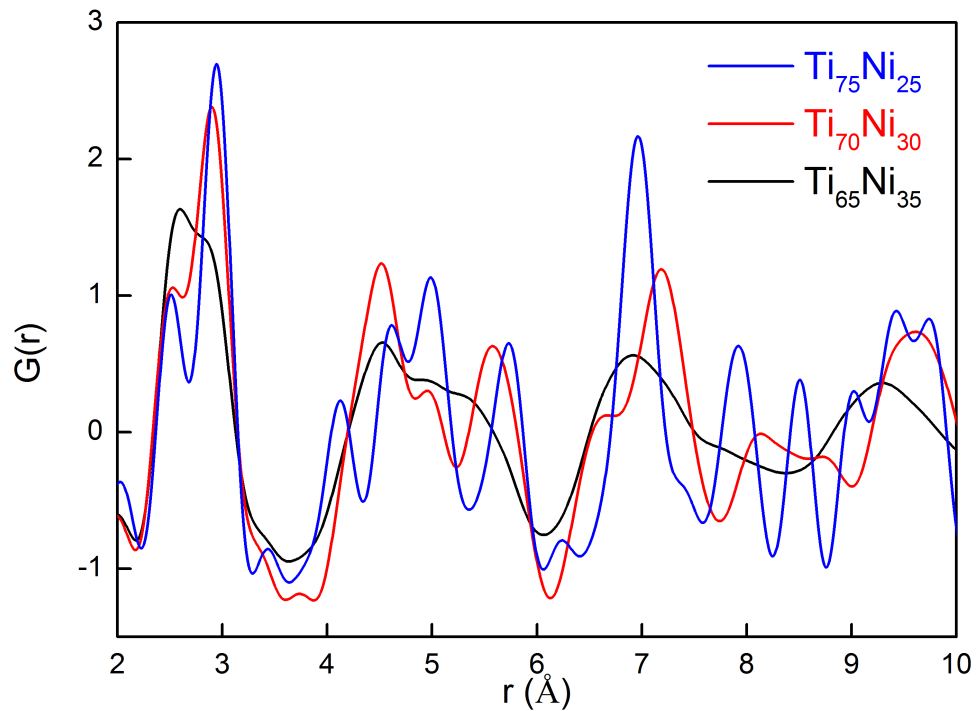
Fig. 4.6 The pair distribution function curves, G(r) for the three NiTi alloys calculated using the I(Q) shown in Fig. 4.5a. (a) The G(r) superimposed with an equal offset spacing of 2.0 in y direction. (b) The enlarged view of G(r) in the the r range of 2 ∼ 10 Å.

Fig. 4.6a shows the stack of G(r) superimposed from the individual G(r) shown in the 3rd column of Fig. 4.4, and the enlarged view in the r range of $2.0 \sim 10.0$ Å is given in Fig. 4.6b.

Fig. 4.6 shows that, for $Ti_{65}Ni_{35}$, the 1st peak located at 2.80 Å has a maxima of ~ 1.8, and the maxima of other peaks decrease as r increases from 5.0 to 20.0 Å. For $Ti_{70}Ni_{30}$ the maxima of the 1st and 2nd peaks increases as compared to those of $Ti_{65}Ni_{35}$, and more minor peaks appear around the regions of the 1st and 2nd peaks, such as the minor peak at 2.51 Å, growing out of the 1st peak, and two other minor peaks at 4.99 and 5.73 Å splitting from the 2nd peaks.

4.1.3 Local atomic structure of CuZrTi and TiCuNi ternary alloys

Fig. 4.7 presents 2D diffraction patterns (the 1st column) of two ternary alloys, $Cu_{55}Zr_{40}Al_5$, $Ti_{55}Cu_{38}Ni_7$ and the corresponding I(Q) (the 2nd column) integrated from those 2D patterns, and the G(r) (the 3rd column) calculated based on I(Q). Fig. 4.8 shows all I(Q) and G(r) superimposed together.

Comparing I(Q) for each alloy, the locations of the 1st peaks are different from each other as shown in Fig. 4.8a. The peak position for $Cu_{55}Zr_{40}Al_5$ is at around 2.8 Å^{-1}, while that of $Ti_{55}Cu_{38}Ni_7$ is at about 2.9 Å^{-1}. The peak intensity for $Cu_{55}Zr_{40}Al_5$ is 5,000 higher than that of TiCuNi.

Fig. 4.8b shows the peak profile of PDFs for $Cu_{55}Zr_{40}Al_5$ is very different from that of $Ti_{55}Cu_{38}Ni_7$, especially in terms of peak positions. The peak position of the first peak for $Cu_{55}Zr_{40}Al_5$ is at 2.8 Å and that of the peak shoulder is at 3.2 Å. The peak position of the second peak is at 4.8 Å. While, the peak position of the first peak for $Ti_{55}Cu_{38}Ni_7$ is at 2.6 Å and there is no obvious peak separation from the first peak. The peak position of the second peak is located at 4.5 Å.
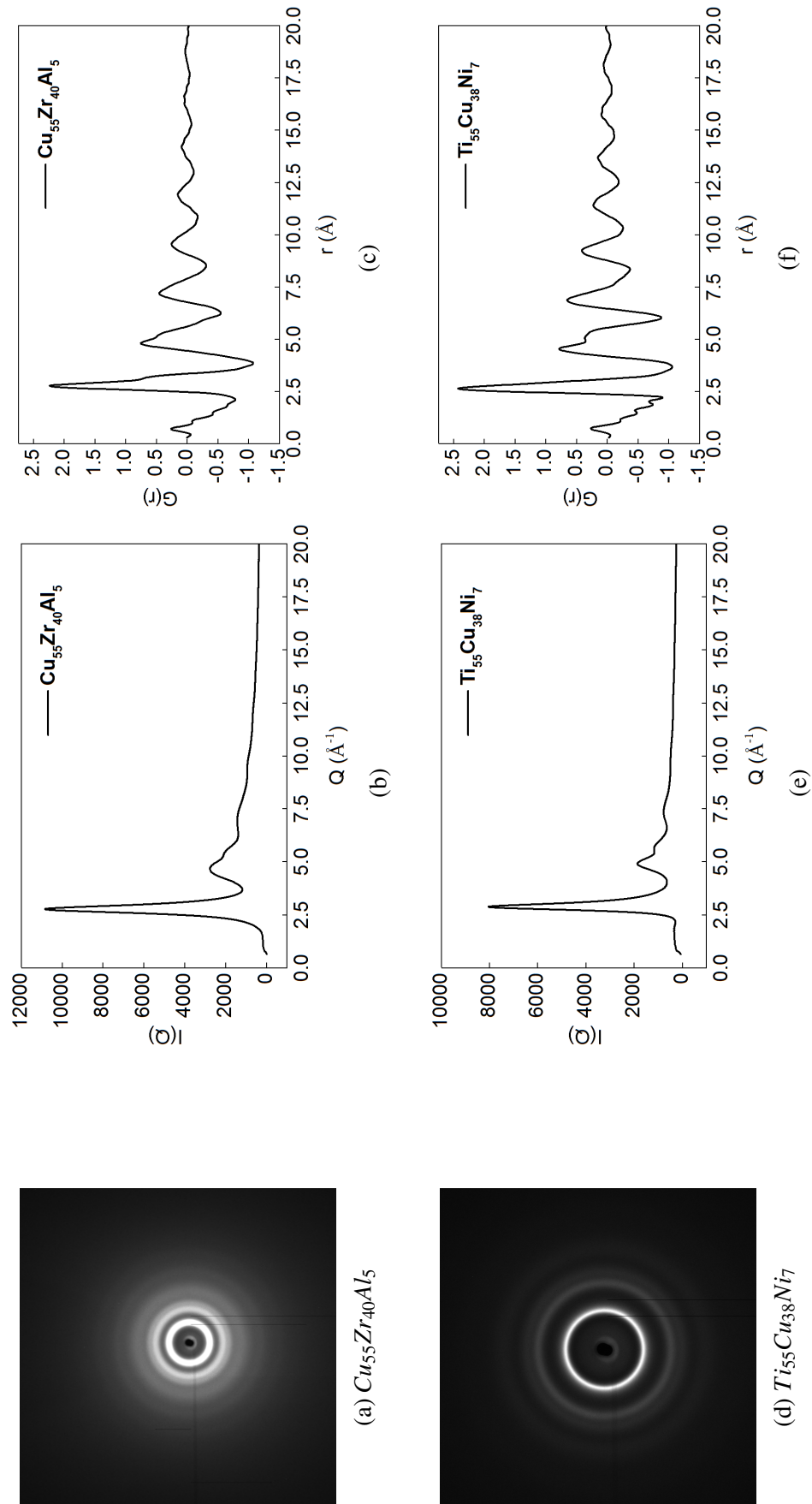
Fig. 4.7 The 2D synchrotron X-ray diffraction patterns (the 1st column), 1D diffraction spectra (the 2nd column), and pair distribution functions (the 3rd column) for $Cu_{55}Zr_{40}Al_5$ and $Ti_{55}Cu_{38}Ni_7$ ternary alloys.
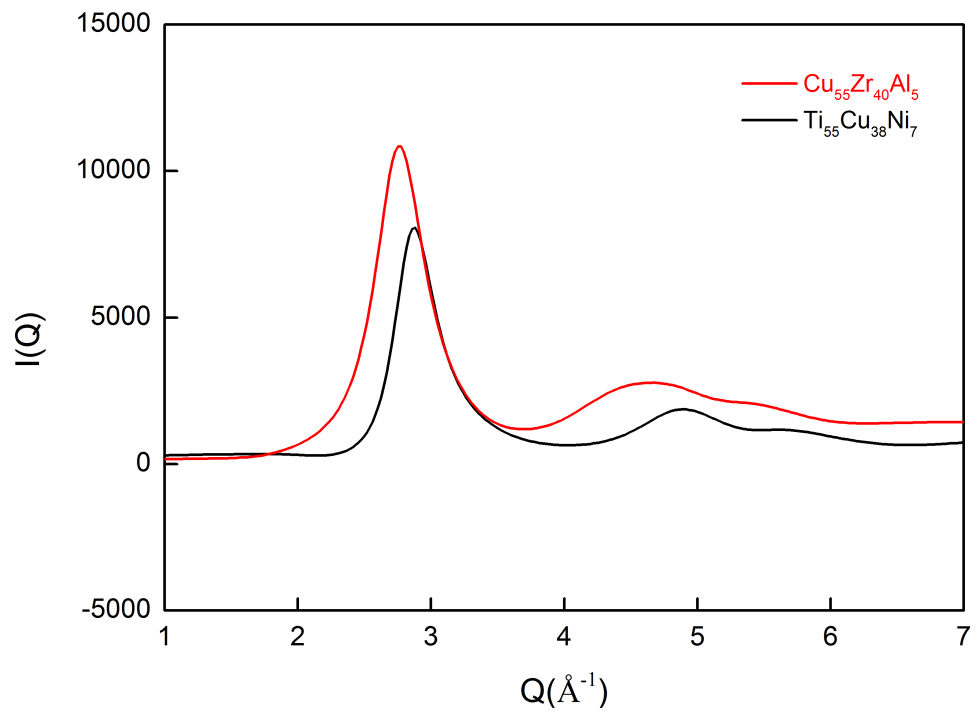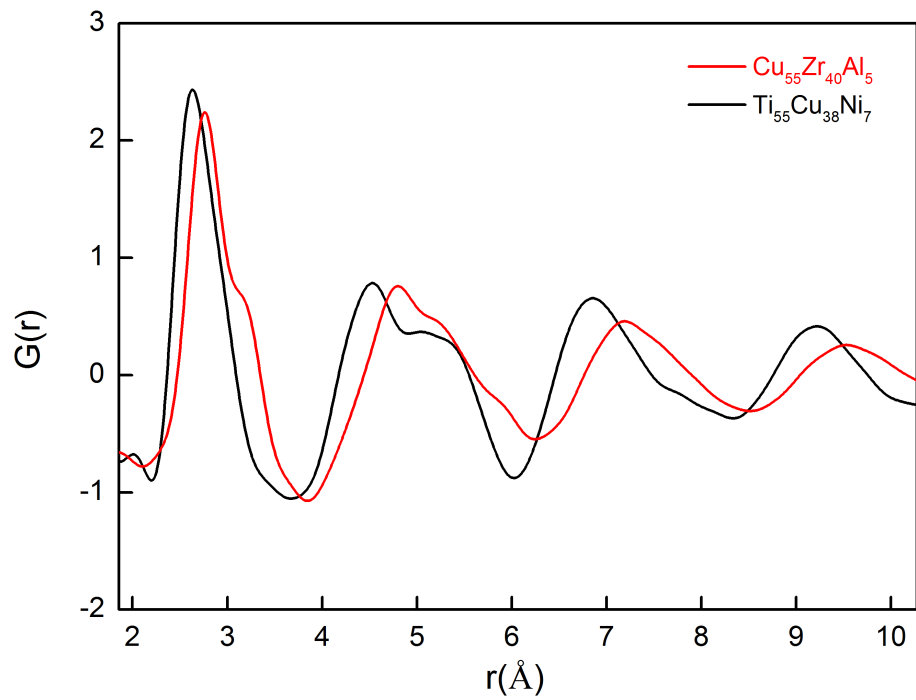
Fig. 4.8 (a) The 1D diffraction spectra I(Q), and (b) pair distribution functions G(r) for $Cu_{55}Zr_{40}Al_5$ and $Ti_{55}Cu_{38}Ni_7$ ternary alloys.

4.2   Temperature dependent atomic structures

The experimental results of *in-situ* total scattering studies of a ZrTi based bulk metallic glass (Vit1) are presented in this section with a focus on analysing peak intensity and peak position of the pair distribution function curves and their evolutions with temperature. Real space refinements of the dominant crystalline phases generated during the heating and cooling processes are also presented in this chapter.

4.2.1   The evolution of atomic structures during heating

4.2.1.1   Structure evolution in Fourier and real space

Fig. 4.9 shows the measured temperature profile of Vit1 sample during the heating experiment using a controlled average heating rate of 1.5 K/s. 2D diffraction patterns were acquired every second during the heating, and the patterns shown on Fig. 4.9 are those obtained at the critical temperatures where structure changes were found to occur with a few more patterns shown between those critical temperatures. In total, 2115 of such diffraction patterns were acquired for the particular heating profile.

Fig. 4.10 shows the stack of I(Q) curves integrated from those patterns shown in Fig. 4.9. Clearly, from room temperature to 459.2 °C, the three I(Q) curves show typical amorphous structure. *i.e*, two broad and diffuse peaks (Fig. 4.10). When temperature reached 467.4 °C in $\sim$ 6 s, tiny diffraction peaks started to appear on top of the original diffuse peak at $\sim$ 2.5 Å^{-1}. This small change can be hardly detected in the corresponding 2D pattern showed in Fig. 4.9. From 467.4 °C to 682.3 °C, the sample experienced structural changes, *i. e*, a process of crystallisation of from the original amorphous state in 350 s.
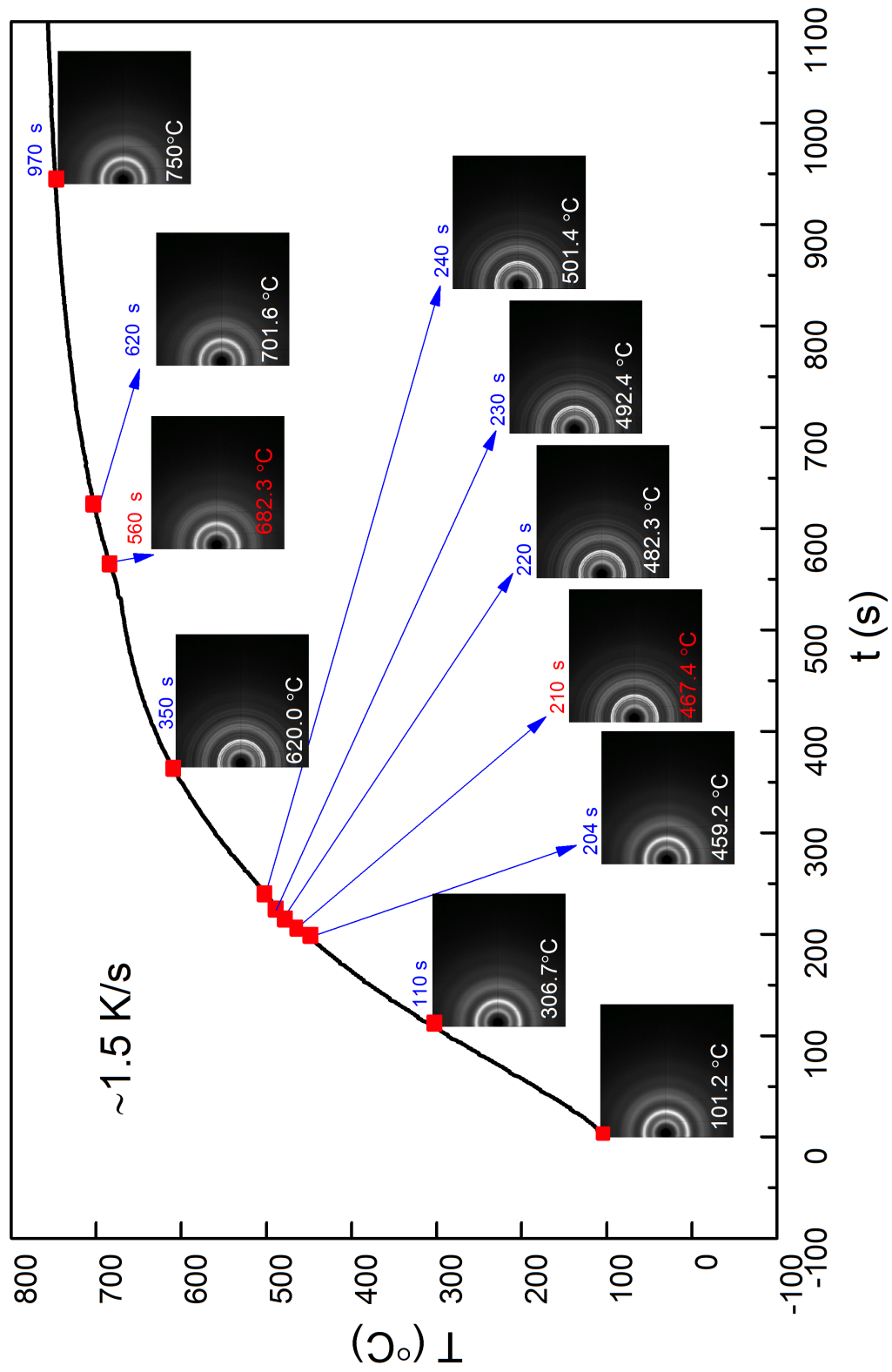
Fig. 4.9 The temperature profile of Vit1 during heating using an average heating rate of 1.5 K/s, and the 2D diffraction patterns acquired at the marked temperatures.

A dramatic structural change occurred when the temperature is increased from 467.4 °C to 482.3 °C in 10 s, while a slow change is observed from 482.3 °C to 682.3 °C. As heating continued, the crystalline phases formed during the crystallisation began to melt at 682.3 °C until it turned into a full liquid state when temperature reached 750.1 °C.
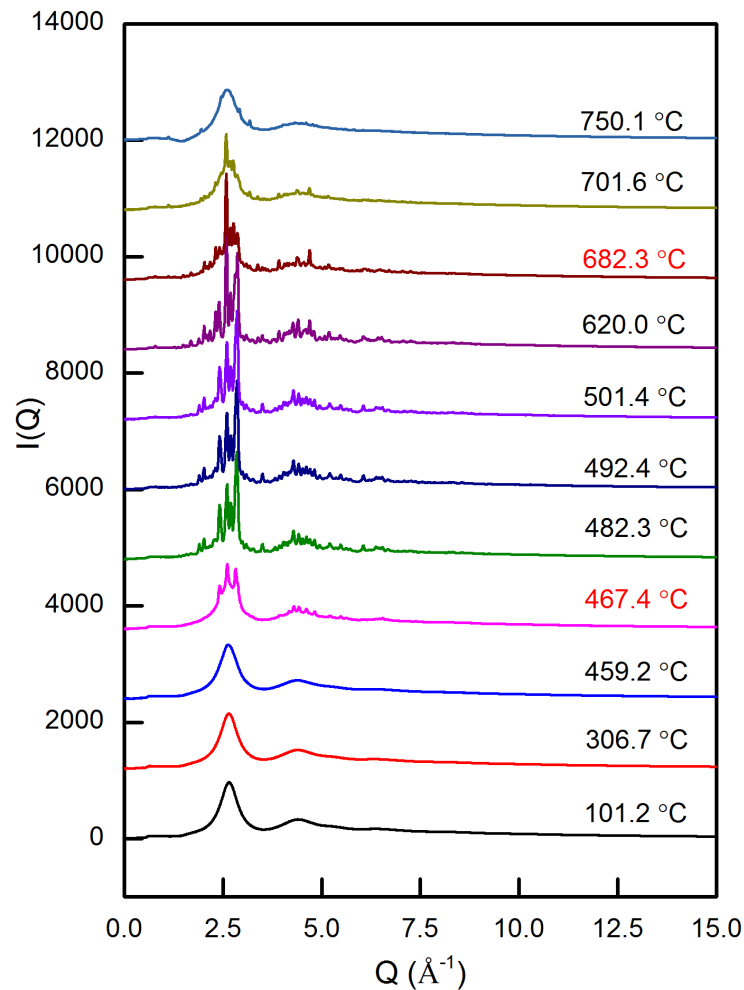
Fig. 4.10 The diffraction spectra acquired for Vit1 alloy at each critical temperature during heating with an average heating rate of 1.5 K/s. The curves are stacked with an equal spacing of 1,200 counts in y direction.

There are many studies on the phase changes and crystallisation behaviour of Vit1 using diffraction. Despite some minor discrepancy among these studies, It is generally agreed on that Zr_2Cu and Be_2Zr are the dominant crystalline phases from the crystallisation of the Vit1 alloy [187].

(a)

(b)

(c)
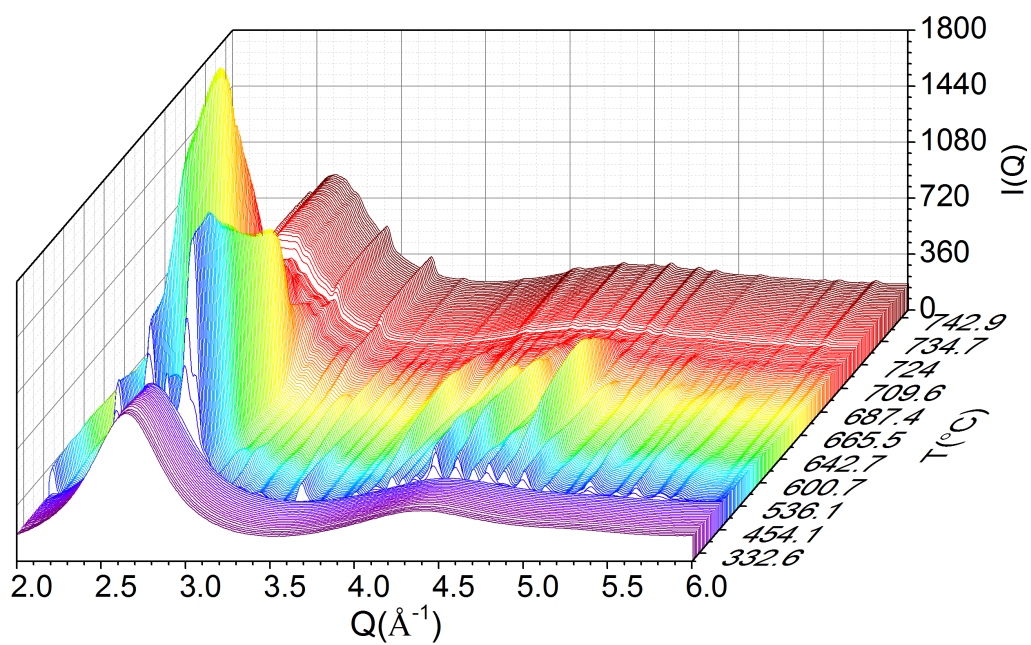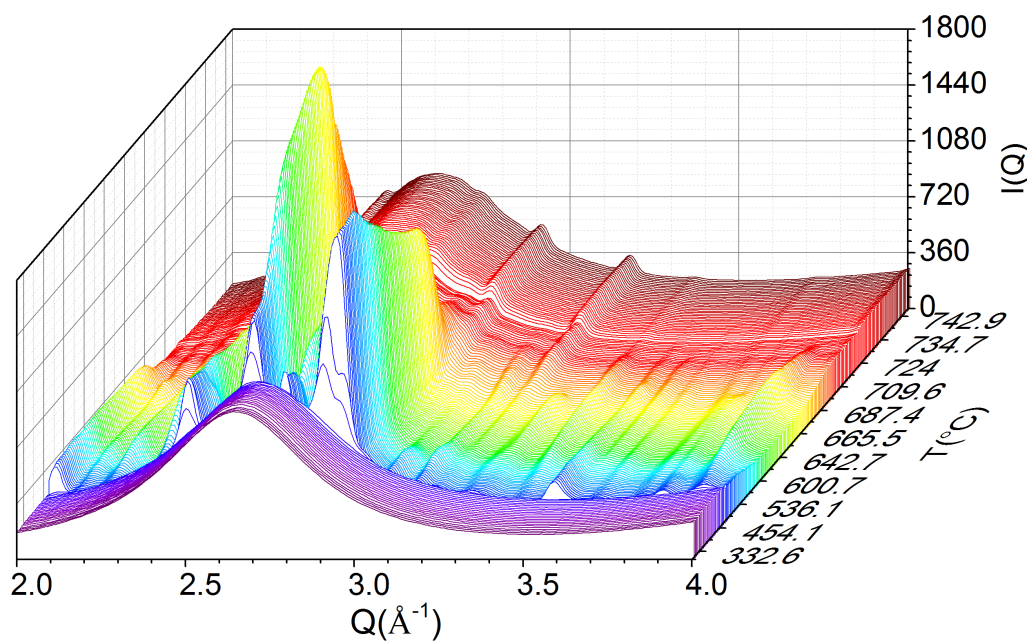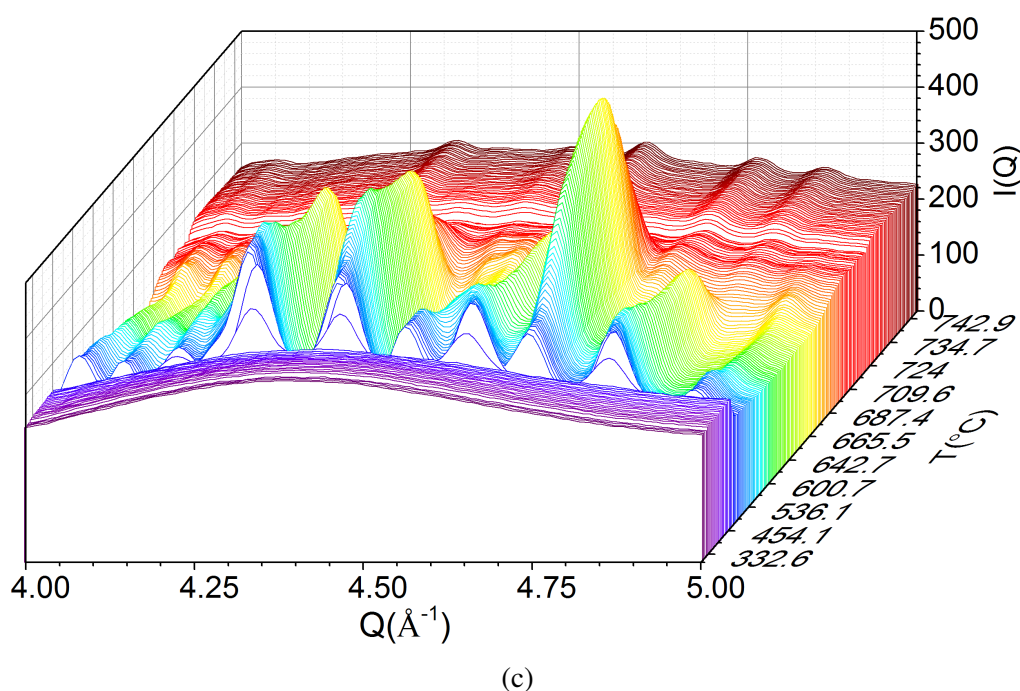
Fig. 4.11 The evolution of diffraction spectra of Vit1 as functions of temperature during the heating process with an average heating rate of 1.5 K/s. (a) the spectra in 2.0-6.0 Å^{-1}, (b) the spectra between 2.0 and 4.0 Å^{-1}, and (c) the spectra between 4.0 and 5.0 Å^{-1}.

Fig. 4.11 shows that the peak maxima remains the same from room temperature to the crystallisation temperature of 467.4 °C, and then increase until 682.3 °C. The maxima then starts to decrease until 701.6 °C where the melting completes. Beyond 701.6 °C, the maxima again stay approximately at the same constant and low value due to the diffraction from full liquid structure. Compared to the spectra obtained from the solid amorphous state, in the spectra obtained from the full liquid state, there are a few very small diffraction peaks superimposed together with the dominant broad diffuse peak, and this may be due to the fact that some small minor oxides coexist in the liquid. These tiny peaks remain during cooling and even after the liquid was cooled back to room temperature.

The corresponding G(r) calculated based on those shown in Fig. 4.10 are showed in Fig. 4.12. Clearly, the transition from a typical disordered glass structure to an ordered crystalline structure during crystallisation, and then to a disordered liquid structure during melting is demonstrated as explained in details below. From room temperature to 459.2 °C, the G(r) curves exhibit characteristic peak profiles of amorphous structures but with
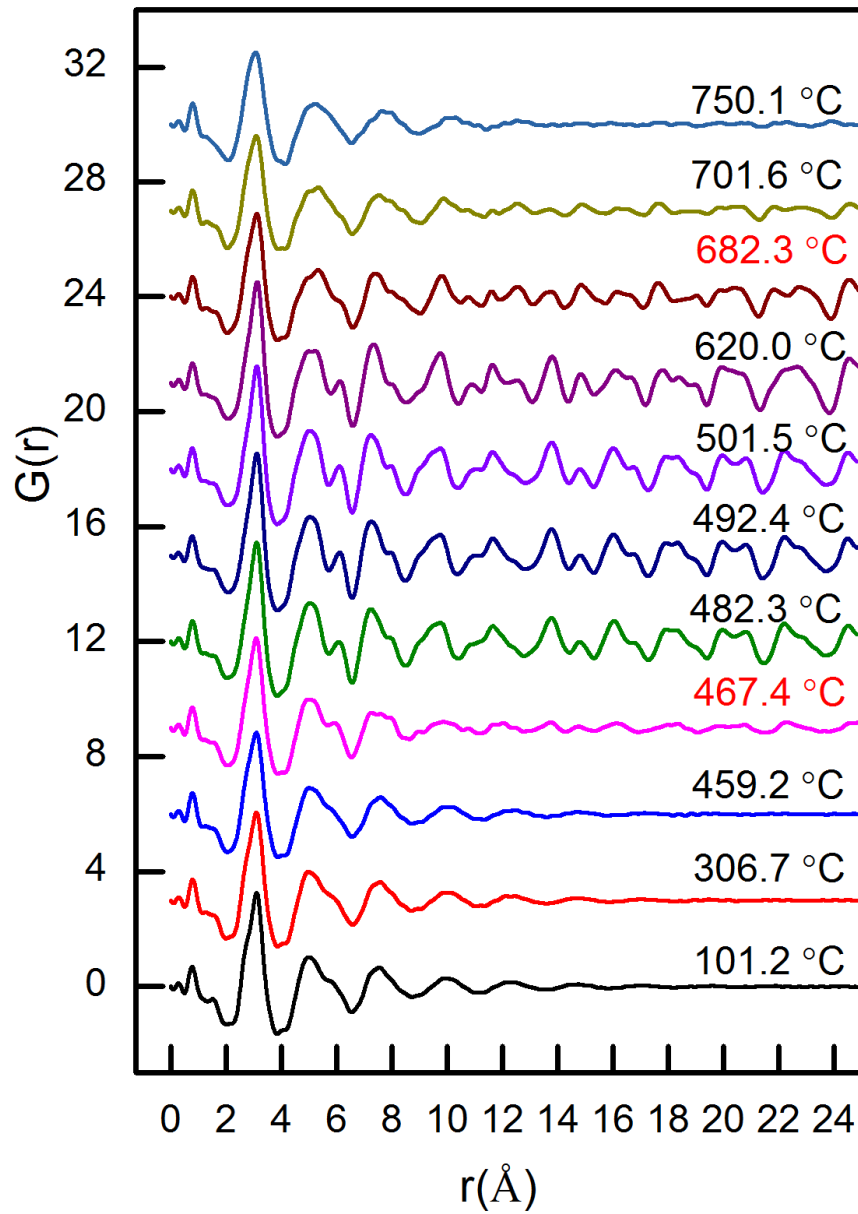
Fig. 4.12 The pair distribution functions acquired for Vit1 alloy at each critical temperature during heating with an average heating rate of 1.5 K/s. The curves are stacked with an equal spacing of 3.0 in y direction.

less dominant peaks (the 3rd, 4th, and 5th peaks are detectable) coexisting in the short to medium r range (2-10 Å).

(a)

(b)

(c)
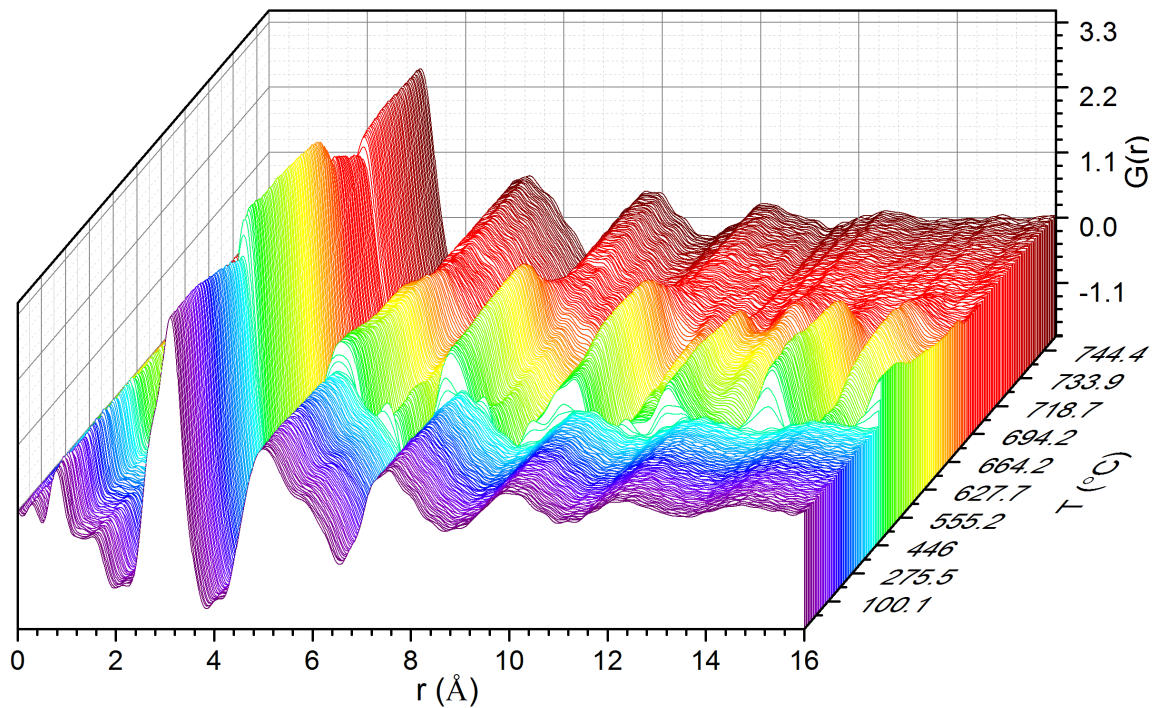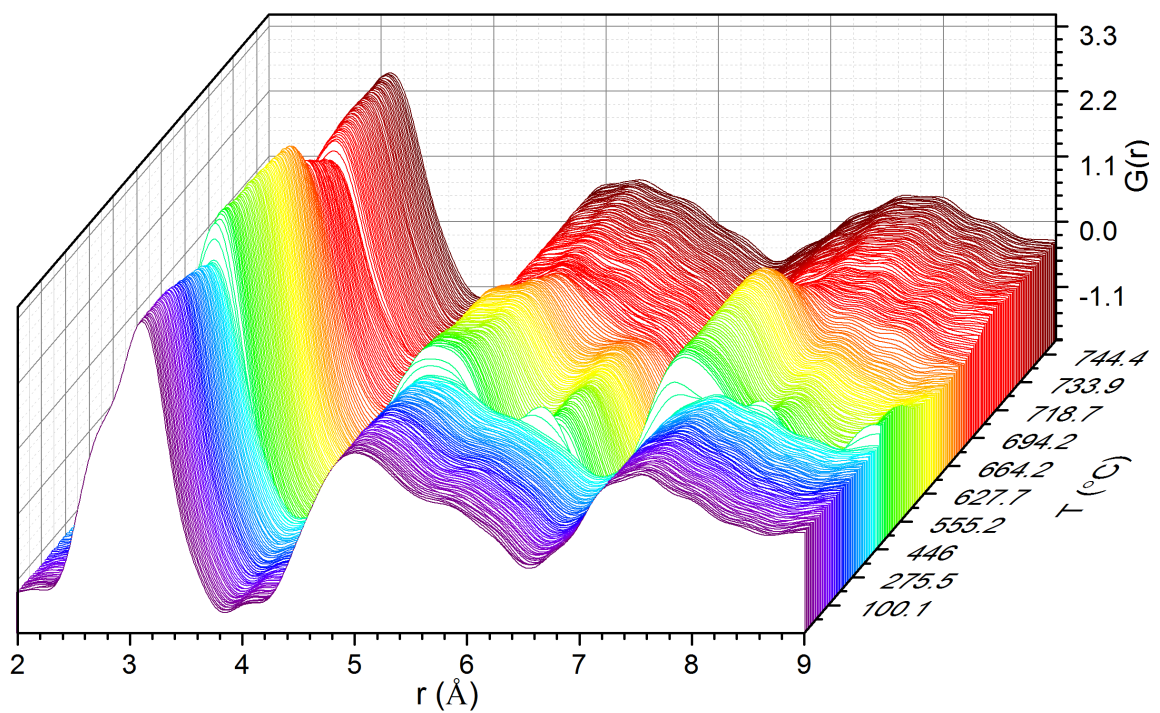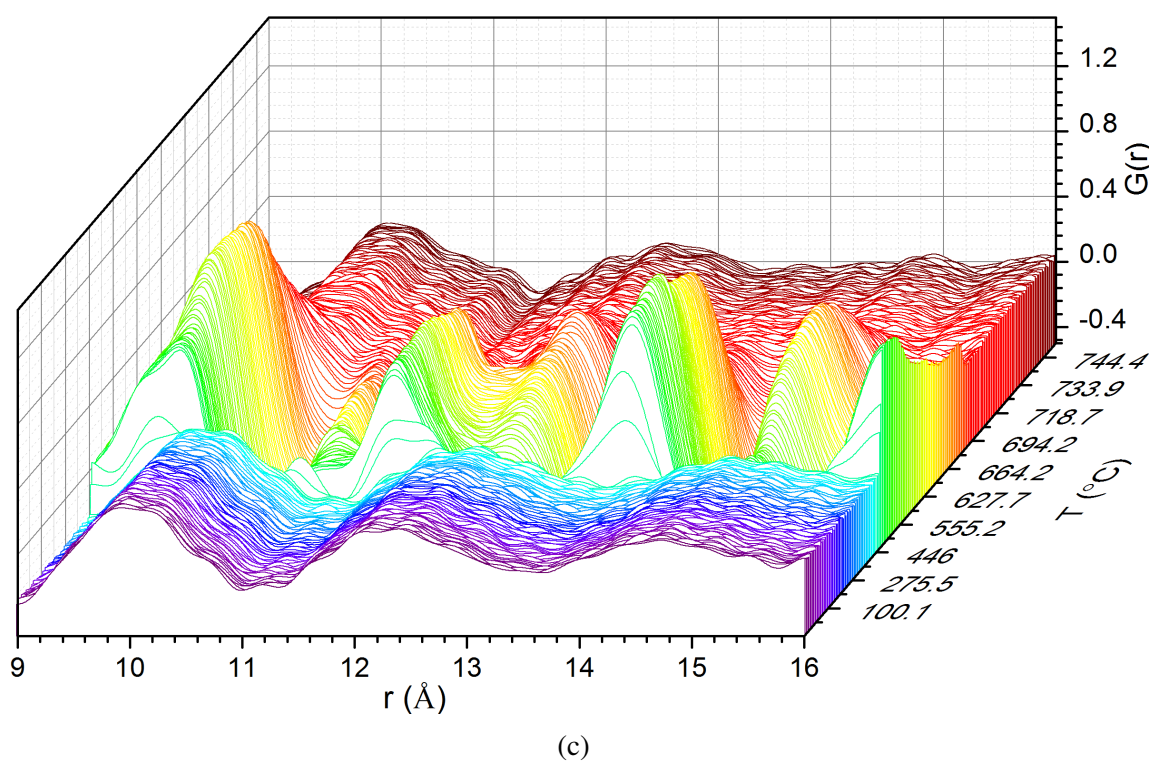
Fig. 4.13 The evolution of pair distribution functions of Vit1 as a function of temperature during the heating process with a heating rate of 1.5 K/s. (a) the G(r) in 0 - 16.0 Å, (b) the G(r) between 2.0 and 9 Å, and (c) the G(r) between 9 and 16 Å.

When temperature increased from 459.2 °C to 467.4 °C in 6 s, a dramatic structure change occurred and shown in the corresponding G(r) obtained at those temperatures. Some new peaks emerged and those pre-existing peaks became more intensive but the level of peak intensity nearly remained unchanged until 682.3 °C. Above that temperature and as the heating continued G(r) slowly evolved back into the characteristic profiles of amorphous state until a steady state was achieved at and above 701.6 °C.

The dynamics of such structural evolution with temperature is again presented in the waterfall plot in Fig. 4.13. Fig. 4.13b and Fig. 4.13c present the enlarged views of the G(r)s for facilitating the views and analyses of the locations of different peaks.

Fig. 4.13 demonstrates more clearly the transition from amorphous structure to crystalline structure, then to liquid structure. The peak intensity of the G(r) nearly remained constant before the onset crystallisation temperature of 459.2 °C, while a dramatic increase of peak intensity occurred from 459.2 °C to 467.4 °C. In the meantime, some minor peaks

began to separate from the shoulder of the main peaks. As temperature increased, the peak intensity almost remained the same until 682.3 °C, then it deceased from 682.3 °C to 701.2 °C and remained constant again after the alloy was in full liquid state.

Analyses of the G(r) peak intensity and peak position shift can give more quantitative information on understanding of how atomic pairs evolve from disordered to ordered state during the changes of atomic structures.

4.2.1.2 Analyses of peak intensity and peak position

Fig. 4.14 presents all the peaks and peak shoulders (hidden peaks), which constitute four primary atomic shells in the r range of 2 to 10 Å. Such r range is chosen because it almost covers the characteristic short and medium r range of amorphous phase. The PDFs of crystalline phases formed during the crystallisation at 620 °C is used for the peak detection, since the formed structure at this temperature is a complete crystalline structure. PDF Peaks are detected using the second derivative detection method described in section 3.3.6. 15 apparent peaks are detected for the four atomic shells, and the peak position of most of these peaks are very close to that of the fitted peaks using real space refinement method [112] (presented in following section).

A special index code is created for easily referencing the peaks and hidden peaks in different atomic shells, for example, in the first atomic shell (S1), the first peak (P1) is referred as S1_P1, while in the second atomic shell (S2), the second hidden peak (HP2) is referred as S2_HP2.

For all G(r) curves showed in Fig. 4.13, the peaks in each G(r) were detected using the above procedure executed in a batch mode using OriginPro 8.0. The changes of maxima of each peak and hidden peak are plotted as functions of temperature and showed in Fig. 4.15.

Fig. 4.15 shows that, in the 1st shell, the maxima of S1_P1 decrease from 3.0 to 2.5 when temperature increased from 100 °C to 459.2 °C. However, from 459.2 °C to 467.3°C ($\sim$ 8 K), the maxima increase dramatically from 2.5 to 3.7 due to crystallisation, and then
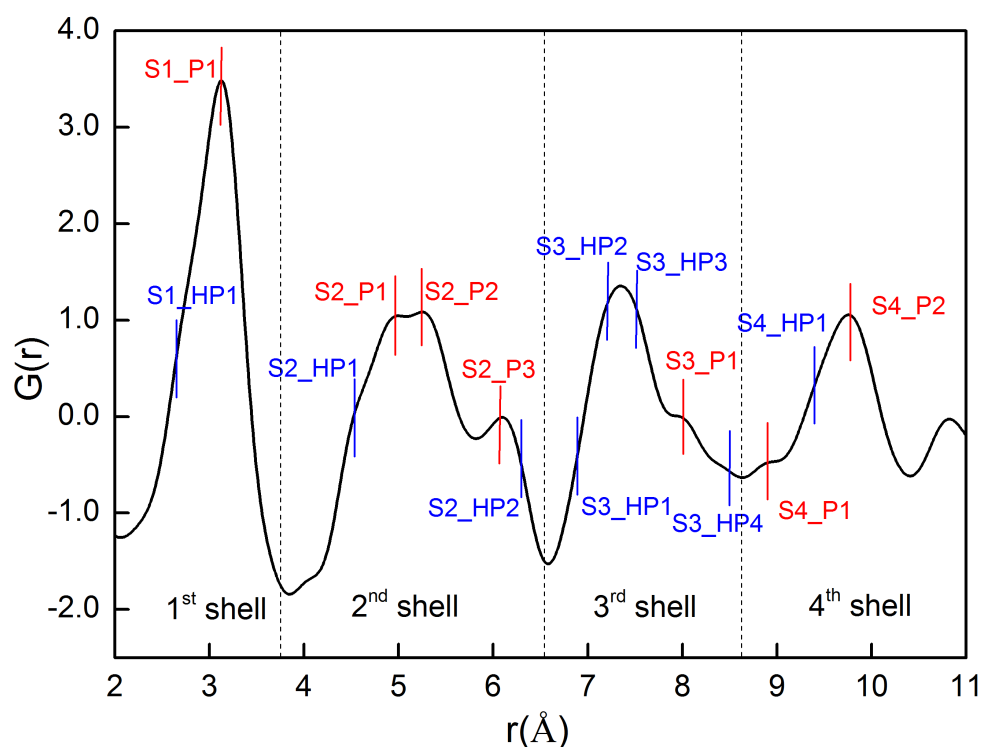
Fig. 4.14 The main and hidden peaks together with their positions detected from the G(r) of the crystalline phases of Vit1 at 620 °C formed by crystallisation.

gradually decreased to ~ 3.5 from 467.3°C to 680 °C. When melting at 682.3 °C, the maxima dropped from 3.5 to 1.5 very quickly. Subsequently, the maxima of S1_HP1 just changed slightly thorough the heating process. In the 2nd atomic shell, the maxima of S2_HP1 and S2_P2 slowly decreased from 100 °C to 250 °C. But from 250 °C to 280 °C they increased dramatically. Those of S2_P1 and S2_HP2 behaved similarly as S1_P1 did.

S3_HP2 in the 3rd shell has the similar trend as S1_P1, while S3_HP3 and S3_P1 experience a slowly decrease from 100 °C to 470 °C, but a sudden increase at 470 °C followed by a rapid decrease from 470°C to 720°C. For the 4th shell, S4_P2 experiences a gentle decrease from 100 °C to 470 °C, then a big jump at 470 °C (0 to 0.8) followed by a slow increase until 700°C and finally another big drop.

The changes of peak maxima as functions of temperature can be generally grouped into two senarios as clearly presented in Fig. 4.16: (1) firstly, those (five main peaks and two hidden peaks) have a sudden jump at 467.3°C (Fig. 4.16a), and (2) those (S2_P2 and

(a) 1st Shell

(b) 2nd Shell

(c) 3rd Shell

(d) 4th Shell
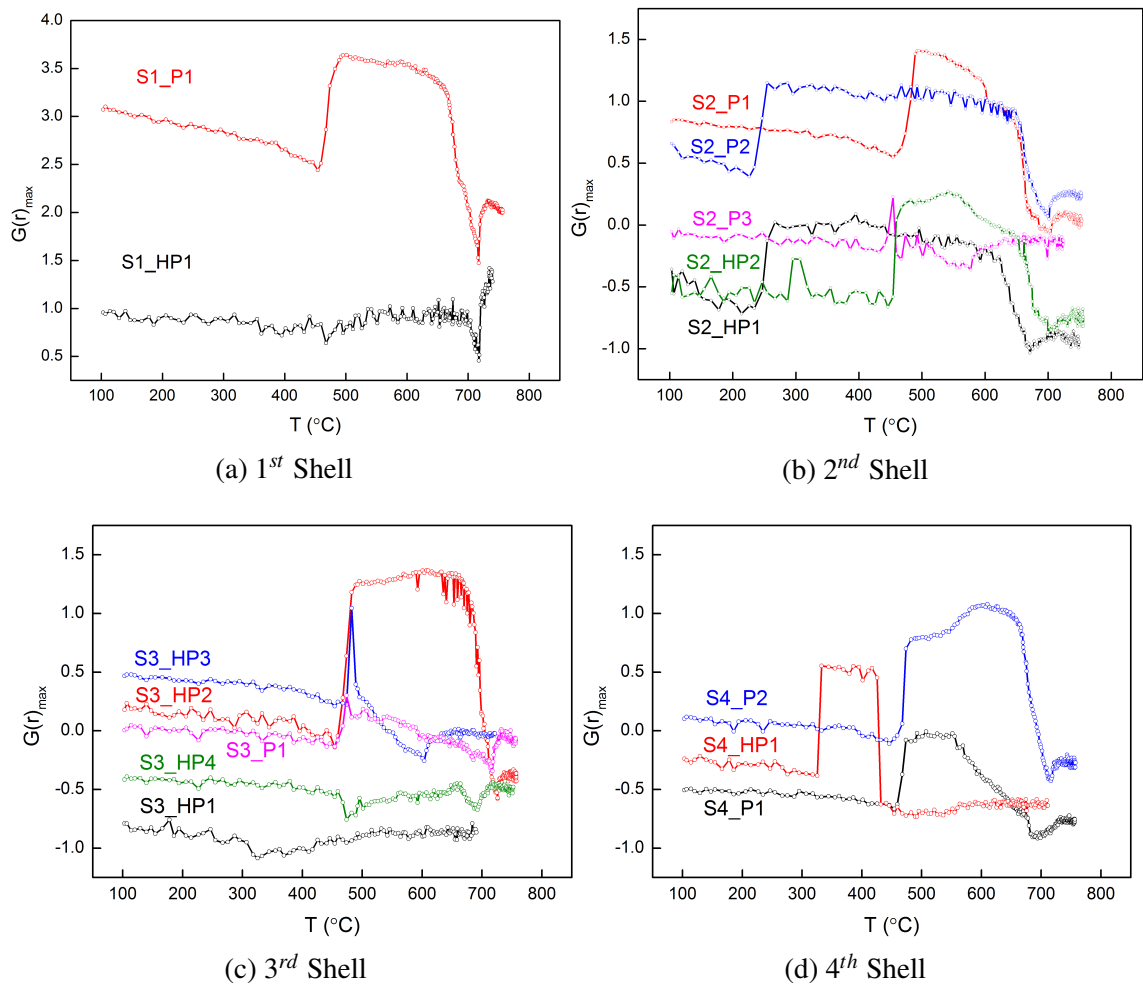
Fig. 4.15 The maxima of all peaks in the four atomic shells as functions of temperature for the case shown in Fig. 4.9.

S2_HP1) have a sudden jump at 270 °C (Fig. 4.16b). The only exception is S4_HP1 with a sudden jump at 350 °C.

During the crystallisation of metallic glass, atomic structure changes from short range ordered to long range ordered structure, in which not only the peak intensity of G(r) changes, the peak positions often changes as well. Fig. 4.17 presents the changes of peak position for all peaks in the range of 2 to 10 Å.

In the 1st shell, the peak position of S1_HP1 shifted from 2.56 to 2.83 Å when temperature increased from 100°C to 459.2°C, however, that of S1_P1 shifted from 3.10 to 3.06 Å. In the 2nd shell, most of the peaks shifted to lower r, except S2_HP2 moved to higher r at 660°C. S3_HP2 and S3_HP3 shifted to higher r when T > 470 °C, while others in the 3rd
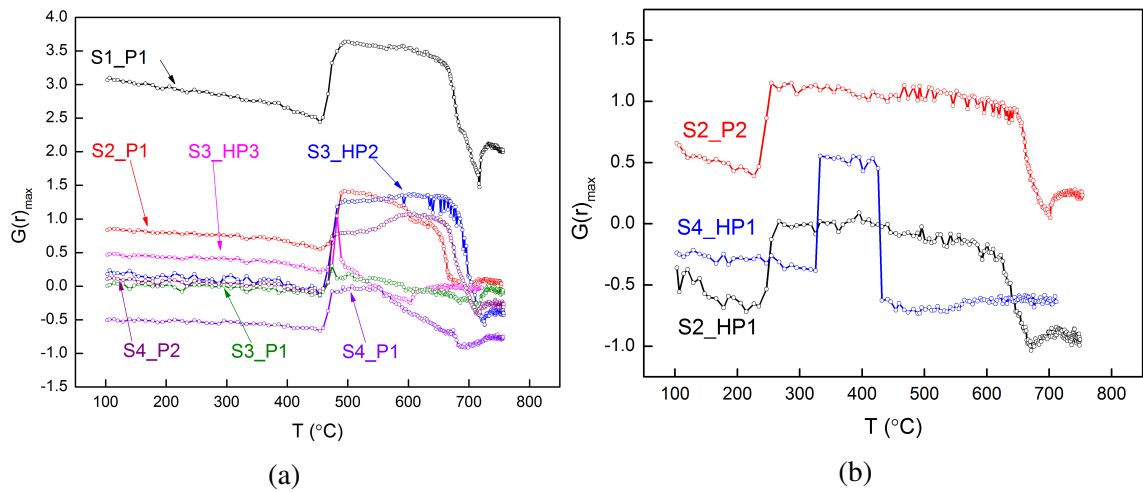
Fig. 4.16 The sudden jumps of the maxima of different peaks and hidden peaks at (a) 467 °C, (b) 270 °C and 350 °C.

shell do not change. S4_P2 in the 4th shell shifted from 9.88 to 9.72 Å at 459.2 °C, and then remained unchanged until full melting occurred.

4.2.1.3 Real space refinement and partial PDF

For a metallic glass system undergoing a crystallisation, crystalline phases induced by crystallisation can be modelled using real space refinement method [111, 35]. The PDF of crystalline phases induced by crystallisation of Vit1 at 620 °C is again used for the real space refinement, which is consistent to the peak detection.

As mentioned, the crystalline phases formed during the crystallisation of Vit1 are primarily Zr_2Cu and $ZrBe_2$. The two phases are used as the structure models for real space refinement using PDFgui (Fig. 4.18). The r range of 2-10 Å is selected.

Fig. 4.18a presents the contribution of each phase, Zr_2Cu and $ZrBe_2$ to the total PDFs. Fig. 4.18b shows the partial PDF of Zr-Zr, Zr-Cu, and Cu-Cu pairs obtained for Zr_2Cu, while Fig. 4.18c presents the partial PDF of Zr-Zr, Zr-Be, and Be-Be pairs obtained for $ZrBe_2$.
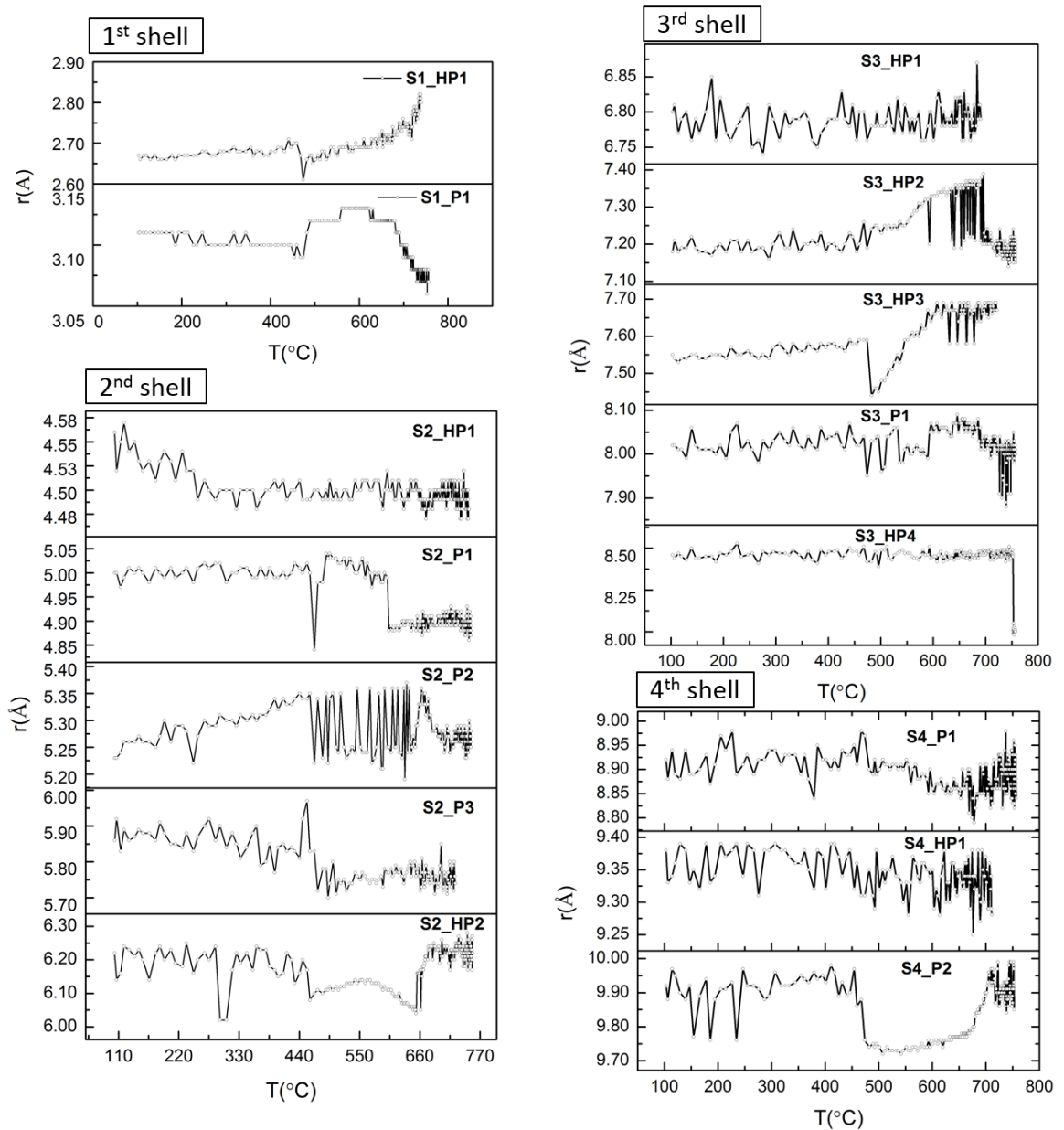
Fig. 4.17 Shifts of all peaks in the four atomic shells as functions of temperature for the case shown in Fig. 4.9.
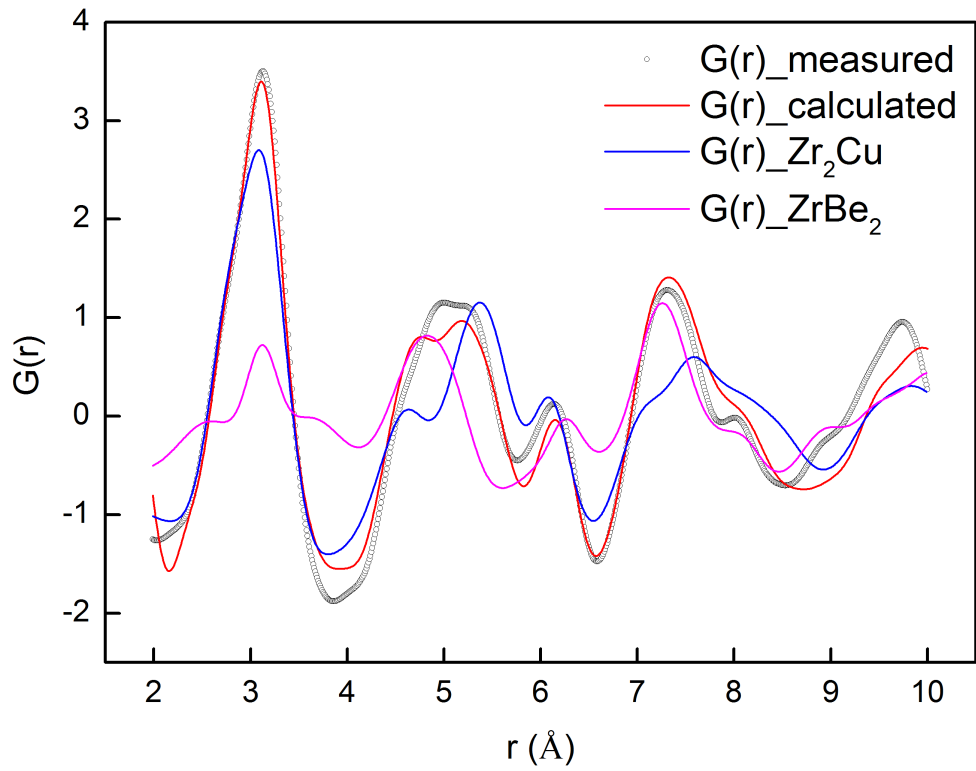
(a)
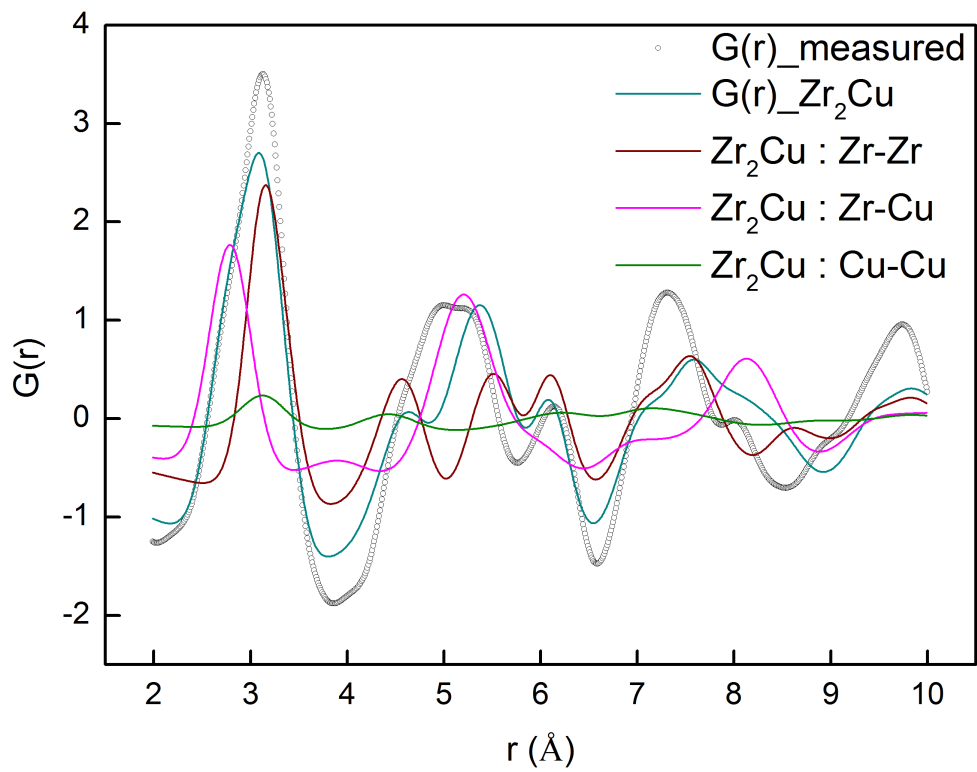
(b)
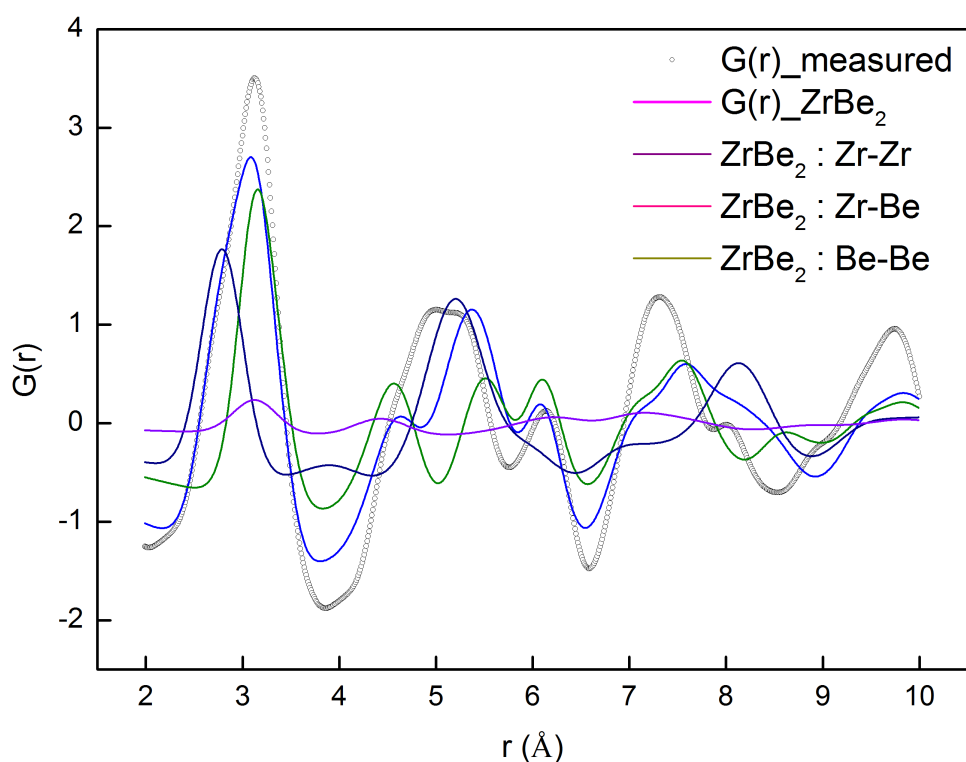
(c)

Fig. 4.18 (a) The PDFs of Zr_2Cu and $ZrBe_2$ phases, and the partial PDFs of the individual atomic pairs from the two phases, *i.e,* (b) $ZrBe_2$,(c) Zr_2Cu.

Based on the real space refinement as shown in Fig. 4.18 and the detected peaks in Fig. 4.14, it is possible to relate the primary atomic pairs, such as Zr-Zr, Zr-Cu, Cu-Cu, to the peak positions for most of the peaks detected.

The correspondence between the peak position of the primary atomic pairs and the peak position of these detected peaks are summarised in Table. 4.1. For example, S1_HP1 can be generated by two possible atomic pairs, *i.e,* Zr-Cu (2.8 Å) and Zr-Be (2.59 Å). However, the peak intensity of the fitted partial PDF of Zr-Be is very low compared to that of Zr-Cu. Therefore, it is reasonable to consider Zr-Cu pairs contributing dominantly for S1_HP1.

The same method can be applied to most of the peaks detected, and the 1st option listed in Table. 4.1 are most likely the dominant atomic pairs to form peaks.

Table 4.1 The correspondence of peak position of the fitted atomic pairs and measured peak positions of Vit1 alloy

atomic shell	r range (Å)	peak code	Zr_2Cu			$ZrBe_2$			partial pairs	
			Zr-Zr(Zr_2Cu)	Zr-Cu	Cu-Cu	Zr-Zr($ZrBe_2$)	Zr-Be	Be-Be	1st option	2nd option
1st		S1_HP1		2.8			2.59		Zr-Cu	Zr-Be
	2.0-3.8	S1_P1	3.17		3.13	3.16			Zr-Zr	
		S2_HP1	4.58		4.44		4.52		Zr-Zr(Zr_2Cu)	
		S2_P1				4.81			Zr-Zr($ZrBe_2$)	
2nd	3.8-6.5	S2_P2		5.21			5.16		Zr-Cu	Zr-Be
		S2_P3					5.97		Zr-Be	
		S2_HP2			6.27	6.3			Zr-Zr($ZrBe_2$)	
		S3_HP1								
		S3_HP2			7.17	7.25			Zr-Zr($ZrBe_2$)	
3rd	6.5-8.6	S3_HP3	7.55				7.44		Zr-Zr(Zr_2Cu)	
		S3_P1		8.14			8.07		Zr-Cu	Zr-Be
		S3_HP4								
		S4_P1			8.97		8.99		Zr-Be	
4th	8.6-10.0	S4_HP1					9.57		Zr-Be	
		S4_P2	9.83		9.85				Zr-Zr(Zr_2Cu)	

The peak position of these primary atomic pairs can be identified based on the correspondence, hence the evolution of the atomic pairs with temperature during the heating and cooling can be better understood by analysing the changes of PDF peak profile.

4.2.2 Structure evolution during cooling

The atomic structure evolutions at three different average cooling rates, *i.e.* 14.7, 3.35, 0.79 K/s are presented in the section. The cooling rate of 14.7 K/s is selected because a typical amorphous structure can be formed with such cooling rate, while the other two slow cooling rates, *i.e,* 3.35, 0.79K/s, leads to typical crystalline structure.

4.2.2.1 Cooling rate of 14.7 K/s

Fig. 4.19 shows the measured temperature profile of the sample during the experiment using a controlled cooling rate of 14.7 K/s, and the diffraction patterns shown in Fig. 4.19 are those obtained at the critical temperatures and the temperatures in between. A total of 413 diffraction patterns were acquired for this case.
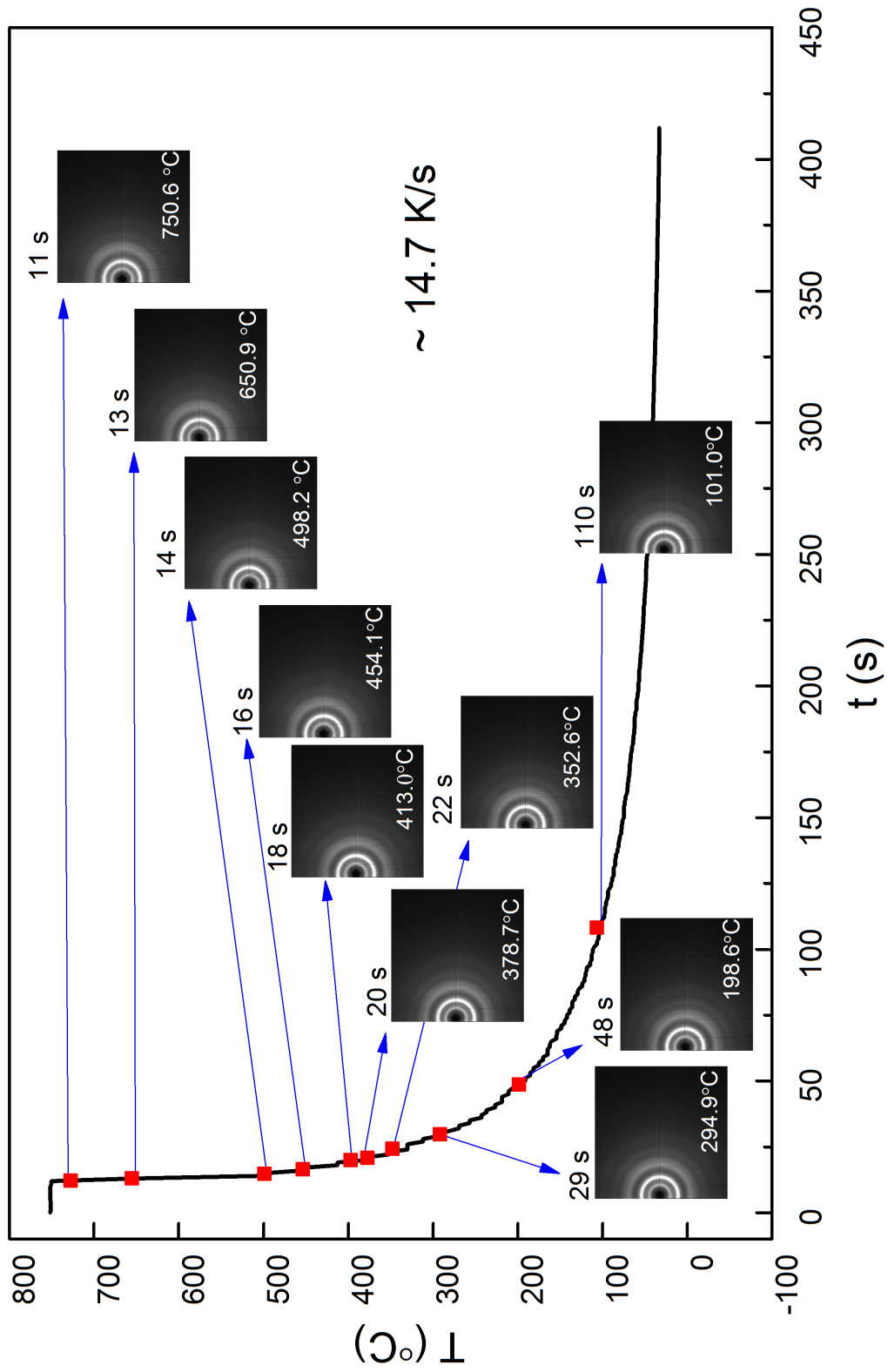
Fig. 4.19 The temperature profile of Vit1 during cooling using an average cooling rate of 14.7 K/s, and the 2D diffraction patterns acquired at the marked temperatures.

Fig. 4.20 shows the stack of I(Q) curves integrated from those patterns shown in Fig. 4.19. No obvious difference of I(Q) from all these patterns at different temperatures can be found.

Fig. 4.21 shows a waterfall plot of diffraction spectra obtained at different cooling temperatures for Vit1 from 2.0-10.0 Å^{-1}. A typical diffraction spectra of amorphous structure can be observed for the whole temperature range. However, the peak maxima of the first peak increases during the glass formation when the temperature decreases from 378.7 °C to 101.0 °C. The small diffraction peaks superimposed together with the dominant broad diffuse peaks remain unchanged.
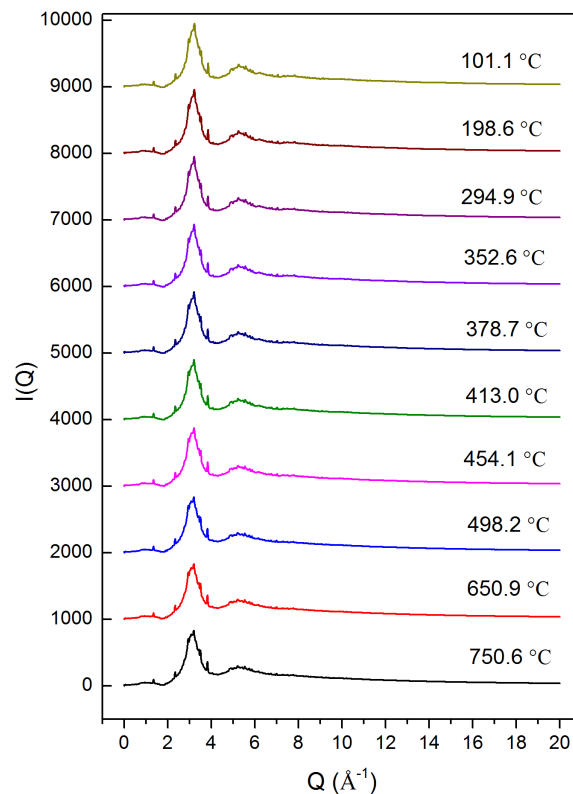
Fig. 4.20 The diffraction spectra acquired for Vit1 alloy at each temperature shown in Fig. 4.19 during cooling with an average cooling rate of 14.7 K/s. The curves are stacked with an equal spacing of 1,000 counts in y direction.

Fig. 4.22 shows G(r) acquired at the marked temperatures in Fig. 4.19. There is no apparent change in the peak profile. The dynamics of such structural evolution with temperature is again presented in the waterfall plot shown in Fig. 4.23. The maxima of
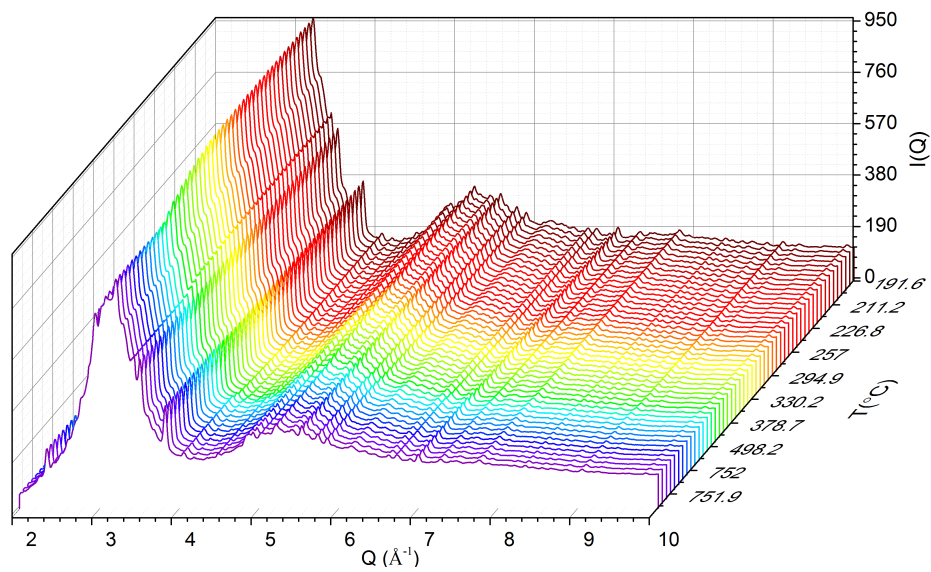
Fig. 4.21 The evolution of 1D diffraction spectra of Vit1 as a function of temperature during the cooling process with an average cooling rate of 14.7 K/s in 2-10 Å^{-1}.
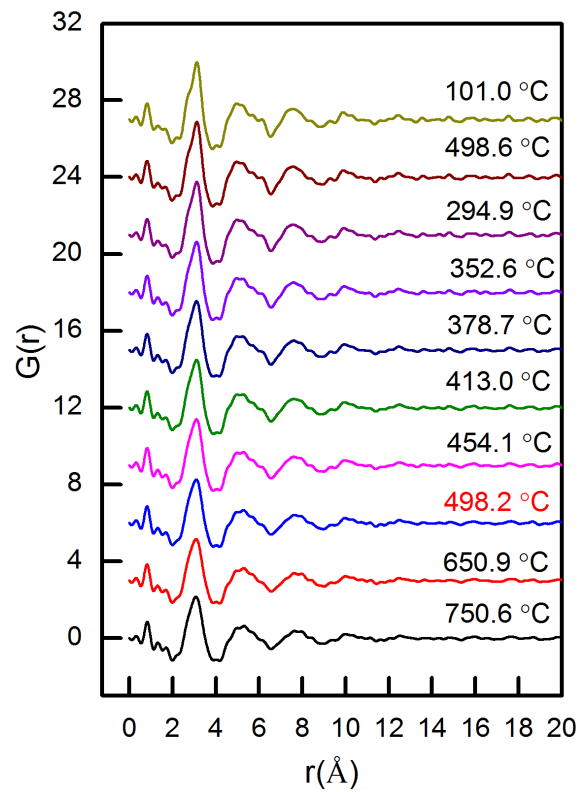
Fig. 4.22 The pair distribution functions acquired for Vit1 alloy at each temperature shown in Fig. 4.19 during cooling with an average cooling rate of 14.7 K/s. The curves are stacked with an equal spacing of 3.0 in y direction.

(a)

Fig. 4.23 The evolution of pair distribution functions of Vit1 as a function of temperature during the cooling process with an average cooling rate of 14.7 K/s.

(a) 1st Shell

(b) 2nd Shell

(c) 3rd Shell

(d) 4th Shell
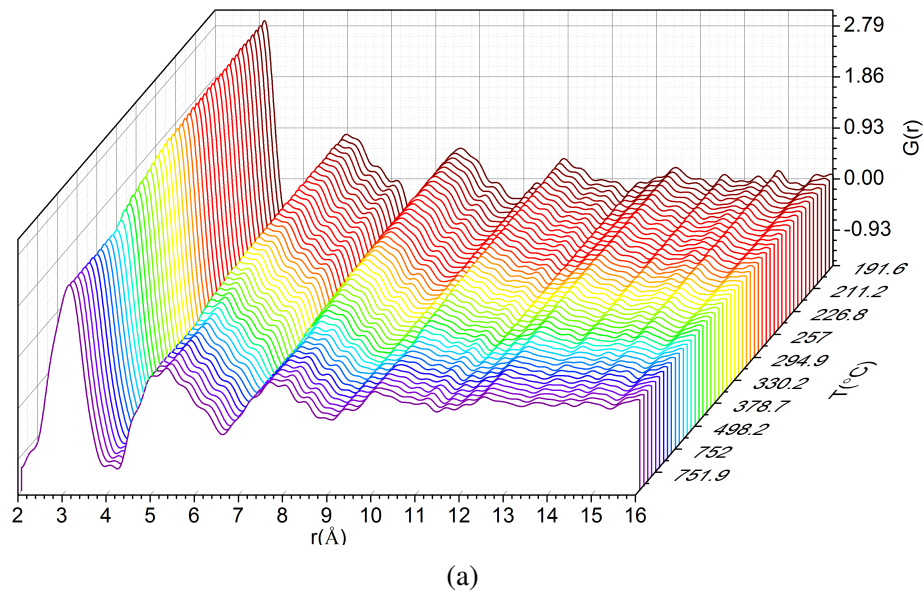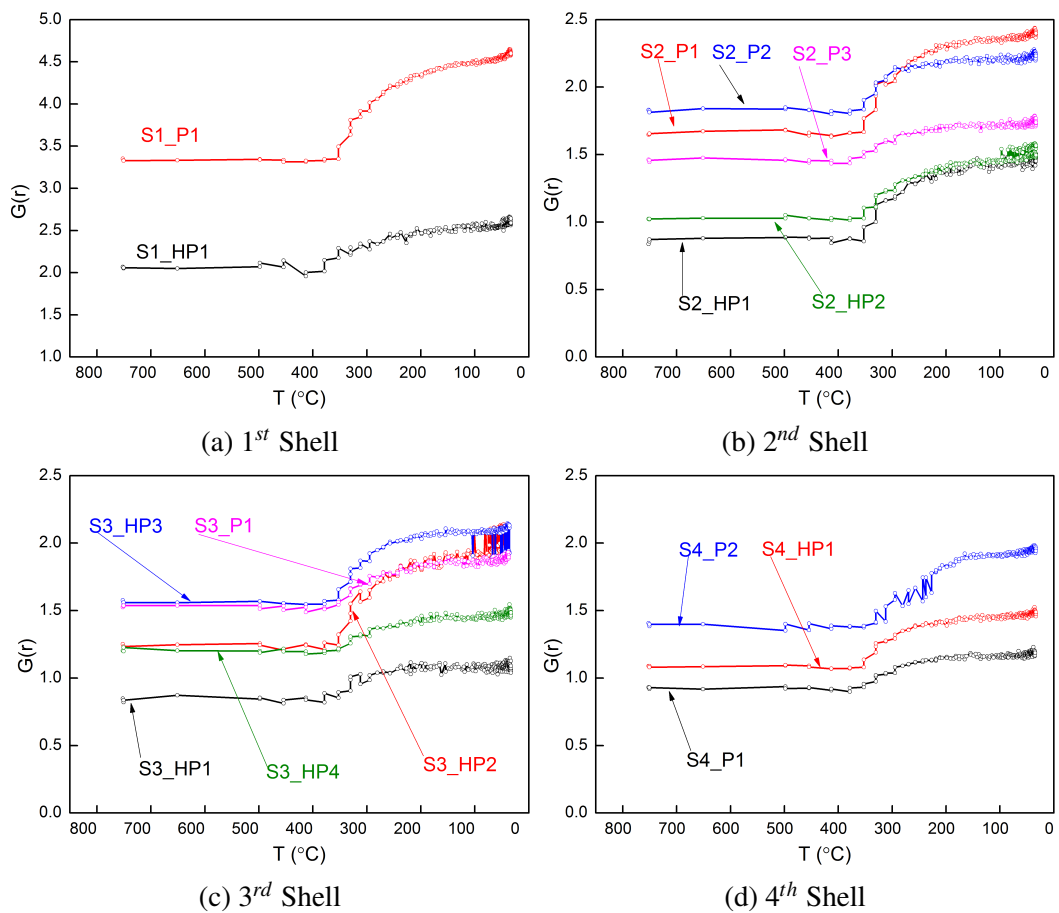
Fig. 4.24 The maxima of all peaks in the four atomic shells as functions of temperature for the case shown in Fig. 4.19.

all the peaks of G(r) increases with the decrease of the temperature. However, there is no dramatic structure change (such as peak separation).

Fig. 4.24 shows the maxima of all peaks as a function of temperature. The peak maxima in the r range of 2 to 10 Å, remained the same for the temperature from 750.6 °C to 378.7 °C. It then followed a rapid increase when the super-cooled liquid experienced the glass formation from 378.7 °C to 198.6 °C. And then the peak maxima slowly increased when the temperature further decreased to 101.1 °C.

Fig. 4.25 shows the changes of peak position for all peaks in the range of 2 to 10 Å. In the 1st shell, the peak position of S1_P1 shifted to high r during the glass formation.
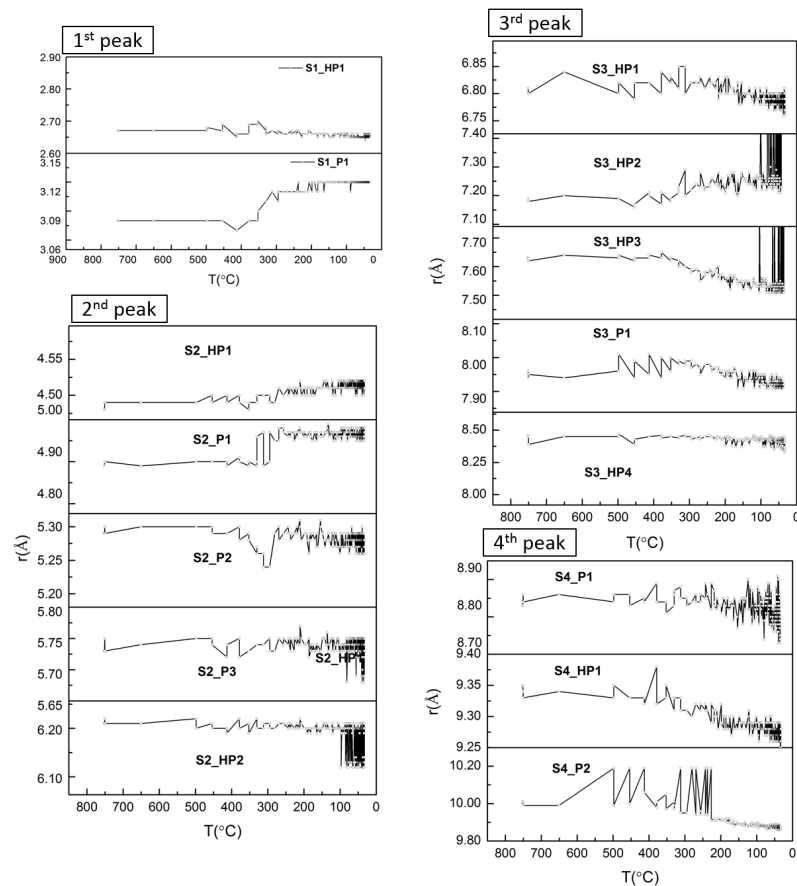
Fig. 4.25 Shifts of all peaks in the four atomic shells as functions of temperature for the case shown in Fig. 4.19.

The similar trend can be observed from the peak positions of S2_HP1, S2_P1 in the 2nd shell, and S3_HP2 in the 3rd shell. The peak positions of S3_HP3, S4_HP1, and S4_P2

slightly shifted to low r during the cooling process. The rest of peaks remained at the same positions, while the peak position of S2_P2 shifted from 5.30 Å to 5.23 Å when the temperature decreased from 459.5 °C to 300 °C, and then it rapidly shifted back to 5.28 Å when the temperature further decreased to 250 °C.

4.2.2.2   Cooling rate of 3.35 K/s

Fig. 4.26 shows the measured temperature profile of the sample during the experiment using a slow cooling rate of 3.35 K/s and the diffraction patterns shown in Fig. 4.26 are those obtained at the critical temperatures and the temperatures in between. Again, a total of 550 diffraction patterns were acquired for this case.

Fig. 4.27 shows the stack of I(Q) curves integrated from those patterns shown in Fig. 4.26. From 750.9 to 627.3 °C, the three I(Q) curves show typical amorphous structure. When the liquid further cooled down from 627.3 °C, tiny diffraction peaks started to appear on top of the original diffuse peak at ~ 2.5 Å^{-1}. When the temperature reached 473.7 °C, it is hardly to detect any changes in I(Q). Clearly, the crystallisation of melt started from 627.3 °C, and ended at 473.7 °C in 28 s.

The dynamics of the structural evolution with temperature is presented by the waterfall plot in Fig. 4.28. It shows when the temperature decreased from 627.3 to 473.1 °C, sharp diffraction peaks appeared on top of the diffuse peaks of the high temperature liquid phase.

The local structure evolution at the atomic scale was also revealed by G(r). Fig. 4.29 shows that no apparent changes in G(r) were observed when the melt was cooled down to 627.3 °C. When the temperature further decreased from 627.3 °C to 473.7 °C, more tiny peaks appeared in the medium r range of G(r). After that, the peak shape of G(r) remained the same during the rest of cooling.
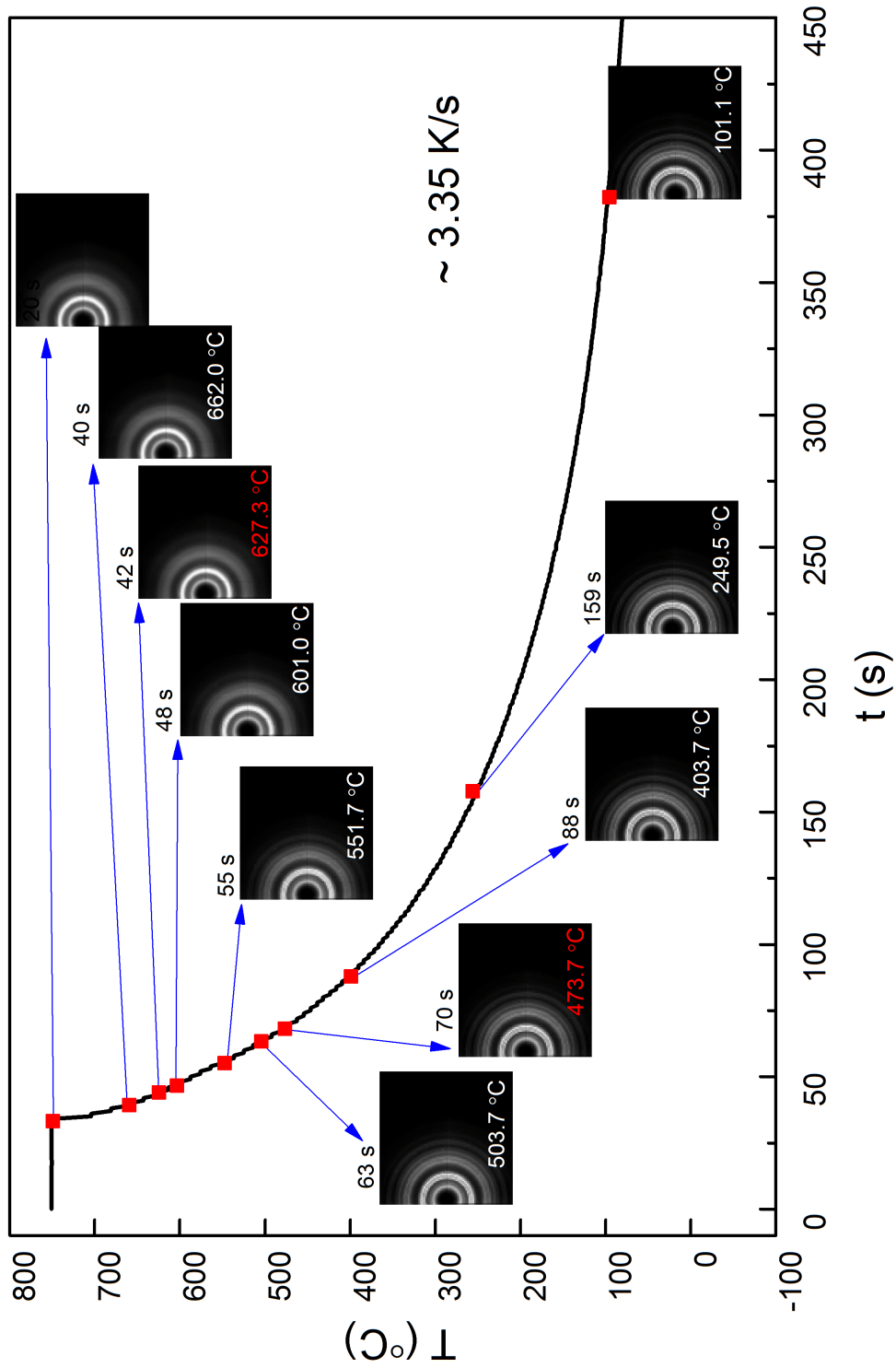
Fig. 4.26 The temperature profile of Vit1 during cooling using an average cooling rate of 3.35 K/s, and the 2D diffraction patterns acquired at the marked temperatures.
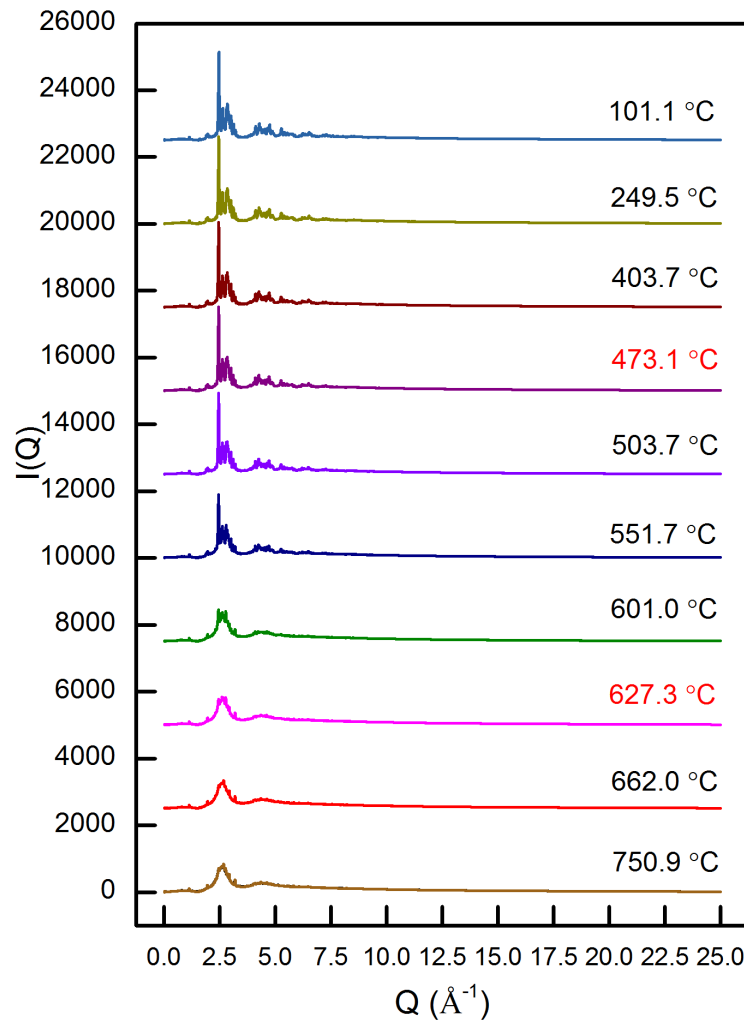
Fig. 4.27 The diffraction spectra acquired for Vit1 alloy at each critical temperature during cooling with an average cooling rate of 3.35 K/s. The curves are stacked with an equal spacing of 2,500 counts in y direction.

A dynamic evolution of G(r) is presented in Fig. 4.30. There are four main diffuse peaks in the liquid region from 750°C to 627.3 °C. As temperature decreased, more sharp peaks appeared in the medium r range during the crystallisation. The structure transition from the liquid to crystalline solid was observed in the temperature range of 627.3 °C to 473.7 °C. Fig. 4.30b shows clear peak separations at certain peak positions, *i.e*, 6.21 Å, 8.01 Å during the crystallisation.

Fig. 4.31 shows the changes of maxima of each peak and hidden peak of G(r) are plotted as functions of temperature. For most of the peaks in the r range of 2 to 10 Å, the maxima
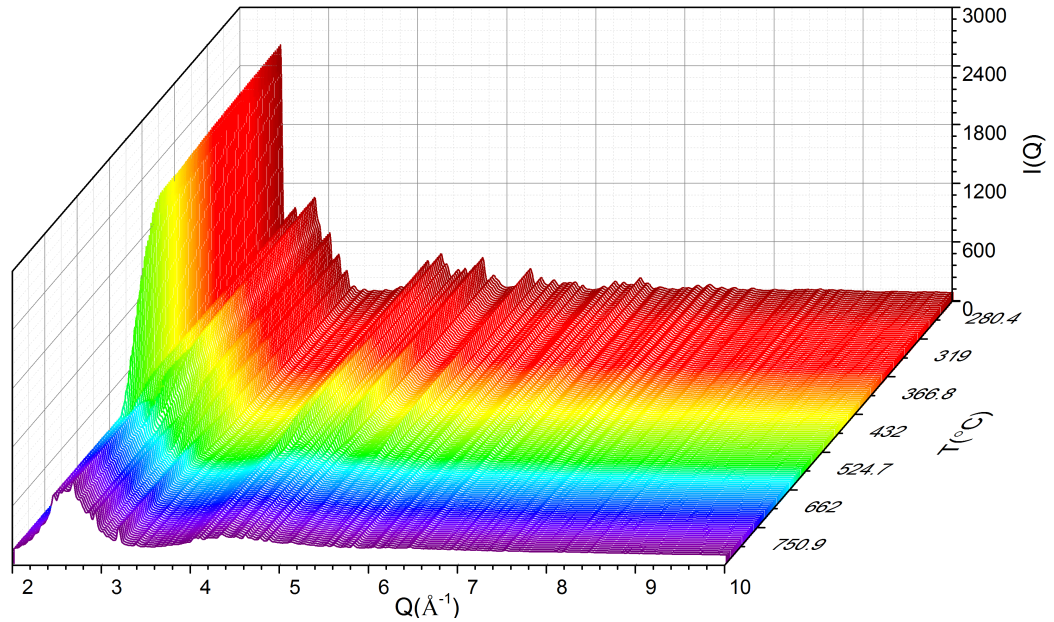
(a)
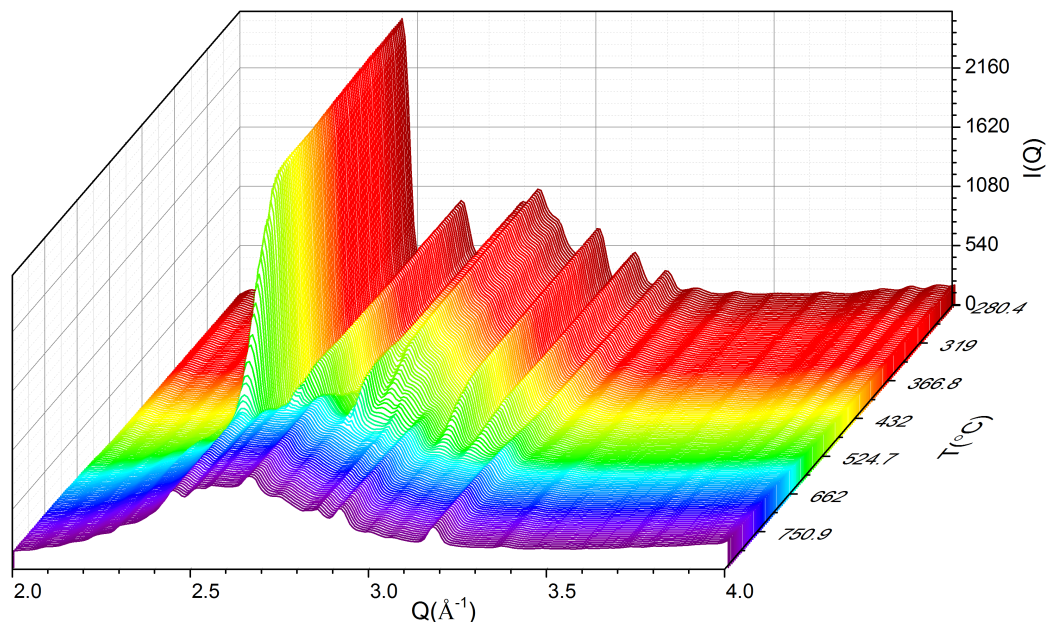
(b)

Fig. 4.28 The evolution of diffraction spectra of Vit1 as functions of temperature during the cooling process with an average cooling rate of 3.35 K/s. (a) the spectra in 2.0-10.0 Å^{-1}, (b) the spectra between 2.0 and 4.0 Å^{-1}.
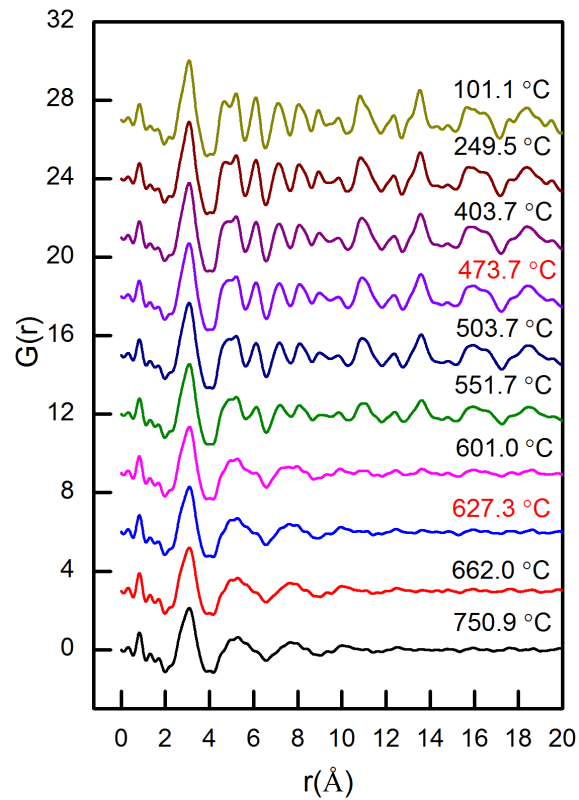
Fig. 4.29 The pair distribution function of Vit-1 alloy at several critical temperatures for phase transition during cooling process at a cooling rate of 3.35 K/s with an offset of 3.0 in y direction.
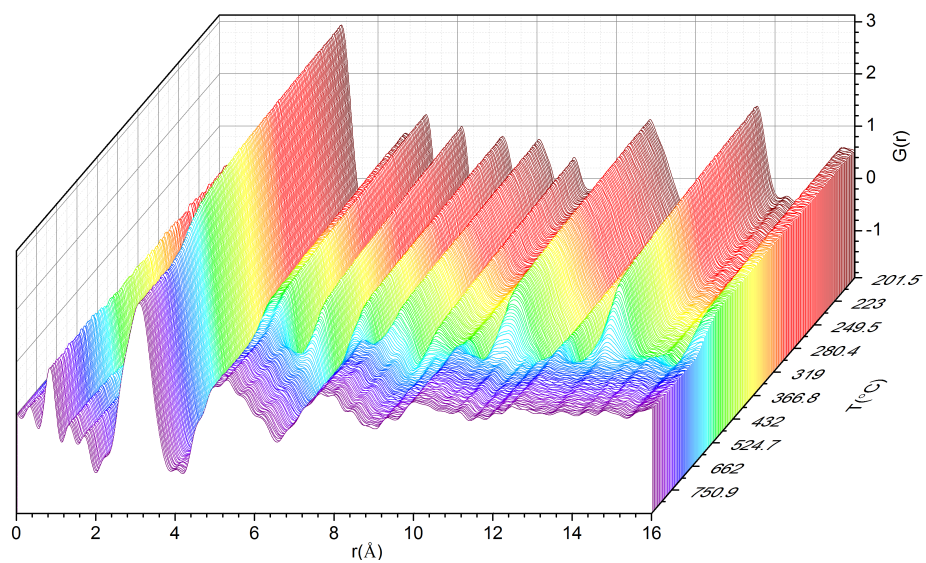
(a)
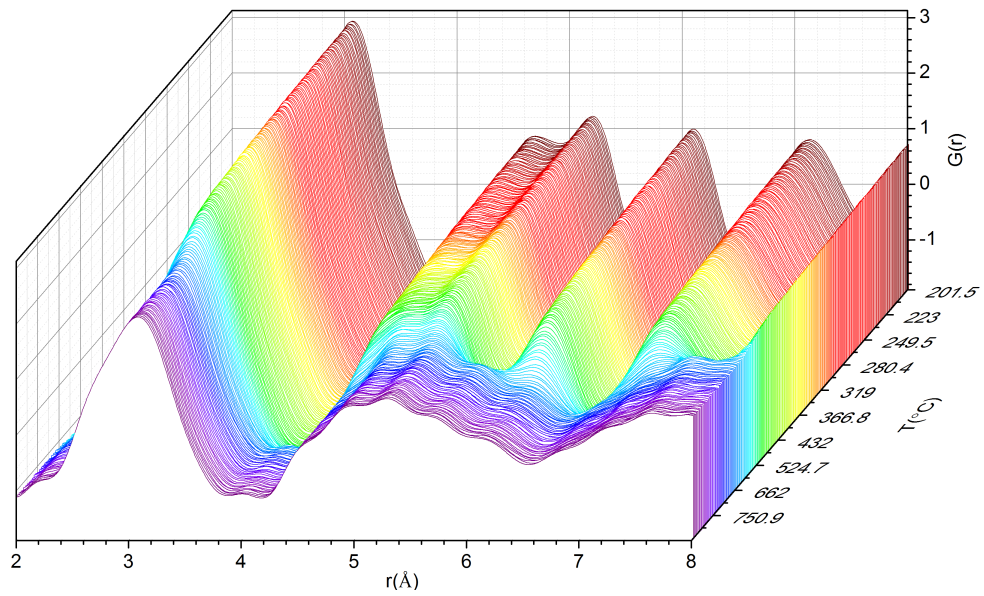
(b)
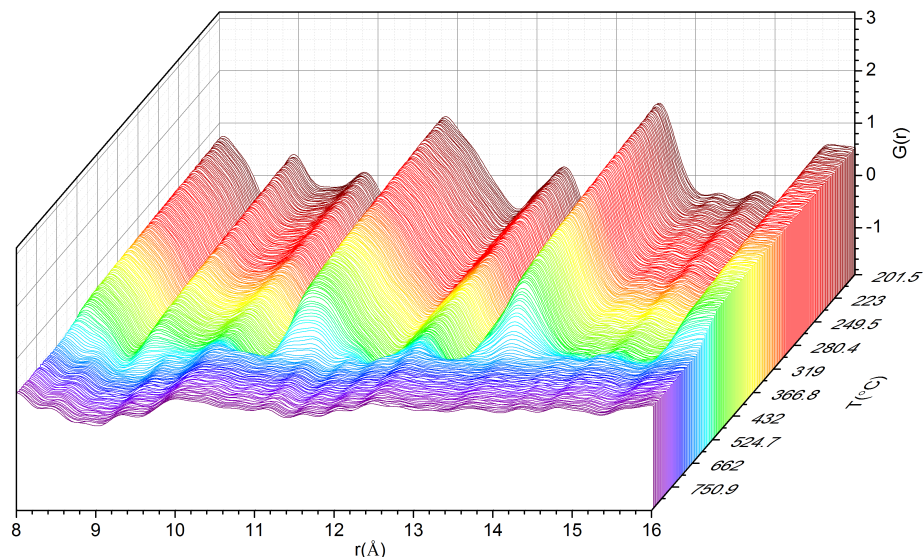
Fig. 4.30 The evolution of pair distribution functions of Vit1 as a function of temperature during the cooling process with an average cooling rate of 3.35 K/s. (a) the G(r) in 0 - 16.0 Å, (b) the G(r) between 2.0 and 8 Å, and (c) the G(r) between 8 and 16 Å.

increased dramatically when the temperature decreased from 627.3 °C to 473.7 °C, then it experienced a slow increase until the temperature further decreased to 200 °C.

Fig. 4.32 shows the shifts of all the peaks of G(r) in the four atomic shells as a function of temperature. In the 2st shell, when the temperature decreased from 627.3 °C to 473.7 °C,
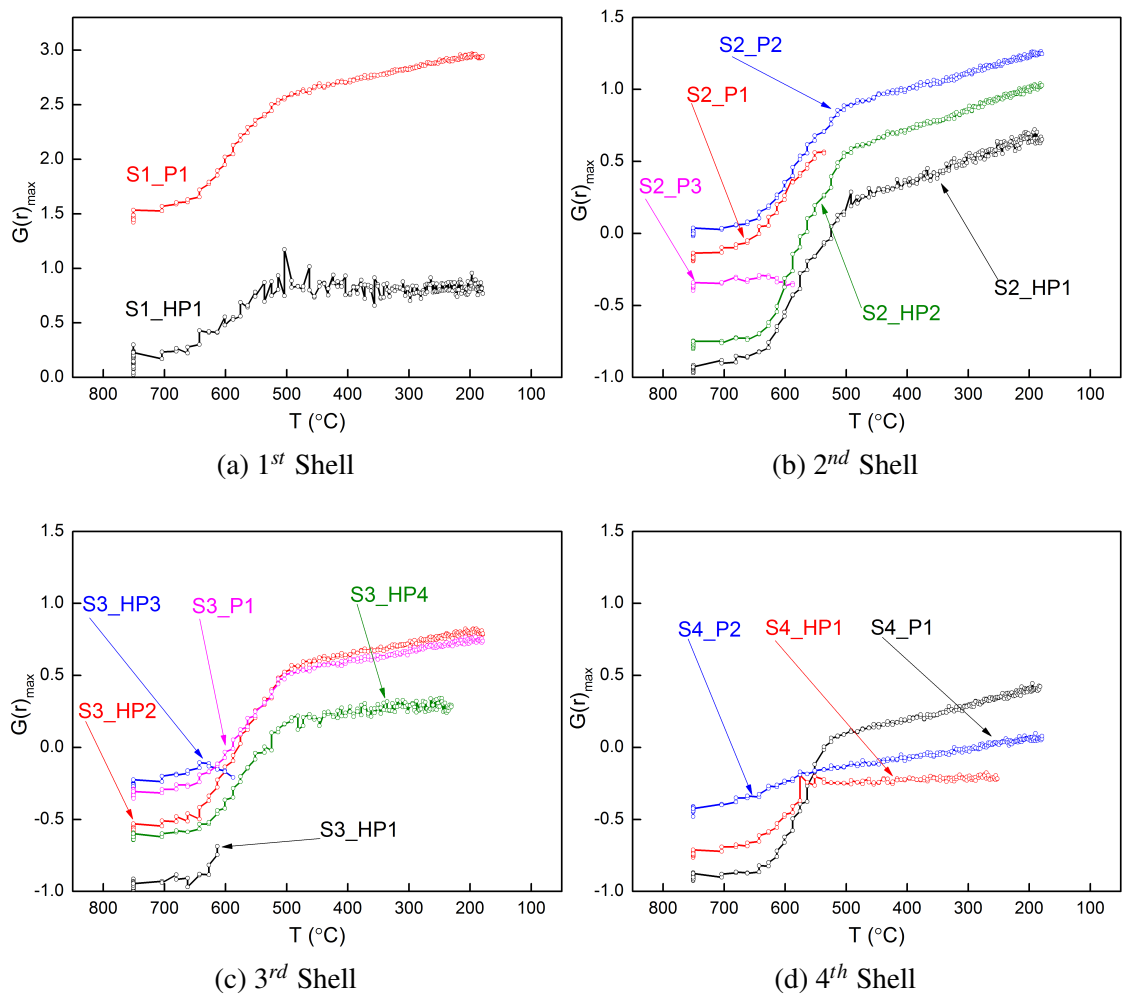
Fig. 4.31 The maxima of all peaks in the four atomic shells as functions of temperature for the case shown in Fig. 4.26.

the peak position of S2_HP1 shifted to 4.58 Å, which is very close to the peak position of S2_P1 (4.80 Å). While the peak position of S2_P2 and S2_HP2 shifted back to low r. The peak position of S3_HP2 and S3_HP4 in the 3rd shell, and S4_P2 in the 4th shell shifted to low r when temperature decreased from 627.3 °C to 473.7 °C. However the peak position of S3_P1, S4_P1 and S4_HP1 shifted to high r. The rest of peaks, S2_P1, S2_P3, S3_HP1 and S3_HP3 disappeared at 627.3 °C.
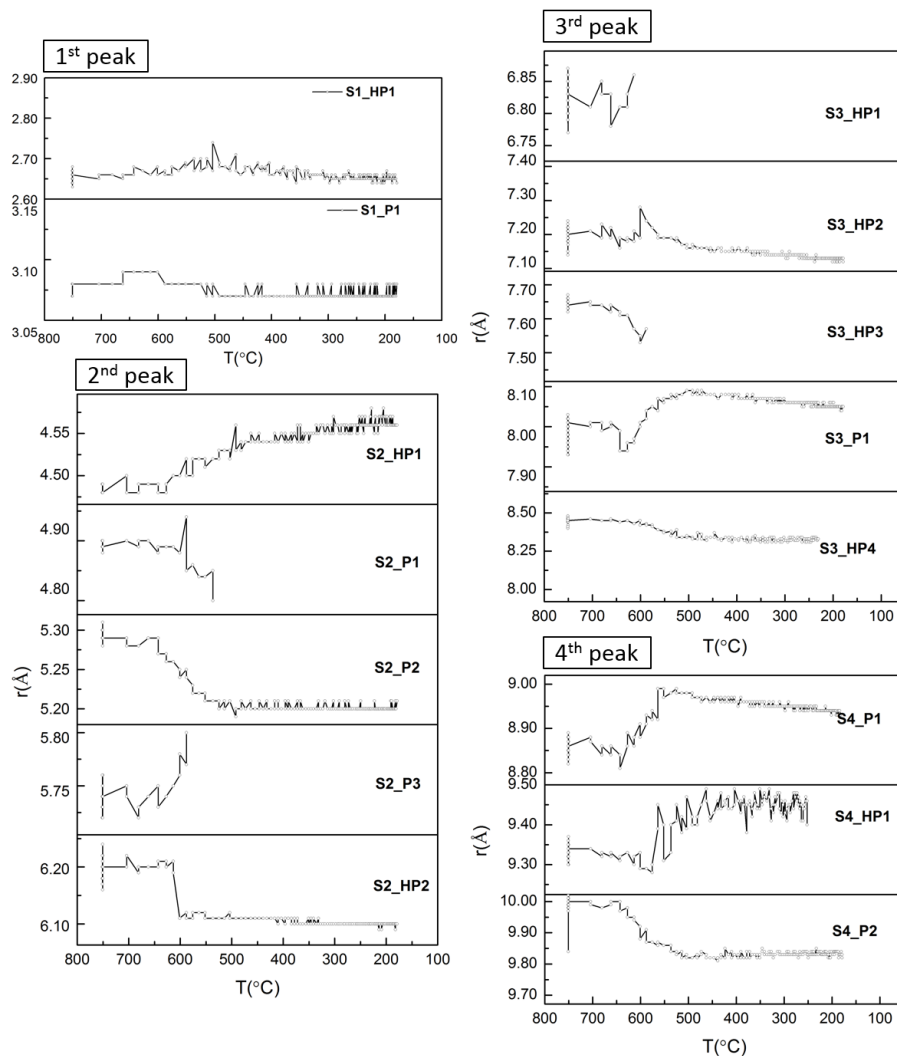
Fig. 4.32 Shifts of all peaks in the four atomic shells as functions of temperature for the case shown in Fig. 4.26.

4.2.2.3   Cooling rate of 0.79 K/s

An effect of even slower cooling rate of 0.79 K/s on the structure changes were studied and presented in this section. Fig. 4.33 shows the measured temperature profile of the Vit1 sample using a controlled average cooling rate of 0.79 K/s. The diffraction patterns acquired at the marked temperatures in Fig. 4.33 were also presented. A total of 1557 diffraction patterns were acquired for this case.
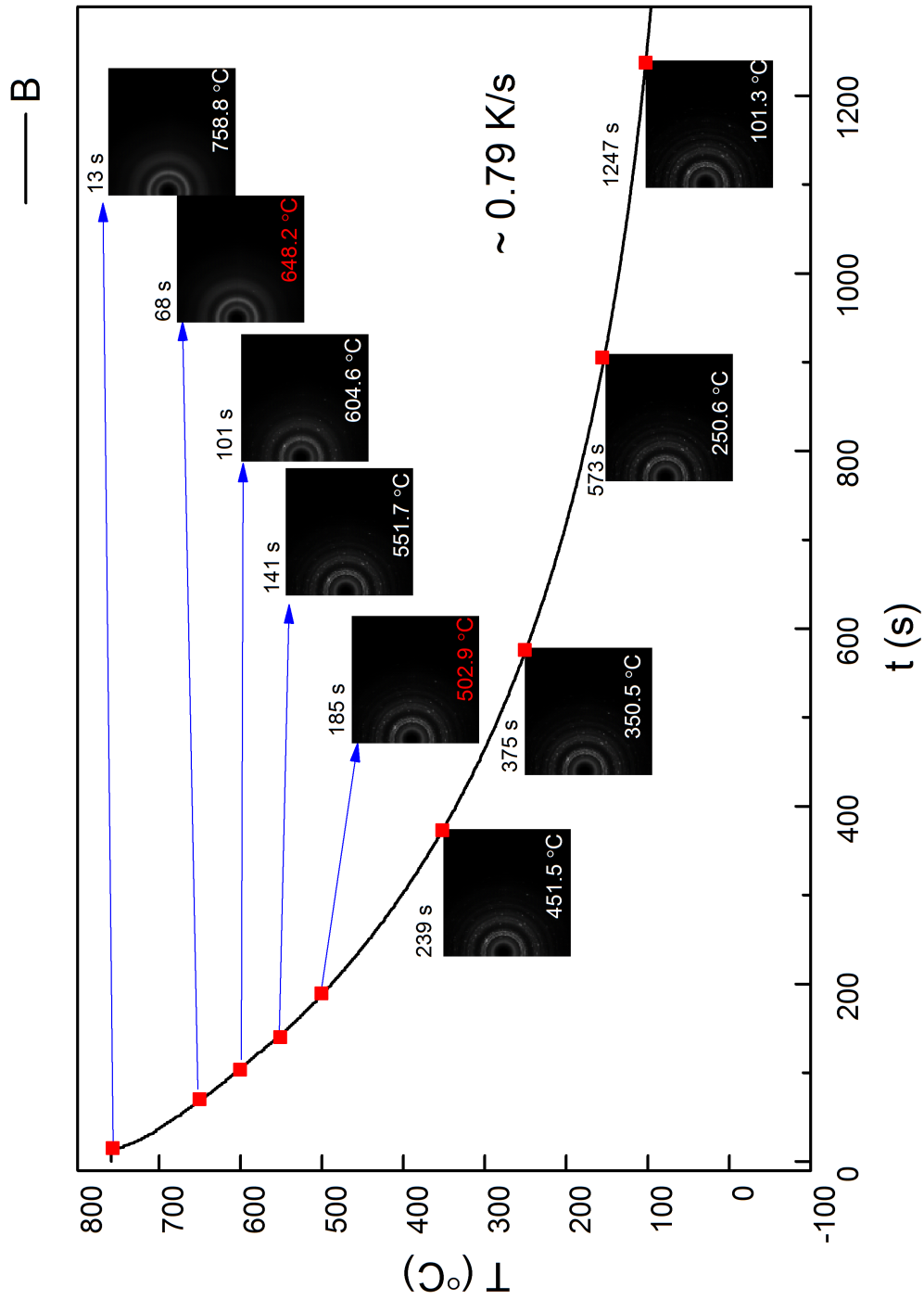
Fig. 4.33 The temperature profile of Vit1 during cooling using an average cooling rate of 0.79 K/s, and the 2D diffraction patterns acquired at the marked temperatures.
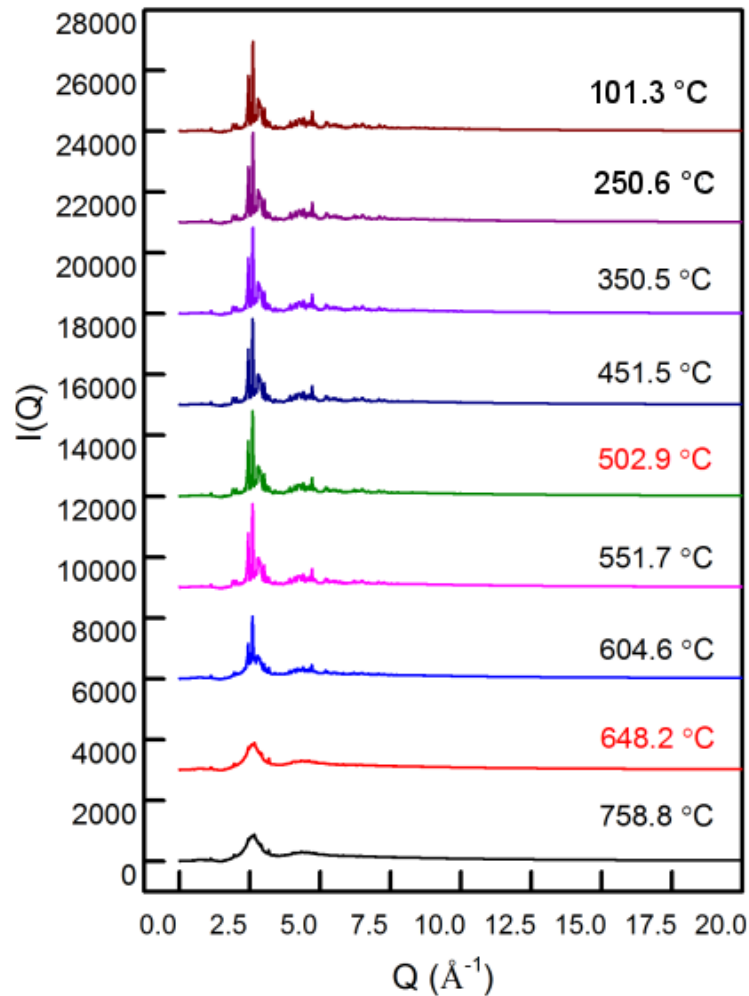
Fig. 4.34 The diffraction spectra acquired for Vit1 alloy at each critical temperature during cooling with an average cooling rate of 0.79 K/s. The curves are stacked with an equal spacing of 3,000 counts in y direction.

Fig. 4.34 shows the stack of I(Q) curves integrated from those patterns shown in Fig. 4.33. The crystalline phases were formed when the temperature decreased from 648.2 °C to 502.9 °C, which is clearly revealed by the changes of the diffraction spectra with temperature.

Fig. 4.35 shows a waterfall plot of diffraction spectra obtained at different cooling temperatures. The maxima of the diffraction peaks slowly increased when the temperature decreased from 648.2 °C to 502.9 °C, which is very similar to the previous cooling case. However the maxima of first peak is ~ 3000, which is much higher compared to the previous cooling case (~ 2300) at the temperature of ~ 101.0 °C.
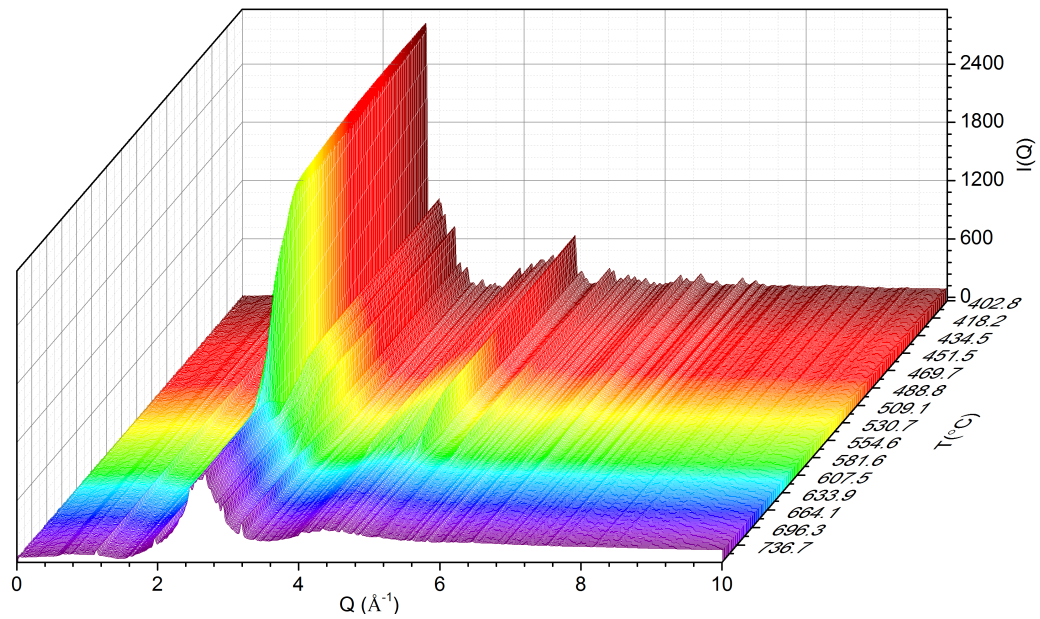
(a)
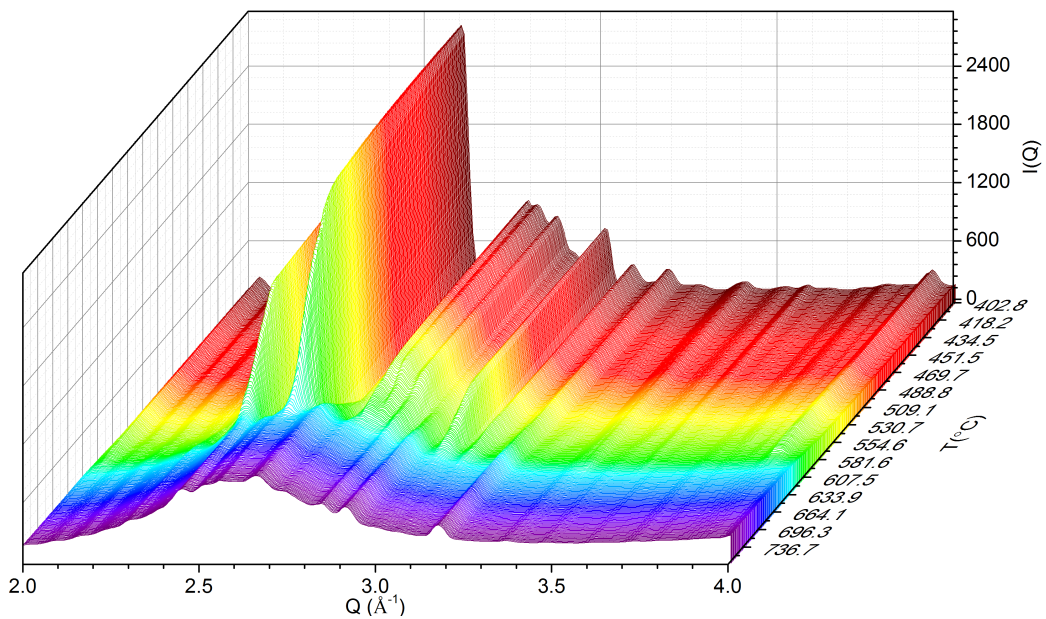
(b)

Fig. 4.35 The evolution of diffraction spectra of Vit1 as functions of temperature during the cooling process with an average cooling rate of 0.79 K/s. (a) the spectra in 0.0 to 10.0 Å^{-1}, (b) the spectra between 2.0 and 4.0 Å^{-1}.

Fig. 4.36 shows the corresponding G(r) at each temperature marked in Fig. 4.33. A dramatic increase of peak intensity can be found from 648. 2 °C to 551.7 °C in 73 s. Then
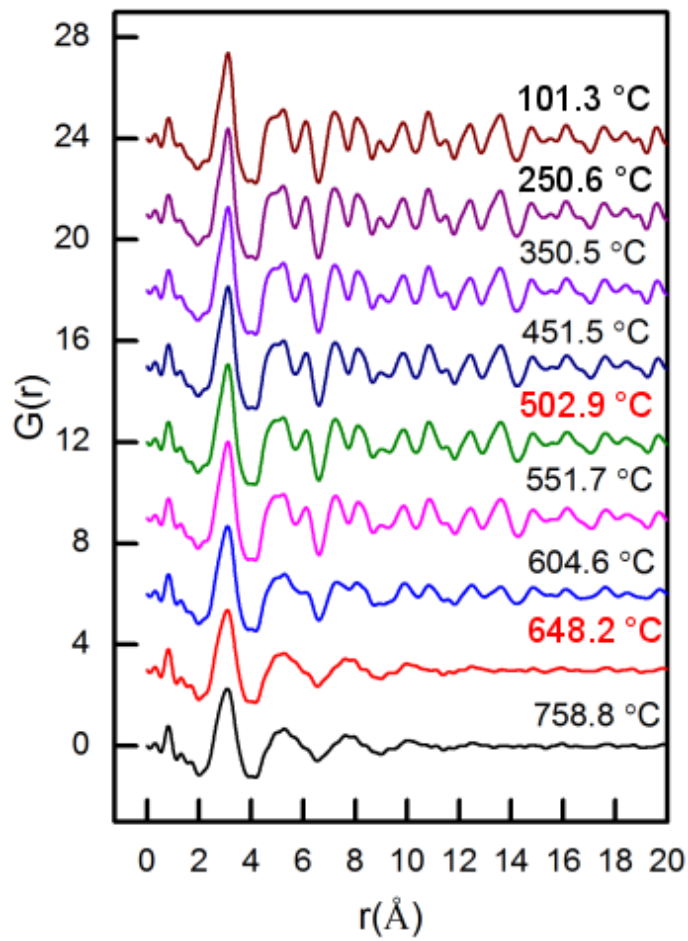
Fig. 4.36 The pair distribution functions acquired for Vit1 alloy at each critical temperature during cooling with an average cooling rate of 0.79 K/s. The curves are stacked with an equal spacing of 3.0 in y direction.

(a)
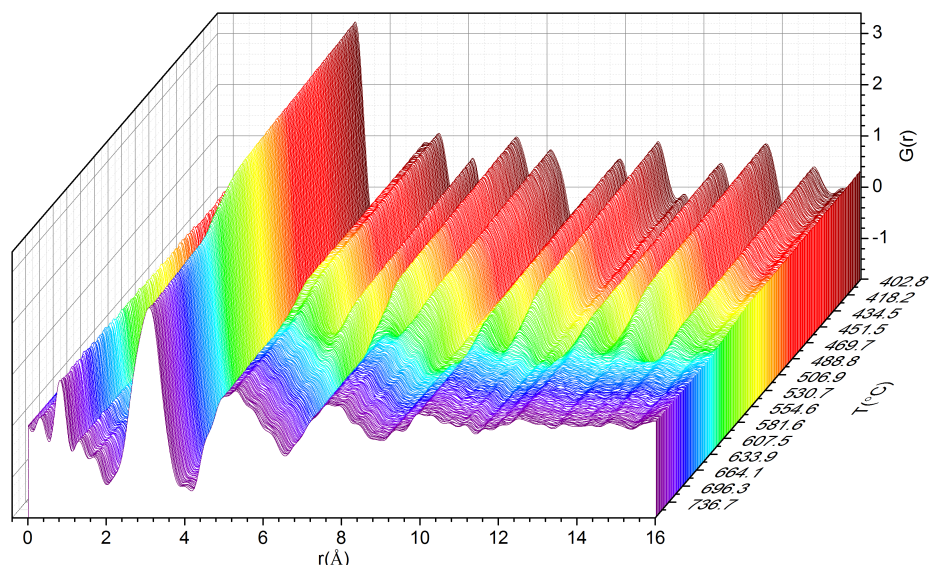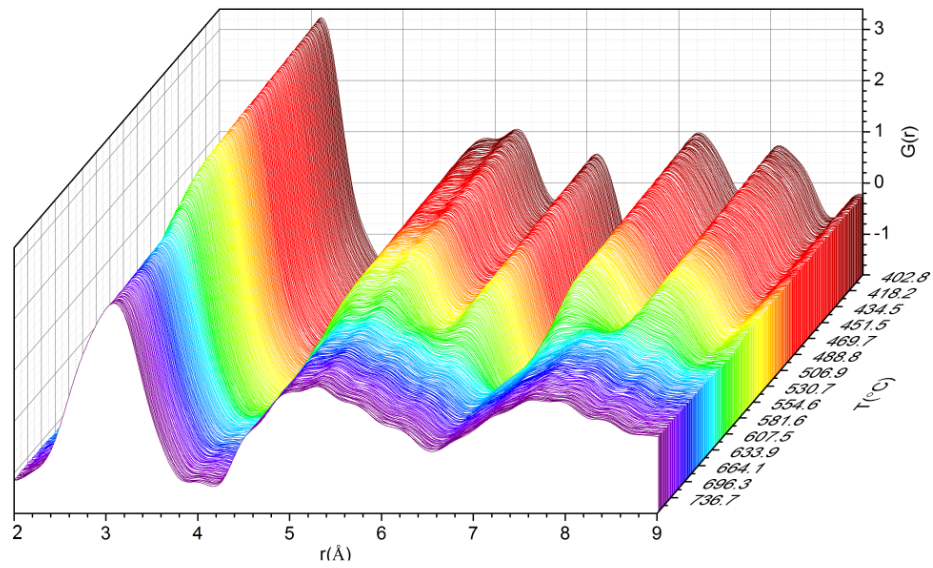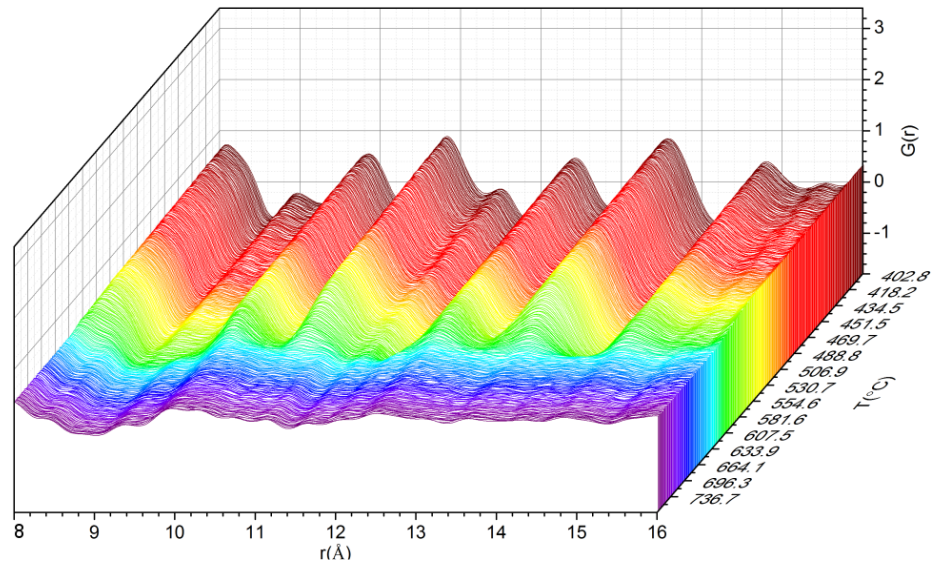
Fig. 4.37 The evolution of pair distribution functions of Vit1 as a function of temperature during the cooling process with an average cooling rate of 0.79 K/s. (a) the G(r) in 0 - 16.0 Å, (b) the G(r) between 2.0 and 9 Å, and (c) the G(r) between 8 and 16 Å.

it followed by a slow increase from 551.7 °C to 502.9 °C in 44 s. The dynamic evolution of G(r) with temperature is given by the waterfall plot in Fig. 4.37.

Fig. 4.38 shows the changes of peak maxima with temperature. The maxima increased slowly when the liquid cooled down from 758.8 °C to 648.2 °C. Then it increased rapidly

(a) 1st Shell

(b) 2nd Shell

(c) 3rd Shell

(d) 4th Shell
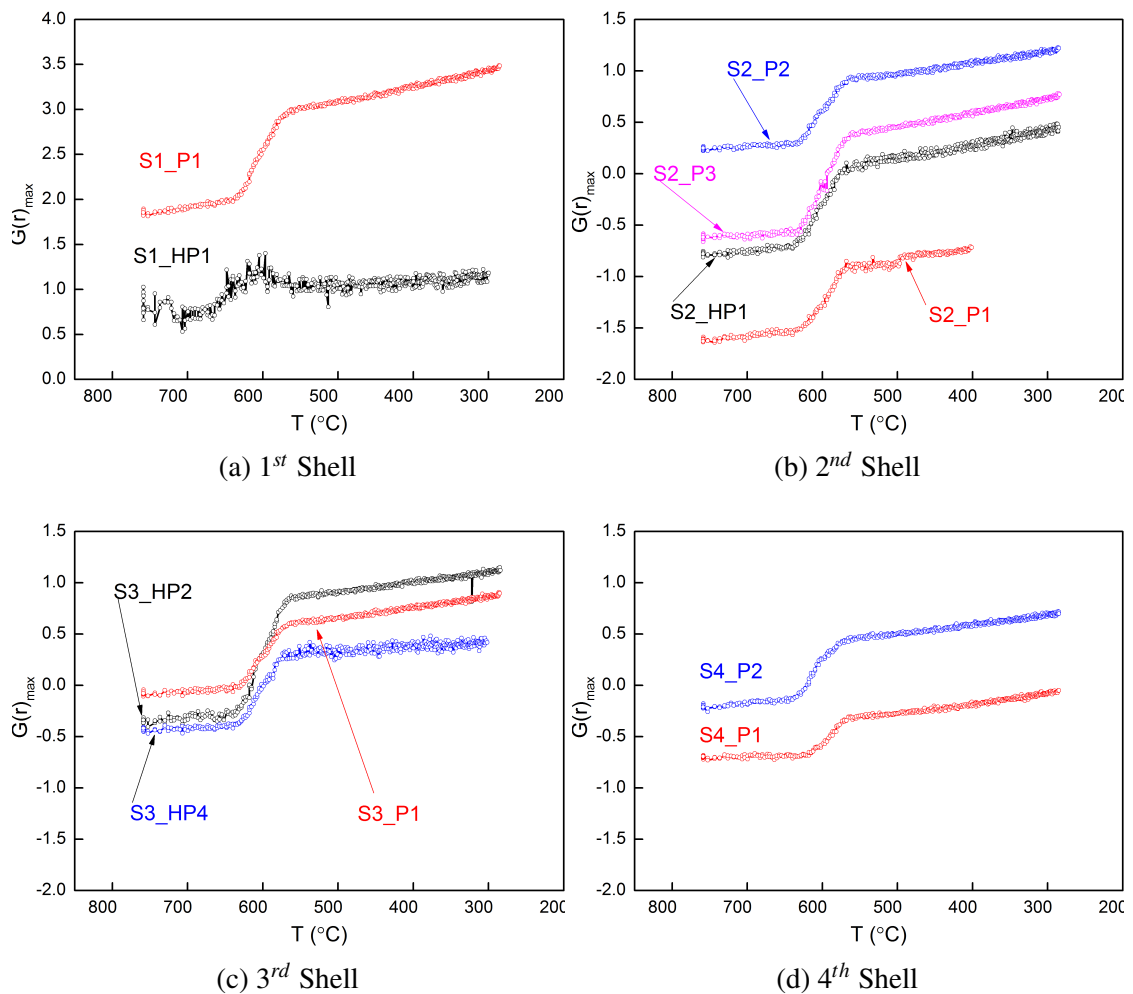
Fig. 4.38 The maxima of all peaks in the four atomic shells as functions of temperature for the case shown in Fig. 4.33.

during crystallisation when temperature further decreased from 648.2 °C to 502.9 °C in 117 s. In the rest of the cooling process, the peak maxima continued to increase.

Fig. 4.39 shows the shifts of all peaks in the four atomic shells with temperature. The peak position of S2_HP1 shifted to high r, while that of S2_P1 shifted to low r during the crystallisation. The peak position of S2_P2 and S2_P3 in the 2nd shell dramatically shifted to low r at 604.6 °C. Then they remained the same positions during the rest of cooling process. The peak position of S3_HP2 suddenly shifted to the high r at 604.6 °C, and then slowly shifted back to low r. The peak position of S3_P1 and S3_HP4 shifted close to each other when the temperature decreased from 648.2 °C to 551.7 °C. The same trend was observed from the peak shift of S4_P1 and S4_P2.
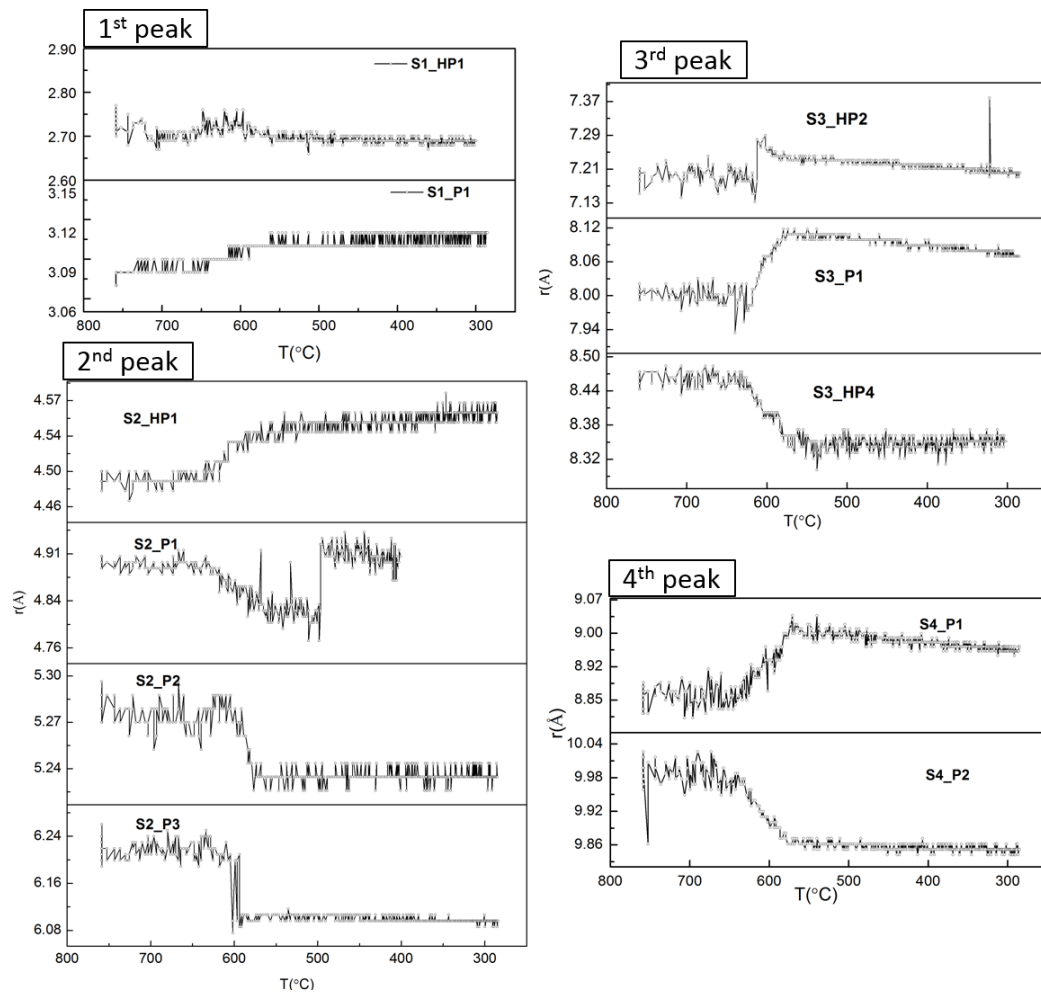
Fig. 4.39 Shifts of all peaks in the four atomic shells as functions of temperature for the case shown in Fig. 4.33.

4.2.2.4   PDFs for all cooling rates

Fig. 4.40a shows PDFs of Vit1 after solidification and measured at room temperature for all the average cooling rates studied in this research, and clearly it can be seen that, the structure formed at the average cooling rate from 0.79 K/s to 4.44 K/s is crystalline structure, while the structure formed at the rest of cooling rates is amorphous structure.

Fig. 4.40b shows the changes of peak intensity of the first PDF peak with different cooling rates. In general, as average cooling rate increases, the peak intensity is decreased. The peak intensity experiences a rapid decrease from 0.79 K/s to 4.44 /s as shown in Fig. 4.40b.
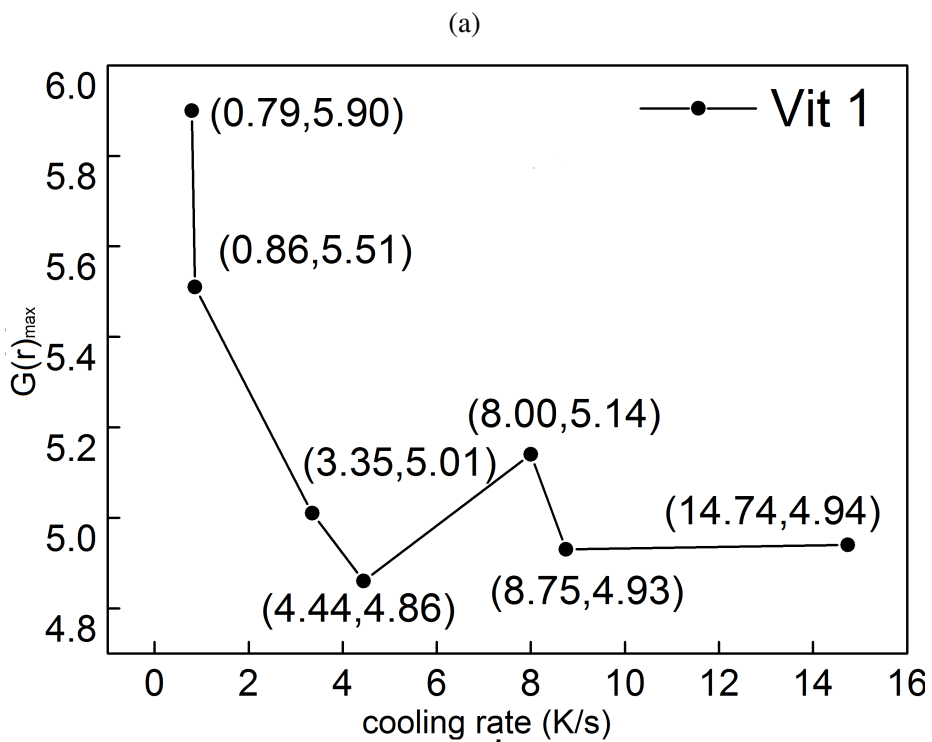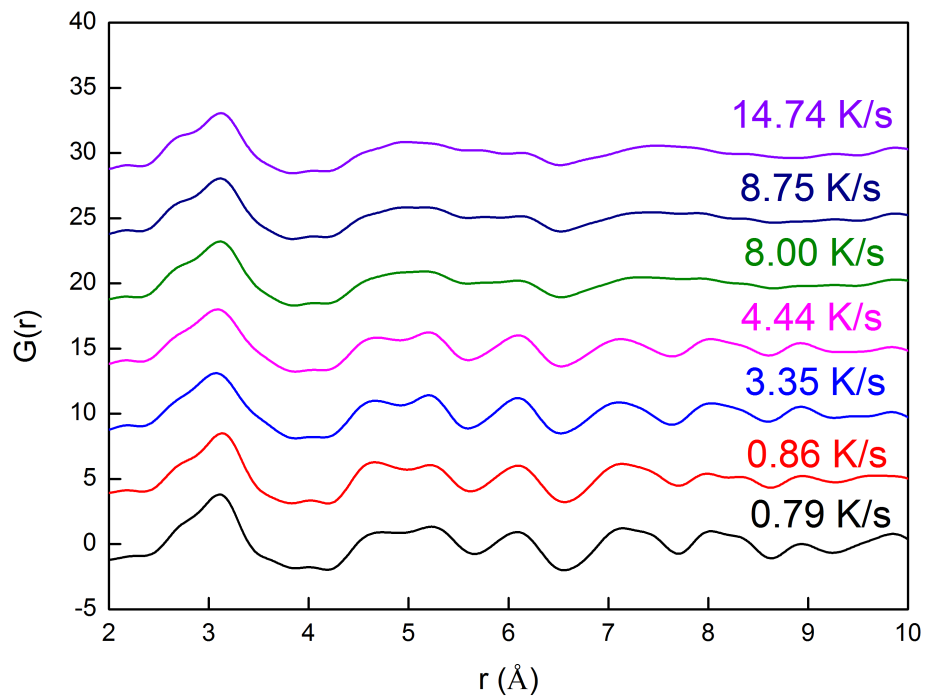
Fig. 4.40 (a) Pair distribution functions for Vit1 with all the average cooling rates studied, and (b) the changes of peak intensity of the first PDF peak with the average cooling rate.

4.3   Summary

In this chapter, the composition dependant structure changes, and temperature dependant structure evolution were presented. The composition dependant studies revealed that the structure order is very sensitive to alloy composition. As demonstrated by the PDF study of CuZr binary alloy, although a wide glass formation range for different concentration of Zr, the local structure changes with composition. The PDF study of NiTi alloy suggested that a small variation of composition leads to a dramatic change of structure.

For Vit1 alloy, the evolution of structure is very sensitive to the history of processing. Clearly different structure was formed at different thermal conditions, *i.e*, heating rate of 1.5 K/s, and different cooling rates of 14.7 K/s, 3.35 K/s and 0.79 K/s. The crystallisation temperature changes with the cooling rates. Different critical temperatures for phase transition, and atomic structure evolution with temperature which were revealed by the evolution of scattering spectra in Fourier space and pair distribution functions in real space. Using a real space refinement method, the reconfiguration of several dominant partial atomic pairs, such as Zr-Zr, Zr-Cu, Cu-Cu, were found to be responsible for structure evolution.

Chapter 5

Experimental result 2 – the structure of bulk metallic glass matrix composites

In this Chapter, a ZrTi based bulk metallic glass matrix composite, DH3 originally developed by Hofmann, et al [62] was chosen to study and characterise (1) the atomic structure across the amorphous-crystalline interface, (2) the 3D morphologies of the crystalline dendrites, and (3) the nano and microstructure evolution when the composite is subject to thermal shock, *i.e*, fast Joule heating induced by a high density electric current.

5.1   As-cast microstructure and amorphous-crystalline interface

Fig. 5.1 shows a typical as-cast microstructure. The dendrite-shaped phase is crystalline β-Zr dendrite, and the rest is amorphous matrix [62]. The 2D images show that β-Zr dendrites are a few to a few tens of μm in length and uniformly distributed within amorphous matrix. The true 3D morphology of β-Zr dendrites is described in section 5.2. Between amorphous matrix and β-Zr dendrites, there exists a distinct interface as highlighted in Fig. 5.1b, across which a structure transition from amorphous to crystalline state occurs.

(a)

(b)
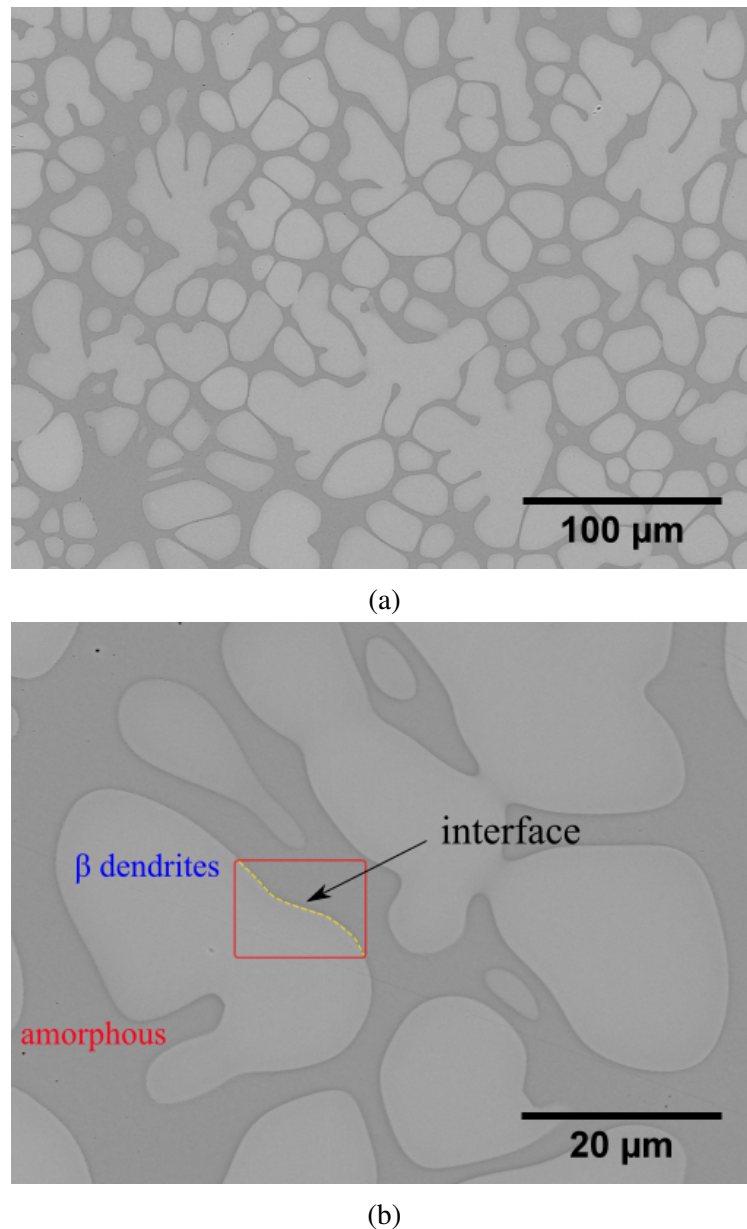
Fig. 5.1 Typical SEM images of as-cast microstructure of DH3 alloy at (a) low and (b) high magnification.

Fig. 5.2 presents the elemental distribution across the amorphous-crystalline interface along the red line in the inserted TEM image. Line scans clearly show the concentrations of Zr, Ti and Nb are lower, but that of Cu is higher in amorphous region. Hence, the concentrations of Zr, Ti and Nb are higher in β-Zr dendrites. Be element can not be detected by EDX. The average width of amorphous-crystalline interface is proximately 50-100 *nm*, as clearly seen by the composition profiles in Fig. 5.2.
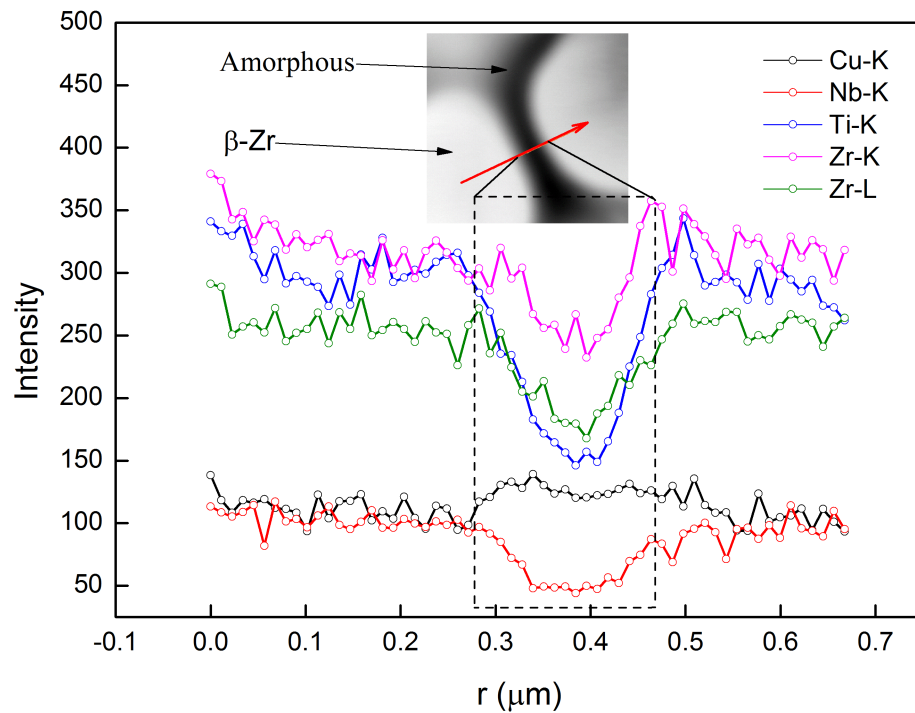
Fig. 5.2 Elemental line scans across amorphous-crystalline interface using EDX.

Fig. 5.3 shows four typical HRTEM images for the crystals, fully amorphous matrix, nanocrystals, and the transition region within the interface, where, transition of atomic structure from randomly arranged patterns to more regularly-arranged patterns is clearly demonstrated Fig. 5.3d.

Two conventional reciprocal (Fourier) space methods, FFT, ACT were used to analyse and characterise the atomic structure transition in the interface region. FFT diffraction patterns can be used to characterise the structure transition in a relatively long range, *i.e*, a few nano metres, while ACF is able to provide more structure information in medium range order (5 - 10 Å) [4].

In addition, two real space methods are used to characterise the atomic structure transition in a short and medium atomic range based on the HRTEM images. Firstly, the HRTEM was processed to extract the "atoms" like particles and their coordinates. Secondly, VT and 2D PDF methods were used to assess the local structural ordering across the amorphous-crystalline interface. The details of each method are described in section. 3.5.2.2.
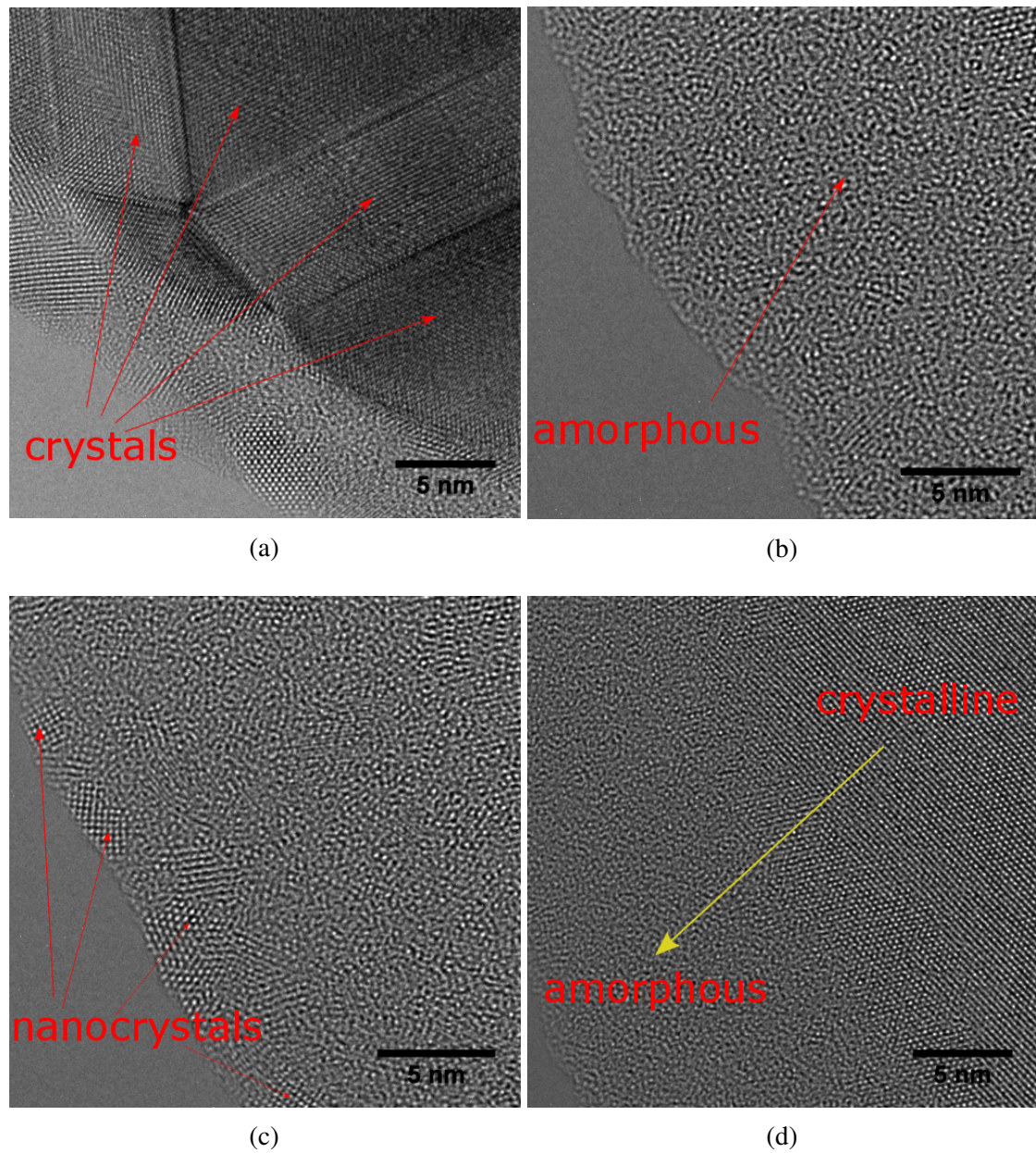
Fig. 5.3 Four typical HRTEM images of (a) crystals, (b) amorphous matrix, and (c), nanocrystals near the interface, (d) a transition from amorphous matrix to crystalline phase.

5.1.1 Local order characterisation using FFT and ACF in Fourier space

Fig. 5.4a shows a HRTEM micrograph that contains structure transition, and the interface is marked by a yellow dotted curve. The micrograph is divided into 16 templates, each with a
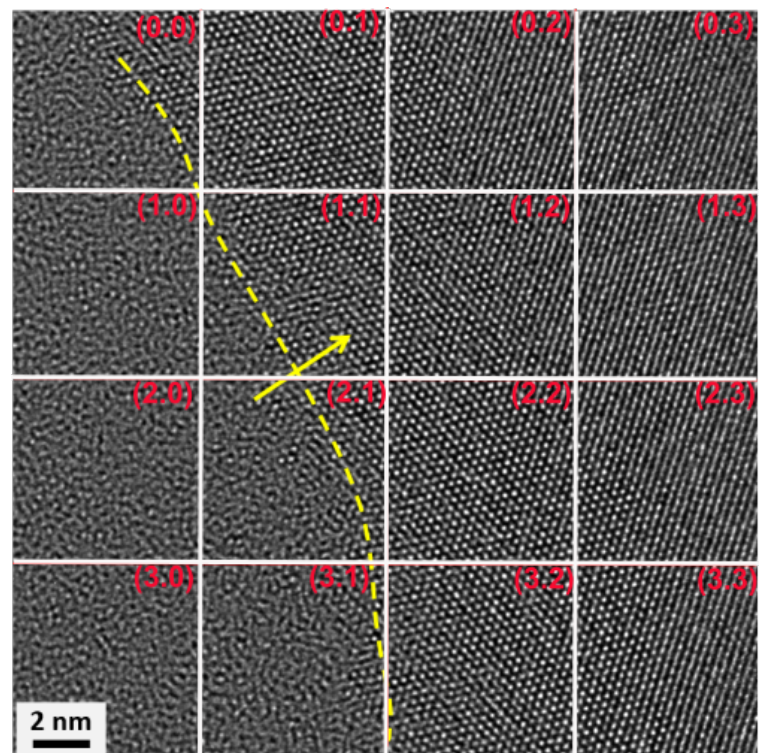
(a)
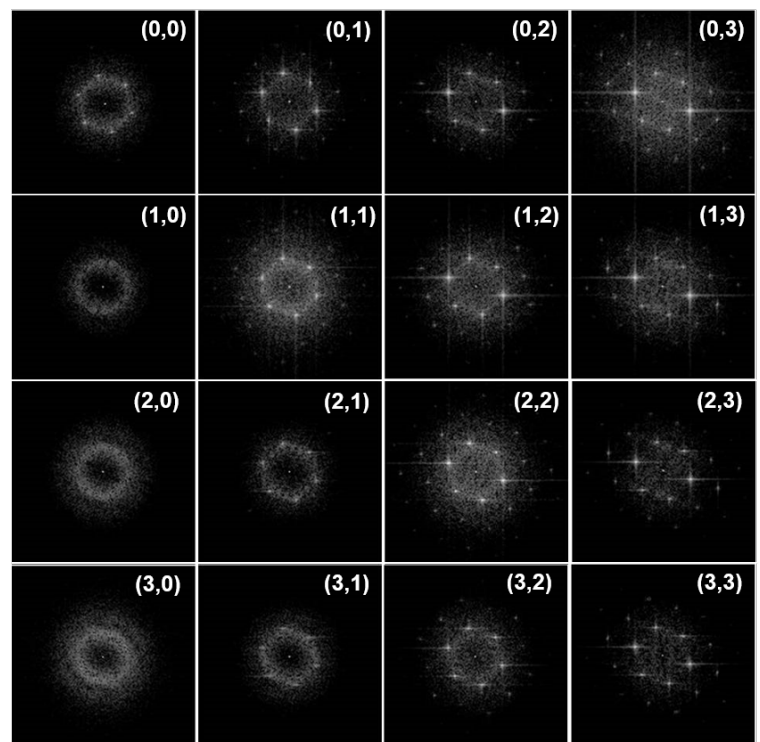
(b)

Fig. 5.4 (a) A TEM image taken in the amorphous-crystalline interface region, and the defined templates for FFT operation with index. (b) The corresponding patterns for each template after FFT operation.

size of 6.4×6.4 nm and with an X-Y index assigned as shown in Fig. 5.4a. Each template is Fourier transformed to obtain its diffraction pattern as shown in Fig. 5.4b.

For example, template (0, 3) has several bright spots, and is typical diffraction pattern for ordered crystalline structure. While, template (3, 0) is characterised by a faint and diffuse halo, indicating a fully amorphous structure.

Fig.5.4b shows the FFT patterns for all templates. Clearly, (1, 0), (2, 0) and (3, 0) are fully amorphous with the typical diffuse halo. While, (0, 1), (0, 2), (0, 3), (1, 2), (1, 3), (2, 2), (2, 3), (3, 2), (3, 3) have bright spots, and are typical diffraction pattern of crystalline phases. The rests labelled as (0, 0), (1, 1), (2, 1), (3, 1) are located in the amorphous-crystalline interface region, which are characterised by a combination of bright diffraction spots and faint diffuse halo.

Clear, the change of the features of the FFT pattern for each template reveals the transition from amorphous to crystalline state. For example, in second column from (0, 1) to (3, 1) in Fig. 5.4b, the bright diffraction spots gradually fade out and diffusive halo became more obvious. This gradual change on the FFT image reflects the atomic structure change shown in Fig. 5.4a.

MRO is also an important characteristic structure of bulk metallic glass [68, 4], which significantly affects the mechanical properties [191]. ACF is a commonly used method to characterise the MRO in amorphous phases [133, 191]. The size of ACF template is often chosen to be very close to the dimension of MRO, *i.e*, 5–20Å. The ACF template presented in Fig. 5.5 is obtained by further dividing the template used in the FFT analysis into 3×3 sub-templates, each of which has the size of 2.13×2.13 nm. These ACF templates are re-indexed as (x,y) in the range of $(0 \sim 12, 0 \sim 12)$.

As shown in Fig. 5.5a, for the crystalline phase, the ACF templates exhibit periodic ordered patterns, while for amorphous phase, they have disordered aperiodic patterns. No apparent MRO transition from crystalline to amorphous state within the interface region is observed.

The 3D surface plot of ACF patterns in Fig. 5.5b provides more information about the distribution of MRO within the interface. The altitude of the 3D surface reflects the grayscale for each pixel in 2D ACF patterns.
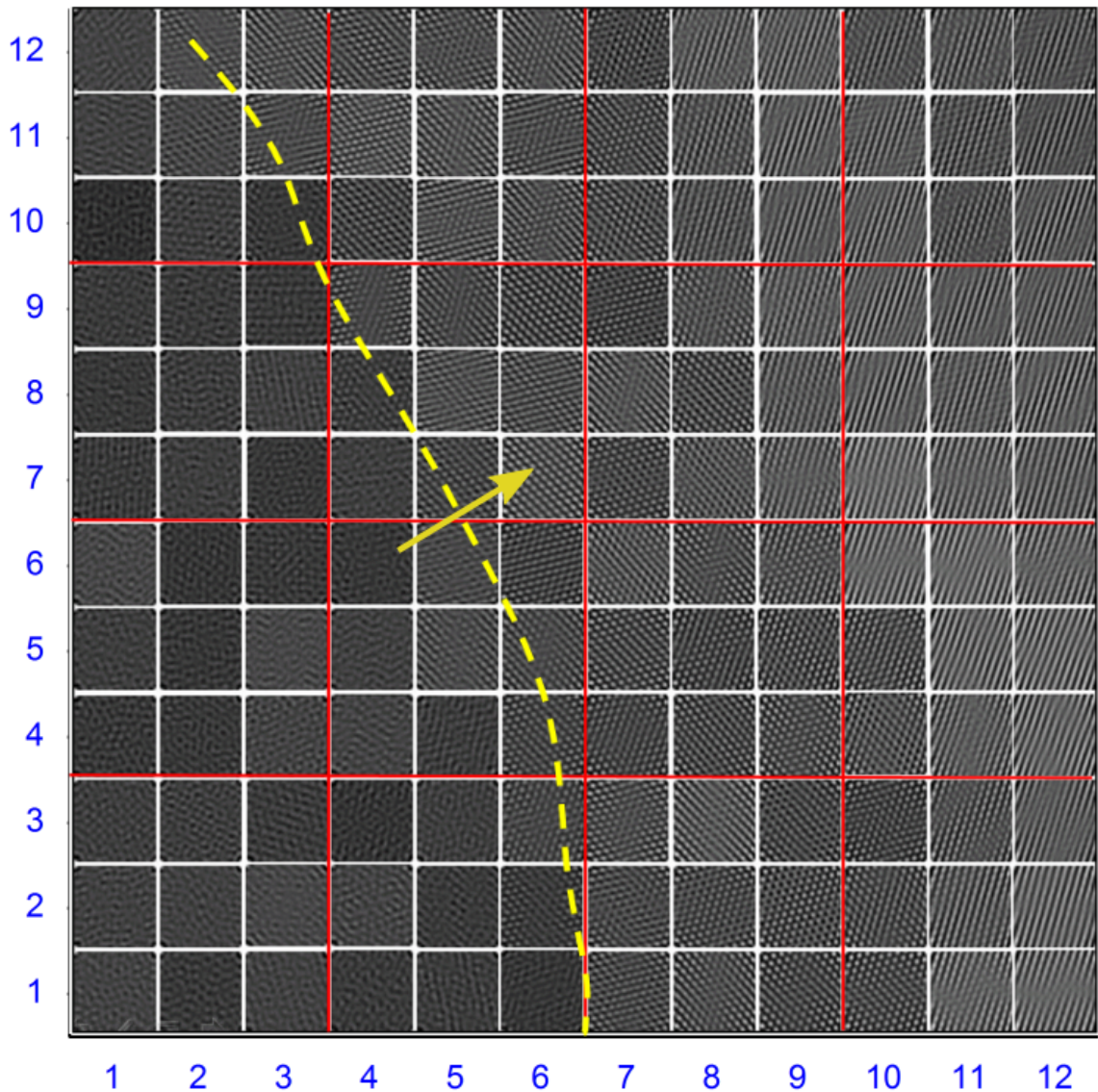
(a)

In Fig. 5.5b, the ACF patterns with low grayscale (represented in z-axis) often reveal more disordered structure, while the ones with high grayscale intensity often reveals more ordered structure. Within the crystalline region, all the ACFs display regular periodic patterns with similar grayscale intensity, which altogether form a flat surface. However,
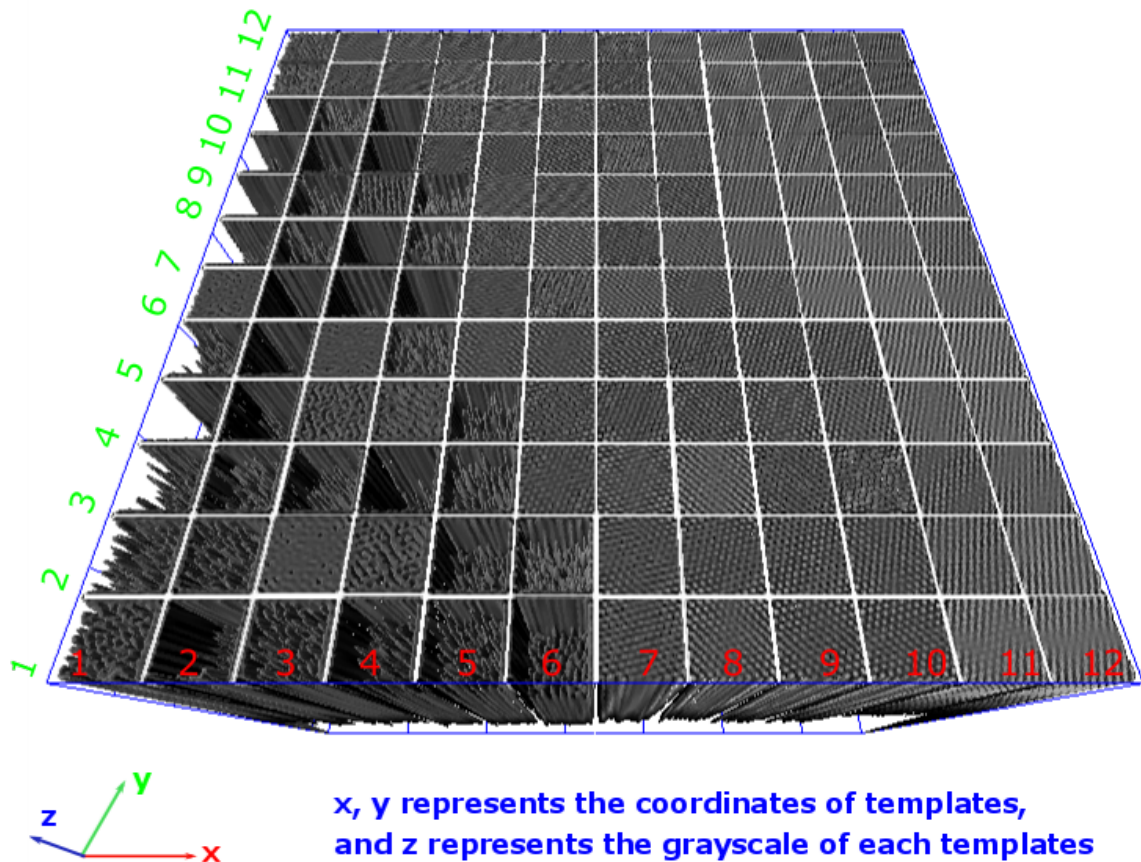
(b)

Fig. 5.5 The 2D and 3D surface plot of the Autocorrelation function templates calculated based on HRTEM image presented in Fig. 5.4.

for the amorphous region, the surface plot of ACF patterns are distributed with rising and falling, and the altitude of each pattern is different from each other.

In general, Fig. 5.5b shows that the high level of grayscale can represent a high level of MRO, and vice versa. The ACF templates such as (4,2) (5,2) (6,2), show different level of grayscale, which reveal these three local regions have different level of medium range order, although they are identified as the amorphous structure using FFT.

5.1.2 PDF "atoms" and local ordering in real space

The FFT and ACF are useful for characterising the local ordering in the medium to long r range, while the image processing based real space method can provide more structure information for the local region.

Using the image processing method described previously in section 3.5.2.2, the original HRTEM image (Fig. 5.6a) was transformed into the image as shown in Fig. 5.6b. This processing transforms the atom-like dots (Fig. 5.6a) into indexable particles (Fig. 5.6b). Based on these indexable particles, then VT and 2D pair distribution function were used to analyse the atomic structure.

Although it is intuitive to consider these "atoms" like particles as atoms, in reality, they are formed as the cumulative effect of all the atoms been imaged along the electron beam path across the sample thickness of $\sim$ 30-40 nm. However, the local order shown in the original HRTEM is not altered by the grayscale manipulation during image processing because it can be validated by the fact that the ACF of the "atoms" like particles in the processed image are identical to that from the original HRTEM. Statistically, the local order of the processed image should be similar to the original image, in other words, the "atoms" like particles configuration obtained from processed micrograph can be used to reveal the nature of the local ordering.

Fig. 5.7a presents some nanocrystals that are formed within the amorphous matrix, and each is isolated by amorphous matrix. The ordered to disordered structure transition from nanocrystalline-amorphous-nanocrystalline in real space can be revealed by Voronoi cell analysis.

Fig. 5.7b presents Voronoi cells calculated based on all the centroids of "atoms" like particles from Fig. 5.7a. In Voronoi tessellation analysis, a 2D lattice often gives an irregular honeycomb tessellation with equal hexagons. As shown in Fig. 5.7b, the body centred cubic β-Zr crystalline phase has a regular honeycomb cell with equal hexagons, which is normally
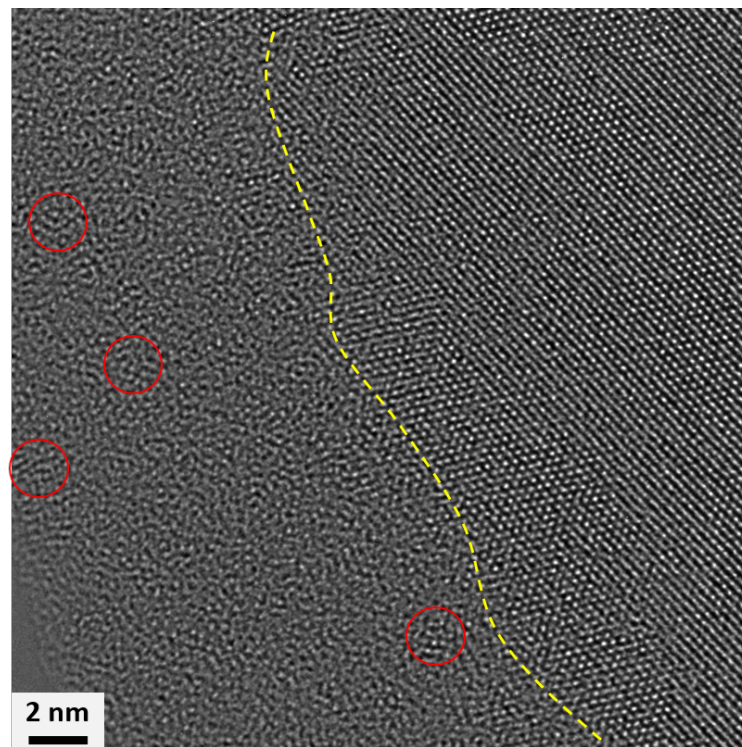
(a)
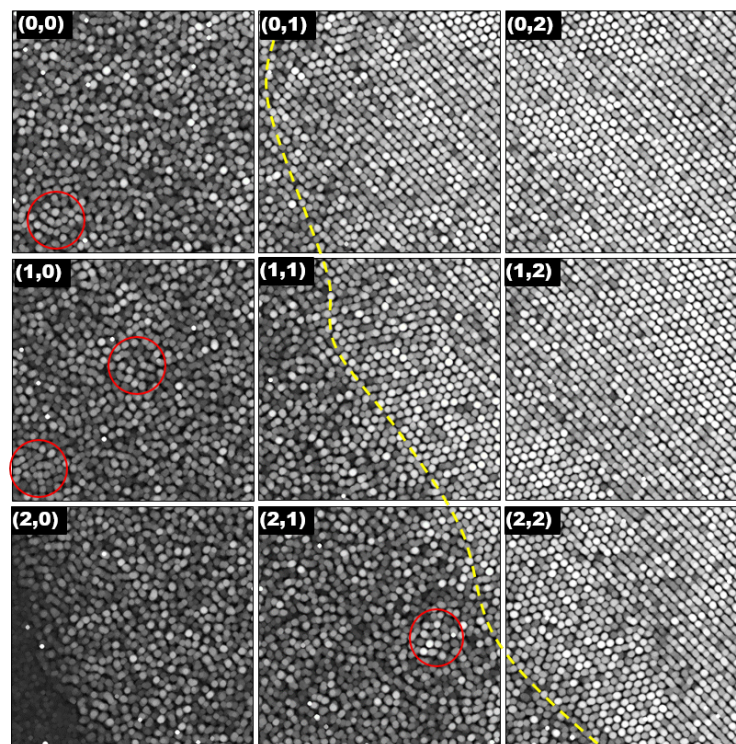
(b)

Fig. 5.6 (a) The original HRTEM image showing order to disorder transition in the interface region. (b) "Atoms" like particles reproduced from (a) through image processing, and the image processing method is detailed in section 3.5.2.2.
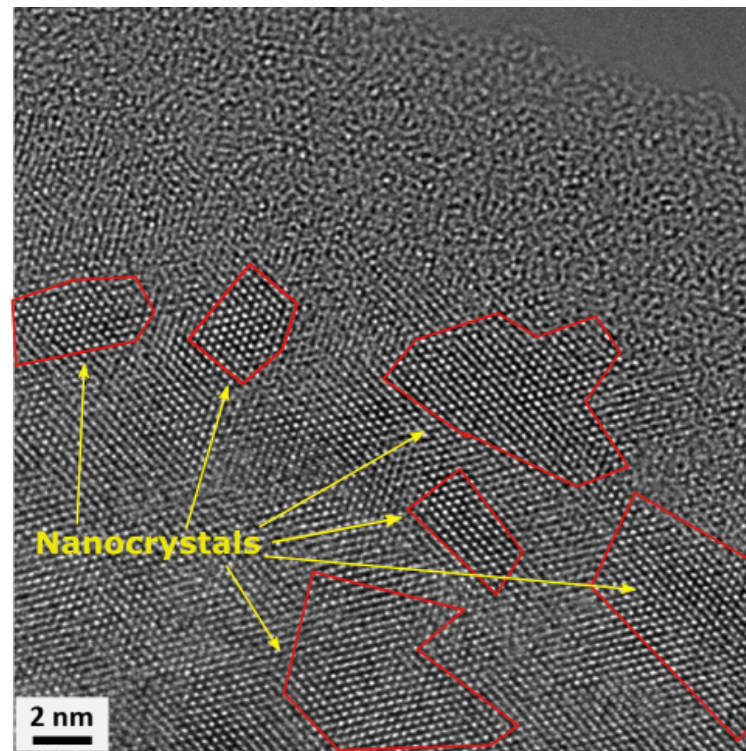
(a)
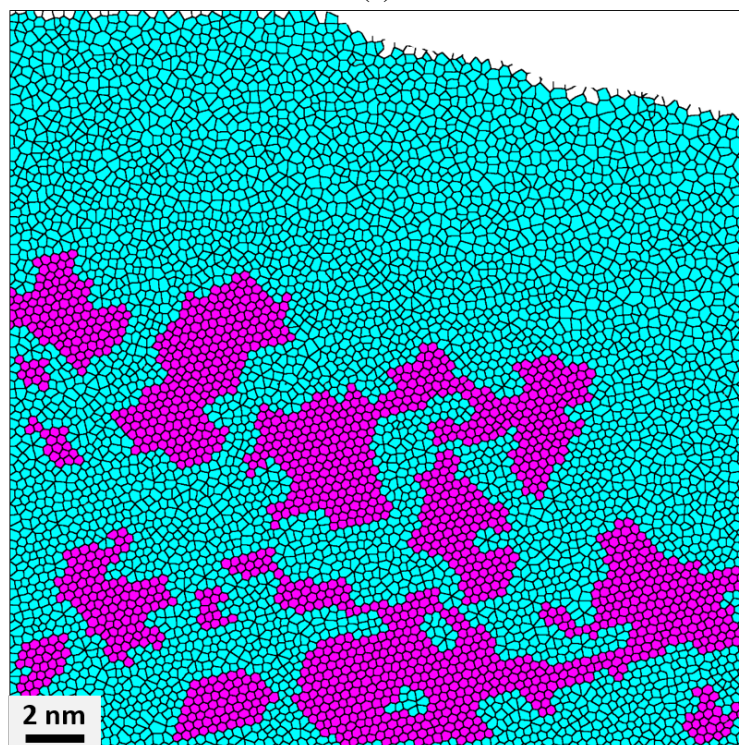
(b)

Fig. 5.7 (a) The original HRTEM image showing nanocrystals separated by amorphous matrix. (b) the corresponding Voronoi cells calculated based on (a).
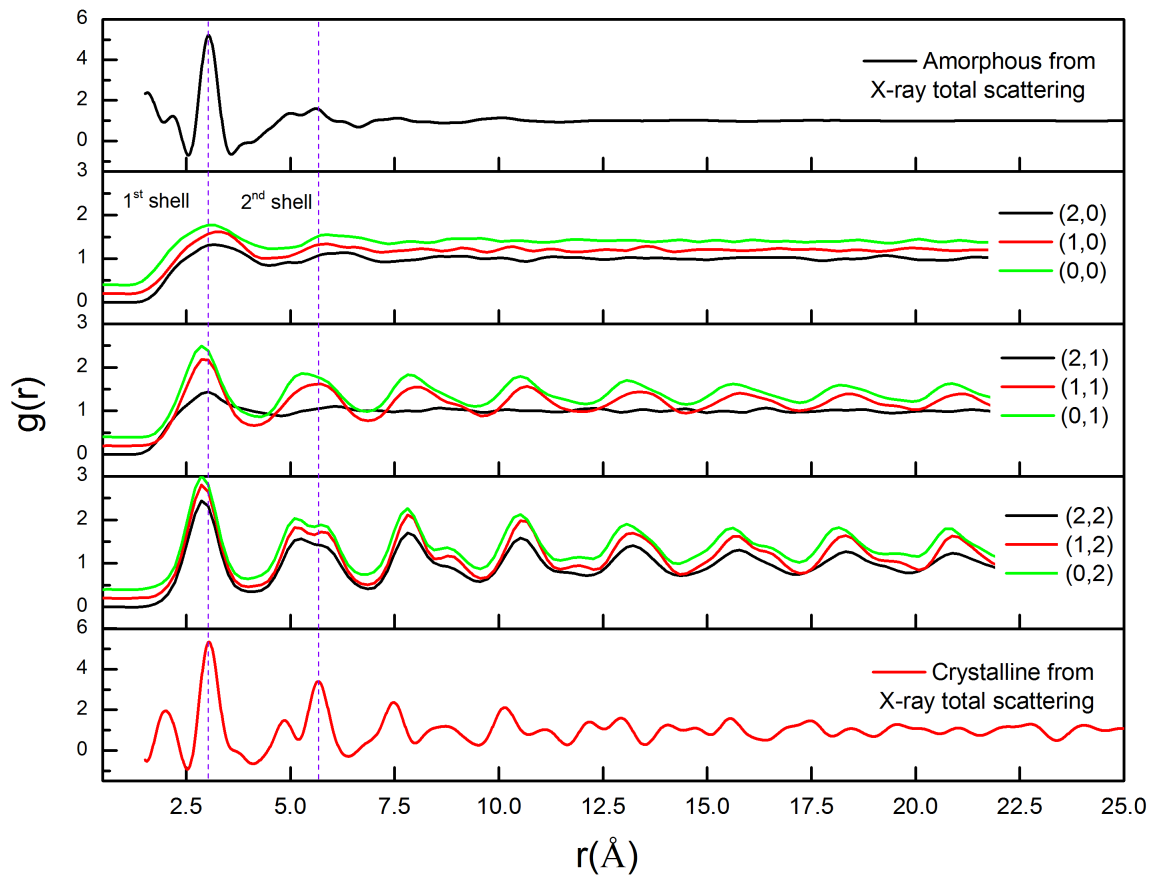
Fig. 5.8 The pair distribution function of each template shown in Fig. 5.6b calculated from the processed HRTEM. The top row is the PDF of amorphous matrix from X-ray scattering; The second is the 2D PDF for the templates (0, 0), (0, 1), (0, 2) from the processed HRTEM; The third is for the templates (1, 0), (1, 1), (1, 2); The fourth is for the templates (2, 0), (2, 1), (2, 2);The bottom row is for the PDF of crystalline phases from X-ray scattering.

given by 2D triangular lattice. The Voronoi cells of β-Zr crystals tend to be irregular near amorphous-crystalline phase interface.

In Fig. 5.7b, from bottom to top, the Voronoi cells gets more disordered and irregular due to the structure transition, however the decreasing density of the Voronoi cells is caused by less particle centroids extracted from the processed image, due to the grayscale variation in amorphous region.

5.1.3 Pair distribution function from HRTEM and X-ray total scattering

Pair distribution function is often used to characterise the local structure in atomic scale experimentally using X-ray or neutron scattering as presented in Chapter 4. Here, a 2D HRTEM image based PDF method is used to characterise the local order within the interface region. All the centroids of the "atoms" like particles in Fig. 5.6b are extracted , then these centroids are used to calculate the 2D PDF using the method described in section 3.5.2.2.

It is necessary to compare and validate the pair distribution function $g(r)$ obtained from the HRTEM image with the reduced pair distribution function $G(r)$ from synchrotron X-ray total scattering. $G(r)$ can be theoretically converted to $g(r)$ through the inverse relation of $g(r) = G(r)/4\pi\rho_0 r + 1$ with a known number density, which can be evaluated from the slope of straight line of $G(r)$ as $r \to 1$ [21]. However, practically it is difficult to obtain the exact value of ρ_0, and also it is not necessary to get the exact value of $g(r)$ for comparison. Hence, it is reasonable to find a coefficient $C \propto 4\pi\rho_0$ to rescale the $G(r)$ to the similar intensity with $g(r)$. The pair distribution function $g(r)$ calculated from the processed HRTEM micrograph is quite noisy due to the limited centroids of particles for the PDF calculation. Therefore before comparison, the FFT filter is used to filter out the high-frequency noise and smooth the original PDF spectra.

As revealed in Fig. 5.8, the pair distribution function, $g(r)$ of templates (0, 0), (0, 1), (0, 2) in Fig. 5.6b, is characterised by two dominant peaks at 2.7 Å and 5.1 Å, and the rest of $g(r)$ in long r range (7.5–25.0 Å) tends to be 1, which is very similar to the g(r) obtained using x-ray total scattering for amorphous phase. The resulting g(r) is consistent with the disordered "atoms" like particle configuration of the processed HRTEM micrograph within the templates (0, 0), (0, 1), (0, 2) in Fig. 5.6b. For $g(r)$ of crystalline phase, in addition to the two dominant peaks having the similar peak position as amorphous phase, there are many minor peaks existing in the medium to long r range. The peak splits due to separation

of two neighbouring atomic shells, are apparent in the $g(r)$ for templates (2, 0), (2, 1), (2, 2) in Fig. 5.6b, which is also validated against to the $g(r)$ obtained using X-ray total scattering.

As shown in Fig. 5.8, a transition from the amorphous to crystalline phase is revealed through $g(r)$ from templates (2, 1), (1, 1), (0, 1) within the phase interface marked in Fig. 5.6b, in which more medium range peaks emerge and oscillate around unity in templates (1, 1), (0, 1), while only two broad dominant peaks exist up to 7 Å in template (2, 1). The peak intensity of $g(r)$ in template (0, 1) is relatively higher than that for the template (1, 1), which implies an increase of local structural contribution from crystalline phase to total $g(r)$. For the $g(r)$ of crystalline phase in the templates (0, 2), (1, 2), (2, 2), there are apparent peak splits in the second shell comparing to the amorphous phase.

5.2 Structure change of bulk metallic glass matrix composite under thermal shock

The morphology, size, volume fraction and distribution of the dendrites are key factors that control the mechanical properties of the bulk metallic glass matrix composite [62]. In addition to the conventional 2D characterisation, 3D morphologies revealed by tomography can provide more rich information about the true structure. Also as an extreme case of heating process, thermal shock process significantly affects the behaviour of structure transition and thermal stability of the BMGMCs.

In this section, a multiscale structure characterisation of as-cast and thermally shocked DH3 alloy is presented, including 2D and 3D morphologies of as-cast and thermally shocked DH3 revealed by SEM, X-ray microtomography, FIB-SEM nanotomography; phase identification and volume fraction by neutron diffraction; nucleation and growth of the newly formed crystalline phases reveal by SEM.

5.2.1 2D characterisation of microstructure changes

Fig. 5.9a shows a typical backscatter scanning electron micrograph for the as-cast sample. Dendrites (light regions with composition of $Zr_{43.2}Ti_{41.1}Nb_{14.3}Cu_{1.4}$, often called β-Zr) are uniformly distributed in the amorphous matrix ($Zr_{32.1}Ti_{18.8}Nb_{3.3}Cu_{9.8}Be_{36.0}$ [62]). For the sample thermally shocked to 650 °C, two more phases (light and dark) are visible in Fig. 5.9 b,c.
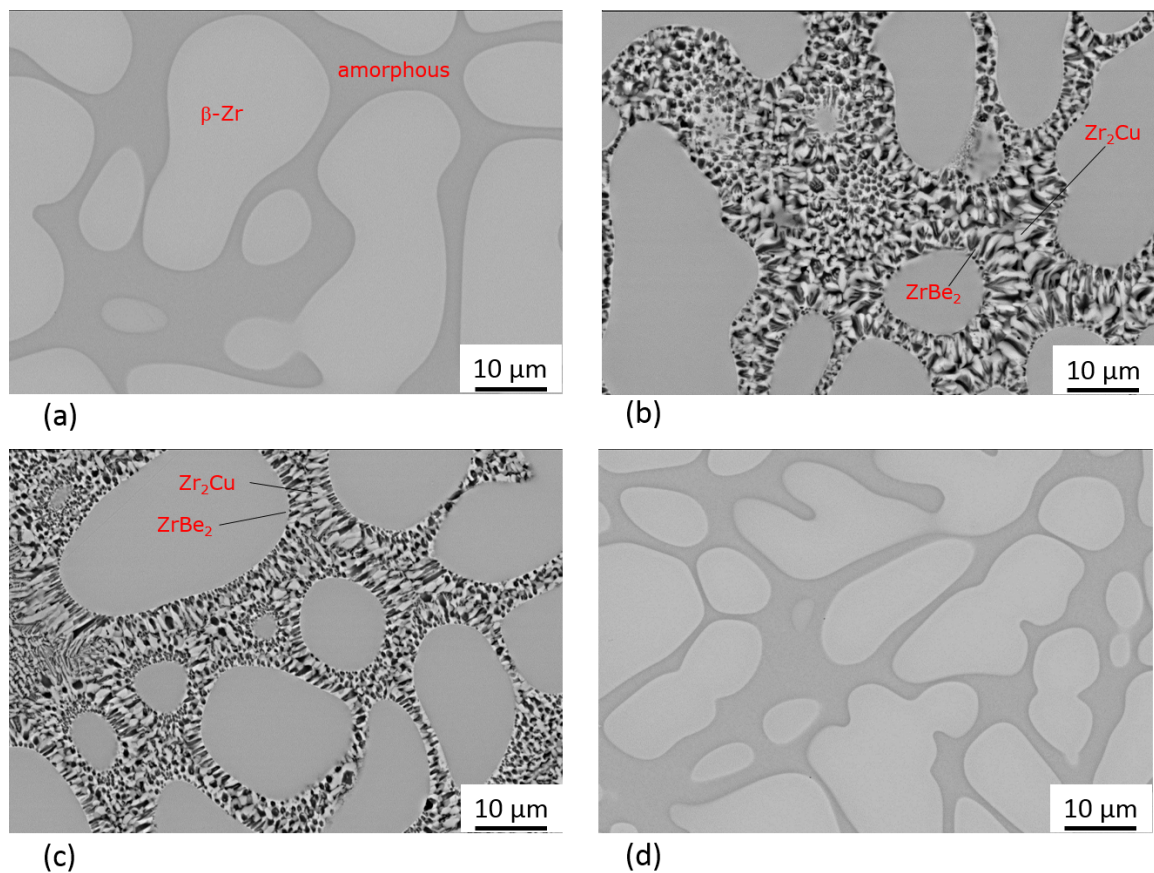
Fig. 5.9 Typical SEM for (a) the as-cast sample; and samples thermally shocked to (b) 650 °C (550 °C preset), to (c) 650 °C (600 °C preset) and (d) to the point of melting (700 °C preset).

5.2.2 Phase characterisation using neutron diffraction

Fig. 5.10 shows neutron diffraction patterns for the as-cast region and 650 °C thermally-shocked region of rod bar. For the as-cast region, the dominant β-Zr phase (magenta)

was found within the amorphous matrix (green) together with a small trace of $ZrBe_2$ and Zr_2Cu phases. The $ZrBe_2$ and Zr_2Cu signals may arise from diffraction of the large neutron beam (15×15mm) from the thermally shocked region, because neither of these phases was observed in the SEM images of the as-cast sample. For the 650 °C thermally-shocked sample, the aforementioned three crystalline phases were also observed.
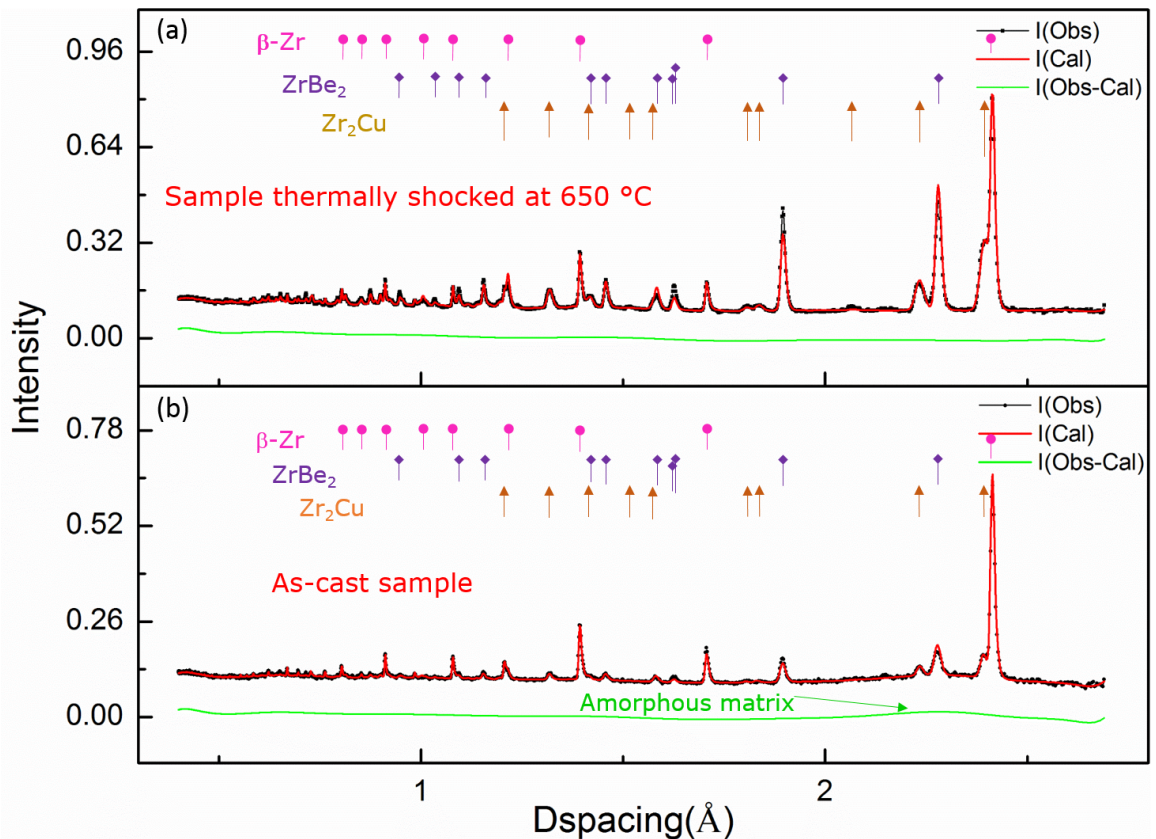
Fig. 5.10 Neutron diffraction spectra for (a) the sample thermally-shocked to 650 °C, showing profile fits for the β-Zr, $ZrBe_2$, and Zr_2Cu phases, and (b) the as-cast sample with fits for the β-Zr, amorphous matrix, $ZrBe_2$ and Zr_2Cu phases.

Volume fractions, calculated from the fitted spectra, are summarised in Fig. 5.15. Much higher volume fractions of the Zr_2Cu, and $ZrBe_2$ are present in the thermally-shocked samples. The crystallisation of DH3 is different from the nanocrystallisation behaviour of Vit1 [58] induced by pulsed electric current reported by Yao [197], which followed the sequence of amorphous $\rightarrow$ amorphous + icosahedral phase$\rightarrow Be_2Zr + Zr_2Cu + Ni_7Zr_2 +$ FCC structure phase + others$\rightarrow Zr_2Cu + Ni_7Zr_2 +$face-centred cubic (FCC) structure phase

+ others. $ZrBe_2$ and Zr_2Cu appeared to grow together into the amorphous matrix. For the as-cast sample, it was not possible to calculate the volume fraction for the amorphous matrix from the diffraction data since amorphous material cannot be modelled crystallographically without employing auxiliary methods, such as introducing the internal or external standard to compare with the unknown amorphous phases [198].

5.2.3   3D characterisation of microstructure changes

5.2.3.1   3D microstructure of β-Zr dendrites

Fig. 5.11 and 5.12 show the 3D microstructures of the as-cast and thermally shock DH3 obtained using synchrotron X-ray microtomography, respectively. As shown in Fig. 5.13a, the quantitative information extracted from this single dendrite indicates that most of the secondary dendrite tips have curvature radii ranging from 35 to 80 μm; their roots have curvature radii ranging from 8 to 15 μm; arm spacing ranges from 4.4 to 6.5 μm. And a 3D measurement was also given to characterise the mean curvature distribution of the dendrite surface. Fig. 5.13b shows the mean curvature ranged from -1.2 to 1.2, where the dendrite tips primarily have a curvature of 1.2, while the dendrites roots have a curvature of -1.2.

5.2.3.2   3D nanostructure of the intermetallic phases

Fig. 5.12 shows that, for the thermally shocked sample, the primary β-Zr dendrites were slightly dissolved at the dendrite-amorphous matrix interface and the dissolved layer turned into the two new phases (Zr_2Cu and $ZrBe_2$), and almost all amorphous matrix had been transformed into these two phases. However, the spatial resolution of the X-ray microtomography was insufficient to allow intermetallic grains (some of which were sub-μm in size) to be differentiated clearly. Therefore FIB-SEM nanotomography with the effective pixel size of $25 \times 25 \times 50$ nm, was used to study these phases.
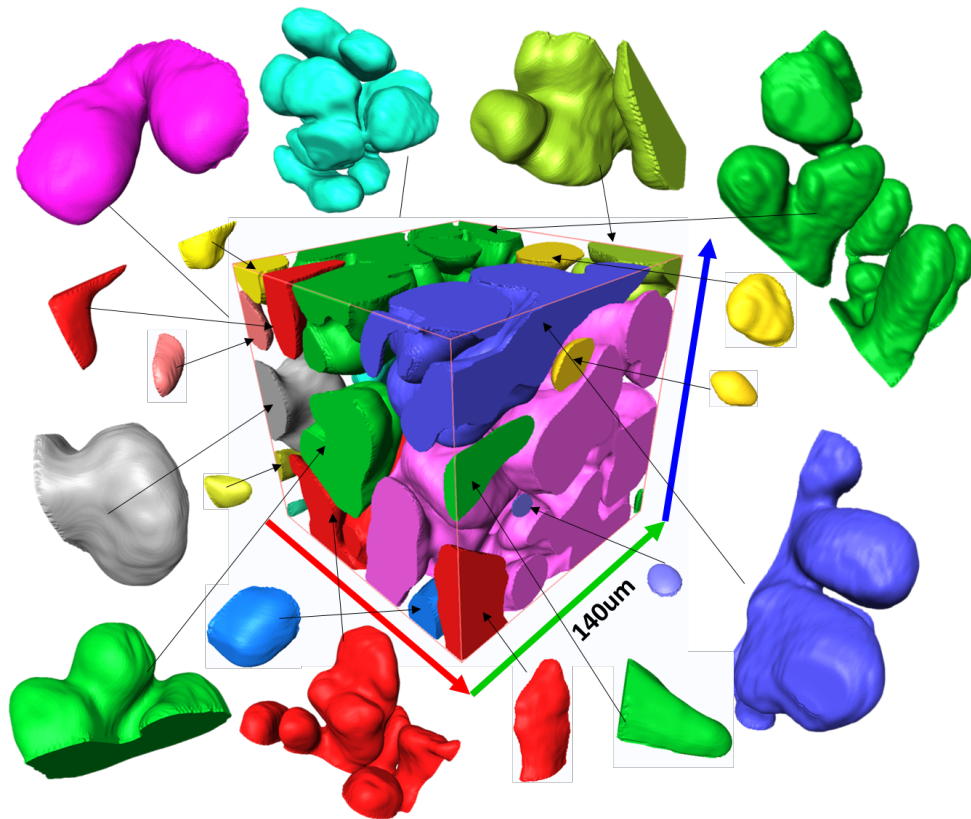
Fig. 5.11 3D morphologies of primary β-Zr dendrites in the as-cast sample, with the amorphous matrix hidden for ease of visualisation.
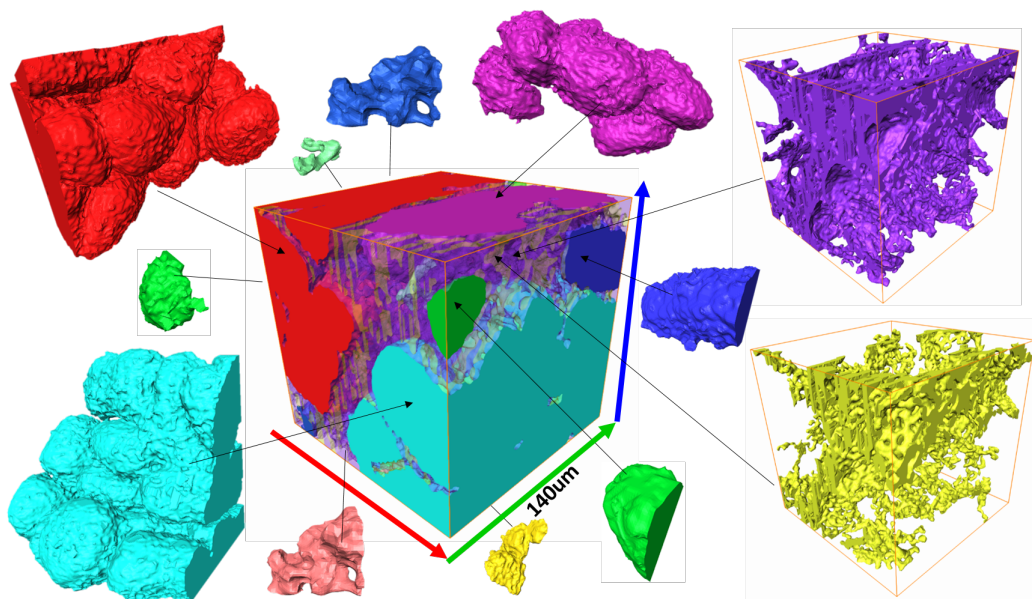
Fig. 5.12 3D morphologies of secondary $ZrBe_2$ (yellow), Zr_2Cu (purple) intermetallics and primary β-Zr dendrites (other colours) of the 650°C thermally-shocked sample.
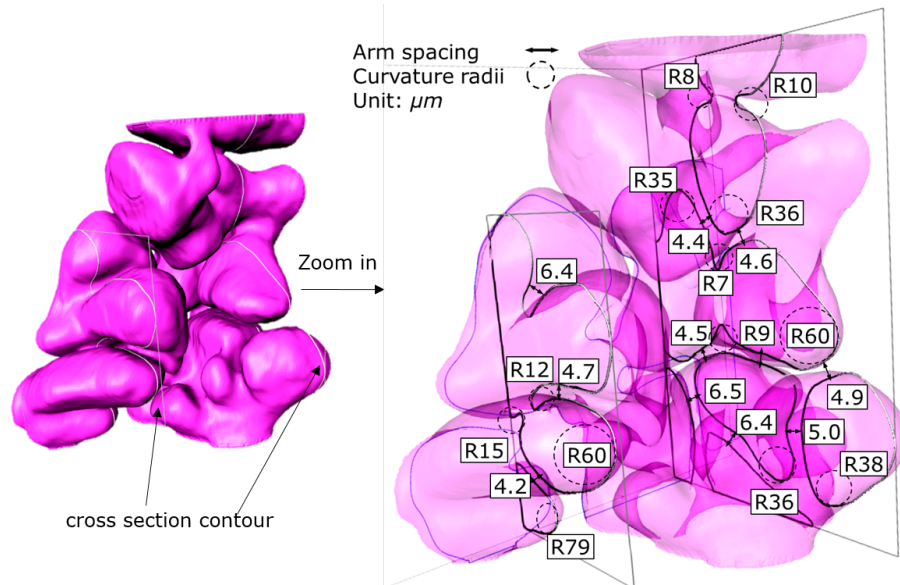
(a)
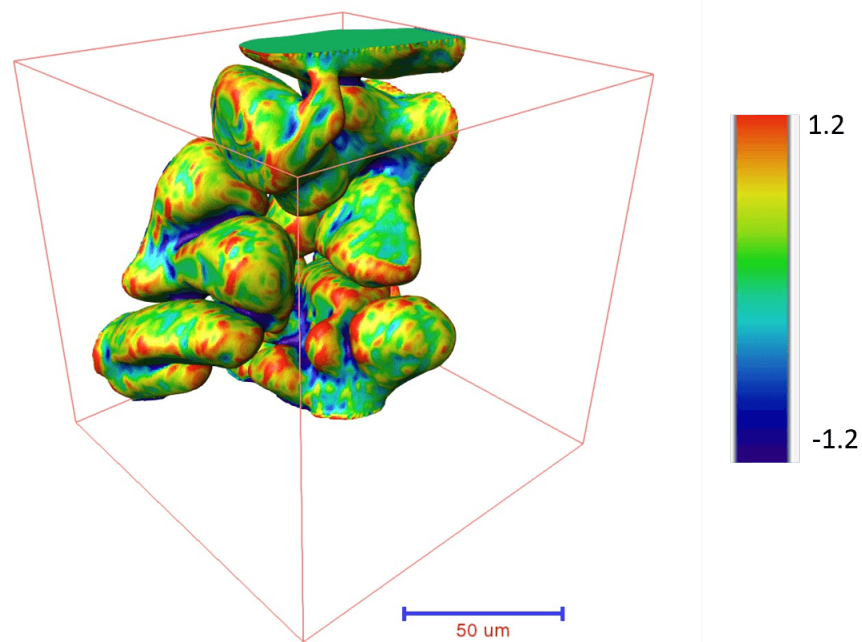
(b)

Fig. 5.13 (a) A typical β-Zr dendrite and measurement of arm spacing and curvature radii. (b) 3D mean curvature of the typical β-Zr dendrite, the colour band is in the range of -1.2 to 1.2 (μm^{-1}).
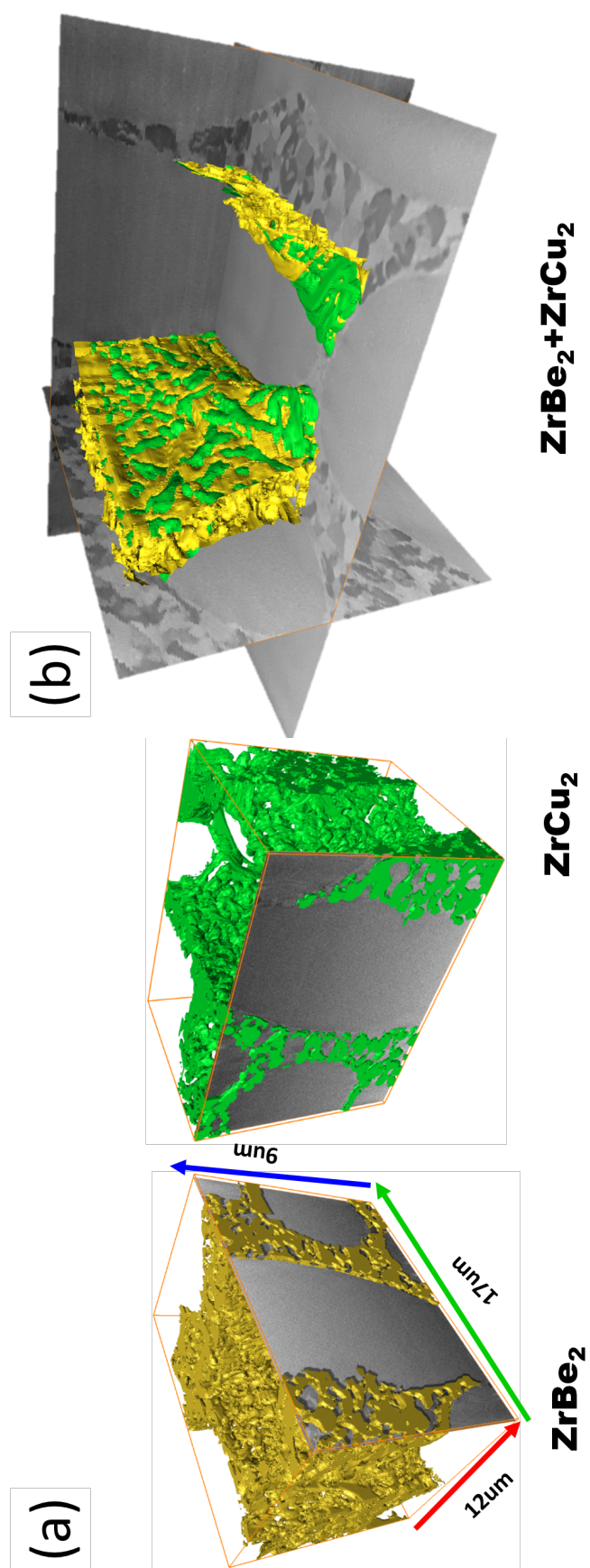
Fig. 5.14 FIB-SEM sectioning nanotomography of the 650°C thermally shocked BMGMC sample.

Fig. 5.14 shows that the amorphous matrix was completely transformed into a highly interconnected 3D network of eutectic microstructure of Zr_2Cu and $ZrBe_2$ with a minor change of β-Zr dendrites, which is different from the amorphous matrix within the as-cast sample. The powerful combination of X-ray microtomography with FIB-SEM nanotomography allowed to characterise the 3D structure from nano- to micro- scale.

5.2.4   Volume fraction and thermal stability

Volume fractions calculated for the different phases from SEM imaging, X-ray microtomography and neutron diffraction are summarised in Fig. 5.15. For β-Zr dendrites in the as-cast sample, results from SEM and tomography are very similar. However for the thermally shocked region, data from tomography for the β-Zr dendrites are 10% higher than those obtained from neutron diffraction and SEM, and lower for the two new $ZrBe_2$ and Zr_2Cu phases. This is most likely due to the difficulties in segmentation of $ZrBe_2$ and Zr_2Cu phases. The grain sizes are typically just a few micrometre in length, approaching the spatial resolution of the X-ray tomography. Therefore the volume fractions derived from neutron diffraction and SEM are more accurate.

The data in Fig. 5.15 indicate that during thermal shock process (650 ºC), 8 % (by volume) of the β-Zr dendrites were converted into the two new phases. The sample thermally shocked to above 700 ºC was completely melted and regained its as-cast microstructure after solidification.

5.2.5   Structure changes in the transition region

Previous studies [199, 200] of isothermal annealing have found that quasicrystals nucleate (and then grow into nanocrystals) within the glassy matrix. However, in this study it is found that nucleation and growth occur predominantly at dendrite-matrix interfaces.

Fig. 5.16a-c show the typical microstructure of the transition region between the as-cast and the thermally-shocked region for the 650 °C sample. It indicates that the majority of
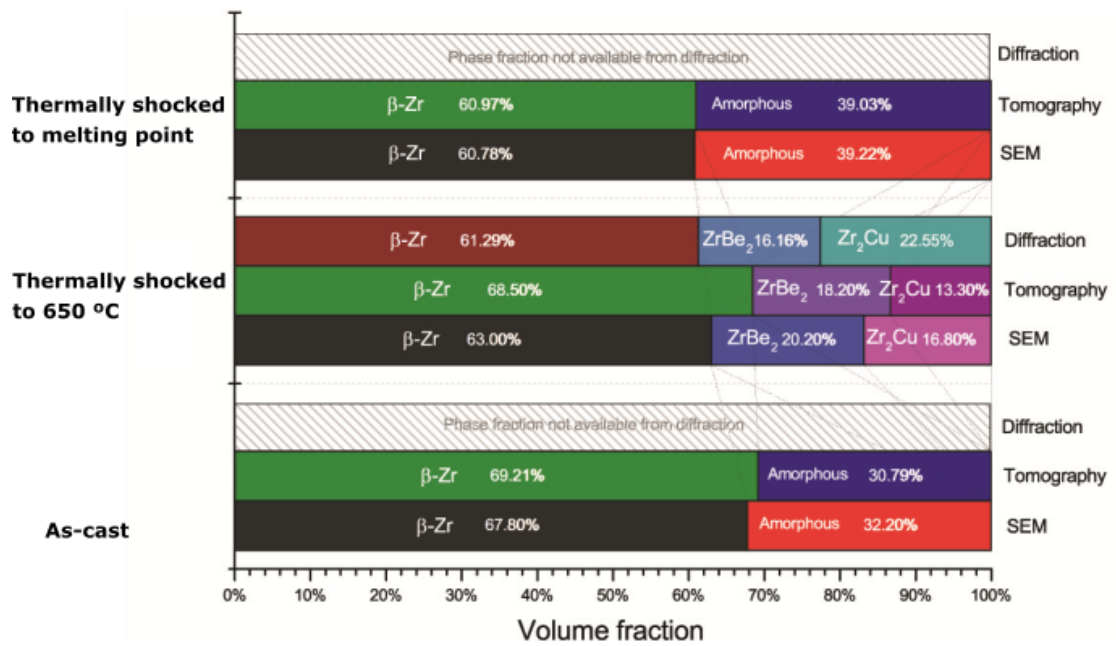
Fig. 5.15 Volume fractions of β-Zr, $ZrBe_2$ and Zr_2Cu calculated from SEM 2D images, X-ray tomography and neutron diffraction.

the new Zr_2Cu and $ZrBe_2$ crystalline phases, nucleated at the interface and grew together into the amorphous matrix in a form of eutectic growth [66]. Some of the Zr_2Cu and $ZrBe_2$ phases (Fig. 5.16 d,e) were also found to nucleate directly from the amorphous matrix and grow into the surroundings, similar to those found in most nanocrystallization studies [201, 189, 202]. Fig. 5.17 shows a gradual growth of intermetallic phases from the as-cast region to the thermally shocked region, which covers the whole transition region.
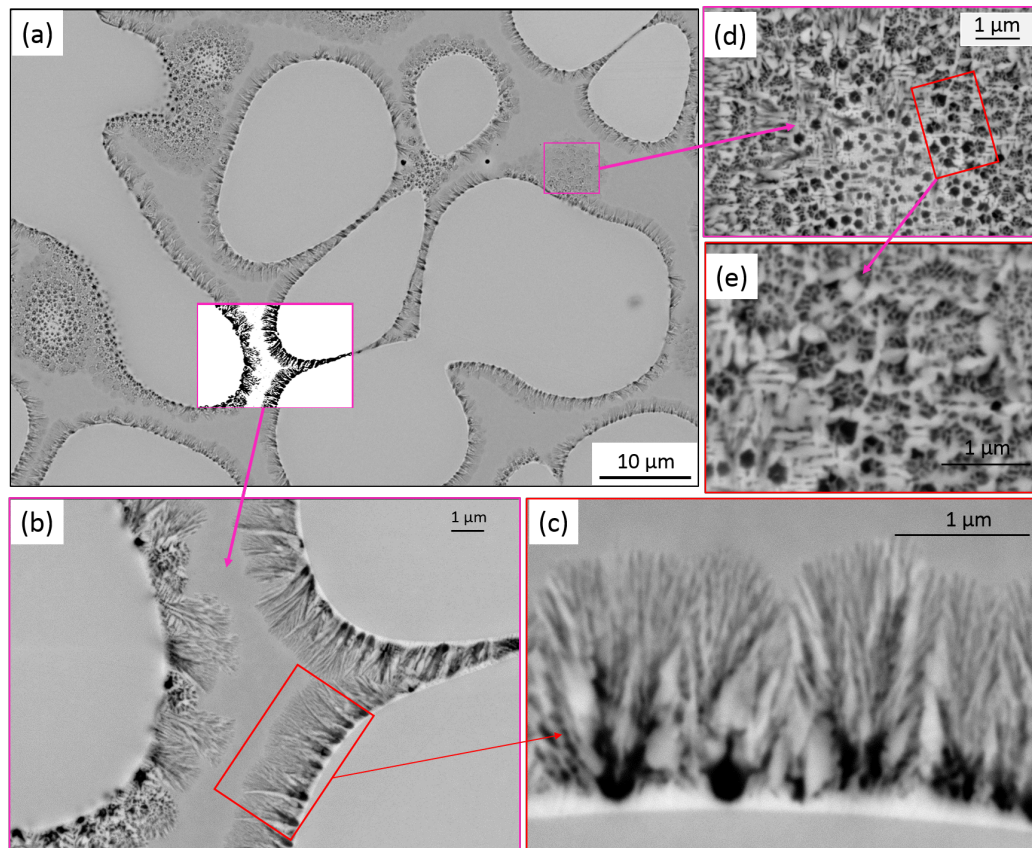
Fig. 5.16 (a) Eutectic growth of the needle phases Zr_2Cu (dark) and $ZrBe_2$ (light) found in the transition zone between the thermally shocked region and the as-cast region for the sample shocked to 650°C (marked by a red oval in Fig. 3.14). (b) and (c) are the enlarged magnification of the framed areas in (a) and (b) respectively.(e) and (f) are the enlarged magnification of the framed areas in (a) and (e), illustrating the intermetallic phases nucleated directly from the amorphous matrix and grew into the surroundings.
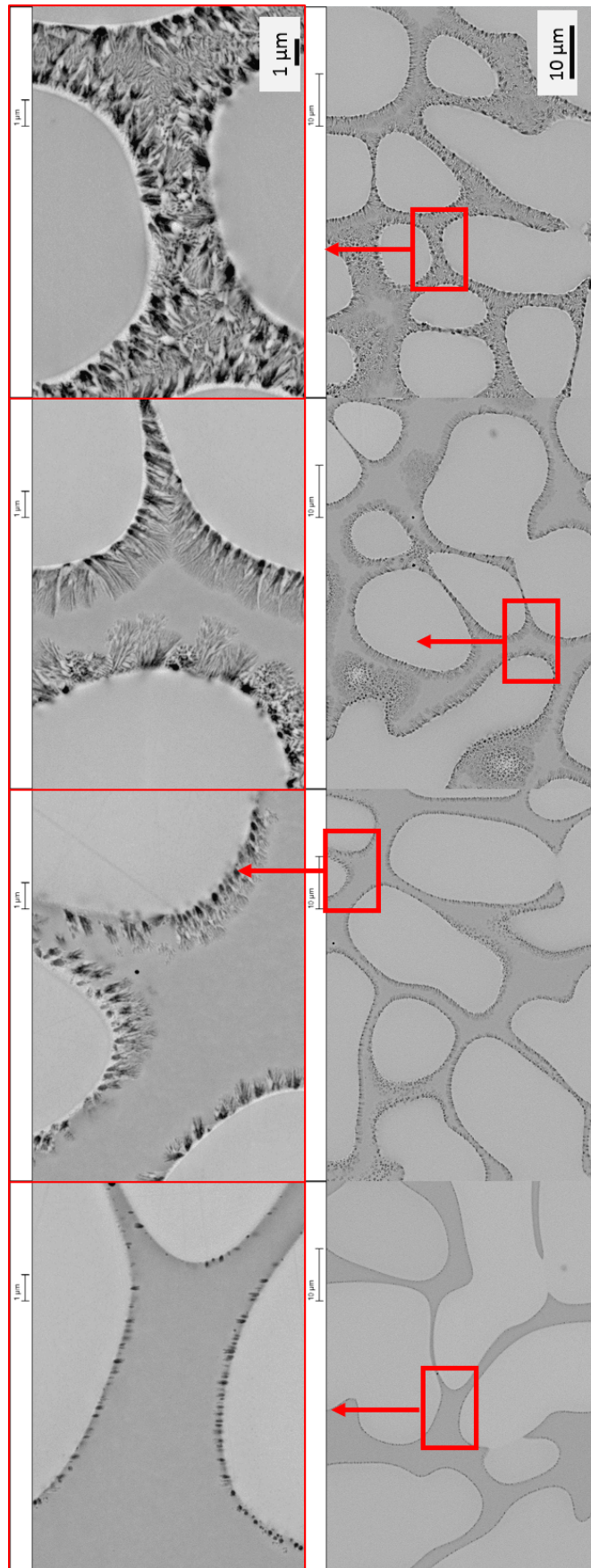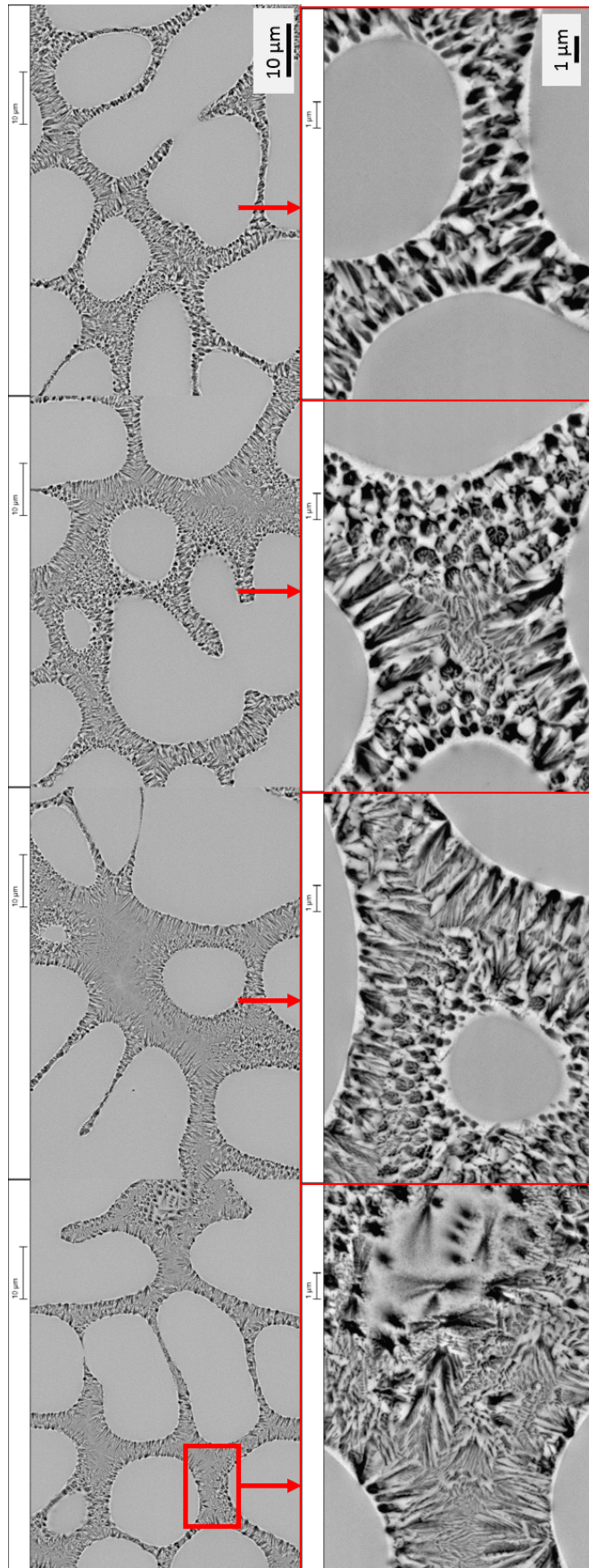
Fig. 5.17 The growth of the intermetallic phases, Zr_2Cu and $ZrBe_2$ nucleating from the phase interface, is presented from left to right; The red framed images are the higher magnification SEM micrographs.

5.3   Summary

In this chapter, structure studies of a bulk metallic glass matrix composite *i.e,* DH3, were presented. Section 5.1 presented the ordered to disordered structure transition within the amorphous-crystalline phase using HRTEM. Several HRTEM image based methods, *i.e,* FFT, ACF, voronoi tessellation, 2D PDF, were employed to characterise the structure transition.

Section 5.2 presented the multi-scale structure characterisation of DH3 alloy under thermal shock using several characterisation methods. The X-ray microtomography and FIB-SEM nanotomography revealed the 3D morphologies of the β-Zr dendrites and intermetallic phases induced by thermal shock. The event of nucleation and crystal growth of the newly formed intermetallic phases was also revealed using SEM.

Chapter 6

Phase-field crystal modelling of ordered to disordered structure changes

A number of theories and models have been developed in the past 30 years [203] to study and understand the fundamentals of order-to-disorder structure transition [204]. For example, in the condense matter physics community, mode coupling theory [205] and molecular dynamics (MD) method [**?**] have been used to study the initial stage of atom slowing down in a supercooled liquid due to the increase of viscosity. The dynamic density functional theory (DDFT) method [206, 77, 207] with a conserved form of motion equation has also been used to resolve the order-to-disorder transition in glass formation [164, 208]. However, as explained by Jaatinen [169], using DDFT to resolve the sharp peaks in density field leads to serious computing problems. Therefore, physics and materials science communities are currently developing more generic modelling frameworks to study and understand the order to disorder structure transition.

Elder, *et al* [165] firstly proposed the phase-field crystal (PFC) methodology for such research in 2002, Since then, extensive studies and model development have been made in physics and materials science communities concerning PFC. Recently, dynamic density functional theory and thermodynamic concepts have been also linked to PFC to extend the modelling framework. PFC model operates at atomic length scale (Å–nm) and diffusive

time scales (μs–ms), and is a computationally efficient alternative to molecular dynamics simulation methods. In 2009, Chan [170] developed the vacancy PFC model, which can be used as a MD model to simulate the liquid structure and also the vacancy diffusion in amorphous solid at atomic scale. In 2011, Berry [209, 172] successfully employed vacancy PFC to investigate glass transition and crystallisation in a super-cooled liquid.

In this chapter, the VPFC model is used to study the atomic ordered-to-disordered structure transition for a binary and a ternary alloy in different thermal and compositional conditions including the effect of different cooling rates, atomic size ratio, and chemical composition, providing more quantitative insight on understanding the ordered-to-disordered transition of the materials studied.

6.1   Vacancy phase-field crystal model for binary alloys

The VPFC model used in this research is based on the conserved form of motion equation of a binary alloy PFC model first proposed by Elder, *et al* [165], and the modified highly nonlinear free energy functional from the pure VPFC proposed by Chan *et al* [170]. The modified alloy coupling term proposed by Robbin *et al* [171] is also adapted here.

Firstly, the dimensionless free energy functional of a binary alloy can be described by:

$$F = \int d\vec{r} [f_{AA} + f_{BB} + f_{AB}] \tag{6.1}$$

Where f_{ii} is the free energy density for pure atom A and B [170], and f_{AB} is the coupling term of free energy density describing the interaction between atoms A and B [171]. A specific form of the free energy density function is used here:

$$f_{ii} = \frac{n_i}{2} [r_i + (q_i^2 + \nabla^2)^2] n_i - \frac{w_i}{3} n_i^3 + \frac{u_i}{4} n_i^4 + H_i (|n_i|^3 - n_i^3) \tag{6.2}$$

and,

$$f_{AB} = r_{AB} \cdot n_A \cdot n_B \tag{6.3}$$

Where n_i is the scaled time averaged number density of atom A and B; r_i is related to the liquid modulus; q_i defines the equilibrium distance between atoms of the same species, and the smaller q_i is, the larger the atomic size; and H_i and r_{AB} are constants for Vacancy terms. The terms multiplied by H_i counter-balance n_i when $n_i < 0$, and are the unique feature of the VPFC model [170]. w_i and u_i are derived from the nonlinear terms of DDFT free energy functional [165]. The physical meaning of these VPFC parameters and the default values for them are listed in Table. 6.1.

The conserved equation of motion, the so-called model B [177] is adopted here to describe the dynamics of the time averaged number density fields. Diffusive relaxations are described through a direct minimisation of the local free energy functional, and all dynamic processes on shorter time scales (*i.e*, atom vibration) can be absorbed into a stochastic noise term, given by

$$\frac{\partial n_i}{\partial t} = \nabla^2 \frac{\delta F}{\delta n_i} + A\xi \tag{6.4}$$

Where, ξ is the conserved noise satisfying the fluctuation-dissipation theorems [210]: $\langle \xi(\vec{x}_1, \vec{t}_1) \xi(\vec{x}_2, \vec{t}_2) \rangle = \eta \nabla^2 \delta(\vec{x}_1 - \vec{x}_2) \delta(\vec{t}_1 - \vec{t}_2)$.

The equation can be rewritten as,

$$\frac{\partial n_i}{\partial t} = \nabla^2 \frac{\delta F}{\delta n_i} + A\nabla\eta \tag{6.5}$$

where η is a 2D vector whose components are independent Gaussian white noise (as shown in Fig. 6.1) - a basic noise model used in information theory to mimic the
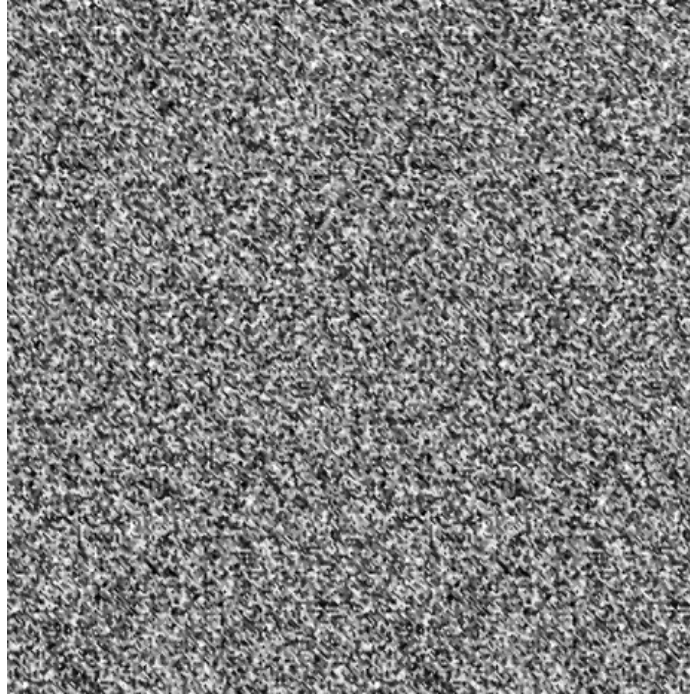
Fig. 6.1 The illustration of Gaussian white noise used in the simulation. The amplitude of noise is set to 0.0001.

effect of many random processes that occur in nature, which can be computed by the Box-Muller transformation [211]. *A* is the amplitude of stochastic thermal noise, which can be considered as temperature [172]. In addition, the parameter r_A, r_B can be also considered as temperature in the simulation (detailed in section 6.4). The functional derivative can be calculated by [212]:

$$\frac{\delta F}{\delta n_A} = \frac{\partial f}{\partial n_A} + \nabla^2 \frac{\partial f}{\partial \nabla^2 n_A} + \nabla^4 \frac{\partial f}{\partial \nabla^4 n_A} \ldots \tag{6.6}$$

Here f is the free energy density, defined as $f = f_{AA} + f_{BB} + f_{AB}$. After substituting $\frac{\delta F}{\delta n_A}$ into Eq. 6.5, the final form of the VPFC model for component A (or B) can be written as,

$$\frac{\partial n_A}{\partial t} = \nabla^2 \left(\frac{1}{2} \left[r_A + \left(q_A^2 + \nabla^2 \right)^2 \right] n_A + N_A + r_{AB} \cdot n_B \right) + A \nabla \eta \tag{6.7}$$

Where, the nonlinear terms is defined as $N_A = -w_A \cdot n_A{}^2 + u_A \cdot n_A{}^3 + 3H_A \cdot (|n_A| - n_A) |n_A|$.

The physical meaning for all the VPFC model parameters and the values used in this study are summarised in Table. 6.1.

Table 6.1 The parameters used for the VPFC model in this study [170, 78, 171].

Parameter	*value	physical meaning
$\bar{n}_i$	0.15	mean value of number density of i, represents composition changes
r_i	-0.9	liquid bulk modulus, represents temperature
r_{AB}	2	coefficient for the coupling term
q_i	1	the equilibrium distance between same atoms, represents atomic size
H_i	1500	coefficient of vacancy term, constant
w_i	0	coefficient of polynomial part of free energy density, constant
u_i	1	coefficient of polynomial part of free energy density, constant
η		thermal noise
A	10^{-5}	amplitude of thermal noise

* represents default values for the parameters.

6.2 Numerical methods, code and parallel computing sch–emes

In Eq. 6.7, there are several high-order, even-powered gradient terms, and it is difficult to derive an implicit Euler numerical scheme for the gradients terms. We therefore adopted the semi-implicit Fourier pseudospectral method (PSM) [176, 177, 213, 214] to solve Eq. 6.7. Using Fourier PSM, all the even-powered gradient terms are converted into even-powered algebraic expressions of the wave vector in the Fourier space (frequency space). PSM is particularly powerful for solving equations that exhibit periodic solutions such as those in this PFC model. After applying Fourier transformation on both sides of Eq. 6.7, and

using the forward finite difference method for time marching, the PSM discretion of Eq. 6.7 without the thermal noise term can be written as:

$$\hat{n}_A^{t+dt} = \frac{1}{1 - dt\Delta_k{}^2 C_{AA}}\hat{n}_A^t + \frac{dt\Delta_k{}^2}{1 - dt\Delta_k{}^2 C_{AA}}N(\hat{n}_A^t) + \frac{1/2dt\Delta_k{}^2}{1 - dt\Delta_k{}^2 C_{AA}}\hat{n}_B^t \qquad (6.8)$$

where $C_{ii} = r_i + \left(q_i^2 + \Delta_k{}^2\right)^2$ is the Fourier transformation of the direct two particle correlation of atom i; $\Delta_k{}^2$ is the discrete Fourier space representation of the ∇^2 for a finite size system; $N(\hat{n}_i) = -w_i\hat{n}_i^2 + u_i\hat{n}_i^3 + 3H_i(|\hat{n}_i| - \hat{n}_i)|\hat{n}_i|$ is the Fourier transformation of nonlinear term; The $\hat{n}$ represents the Fourier transformation of number density. In addition, the thermal stochastic noise term can be discretised as:

$$\vec{\nabla}\vec{\eta}_{i,j} = \sum\left(\frac{\eta_{i+1,j+1} + 2\eta_{i+1,j} - \eta_{i-1,j-1} - \eta_{i-1,j+1} - 2\eta_{i-1,j} + \eta_{i+1,j-1}}{8\Delta x}\right) \qquad (6.9)$$

Where, i, j denote the grid indices in the computational domain, and Δx is the spatial step size.

Table 6.2 The computation parameters used in the simulations

Parameter	value	meaning
N_X	512	Computation domain size in x direction
N_Y	512	Computation domain size in y direction
dx	0.785398	spatial grid size
dt	0.001	time marching step
Nt	500,000	Total computation steps

The PFC simulation is a computationally intensive process and can be speeded up by implementing a parallel computing scheme [215, 216]. In the current model and numerical scheme, there is no data exchange between the current grids and the adjacent grids. Hence,

a parallel computing technique (as detailed below) is employed to solve the discretised equation 6.8.

Message passing interface (MPI) was implemented in the code to achieve the parallel computing during the simulation. MPI is a standard method for distributed-memory parallelism, and each processor has its own separate memory. Hence parallel computing can easily scale up for a cluster of many thousands of processors. Each MPI process only stores a portion of the data to be transformed. In our research group, we have a Dell PowerEdge C6145 Rack Server (AMD Processor-based 2U Rack with 64 cores and 512 GB memory) and is suitable for using MPI parallelism.

Fig. 6.2 shows the flow chart for the simulation. After defining the necessary variables and arrays, the model parameters, such as r_i, q_i, initial values of number density, *i.e, $\bar{n}_i$*, and computation parameters, *i.e, dt*, *dx* and *Nt* as listed in table. 6.2, are assigned by the values provided in the parameter input file. Since the current numerical scheme involves the parallel computing, the MPI environment has to be established initially, which is called MPI plan in FFTW library terminology.

After the initialisation of model parameters and number density field, the solving of discretised equations can be allocated to each MPI process, *i.e*, $np = 0$, $np = 1$ (No. of process) as presented in Fig. 6.2. For each MPI process, the linear factors and non-linear factors of number density and non-linear term, such as $\frac{1}{1-dt\Delta_k{}^2 C_{AA}}$ in Eq. 6.8 are calculated before evaluating the increment of number density.

For each time step, the non-linear term is computed in real space, then it is Fourier transformed to Fourier complex number. In the Fourier space, the Fourier transformed number density, a complex variable, is incremented for each step. After, the Fourier number density is inverse Fourier transformed back to the real space, and then output by main MPI process. The number density field, *i.e*, n_i is incremented until the maximum time step is reached during the computation loop.

During the computation, the Fourier transform and inverse Fourier transform was performed using the routines defined in the Fast Fourier Transform West library (FFTW)
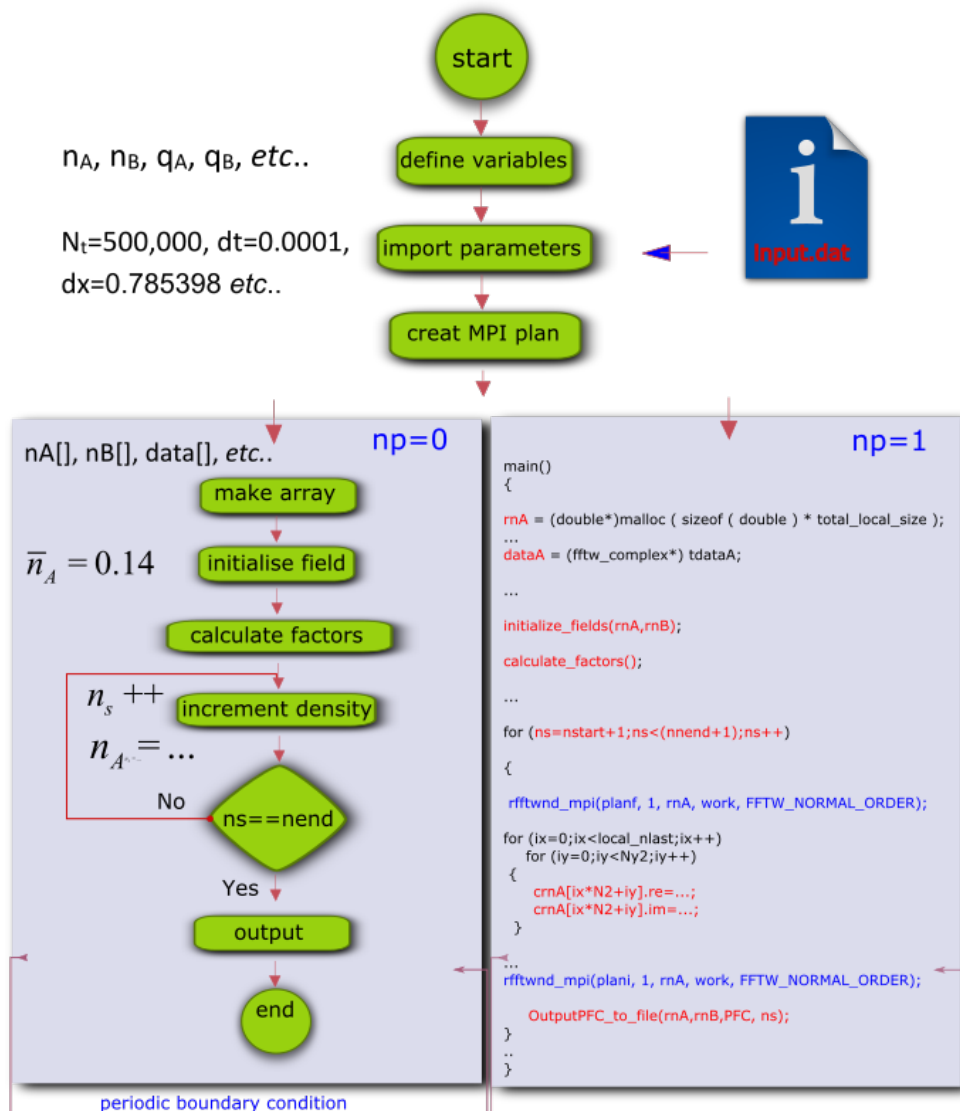
Fig. 6.2 The flow chart for the numerical implementation of the VPFC model.

3.3.4 [178], which is a comprehensive collection of fast C routines for computing the discrete Fourier transform (DFT). FFTW also implements the parallel FFTW routines for parallel computing, which supports the MPI message-passing interface.

All these calculations are implemented by many processors using FFTW-MPI. The total number of MPI processes can be assigned when launching the computation. For many simulation cases, distributed-memory parallelism can easily pose an unacceptably high communications overhead for small problems. However, as mentioned in previous section, for VPFC simulations performed here, there is no data communication involved. Therefore,

maximum computing capability (64 cores) can be employed to speed up the computation without the communications overhead.

6.3 Computing environment, data processing and visualisation

The numerical model is implemented in C language. All simulations were performed in parallel using a 64-core linux computing server (Dell PowerEdge C6145) housed in our research group. MobaXterm is used to remotely access the computing server. The OpenMPI-1.6.5 library [217] is installed and configured for the MPI parallelism. The GNU gcc compiler is used to compile the codes. The FFTW-3.3.4 library is installed and linked during the compilation. When performing the simulation, the processor numbers can be assigned by "-np" option right after "mpirun" command. For all the simulations, 32 MPI processes are invoked during the computation.

The simulation data is output as Tecplot format. In addition to the indices i , j, three number density fields, n_A, n_B and n_{mix} for each grid are also output in the dataset. n_{mix} represents the total number density field, which is the maximum value from pure number density field, n_A and n_B.

Based on those simulated patterns, FFT is used to convert them into the corresponding reciprocal space patterns using the built-in function in ImageJ. Assuming simulated particles are atoms, the FFT patterns are equvilant to the diffraction patterns as explained in section. 2.3.5.1. The FFT patterns can be used to study the order of the atomic structure from different perspective. A false colour (look up table) [218] in imageJ is also used to adjust the contrast of the default brightness and contrast.

The pair distribution function spectra presented in the chapter, are calculated using the same method described in section. 2.3.5.1. The orientations of the simulated structure

(ordered or disordered) are characterised by the orientation of each side of the Voronoi cell of the particle patterns.

Firstly, the Voronoi cell map is obtained from the simulated particle patterns using the same approach described in section. 2.3.5.1. Then the orientation angle of each side of Voronoi cells is calculated using the "OrientationJ" plugin function in imageJ which is based on the evaluation of the structure tensor in a local neighbourhood [219].

Delaunay triangulation often used in colloidal studies [220], is dual construction of the Voronoi tessellation, where all the nearest neighbour pairs are connected by "bonds". More focuses are often given to the bond length and bond angle. The Delaunay triangulation is calculated based on the Voronoi cells using the "Delaunay Voronoi" plugin in Fiji [221]. The coordinates of all the vertex of the triangles generated in Delaunay triangulation is output for bond angle calculation. Bond angle of the atoms, *i.e*, the angle of the Delaunay triangles, is calculated using Cosine rule.

6.4 Numerical experiments and model sensibility studies

6.4.1 Parameters for temperature dependent simulations

The PFC free energy functional is derived from the Ryoichi Yamamoto functional [222], a typical representative of the DFT functionals in solidification. Actually, all coefficients and variables in PFC models are temperature related parameters [223, 166]. A widely accepted and used variable to represent temperature in PFC model [78, 171] is r_i, *i.e*, the liquid bulk modulus[223, 166], and it has been shown to vary proportionally to T^2 for metallic ally systems [224, 225], but has a linear relationship of T for refractory oxides [225]. Therefore, for all simulations presented in this chapter, r_i is referred as temperature [170, 172] and in this study, temperature is simply defined as $T = -r$. The amplitude of the stochastic noise term, A, remains constant, and it is considered as the energy fluctuations for the dynamic process of structure evolution.

In order to investigate temperature dependent atomic structure changes, a series of isothermal transitions was simulated to test the sensibility of the model for structure changes. The parameters tested for r_A, r_B are shown in Table 6.3, while other parameters showed in Table. 6.1 and Table. 6.2 remains the same.

Table 6.3 The parameters used for simulating the isothermal transitions for binary alloys

Parameter	value	*T	structure
	-1.7	1.7	liquid
	-1.3	1.3	liquid
r_i	-0.9	0.9	crystalline
	-0.5	0.5	crystalline
	-0.3	0.3	crystalline

For simplicity, the temperature is defined as $T = -r$.

Fig. 6.3 presents the simulated structures, FFT patterns and pair distribution function for all isothermal transition cases. The Fourier transformation and pair distribution function calculation procedure are described in section 3.5.2.2. When $T = 1.7$, a disordered structure is formed as revealed by the simulated atomic pattern, the FFT patterns (several concentric halos in the Fourier space) and the pair distribution function. The simulated structure feature resembles the pair distribution function of a liquid structure – a correlation hole, a strong nearest–neighbour correlation, and a weak correlation with the atoms one or two atomic spacings apart [161, 170].
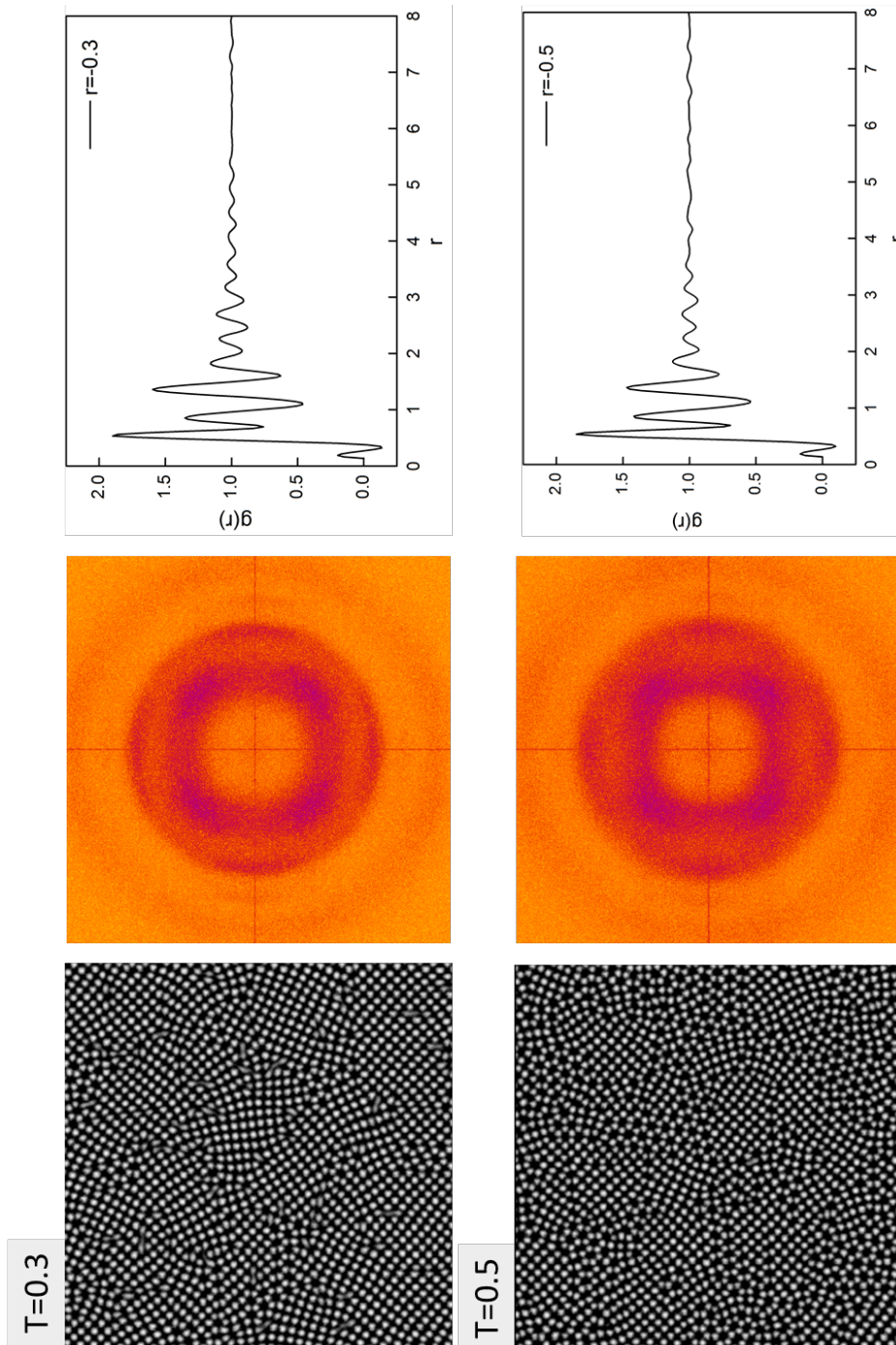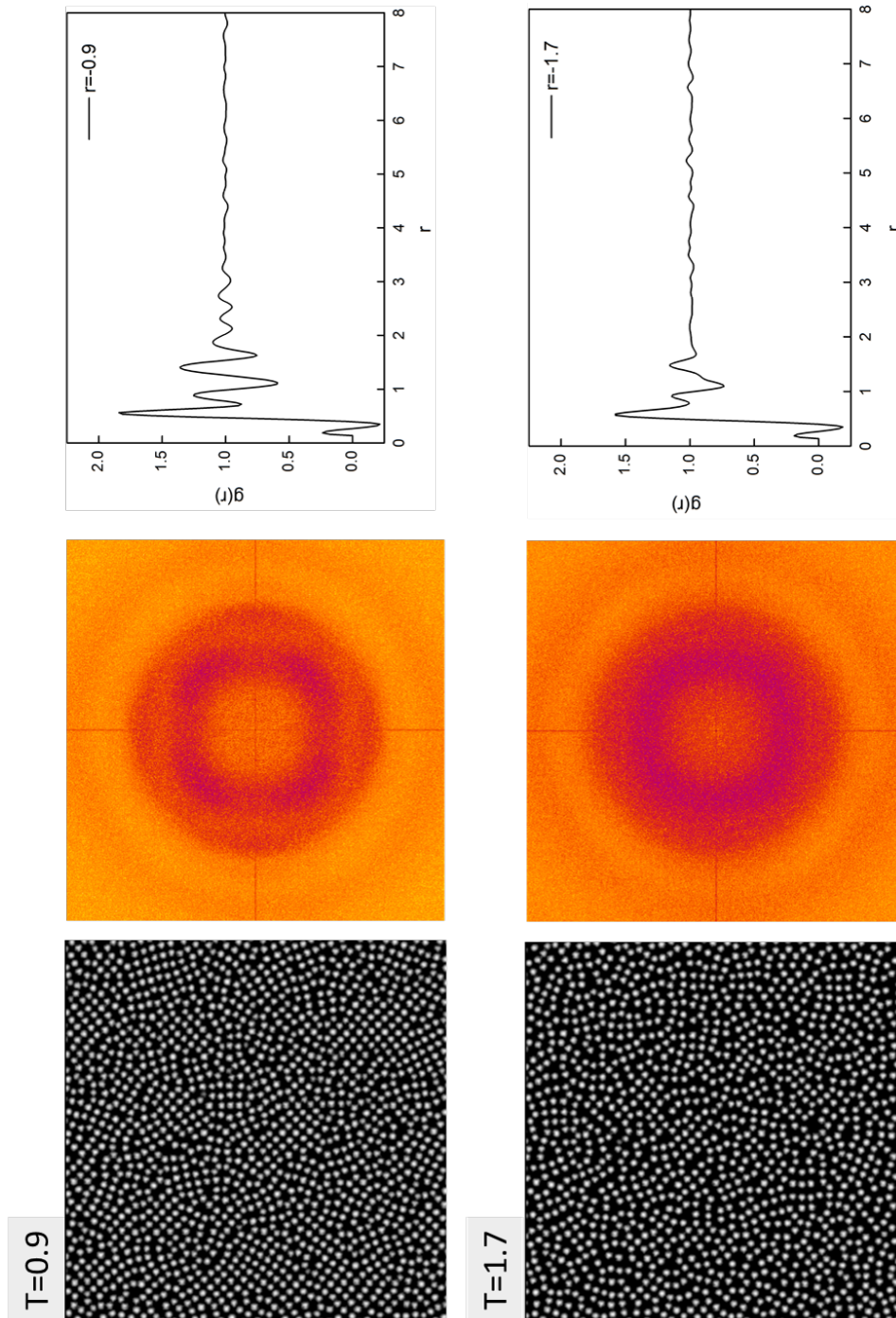
Fig. 6.3 The simulated structure changes with temperature. The patterns in the 1st column are the simulated atomic configuration. The patterns in the 2nd column are the corresponding FFT patterns, and the figures in the 3rd column are the calculated PDF spectra.

When $T = 0.3$, the simulated equilibrium phase is a well developed square-ordered structure. The simulated pattern is made up of nano-crystals (tens of atoms) with different orientations. In addition, there is sign of anisotropic features found in the diffraction pattern for ordered structure in Fourier space. A more quantitative characterisation of the simulated structure is shown more clearly by the pair distribution function where there is a series of successive peaks in the range of $r < 5$. The peak height of the dominant peak is about 1.8. For $T = 0.5$, $T = 0.9$, the simulated structure is still made of nanocrystals but with smaller size comparing to those at $T = 0.3$. When $T < 0.3$, strip phases as shown in Fig. 6.4 were found to appear [171]. Therefore, in the reasonable T range, $T = 0.3$ is taken as the lowest temperature for a stable square crystalline structure [171].
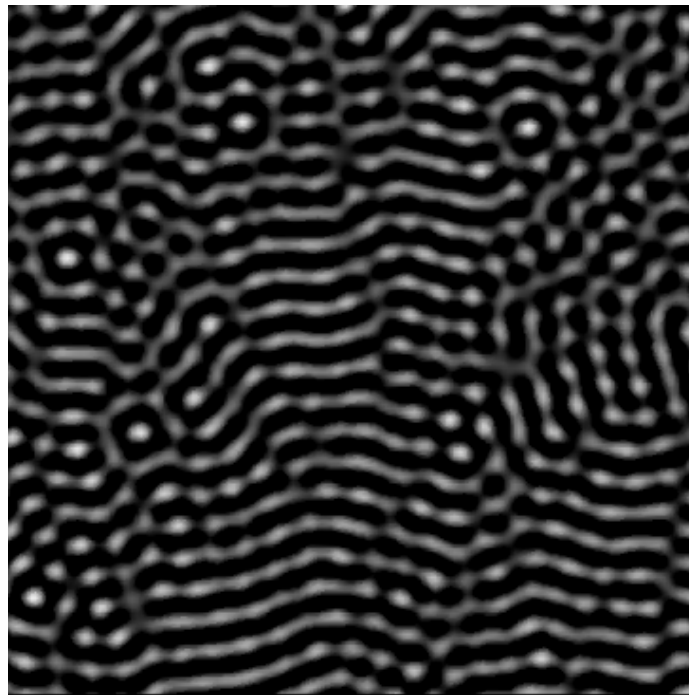
Fig. 6.4 Simulated structure of the strip phase formed when $T < 0.3$.

Based on the above simulation, if it is assumed that $T=1.7$ represents the liquidus temperature T_l of the binary alloy, while $T=0.3$ is the lowest temperature T_a. The cooling rate then can be defined as $C = \frac{T_l - T_a}{N_t}$. The different cooling rates can be obtained by setting different values for the total computation step N_t, while T_l and T_a remain the same

Table 6.4 Cooling rates used in the cooling effect studies for binary alloys

Simulated case	T_l	T_a	N_t	Cooling rate (C)
C1	1.7	0.3	5.5×10^4	2.8×10^{-4}
C2	1.7	0.3	1.0×10^5	2.8×10^{-5}
C3	1.7	0.3	2.0×10^5	9.3×10^{-6}
C4	1.7	0.3	3.0×10^5	5.6×10^{-6}
C5	1.7	0.3	4.0×10^5	4.0×10^{-6}

T_l and T_a, represent the liquidus and lowest temperature, respectively.
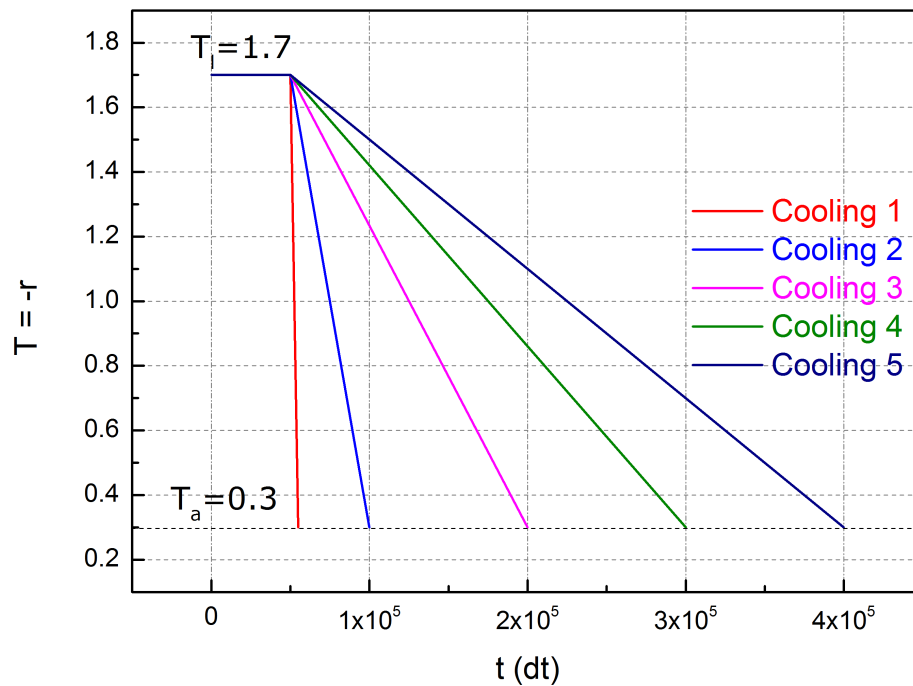
Fig. 6.5 The cooling profiles used in the simulation.

thoroughly for all the simulation. Table 6.4 lists all the cooling rates studied, and Fig. 6.5 shows the cooling profiles used in the simulation.

6.4.2 Parameters for atomic size ratio and composition

The parameter q_i, describing the equilibrium distance between the atoms of the same elements in the PFC model [78, 171], can be used to represent the atomic size of the specie i.

In the simulations, if q_B for atom B is set to unity, while q_A for atom A is changed, different atomic ratios can be selected for the simulation. In this study, a cooling rate of 9.3×10^{-6} is chosen because it is the critical cooling rate for the formation of disordered structure in the subsequent studies of cooling rates. Table 6.5 lists a set of atomic size ratios used in the simulation.

Table 6.5 The atomic size ratio used in simulation for binary alloys

q_A	q_B	q_A/q_B	cooling rate
1.0	0.1	1.0:0.1	9.3×10^{-6}
1.0	0.3	1.0:0.3	9.3×10^{-6}
1.0	0.5	1.0:0.5	9.3×10^{-6}
1.0	0.7	1.0:0.7	9.3×10^{-6}
1.0	0.9	1.0: 0.9	9.3×10^{-6}

Average number density: n_i=0.14.

The composition-dependent atomic structure can be simulated by setting different $\bar{n}$, the mean value of number density for element A and B. Chan [170] investigated the relationship between the PFC atomic density, *i.e*, the number of atoms per unit area, and the mean value of the number density $\bar{n}_i$. It is found that the PFC atomic density increases linearly with $\bar{n}_i$ until $\bar{n}_i$=1.5.

Robbin [171] also studied the effect of mean value of number density, $\bar{n}_i$ on the formed structure. It is observed from the simulation of the equilibrium state, a low $\bar{n}_i$ leads to a gas-like structure, a medium $\bar{n}_i$ can form typical liquid like structure, and a high $\bar{n}_{total}$=0.28 gave an ordered crystalline structure.

In this study, a mean value of total number density of $\bar{n}_{total}$=0.28 is fixed, when that of n_A and n_B varies. The composition is further defined as $c_B = n_B/(n_A + n_B)$. Table. 6.6 summarises the compositions used in the simulation of the composition-dependent atomic structure. The same cooling rate of 9.3×10^{-6} is adopted as before. However, an

asymmetric atomic size ratio, *i.e*, q_B/q_A=0.8 is given for these composition studies. The rest of parameter remains the same as default.

Table 6.6 The compositions used in the simulation for binary alloys

$\bar{n}_A$	$\bar{n}_B$	$c_B = \bar{n}_B/(\bar{n}_A + \bar{n}_B)$	q_B/q_A	cooling rate
0.224	0.056	0.2	0.8	9.3×10^{-6}
0.196	0.084	0.3	0.8	9.3×10^{-6}
0.168	0.112	0.4	0.8	9.3×10^{-6}
0.14	0.14	0.5	0.8	9.3×10^{-6}

6.5 The simulated atomic structure for binary alloys

A series of simulations were made to study the atomic structure changes in different thermal conditions, and with different atomic size ratio of constituent elements and compositions. All model parameters used in the following simulations are described in section 6.4.

6.5.1 Temperature dependent atomic structures

6.5.1.1 The effect of cooling rates

Cooling rate is an important factor in determining the structure of the super-cooled liquid during cooling process. As presented in Chapter 4, a relatively fast cooling rate can freeze the disordered atomic configuration of the super-cooled liquid, but sometimes with a certain degree of relaxation. Nonetheless, a fairly slow cooling rate allows the atoms to have enough time to relax and form a long-range translationally ordered structure, *i.e*, crystalline phase.

In the simulations, the different cooling rates used are, C_1=2.8 × 10^{-4}, C_2=2.8 × 10^{-5}, C_3=9.3 × 10^{-6}, C_4=5.6 × 10^{-6}, C_5=4.0 × 10^{-6}, which were defined in the numerical experiments in section 6.4.
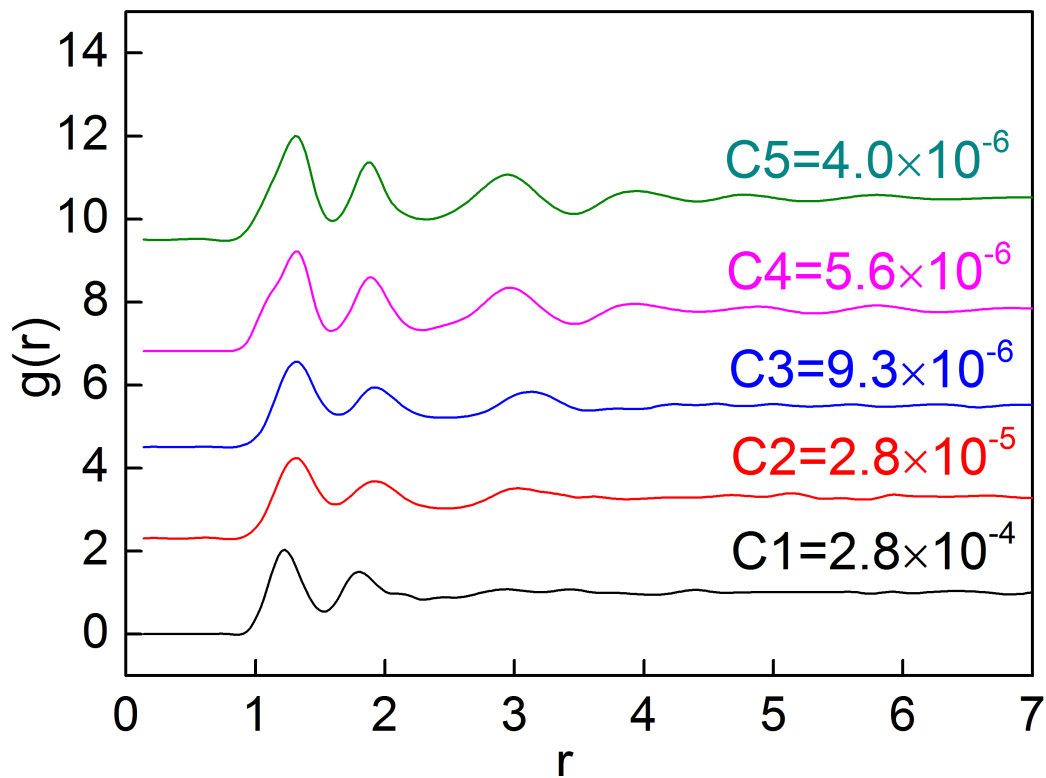
Fig. 6.6 The simulated pair distribution function using different cooling rates; the offset distance for each curve is 2.2 in y direction.

Fig. 6.6 shows the pair distribution function of the simulated atomic structure at different cooling rates. As the cooling rate decreased from $C_1 = 2.8 \times 10^{-4}$ to $C_4 = 5.6 \times 10^{-6}$, The intensity of first peaks of g(r) changed from 1.4 to 2.1; that of the second increased from 0.7 to 1.5; more minor peaks appeared in the medium range from $r = 2.5$ to $r = 7.0$. The required cooling rate for the formation of disordered structure is between C_2 and C_3. Beyond that, further decrease in cooling rates gives enough time for the random atoms in liquid to grow into ordered structure as shown by PDF at the cooling rate of C_4 and C_5 in Fig. 6.3.

To characterise the geometrical characteristics of the crystalline structures formed, Voronoi tessellations are used to analyse the simulated patterns. The orientation of the Voronoi cells of the disordered structure obtained at $C_1 = 2.8 \times 10^{-4}$ and that of the ordered structure at $C_5 = 4.0 \times 10^{-6}$ were shown in Fig. 6.7a, and Fig. 6.7b. The colours indicate the orientation of the each side of the Voronoi cell, and the colour maps clearly show the difference in orientation of the atomic clusters formed at different cooling rates.
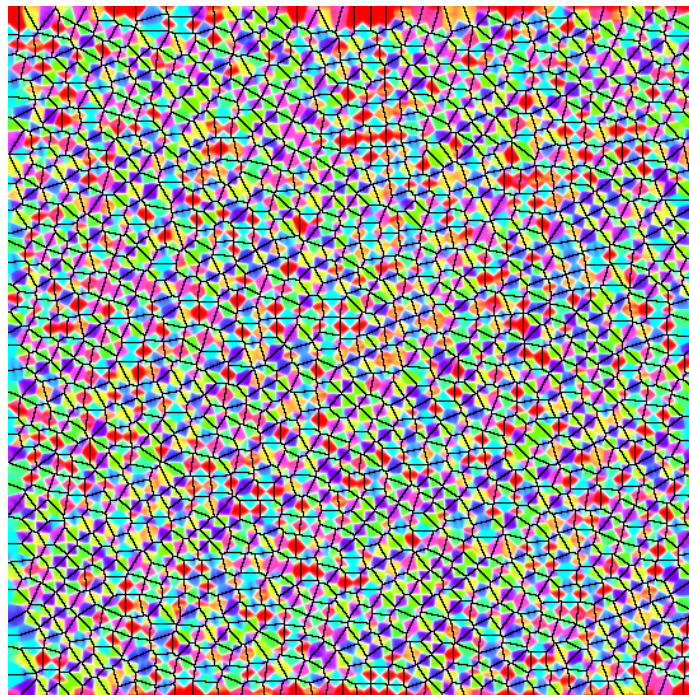
(a)
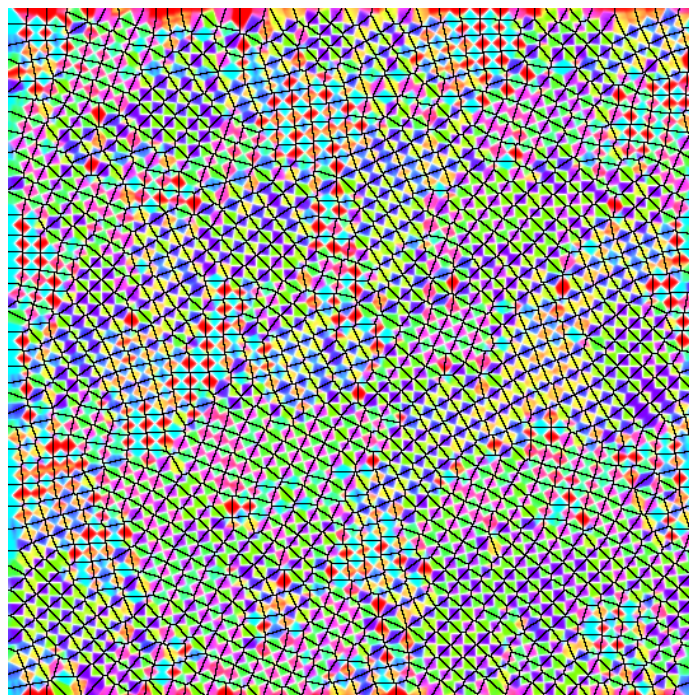
(b)

Fig. 6.7 The orientation of the Voronoi cells of the disordered and ordered structure formed at two different cooling rates: (a) $C_1 = 2.8 \times 10^{-4}$, and (b) $C_5 = 4.0 \times 10^{-6}$.
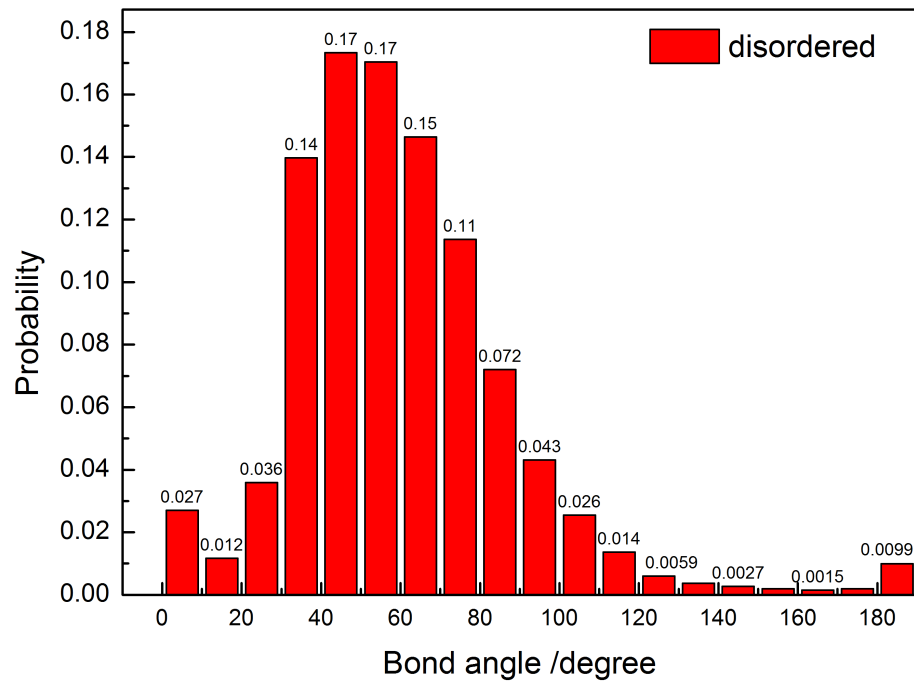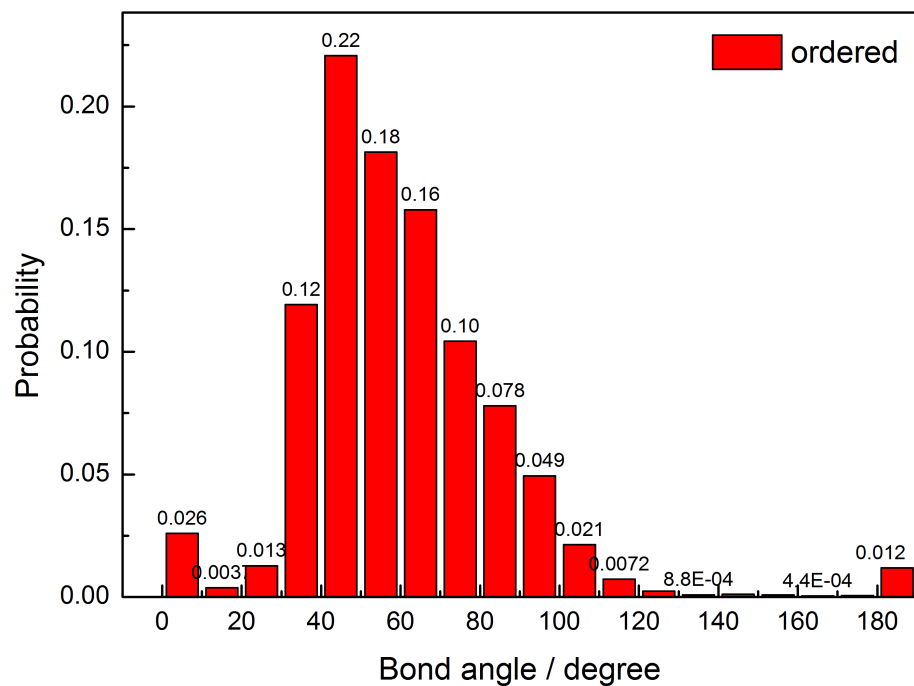
Fig. 6.8 The bond angle distribution of (a) the disordered structure formed at $C_1 = 2.8 \times 10^{-4}$, and (b) the ordered structure formed at $C_5 = 4.0 \times 10^{-6}$.

For the disordered structure in Fig. 6.7a, the colours along each side of the Voronoi cell are randomly distributed, implying the whole atomic pattern is isotropic. While, for the ordered structure in Fig. 6.7b, a preferred orientation is observed.

The bond angle is calculated based on the Delaunay triangles consisting of the centre atom and its nearest-neighbor atoms. Interestingly, Fig. 6.8a and Fig. 6.8b show that most of the bond angles were distributed in the range of 20-120 °, and the dominant bond angle is between 40-50° for both ordered and disordered structure. The probability for each is 22% and 17%. However there are more bond angles with the probability of 14% in the range of 30-40°and 17% in the range of 50-60 ° for the disordered structure. In general, it is found that the disordered structure has a more widely distributed bond angles, as opposed to the ordered structure.

6.5.2 Composition dependent atomic structures

In addition to the cooling rates, the atomic structure of metallic glass is extremely sensitive to the constituent elements and their chemical composition.

6.5.2.1 The effect of atomic size ratio

There are several aspects needed to be considered in constituent elements, such as heat of mixing, and atomic size ratio. In this section, only the atomic size ratio is investigated by simulation using different combination of q_A/q_B, *e.g*, 1.0 : 0.1, 1.0 : 0.3, 1.0 : 0.5, 1.0 : 0.7, 1.0 : 0.9 corresponding to the atomic size ratio as shown in Table. 6.5.

Fig. 6.9 presents the effect of the atomic size ratio on the order of the atomic structures. When the atomic size of component *B* increased, that of the component A remains the same thoroughly. A different atomic size ratio is elegantly reflected in the simulated patterns.

Fig. 6.10a shows that there are three peaks in the r range from 1 to 4 for q_A/q_B=1.0 : 0.9, 1.0 : 0.7, however for q_A/q_B=1.0 : 0.5, 1.0 : 0.3, 1.0 : 0.1, these peaks are dominant in
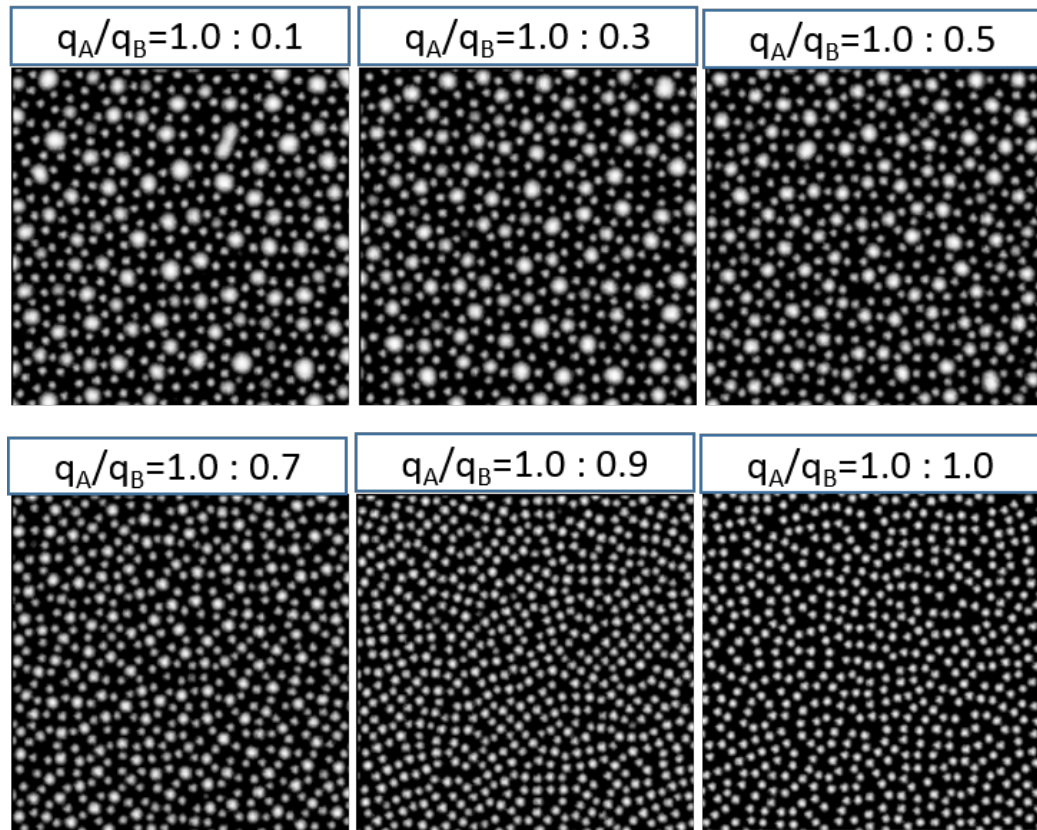
Fig. 6.9 The effect of ratio, q_A/q_B on the structure changes of a binary alloy, reflecting the effect of different atomic size ratio on the atomic structures.

the r range of 1 to 8. The intensity of the first peak for all the simulations decreases from 3 to 1.5 with the increasing q_A/q_B.

In addition, there is a minor peak separating from the first peak located at $r = 2.3$ for q_A/q_B=1.0 : 0.9, 1.0 : 0.7, which can be explained by the partial PDFs for each component presented in Fig. 6.10b. The first peak of the partial PDF of the component A remains at the same position for all different atomic size ratio, however, the peak position of the dominant peak of the component B is shifted to the high r position with the increase of q_A/q_B. Therefore, the minor peak separation from the first peak of A-A pair, is formed by the peak addition of the B-B pairs.
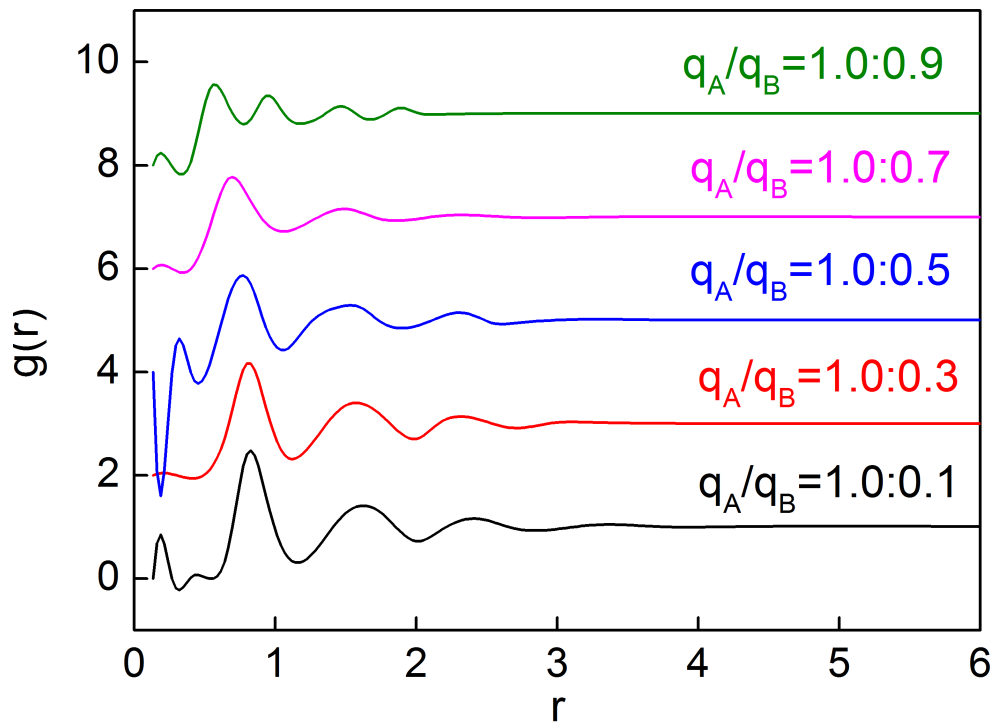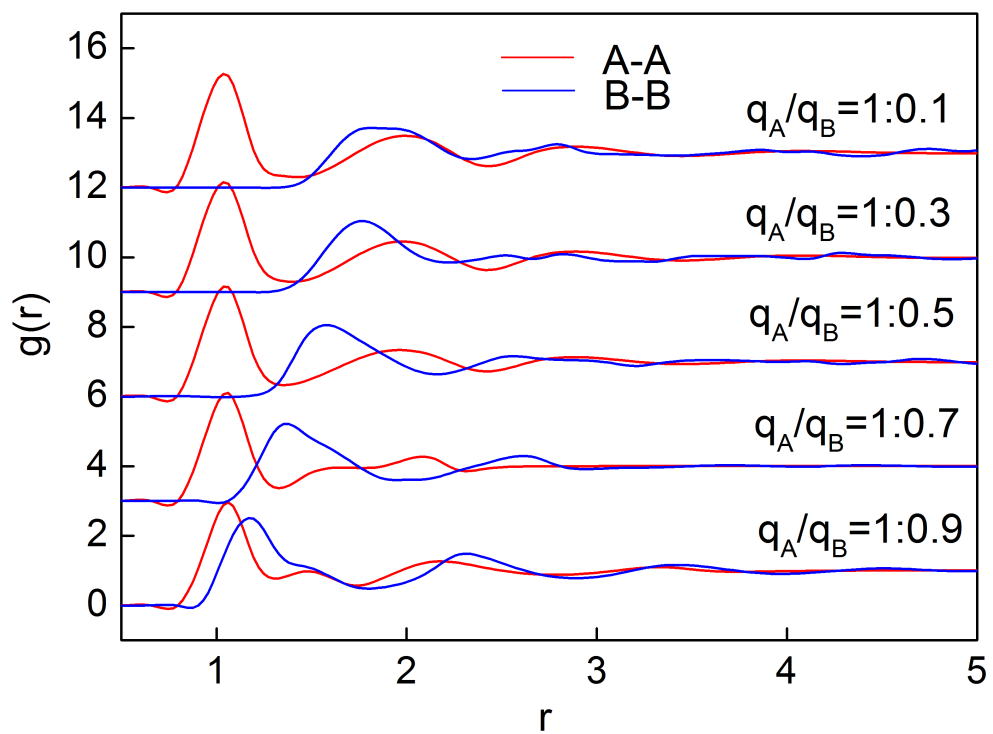
Fig. 6.10 The (a) total and (b) partial PDFs of the simulated structures with different atomic size ratio.

6.5.2.2   The effect of composition

The parameters for composition study are listed in Table. 6.6. Four compositions, *i.e*, c_B=0.2, c_B=0.3, c_B=0.4, c_B=0.5, are chosen for the simulations during the cooling process with a cooling rate of $C_3 = 9.3 \times 10^{-6}$.

The pair distribution function analyses for all cases are presented in Fig. 6.11a. There are several peaks located in the r range of 1 to 8. For c_B=0.2, 0.3, the dominant peak is at r = 2, however for the c_B=0.4, 0.5, the dominant peak is located at r = 1.5, where the minor peaks for the case of c_B=0.2, 0.3 are also present. In addition, the peaks in the medium r range for c_B=0.2, 0.3 are more intense than those for the cases c_B=0.4, 0.5. Fig. 6.11b shows the partial PDFs of A-A and B-B pairs. The peak intensity of the first peak for partial PDFs of B-B decreases with decreasing composition of B. While, the first peak of element A is get more intense.

(a)

(b)
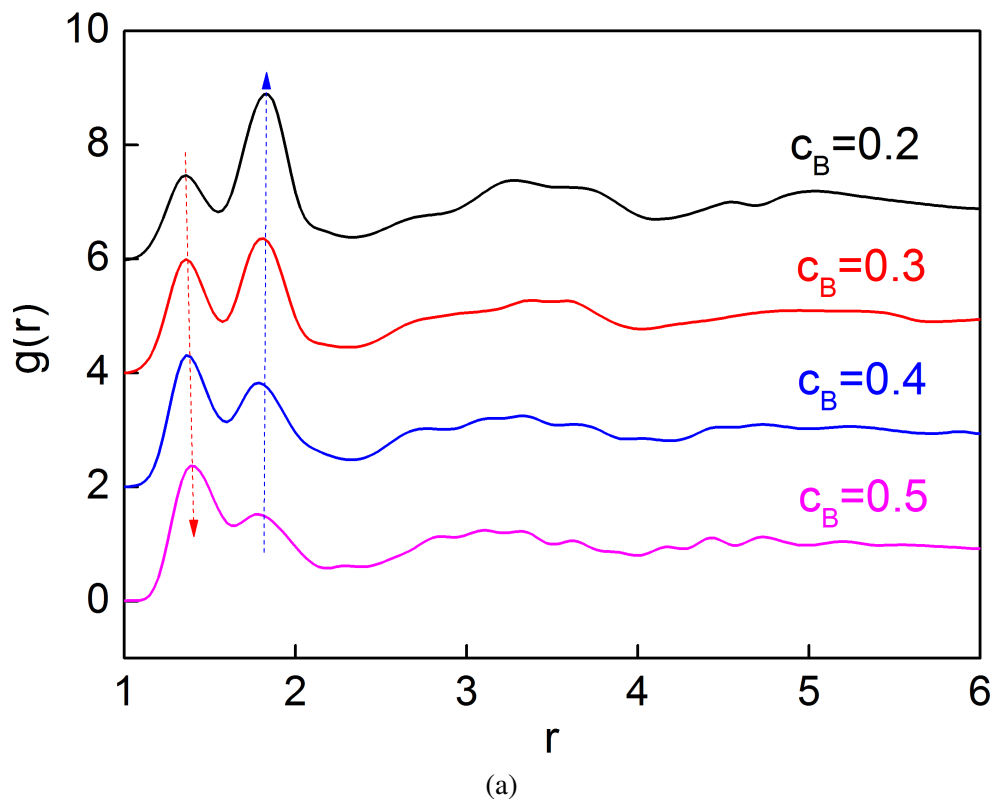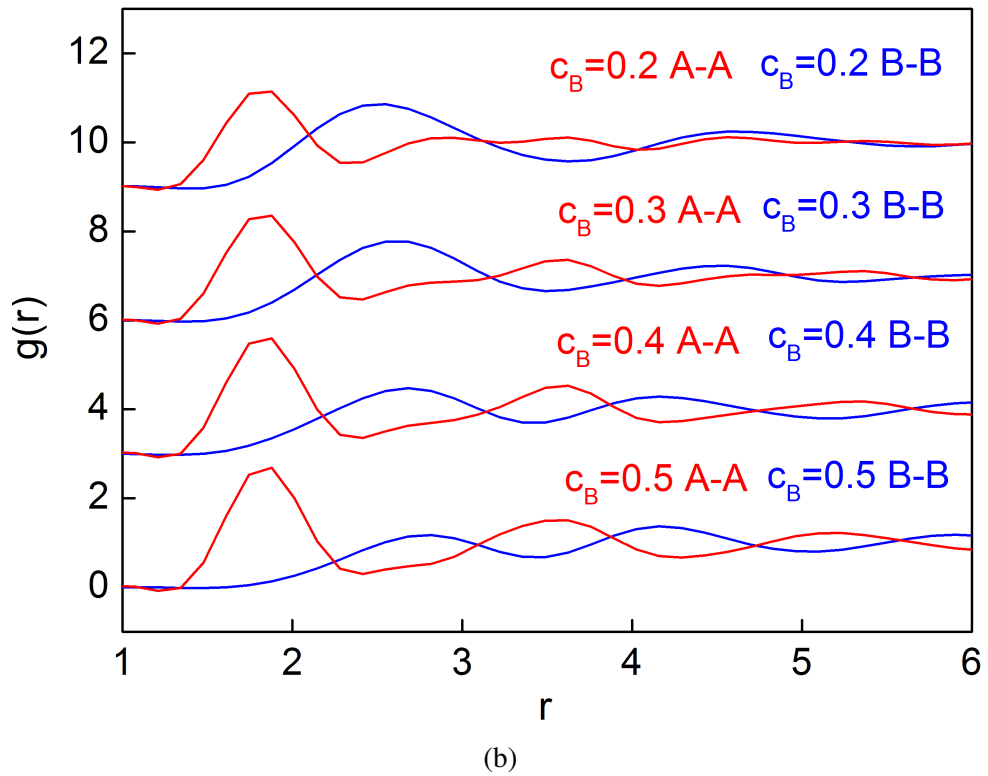
Fig. 6.11 (a) The total PDFs, and (b) the partial PDFs, $g(r)_{A-A}$, $g(r)_{B-B}$ of the binary alloy with the different compositions of $c_B = 0.2, 0.3, 0.4, 0.5$.
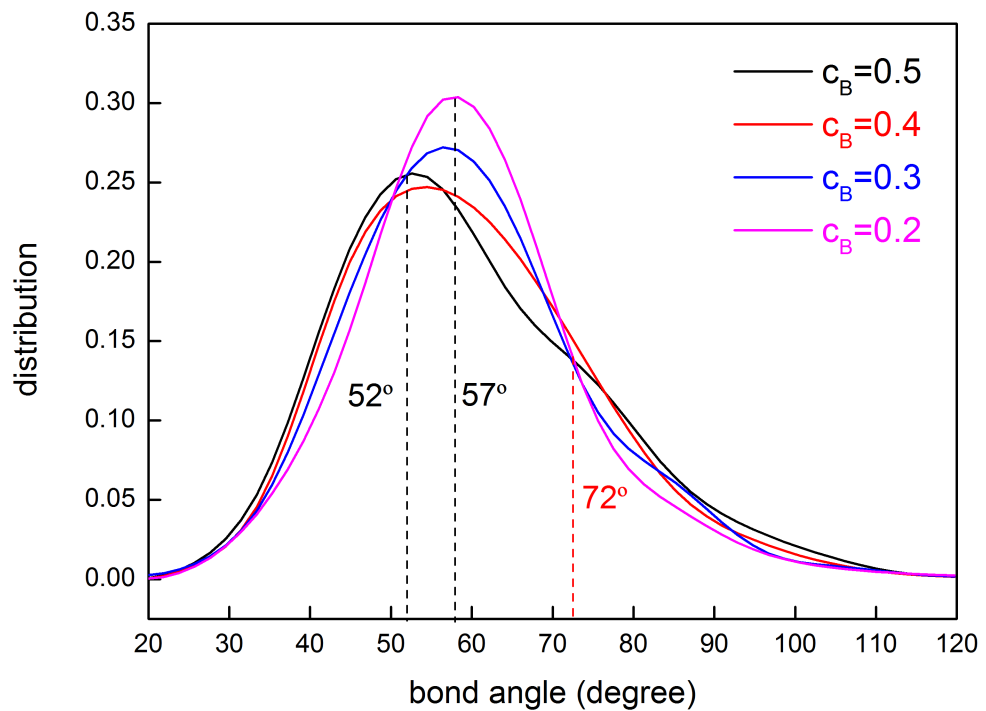
Fig. 6.12 The bond angle distributions of the binary alloys with different chemical compositions of $c_B = 0.2, 0.3, 0.4, 0.5$.

Fig. 6.12 shows the bond angle distribution of the simulated atomic structures with different compositions. For all the compositions, the bond angle is dominantly distributed in the range of $30 - 90°$. For c_B=0.5 the bond angle is main distributed around 52 ° and 72 °. As c_B decreases to 0.4, the bond angle is distributed around 54 °, and is more diffuse (larger peak width). While for c_B=0.3, and 0.2, the bond angle is dominantly distributed around 57 °. As c_B decreases, the peak of bond angle distribution gets more intense.

6.6 Vacancy phase-field crystal model for ternary alloys

In this section, a ternary vacancy phase-field crystal model is developed based on the binary VPFC model. A free energy density term f_{CC} is introduced into Eq. 6.1 to account for the two particle correlation of the component C. The coupling term f_{AC}, and f_{BC} are also included to realise the two body correlation between atoms of component C and atoms from other components. The dimensionless free energy functional for ternary alloys is formulated as:

$$F = \int d\vec{r}[f_{AA} + f_{BB} + f_{CC} + \sum_{i \neq j}^{A,B,C} f_{ij}]$$
(6.10)

Where f_{ii} is the same free energy density function of the pure element part for binary alloys. The coupling term f_{ij} is defined as,

$$f_{ij} = r_{ij} \cdot n_i \cdot n_j$$
(6.11)

The same stochastic conserved equation of motion is employed,

$$\frac{\partial n_i}{\partial t} = \nabla^2 \frac{\delta F}{\delta n_i} + A\nabla\eta \qquad (6.12)$$

For the ternary VPFC model, the same numerical scheme described in section 6.2, *i.e*, Fourier PSM method, is used to discretise the partial differential equations. In addition, MPI parallelism are employed in the computation.

6.7 The simulated atomic structure for ternary alloys

6.7.1 Temperature dependent atomic structure

For ternary alloys, the same simulation methods in section 6.4 are used to investigate the effect of cooling rate on the atomic structure. Firstly, a series of simulations at isothermal transition at different temperatures are performed to obtain the meaningful thermal parameters for the simulation.

6.7.1.1 Isothermal transition

Table. 6.7 lists all temperature parameters used for the simulation of isothermal transition. Six different temperatures are investigated by changing r_i. The PDFs of simulated atomic structures at different temperatures are presented in Fig. 6.13.

Fig. 6.13a shows the stack of PDFs simulated at different isothermal conditions for a ternary alloy. For the structure formed at T=1.1, 0.9, only three peaks can be observed in the short r range, Therefore, temperature of T=1.1, T=0.9 can be considered in the liquid region.

When the liquid is isothermally cooled to the lower temperature, *i.e*, T=0.5, more minor peaks appear in the medium r range, as shown in Fig. 6.13b. It implies the ordered structure starts to be formed during the cooling.
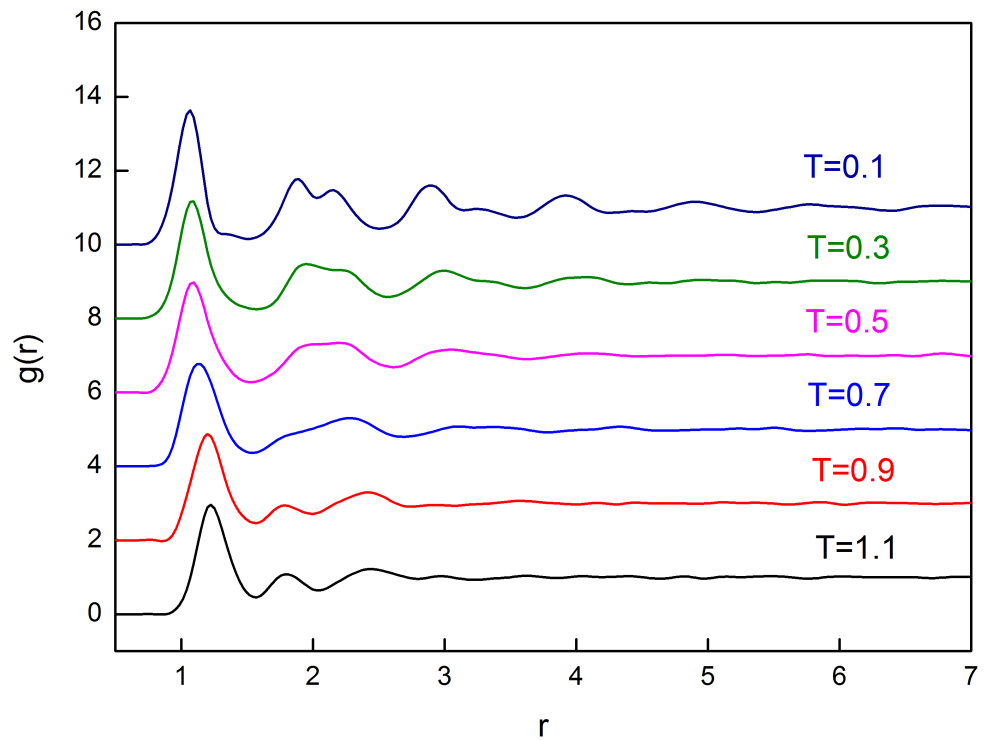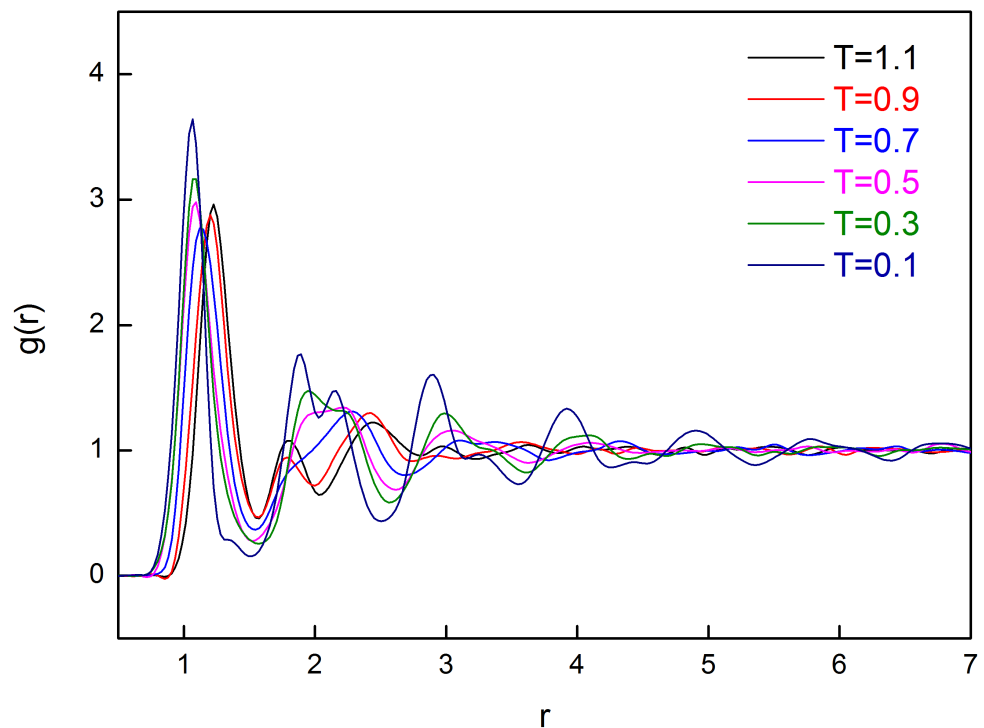
Fig. 6.13 PDFs simulated at different isothermal conditions for a ternary alloy. (a) The stack of PDFs with an offset distance of 2.0 in y direction. (b) The PDFs superimposed together for all temperatures.

Table 6.7 The simulation parameters for isothermal transition of ternary alloys

Parameter	value	*T
	-1.1	1.1
	-0.9	0.9
	-0.7	0.7
r_i	-0.5	0.5
	-0.3	0.3
	-0.1	0.1

The temperature is defined as $T = -r$.

As temperature is further decreased, increasing amount of long range ordered structure is formed at T=0.3 and 0.1. Fig. 6.13b shows that the peak intensity of the first peak increases from 2.8 for the liquid structure (T=1.1) to 3.7 for the ordered structure (T=0.1). In addition, more consecutive peaks appears in the medium r range from 2 to 6, which suggests a formation of medium range order of structure.

6.7.1.2 The effect of cooling rates

The alloys are cooled down continuously from T_l=1.1 to T_a=0.1 with six different cooling rates, which are listed in Table. 6.8.

Fig. 6.14 shows the pair distribution function of a ternary alloy at different cooling rates. It shows a clear transition from disordered to ordered structure with the decrease of cooling rate. With the cooling rate of C1, a typical short range ordered structure is formed, as revealed by the PDF peaks at short r range in Fig. 6.14b. Fig. 6.14a shows that, as the cooling rate decreases, the peak intensity of the first and second peaks get more intense, and the second peak gradually splits. In addition, more medium range peaks, *i.e,* the peaks at r=3.3, r=4.5, get more apparent as shown in Fig. 6.14a.
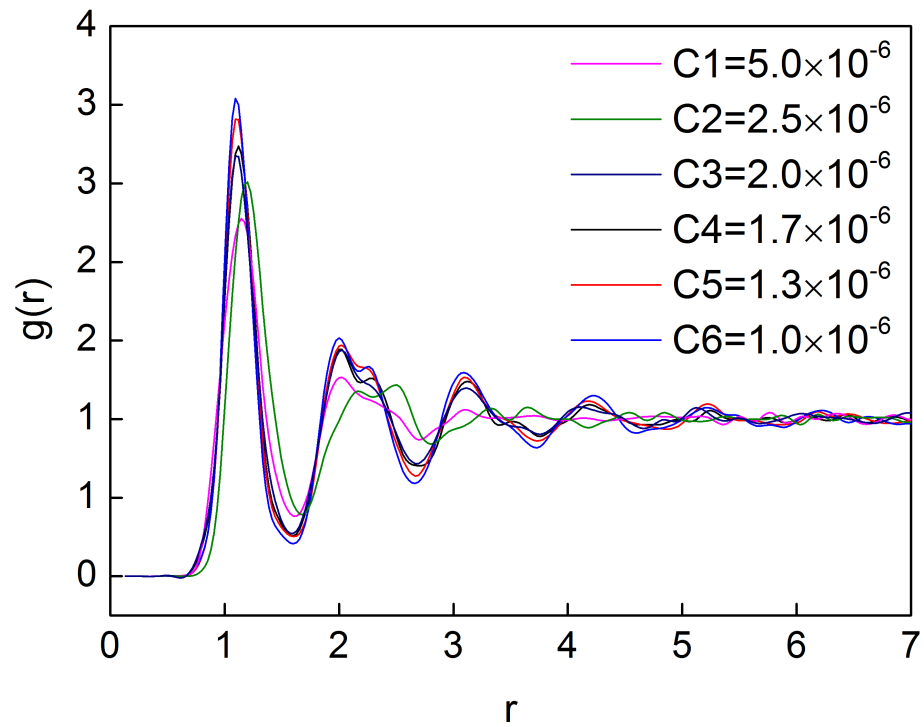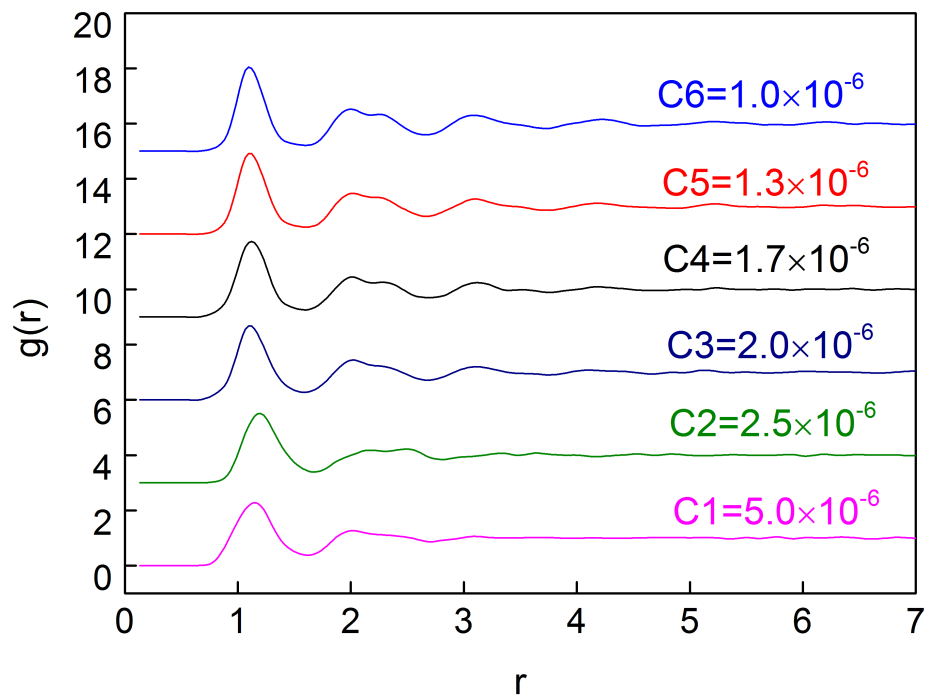
Fig. 6.14 (a) The stack of PDFs, and (b) the superimposed PDFs at different cooling rates. The Y offset for each PDF is 3.

Table 6.8 Cooling rates used in the cooling effect studies for ternary alloys

Cooling case	T_l	T_a	N_t	cooling rate (C)
C1	1.1	0.1	2.0×10^5	5.0×10^{-6}
C2	1.1	0.1	4.0×10^5	2.5×10^{-6}
C3	1.1	0.1	5.0×10^5	2.0×10^{-6}
C4	1.1	0.1	6.0×10^5	1.7×10^{-6}
C5	1.1	0.1	8.0×10^5	1.3×10^{-6}
C6	1.1	0.1	10.0×10^5	1.0×10^{-6}

T_l and T_s, represent the liquidus and ambient temperature, respectively
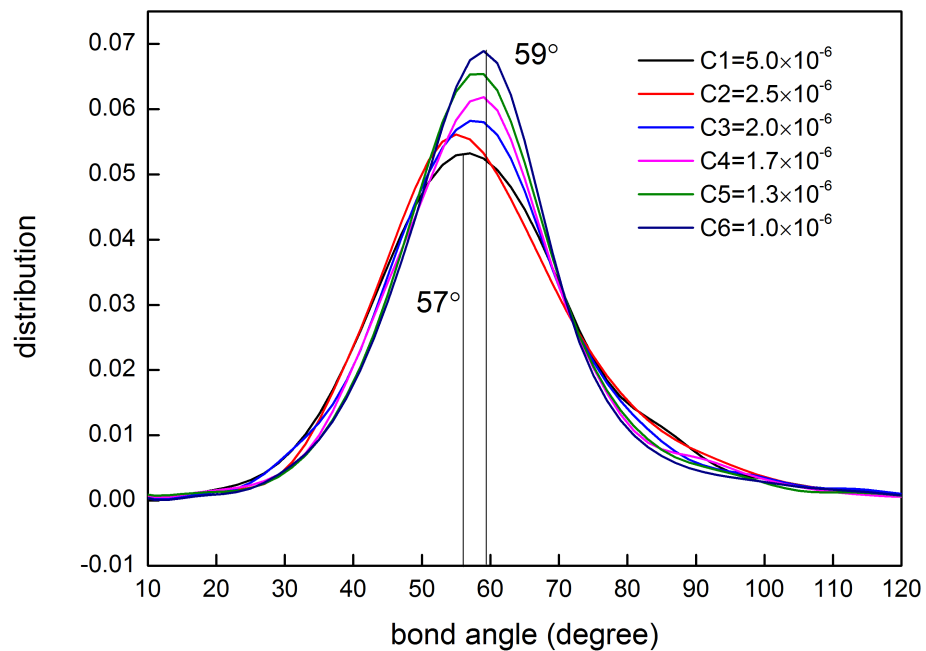
Fig. 6.15 The bond angle distribution of formed structures at different cooling rates.

Fig. 6.15 shows that, the bond angle of the atomic structure formed during the cooling processes is mainly distributed in the range of 20 ° to 100 °. The bond angle of disordered structure formed with rapid cooling rates, such as C1, C2, is distributed in a relatively wide range. However, the bond angle with at slow cooling rates, *i.e*, C3, C4, C5, C6, is distributed in a narrow range. The dominant bond angle is 57 ° for the structure formed at the slow cooling rate. As the cooling rates increase, increasing number of bond angle is distributed at 59 °.

6.7.2   Composition dependent atomic structures

6.7.2.1   The effect of atomic size ratio

Table 6.9 summarises the key parameters used in the studies for the effect of atomic size ratio on the atomic structures. Five different combinations of atomic size for each element are simulated using the cooling rate of 2.0×10^{-6}. The average number density for each element is set to n_i=0.08.

Table 6.9 Atomic size ratio used in the simulation for ternary alloys

q_A	q_B	q_C	q_A:q_B:q_C
1.0	0.9	0.8	1.0:0.9:0.8
1.0	0.9	0.6	1.0:0.9:0.6
1.0	0.9	0.4	1.0:0.9:0.4
1.0	0.7	0.6	1.0:0.7:0.6
1.0	0.5	0.3	1.0: 0.5:0.3

Average number density: n_i=0.08.

Fig. 6.16 shows the simulated atomic structure for each case. The simulated patterns on the left panel present the atomic structure, while those on the right panel show the networks formed by the two element species with the smaller atomic size.

Fig. 6.16a shows that atoms are randomly distributed for the system with a relatively large atomic size ratio. The simulated particles are not well developed, and some strip phases are formed simultaneously with particles. Fig. 6.16b shows atoms of species A and B randomly surround centre atoms.

A similar patterns are formed for the case of q_A:q_B:q_C=1.0:0.7:0.6, however a smaller difference exists between species A and B. Atoms A and B formed an irregular network around atoms C (in blue) with a big atomic size as presented in Fig. 6.16c and Fig. 6.16d.

Fig. 6.16e shows that, for q_A:q_B:q_C=1.0:0.9:0.4, the atoms of species C with a larger atomic size are formed randomly, while atoms of species A and B, which have a similar atomic size, form a network which is a cluster of rings connected with each other, as shown in Fig. 6.16f. Each ring consists of ~ 10 atoms of A and B. The diameter of these rings is determined by the centre atoms of species C. The neighbouring rings share 2 or 3 atoms with each other. For some regions small square structure is formed nearby the irregular rings with atoms less than 10.

Fig. 6.16g presents the atomic structure for q_A:q_B:q_C=1.0:0.9:0.6. As the atomic size of centre atoms C decreases, although a similar atomic network is formed by atoms of species A and B as shown in Fig. 6.16h, the rings- as a basic construction unit of network - are more irregular than the previous case. Each ring consist of 10 or less number of atoms.

Fig. 6.16i presents, with the further decrease in atomic size for species C, the network formed by atoms A and B get more disordered. The average ring unit is formed by even less atoms. These rings in Fig. 6.16j are in the form of distorted square, instead of the distorted circles in previous simulations. Each distorted ring has approximately 8 atoms, which surround the centre atoms.

Fig. 6.17 shows the PDFs of the simulated structure with different atomic size ratio. For q_A:q_B:q_C=1.0:0.5:0.3, there are several diffuse PDF peaks which cover 1-2 atomic size. The peak intensity is ~ 2.6 for first peak and ~ 1.5 for second peak. The PDF for q_A:q_B:q_C=1.0:0.7:0.6 is similar to the previous case. However, the peak intensity is lower, and also the peak is less diffuse.
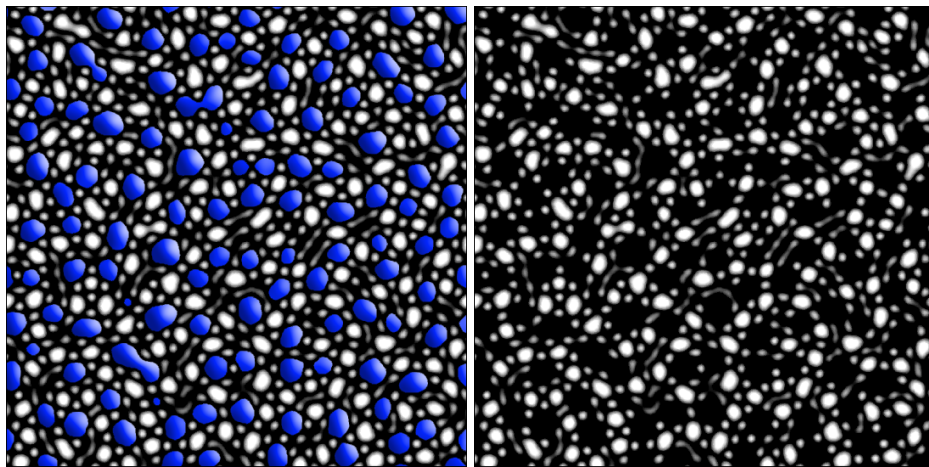
(a) q_A:q_B:q_C=1.0:0.5:0.3

(b) q_A:q_B:q_C=1.0:0.5:0.3
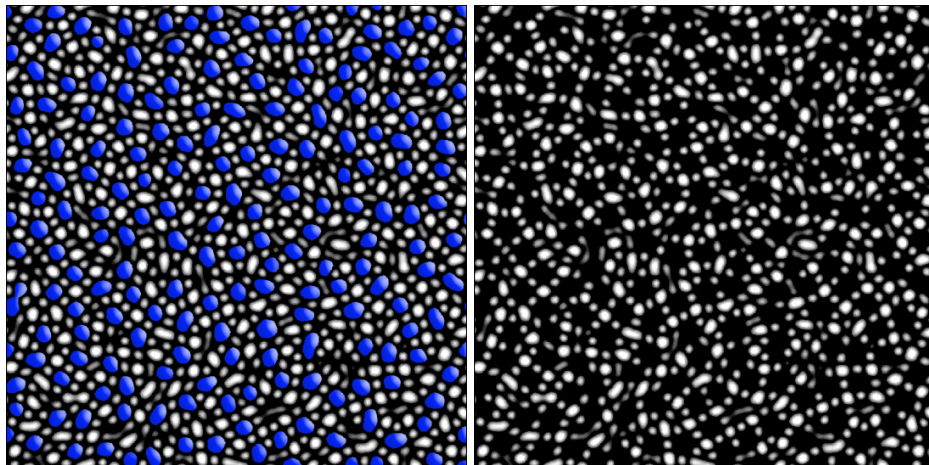
(c) q_A:q_B:q_C=1.0:0.7:0.6

(d) q_A:q_B:q_C=1.0:0.7:0.6
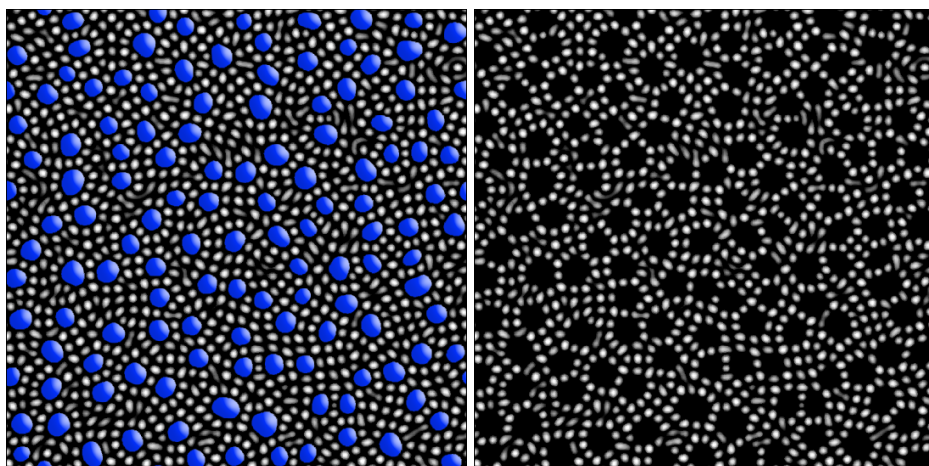
(e) q_A:q_B:q_C=1.0:0.9:0.4

(f) q_A:q_B:q_C=1.0:0.9:0.4

(g) q_A:q_B:q_C=1.0:0.9:0.6

(h) q_A:q_B:q_C=1.0:0.9:0.6

(i) q_A:q_B:q_C=1.0:0.9:0.8

(j) q_A:q_B:q_C=1.0:0.9:0.8
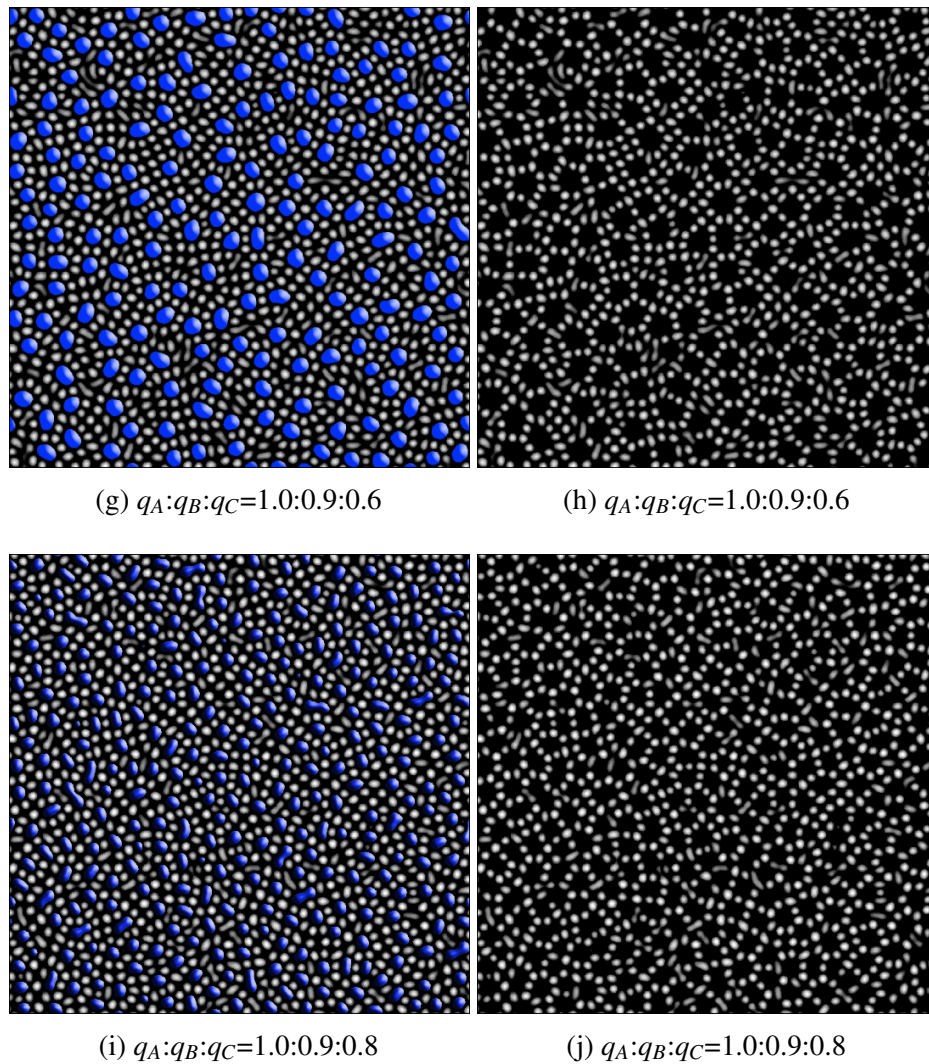
Fig. 6.16 The effect of different atomic size ratio on the simulated atomic structure. The left panel shows the whole configuration of atoms A, B, C. The right panel shows the network formed by atom A and B, while C atoms in blue are not presented.

For q_A:q_B:q_C=1.0:0.9:0.4, in the r range of 1 to 2, two peaks are formed at r=1.5 and r=2.0 as shown in Fig. 6.17b. The peak intensity of the first peak is decreased to 1.6. The third peak has the same peak position as the second peak for the previous case.

Fig. 6.17b shows the PDF for q_A:q_B:q_C=1.0:0.9:0.6. A peak shoulder is separated from the first peak at r=2. The first peak at r=1.5 gets more intense. For the second peak at r=3.5, the peak position does not change.

For q_A:q_B:q_C=1.0:0.9:0.8, Fig. 6.17b shows a different PDF comparing to the others. The dominant peak is located at r=1.5, and the peak intensity increases from 1.5 to 2.0.
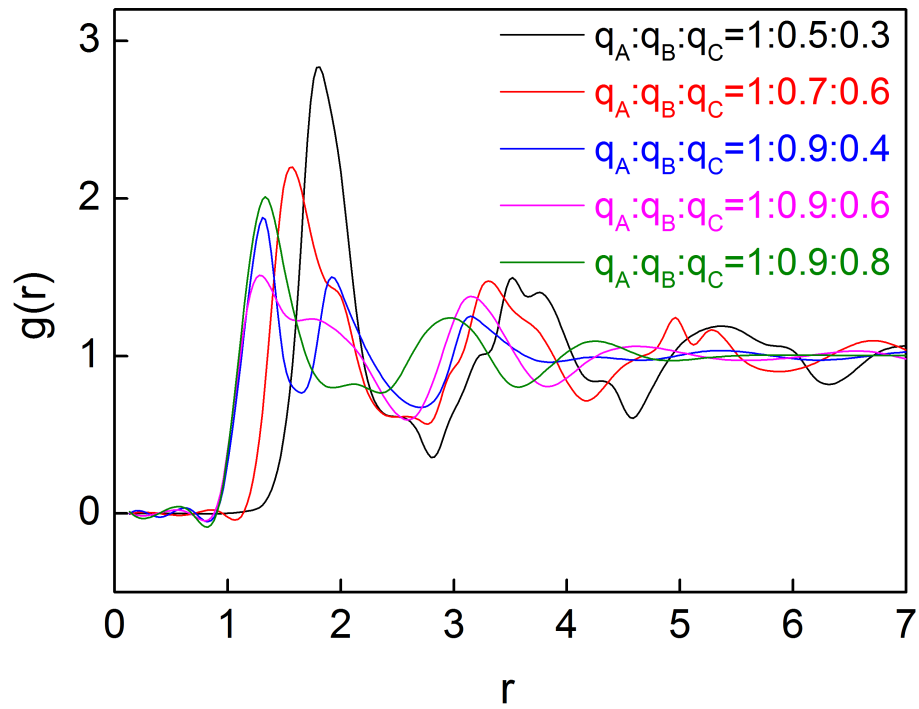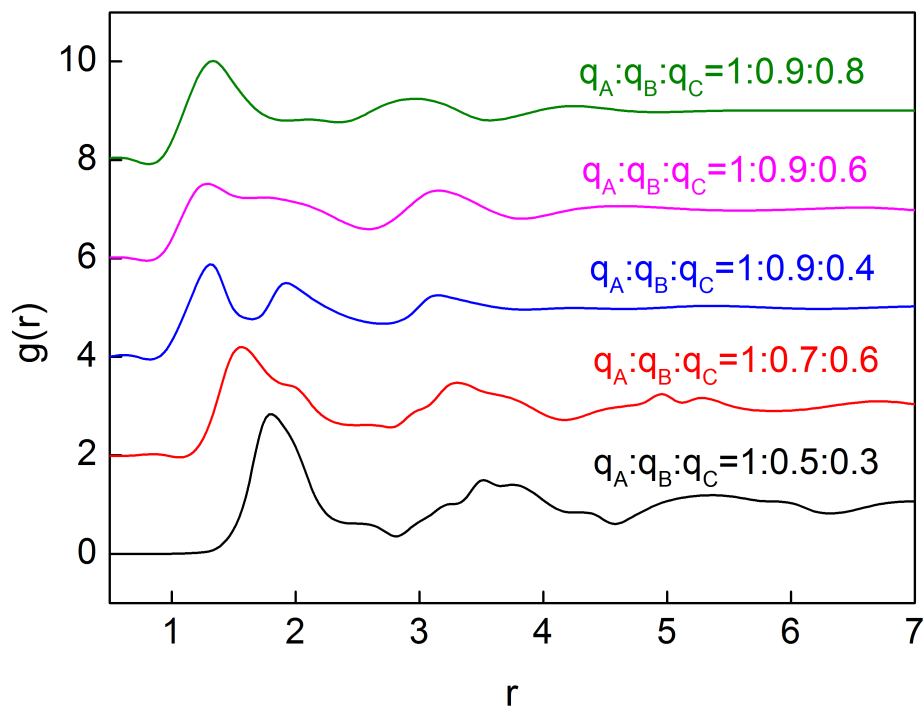
Fig. 6.17 (a) The stacked pair distribution function, and (b) the superiposed PDFs of the simulated atomic structure with different atomic size ratio. The Y offset for each PDF is 2.

While there is no peak separation from the first peak, which is major difference from the previous case. The second peak is shift from r=3.5 from previous case to r=3.0. The third peak is also shifted to the low r.

6.7.2.2   The effect of composition

The effect of different compositions on the atomic structure during the cooling process is simulated using the parameters listed in Table. 6.10. Five different compositions are selected. The total average number density is kept as a constant for all cases, *i.e*, $(\bar{n}_A + \bar{n}_B + \bar{n}_C)$=0.24. The atomic size ratio is set to $q_A : q_B : q_C$= 1:0.9:0.8, and the cooling rate is chosen as 1.2×10^{-6}.

Table 6.10 The compositions used in the simulation for ternary alloys

$\bar{n}_A$	$\bar{n}_B$	$\bar{n}_C$	$^1\, c_B$	$^2\, c_C$
0.08	0.08	0.08	0.33	0.33
0.10	0.08	0.06	0.33	0.25
0.12	0.08	0.04	0.33	0.17
0.10	0.06	0.08	0.25	0.33
0.12	0.04	0.08	0.17	0.33

$^1\, c_B = \bar{n}_B/(\bar{n}_B + \bar{n}_B + \bar{n}_C);\, ^2\, c_C = \bar{n}_C/(\bar{n}_A + \bar{n}_B + \bar{n}_C)$

Fig. 6.18 shows PDFs of the simulated atomic structure at different compositions. For $c_B = 0.33, c_C = 0.33$, the peak intensity of the first peak is 1.5, and there is no peak shoulder separated from it. As shown in Fig. 6.18b, there are two other peaks located at r=3.0 and r=4.2 respectively, and also a few minor peaks in the medium r range. For c_B=0.33, c_C=0.25, there is a small peak shoulder located at r=2, which is separated from the first peak, and the peak intensity of the first peak remains 2.0.

Fig. 6.18b shows, as c_C further decreases to 0.17, the first peak of PDF gets more intense, and the peak shoulder at r=2 is separated from the first peak to form a individual peak. The
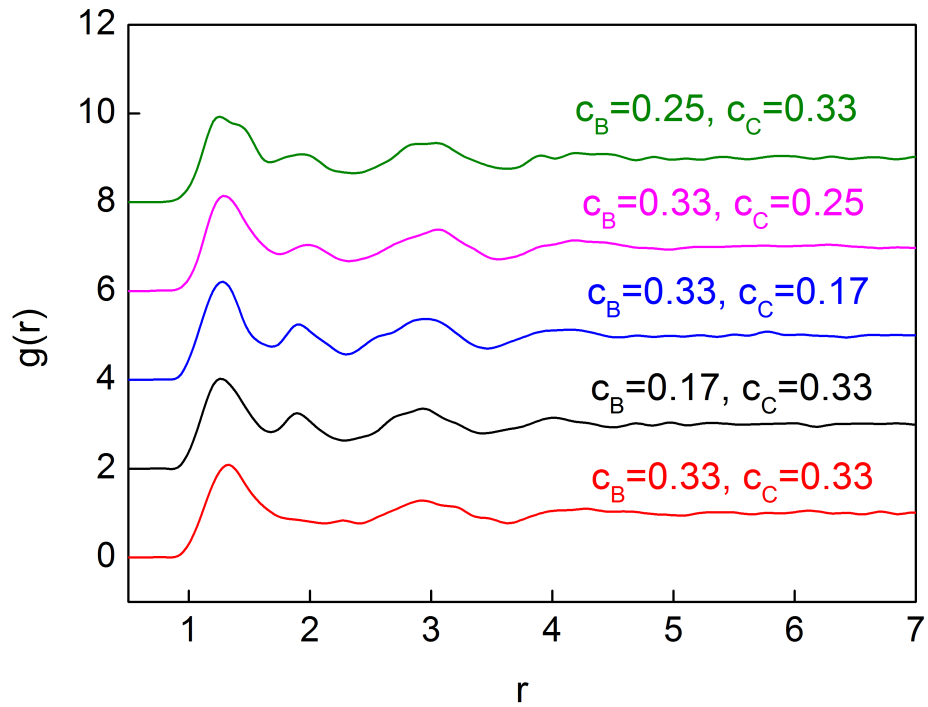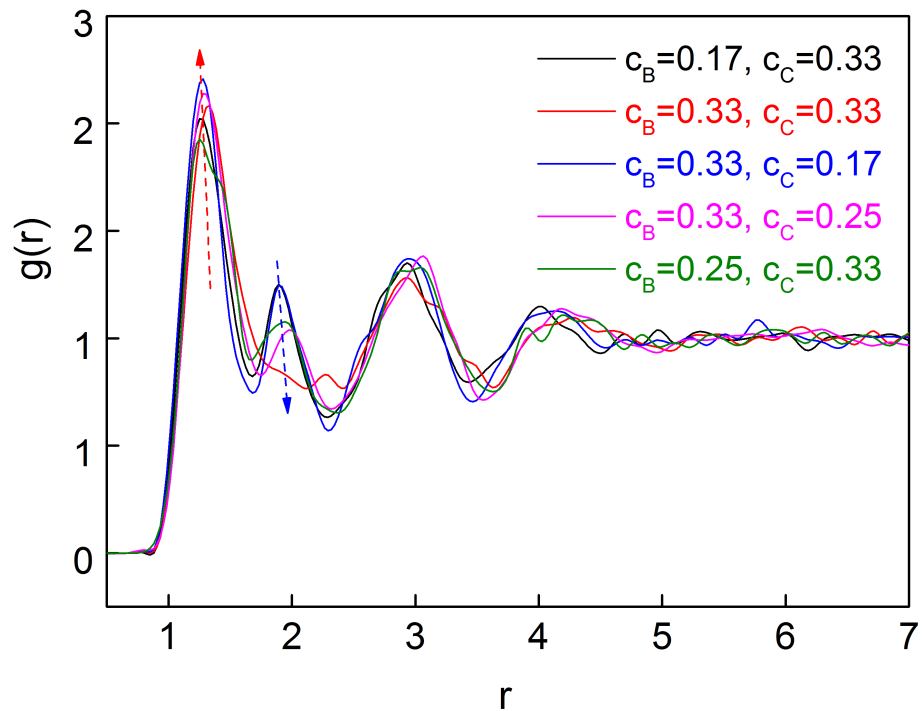
Fig. 6.18 (a) The stacked pair distribution function, and (b) the superimposed PDFs of the simulated atomic structure with different composition. The Y offset of stacked PDFs for each cooling rate is 2.

rest of PDF peaks remain the same position and intensity. The PDF profile for $c_B = 0.25$, $c_C = 0.33$ is similar to that of $c_B = 0.30$, $c_C = 0.25$, however the peak intensity of the first peak (1.9) for $c_B = 0.25$, $c_C = 0.33$, is relatively lower than that (2.1) of $c_B = 0.33$, $c_C = 0.25$. For $c_B=0.17$, $c_C=0.33$, the PDF is also very similar to that of $c_B=0.33$, $c_C=0.17$, while the peak intensity of the first peak and the split peak at r=2.0 is relatively lower.

6.8 Summary

In this chapter, a vacancy binary and also a ternary phase-field crystal model are used to study the effect of cooling rates, and also the intrinsic factors, including atomic size ratio and compositions, on the atomic structure changes.

In section 6.1, a binary phase-field model is introduced, and also the numerical method, *i.e,* Fourier PSM method, is described in section 6.2. The visualisation and simulation methods used for both the binary and ternary alloys are described in section 6.3 and 6.4. Section 6.5 presents all the simulation results for binary alloys, including temperature dependent and composition dependent simulations.

In section 6.6, a ternary vacancy phase-field crystal model is developed based on the binary VPFC model described in section 6.1, which is capable of simulating the multi-component involved atomic structure changes. Section 6.7 presents all the simulation results for ternary alloys. It includes the simulations of temperature-dependent and composition-dependent atomic structure.

Chapter 7

Discussion

A dedicated discussion chapter is presented here to discuss the links between the large amount of experimental data and the relevant simulation results presented in Chapter 4, 5 and 6; and the important scientific findings and major contributions in the relevant research field. The discussion is focusing on,

- The novelties of the experimental methodologies and modelling strategies adopted in the research.

- The important scientific findings and major contributions in understanding of the evolutions of atomic structures of metallic glasses and composites using in-situ pair distribution function and phase-field crystal modelling; and multi-scale 3D structural characterisation of bulk metallic glass composites under thermally shock environment.

7.1   Atomic structures of binary CuZr alloys

Fig. 7.1a is the reproduced PDF for the three binary CuZr alloy from Fig. 4.2b with the r range to 6.5 Å. As already stated in section 4.1.1 of Chapter 4, all three binary CuZr alloys exhibit amorphous structures with typical amorphous PDFs, and the 1st peaks of their PDFs are at the same position, $i.e.$ r = 2.8 Å. However, the maxima of their 1st peak

decreases from 4.7 to 3.7 as Zr decreases from 50% to 35.5% (*i.e.* Cu increase from 50% to 64.5%). In addition, the minor peaks which appeared on the right-hand side of the 1st peak of $Cu_{50}Zr_{50}$ gradually decrease from 2.3 to 1.6 and finally to 1.18 when composition changes from $Cu_{50}Zr_{50}$ to $Cu_{57}Zr_{43}$, and finally to $Cu_{64.5}Zr_{35.5}$. Actually the minor peak in the case of $Cu_{64.5}Zr_{35.5}$ has already become not recognisable. The fact that the 1st peak of all PDFs is at the same atomic distance (r = 2.8 Å) indicates that, there exists a similar short-range ordered atomic structure in the 1st atomic shell (r = 2.8 Å) of all alloys. However, the gradual decrease of their maxima also indicates that the probability of occurrence of such ordered structure becomes less and less as the concentration of Zr decreases (*i.e.* Cu increases). In other words, for the three CuZr binary alloys studied, although they all exhibit similar amorphous structure, especially in the 1st atomic shell, but the degree of order decreases as the composition changes from $Cu_{50}Zr_{50}$ to $Cu_{57}Zr_{43}$ and finally $Cu_{64.5}Zr_{35.5}$. This observation is also supported by the fact that the minor peaks on the right-hand side of the 1st peaks gradually disappear as well.

For the PDF curves in Fig. 7.1a, it is the results of interactions among each atom pair, Zr-Zr, Zr-Cu and Cu-Cu. Using the PFC model (section 6.5.2 of Chapter 6), the contribution of each individual atomic pair to the 1st peak was further quantified. Fig. 7.1b shows the total PDFs and Fig. 7.1c shows the partial pairs obtained from the PFC modelling for the three binary CuZr alloys.

The calculated peak intensity of the first PDF peaks are proportional to the corresponding element concentration as expected for a solid solution behaviour. The increase in the populations of Cu-Cu atomic pairs at 2.8 Å is responsible to the increasing peak intensity of the first peak, while the decrease in the populations of Zr-Zr atomic pairs at 3.2 Å leads to the deceasing peak intensity of the peak shoulder for the first peak.

The experimental and modelling results on the composition dependence of the atomic structure of CuZr metallic glasses point to a solid solution-like replacement of Cu and Zr atoms in the whole composition range [226, 227].

(a)

(b)

(c)
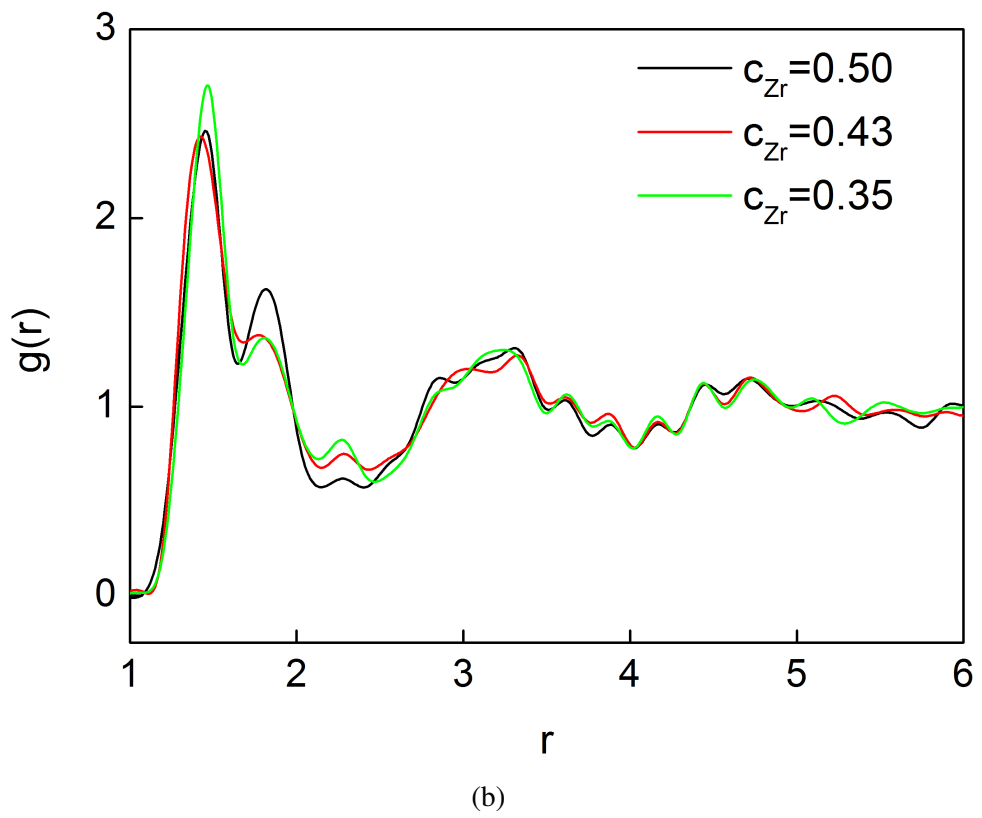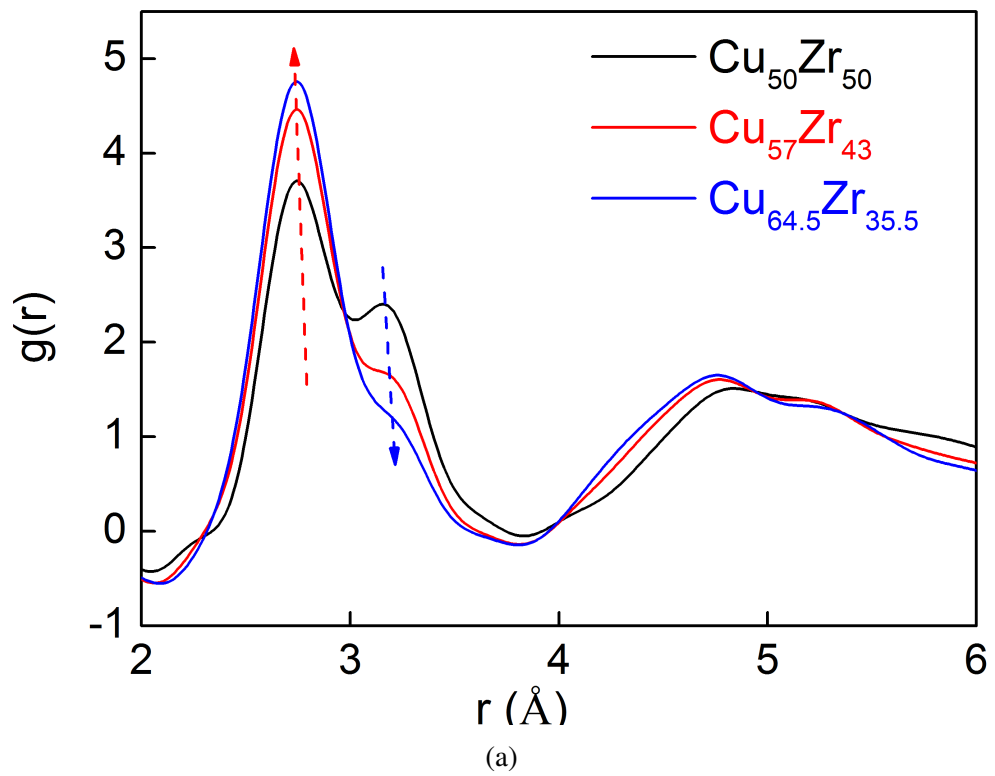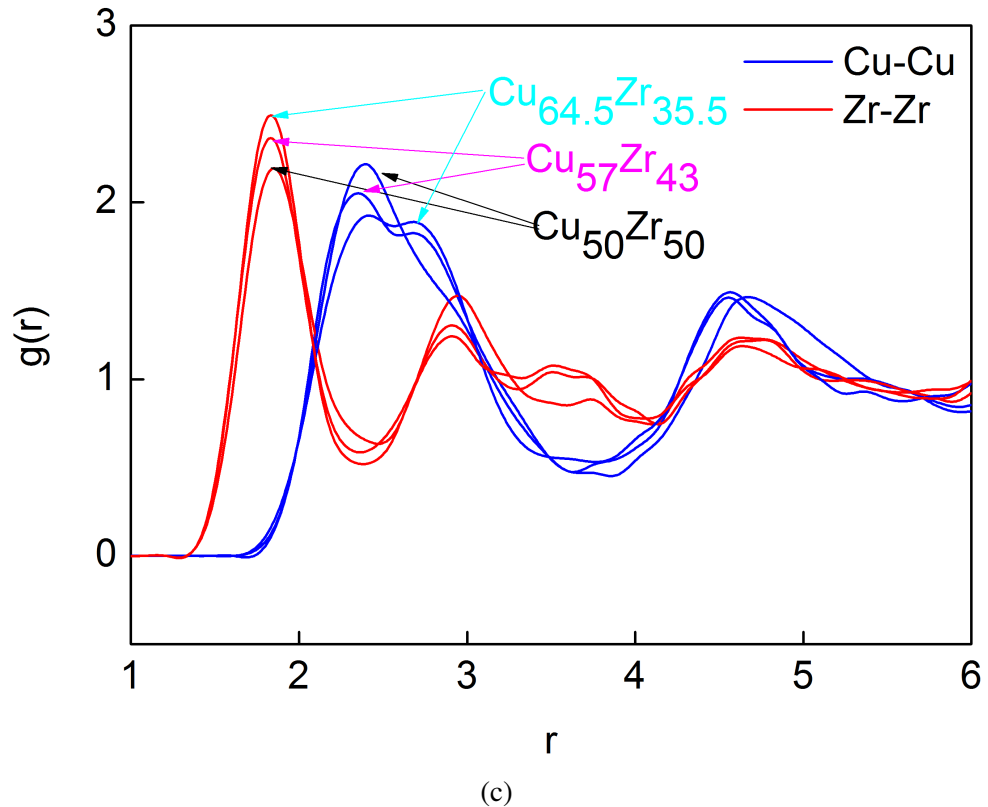
Fig. 7.1 (a) The PDF for the three binary CuZr alloys with the r range to 6.5 Å, (b) the total PDFs simulated, and (c) The partial PDFs for the atomic pairs Cu-Cu, Cu-Zr, Zr-Zr for the three binary alloys simulated using the VPFC binary model described in section 6.4.2 of Chapter 6.

7.2   Atomic structures of binary NiTi alloys

Fig. 7.2a is the reproduced PDF for the three binary TiNi alloys from Fig. 4.6b with the r range to 6.5 Å.

The 1st peaks of their PDFs are at the similar position, *i.e.* r = 2.9 Å. However, the maxima of them decreases from 4.6 to 2.9 as Ti decreases from 75% to 65% (Ni increase from 25% to 35%). In addition, the minor peaks which appeared on the left-hand side of the 1st peak of $Ti_{75}Ni_{25}$ gradually increase from 2.5 to 2.7 and finally to 3.5 when composition changes from $Ti_{75}Ni_{25}$ to $Ti_{70}Ni_{30}$, and finally to $Ti_{65}Ni_{35}$. Different to CuZr alloys, a clear amorphous-crystalline transition took place when the concentration of Ti increased from 65% to 75%.

(a)

(b)

(c)
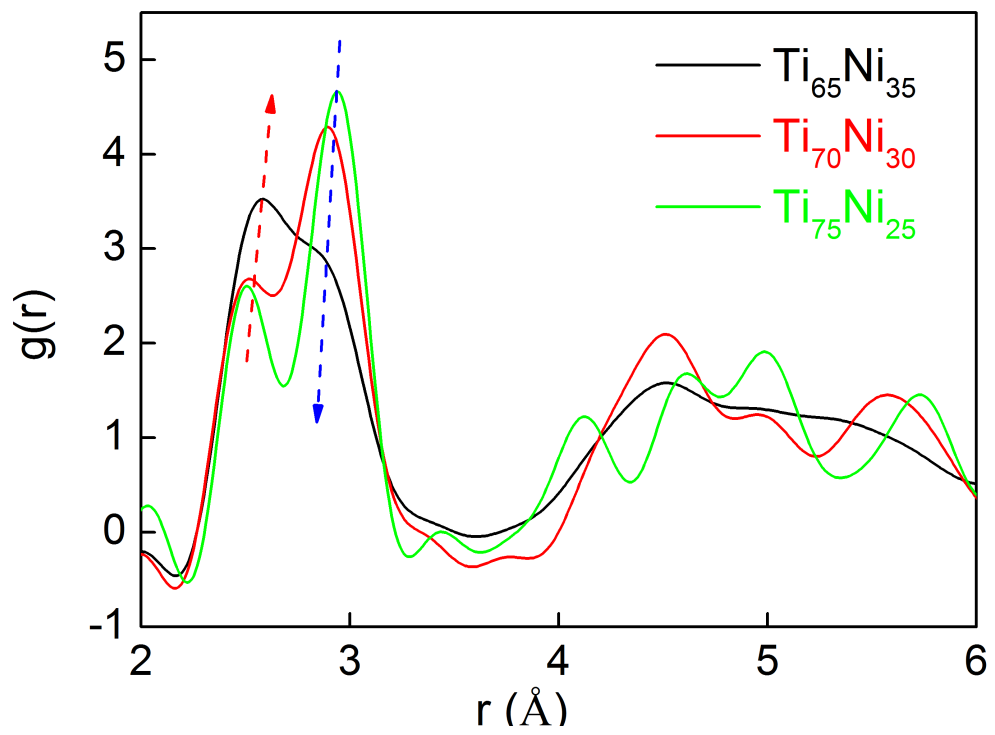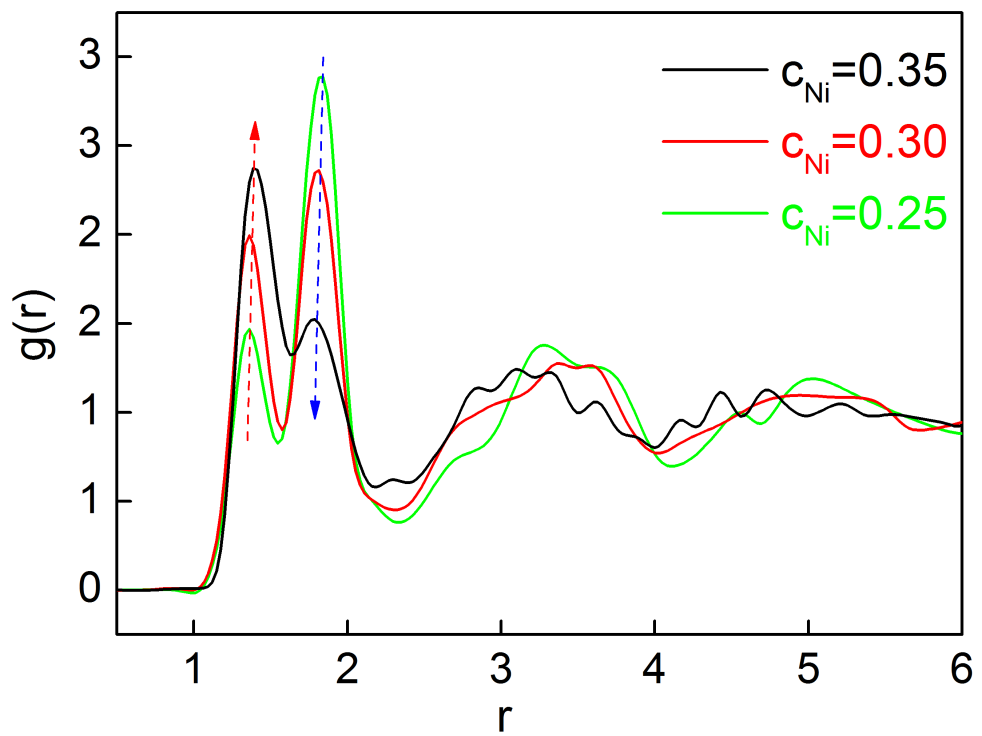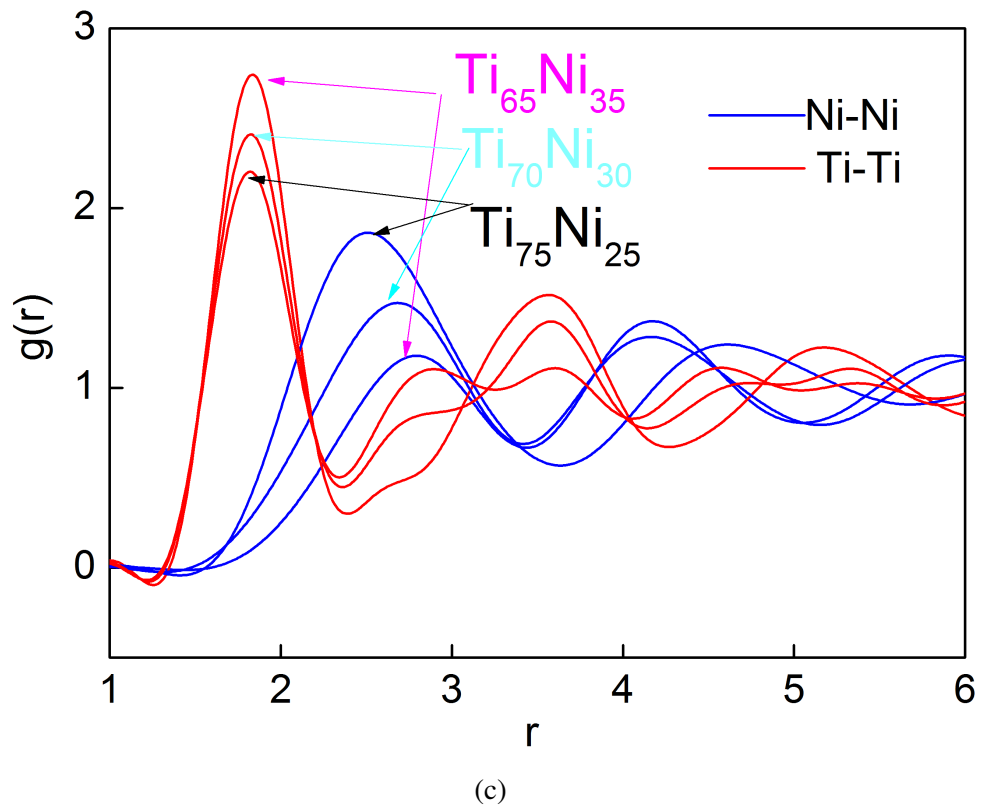
Fig. 7.2 (a) The PDF for the three binary NiTi alloys with the r range to 6.5 Å, (b) the total PDFs simulated, and (c) the partial PDFs for the atomic pairs Ni-Ni, Ti-Ti, Ni-Ti for the three binary alloys simulated using the VPFC binary model described in section 6.4.2 of Chapter 6.

Fig. 7.2b shows the simulated total PDF with the binary VPFC model, which used a very similar atomic size ratio as Ni and Ti. Although the peak position of simulated PDFs do not match the real PDFs, it clearly shows from the simulations that, as the concentration of Ni decreased, the peak intensity of the first peak deceased, while that of the peak shoulder increased. The partial PDFs Ti-Ti and Ni-Ni are calculated and shown in Fig. 7.2c. It is apparent that as the concentration of Ni increased, the peak intensity of first peak of Ti-Ti decreased gradually, while that of the Ni-Ni pairs increased rapidly.

The structure changes in the short range are well captured by VPFC models. However, the phase changes from crystalline to amorphous are not elucidated. The reason is mainly because only the effect of composition on the structure is considered in the simulation. To interpret the structure changes during the phase transition from amorphous to crystalline,

the correlation function needs to be developed based on the true thermodynamic properties of the materials, *i.e*, NiTi.

7.3   Atomic structures of ternary alloys

The studies of ternary alloys are focusing on the effects of different atom size ratio on the resulting atomic structures. Fig. 7.3a is reproduced from Fig. 4.8b. It shows that The peak position of the first peak for $Cu_{55}Zr_{40}Al_5$ is at 2.8 Å and that of the peak shoulder is at 3.2 Å. The peak position of the second peak is at 4.8 Å. While, the peak position of the first peak for $Ti_{55}Cu_{38}Ni_7$ is at 2.6 Å and there is no obvious peak separation from the first peak. The peak position of the second peak is located at 4.5 Å.

In section 7.1 and 7.2, it is clear that the peak position of the dominant PDF peaks does not change with the composition of CuZr and NiTi alloys. It implied that the peak position of PDF peaks is mainly determined by the interatomic distance between the given atomic pairs. In other words, once the constituent elements of alloy system are given, the peak position of PDF peaks does not shift dramatically [228].

However, for the two ternary alloys, *i.e*, $Cu_{55}Zr_{40}Al_5$ and $Ti_{55}Cu_{38}Ni_7$, the peak position of the dominant PDF peaks, *e.g*, the 1st and 2nd PDF peaks changes from 2.8 / 4.8 Å ($Cu_{55}Zr_{40}Al_5$) to 2.6 / 4.5 Å ($Ti_{55}Cu_{38}Ni_7$), respectively. In addition, the peak shoulder of the first peak for $Cu_{55}Zr_{40}Al_5$ does not exist in the case of $Ti_{55}Cu_{38}Ni_7$.

Section 6.7.2.1 of Chapter 6 studied atomic size ratio dependent atomic structure, and clear changes of PDF profile including the peak position, can be observed from the simulated PDFs for alloys with different atomic size ratio.

To interpret the difference of the PDF peak positions for the two ternary alloys using VPFC model, the atomic size ratio, $R_{Zr} : R_{Cu} : R_{Al}$ = 1.0:0.88:0.78 was chosen for $Cu_{55}Zr_{40}Al_5$, and $R_{Ti} : R_{Cu} : R_{Ni}$ = 1.0:0.95:0.95 was set for $Ti_{55}Cu_{38}Ni_7$.

Fig. 7.3b shows the simulated PDF for each alloy, which is similar to the measured one presented in Fig. 7.3a, although the peak position of the simulated PDF (1.3 Å, 1st peak)
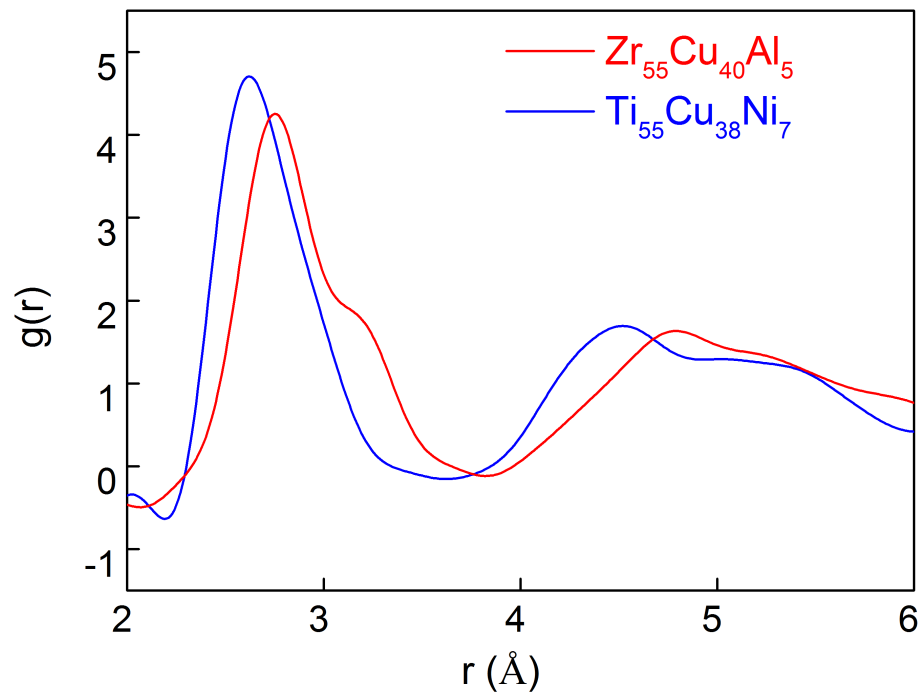
(a)
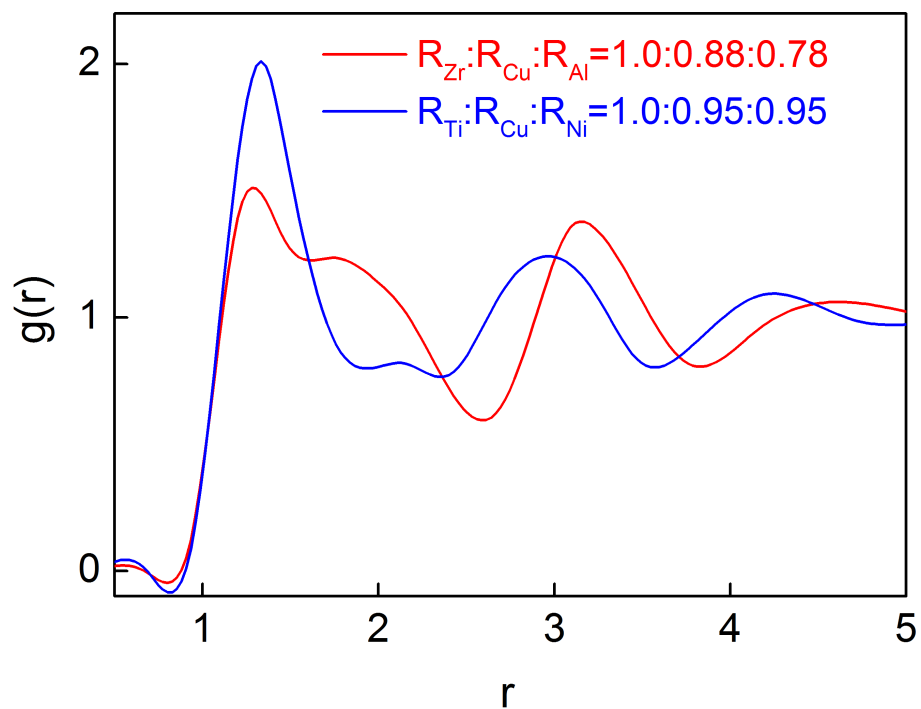
(b)

Fig. 7.3 (a) The measured PDFs for $Cu_{55}Zr_{40}Al_5$ and $Ti_{55}Cu_{38}Ni_7$, and (b) the simulated PDFs for the two ternary alloys with the same atomic size ratio as $Cu_{55}Zr_{40}Al_5$ and $Ti_{55}Cu_{38}Ni_7$.

is different from the measured (2.8 Å, 1st peak) for each alloy. A apparent peak shoulder can be seen from the PDF for $R_{Zr} : R_{Cu} : R_{Al} = 0:0.88:0.78$, and again its peak position is different from that of $R_{Ti} : R_{Cu} : R_{Ni} = 1.0:0.95:0.95$.
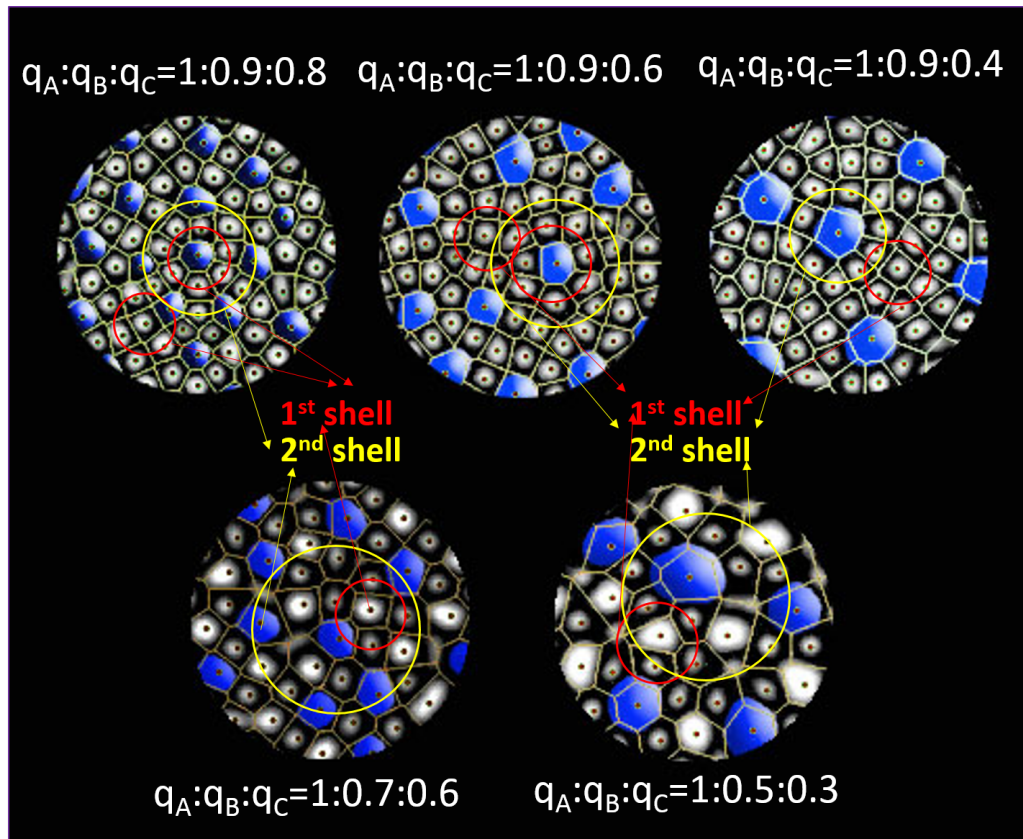
Fig. 7.4 The local structure for alloys with different atomic size ratio of constituent elements. The blue atoms represent C atoms, the bright atoms with larger atomic size are B atoms, and the rests are A atoms. The red circle marked the first shell, and the yellow circle marked the second shell.

To understand the effect of atomic size ratio on the resulting PDFs, the atomic configurations for each case were constructed. Fig. 7.4, reproduced from Fig. 6.16, shows the simulated atomic configurations for each alloy with different atomic size ratio corresponding to the PDFs presented in Fig. 6.17. The 1st and 2nd atomic shells, which correspond to the first and second peaks of PDFs shown in Fig. 7.3b, are marked with red and yellow circles. The diameter of circles represents the PDF peak position of the first or second atomic shells. It can be found that, the first PDF peak for $q_A : q_B : q_C = 1:0.9:0.8, 1:0.9:0.6, 1:0.9:0.4$, primarily consists of A-A and A-B atomic pairs, which have smaller atomic size. While,

the peak shoulder of first peak for $q_A : q_B : q_C$ = 1:0.9:0.8 is from the C-A, and C-B pairs, which have a closed peak position with the first peak. The second peak for $q_A : q_B : q_C$ = 1:0.9:0.4 is from C-A, C-B pairs as well, which is apparently away from the first peak.

Therefore, for $Cu_{55}Zr_{40}Al_5$ the first PDF peak is made of Cu–Cu and Cu–Al atomic pairs, and the peak shoulder is from Zr–Cu and Zr–Al. While for $Ti_{55}Cu_{38}Ni_7$, the first peak is from Cu–Cu and Cu–Ni, however, there is no peak separation from first peak due to the fact that Ti–Cu and Ti–Ni pairs have a very similar bond length with that from Cu–Cu and Cu–Ni.

Furthermore, the first PDF peak for $q_A : q_B : q_C$ = 1:0.7:0.6, $q_A : q_B : q_C$ = 1:0.5:0.3, is formed by B-A, B-B pairs, while the second peak is formed by C-A, C-B, C-C atomic pairs. As q_B and q_C decrease, the atomic size of B and C increase. Hence, for $q_A : q_B : q_C$ = 1:0.7:0.6, $q_A : q_B : q_C$ = 1:0.5:0.3, the bond length of B-A, B-B, C-A. C-B, C-C is relatively longer than that of $q_A : q_B : q_C$ = 1:0.9:0.8, 1:0.9:0.6 1:0.9:0.4. Correspondingly, the first and second PDF peaks for $q_A : q_B : q_C$ = 1:0.7:0.6, $q_A : q_B : q_C$ = 1:0.5:0.3 are shifted to high r position.

7.4   Atomic structure of a multi-component bulk metallic glass

7.4.1   Atomic pairs and partial pair distribution functions

For an alloy of *n* elements, there are $n(n+1)/2$ partial pairs needed to be determined. It is often very challenging to obtain all partial PDFs for an alloy containing more than 3 constituent elements purely by diffraction experiments because a large number of independent diffraction measurements have to be acquired using the anomalous scattering method [68, 21]. For multi-component alloy such as Vit1 ($Zr_{41.2}Ti_{13.8}Cu_{12.5}Ni_{10}Be_{22.5}$) where 5 constituent elements are present, it is virtually impossible to acquire all 15 partial PDFs experimentally.

The crystalline phases formed from slow cooling of Vit1, are mainly composed of Zr_2Cu and $ZrBe_2$. The rest elements, *i.e*, Ti and Ni presented in the alloy occupy certain fraction of atomic sites of Zr_2Cu and $ZrBe_2$, which can be considered as $Zr(Ti)_2Cu(Ni)$ and $Zr(Ti)Be_2$ [185, 186]. It is difficult to determine the atomic fraction of Ti and Ni inside $Zr(Ti)_2Cu(Ni)$ and $Zr(Ti)Be_2$, therefore, it is reasonable to only consider the crystalline phases as Zr_2Cu and $ZrBe_2$.

The crystalline phases (Zr_2Cu and $ZrBe_2$) formed during the crystallisation process have well-defined crystalline structures, and the PDF for their mixture can be modelled by using the real space refinement method [110] as described in section 4.2.1.3 of Chapter 4.

To calculate the total PDF, we can simply select all types of atomic pairs in the structure. However, to calculate the partial PDFs in the structure of, for example, Zr_2Cu, we need to select Zr for atom i and Cu for atom j, and deselect all previously selected atoms for the total PDFs [110].

Based on the crystalline structures of Zr_2Cu and $ZrBe_2$ used in the refinement, the partial PDFs, *i.e*, Zr-Zr, Zr-Cu, Cu-Cu, Zr-Be, Be-Be can be calculated. However, as shown in Fig. 4.18, Cu-Cu and Be-Be pairs contribute very little to the total PDF, and therefore they are negligible due to the low atomic form factor for Be (4 e·atom^{-1}), and low concentration of Cu (12.5 at.%). Their peak positions of the dominant partial PDFs are determined as shown in Fig. 4.14. Although the crystalline phases no longer exist in the liquid and amorphous state, these partial PDFs still can be used to interpret the changes of PDF peaks during the heating and cooling processes, since the PDF peak positions of these atomic pairs do not change abruptly during crystallisation and glass formation [229, 230]. Table 4.1 summarises the possible atomic pairs that contribute to the PDF peaks (Fig. 4.14) of Vit1 alloy.

7.4.2 Temperature dependent atomic structure evolution

7.4.2.1 Novelties of the experimental apparatus for in-situ PDF studies

In-situ imaging and diffraction studies of materials subject to high temperature processing, *i.e.* solidification, heat-treatment, and chemical reactions using synchrotron X-rays are an important advanced research in the fields of materials, physics, chemistry, engineering and manufacturing [231]. A number of either standard furnaces or custom-made reaction cells were used or developed for such studies at different beamlines of different Synchrotron X-ray facilities. For example, the standard hot air blower at beamline I11 of DLS that can heat capillary gas cells up to $\sim$ 1,000 °C [232, 233], the laser heating system at TOMCAT of Swiss Light Source that can provide near-isothermal and linear temperature gradient capabilities ranging from 400 °C to 1,700 °C [234], the Oxford-Diamond in-situ cell which is commissioned in beamline I12 of DLS for studying chemical reactions, can heat up to 1,200 °C using infrared heating [235].

None of the above mentioned furnaces or cell meets the requirement of the in-situ studies described in this thesis. The hot air blower is a standard heating mechanism for powder diffraction with powders or very small samples contained inside the capillary tube. However the hot air blower available at DLS is designed for I11 beamline, which is not suitable for such as rapid acquisition PDF experiment [232, 233], which needs the 2D area detector [105]. In addition, the hot air blower only can provide the heating capability, but it is unable to provide controllable cooling rates.

The laser heating system is a very unique heating system at TOMCAT and the temperature can reach $\sim$ 1,700 °C. It is ideal for such an in-situ diffraction experiment, however it is only commissioned in beamline TOMCAT, and TOMCAT is designed for imaging rather than diffraction measurements [234].

The Oxford-Diamond reaction cell uses infrared (IR) heating to heat up samples up to 1,200 °C [235], the problem of this furnace is that, IR heating constrains the materials for sample container due to that fact that the efficiency of sample heating is dependent upon

the IR absorptivity, thermal conductivity, and emissivity of the container material [235]. For crystalline samples, there are a lot of materials available for sample container, such as recrystallised alumina cruicible [235]. However for PDF studies of metallic glass samples, a very low background from sample container is needed [28], therefore, most of the sample containers used in the beamline are not suitable any more.

To meet the requirement of this research, our research group designed and made a dedicated experimental apparatus with each module showed in Fig. 3.2 in Chapter 3. The detailed CAD design information of each module can also be found in the Appendix A. It is a multifunctional furnace with a module-based design to realise the required functions of heating, cooling, inert gas circulation, temperature data logging and synchronisation with X-ray diffraction pattern acquisition. The furnace has inherited the advantageous features of the solidification apparatus used for the high speed synchrotron X-ray imaging studies of metal solidification under ultrasound [236, 237], and pulse magnetic field [238].

In summary, the unique advantages of the apparatus are:

- The three main physical modules, *i.e.* the heating unit, the gas circulation unit and the sample holder are independent to each other and can be mounted on different linear stages and moved independently. This arrangement allows each module be assembled without interfering with others, achieving a quick setup for in-situ experiments, exchanges of samples, and X-ray beam alignment and focusing onto samples.

- The sample holder (A3 in Fig. 3.2) is designed with multiple functions. It is not only used for holding the samples in place during experiments, but also as a chamber to introduce inert gases for either as a protection medium (from oxidisation in high temperature) or as a cooling medium. Two thermocouples can be also threaded through the tube (P11 in Fig. 3.2) and positioned as close as possible to the samples (< 1 mm) as illustrated in Fig. 3.2. The distance is close enough to monitor and record the actual temperature of the sample but far away enough from the X-ray beam path to avoid any undesired X-ray scattering information from the thermocouples.

- The tube furnace made by fibre mastic with a quartz tube inside the heating wire allows a very controllable and repeatable temperature profile be achieved for each heating cycle, and the heating profile used in experiments is illustrated in Fig. 3.6a. Repeatable cooling rates as shown in Fig. 3.6b, were also achieved by regulating the flow rates of either Ar or He, or both flowing through the sample holder.

Using this unique furnace, the thermal data measured was logged in and synchronised with the acquisitions of X-ray diffraction patterns during experiments, and therefore each diffraction pattern has a registered temperature in the recorded dataset. Using the DAWN v 1.7 [182] and PDFget3 [107], the large diffraction dataset (typically > 1,500 two dimensional diffraction patterns in a single experiment) can be batch processed conveniently, creating the water-fall type diffraction spectra or PDF plots as function of temperature as shown in section 4.2 of Chapter 4.

7.4.2.2   Local atomic structure evolution during heating

Vitreloy with the composition of Ti-Zr-Ni-Cu-Be can be casted into bulk glassy state using relatively low cooling rates, *i.e.* 10^0-10^2 K/s [58], and therefore it has been used as a model alloy system in many previous experiments to investigate the glass formation [239] and crystallisation [240–242] under different thermal conditions. However, most of previous studies were performed ex-situ [239–242, 185], or in-situ however in reciprocal space which cannot reveal the dynamic evolution of the local structure at atomic scale. For example, Yavari studied in-situ the crystallisation behaviour in glassy and liquid state of bulk metallic glasses in 1999 [243], and Uriarte [244] in 2001 and Li [245] in 2009 studied the formation of metastable phases in bulk Zr-based metallic glasses during heating using synchrotron X-ray diffraction in reciprocal space. An in-depth understanding of the structure evolution in real space using pair distribution function is paramount important, and has been rarely reported [246, 247, 230, 228] for establishing the processing-structure relationship.

The water-fall plot of the diffraction spectra shown in Fig. 4.11 clearly captured the structural transition of Vit1 from an amorphous state to crystalline state during the crystallisation process when heated to a temperature above 467.4 °C. The crystallisation process continues until 682.3 °C, followed by the melting process until 720 °C. However only from those spectra (the reciprocal space information), it is not clear how atom clusters in a particular atomic shell evolve from a more disordered state into a more ordered state during the crystallisation process and again back into the more disordered state during the melting process. Such dynamic information at local atomic level can be extracted from the PDF curves (the real space information) as illustrated in Fig. 4.13.

Continuous increase in the short (SRO) and medium range order (MRO) during crystallisation is well characterised by $\Delta G(r)$ functions in Fig. 7.5. The $\Delta G(r)$ function is defined as the difference between $G(r)$ at various temperatures and the one at 750 ° C ($\Delta G(r) = G(r) - G(r)_{750°C}$). The positive $\Delta G(r)$ values at the G(r) maxima as well as the negative $\Delta G(r)$ values at G(r) minima show that the population of atoms contributing to short and medium range order increases during heating [228].

Apparently, any reconfiguration of atoms within different atomic shells is reflected in the shifts of PDF peak positions and changes of peak intensities (the maxima of those peaks) [247, 228]. To fully quantify such reconfiguration of each atomic shell, a full set of the partial PDFs for each atomic pair that constructs the atomic shell needs to be obtained [246, 247], then the contribution of each partial PDFs to the full PDF can be quantified and understood [246, 247].

Fig. 4.18 shows the real space PDF refinement of the dominant crystalline phases of Zr_2Cu and $ZrBe_2$, and also partial PDFs derived from them. Fig. 4.14 shows all the peaks and hidden peaks detected in the PDF profiles using 2nd derivative method as described in section 3.3.6. Each of the peaks and hidden peaks detected is able to be found a corresponding atomic pair according to their peak position, as shown in Table. 4.1.

Fig. 4.15 presents the maxima of all PDF peaks in the r range of 2 to 10 Å, which covers four atomic shells. It shows that the maxima of most peaks decreased by 0 - 0.5 from 100 to

(a)

(b)

(c)
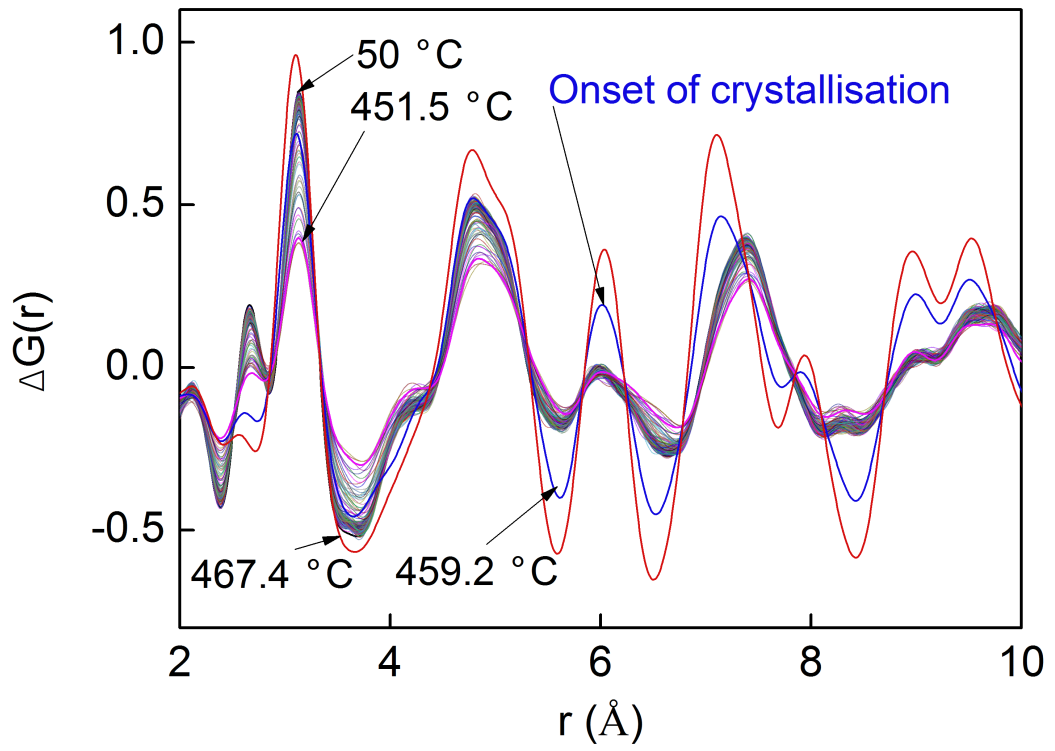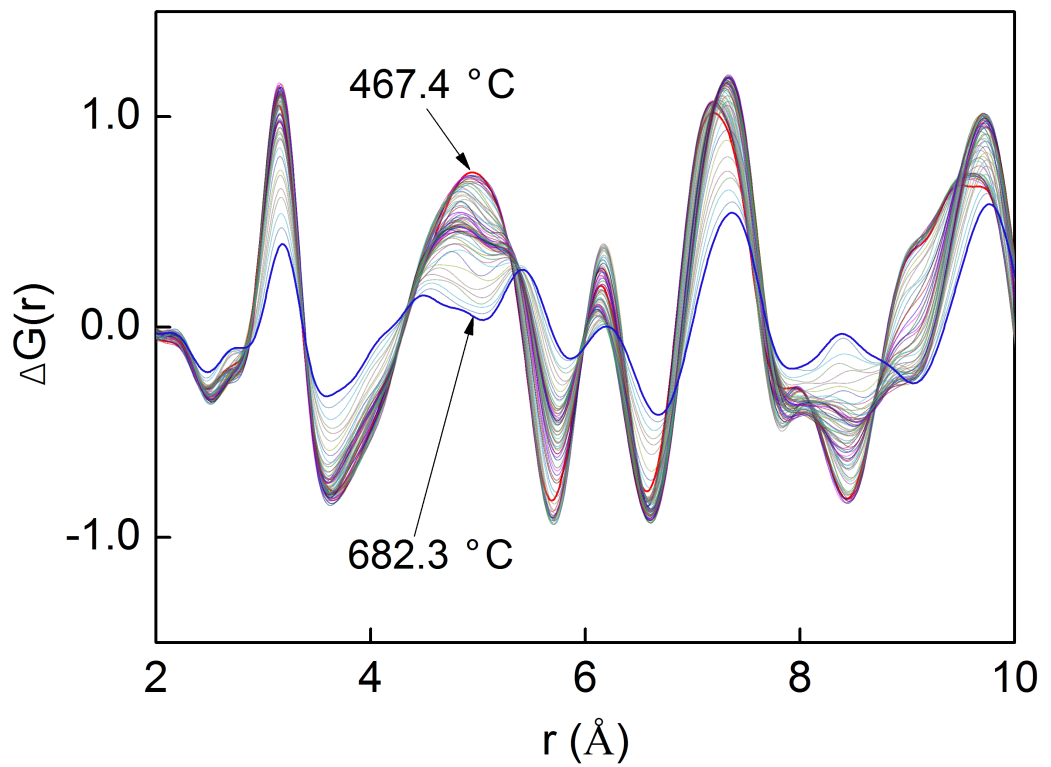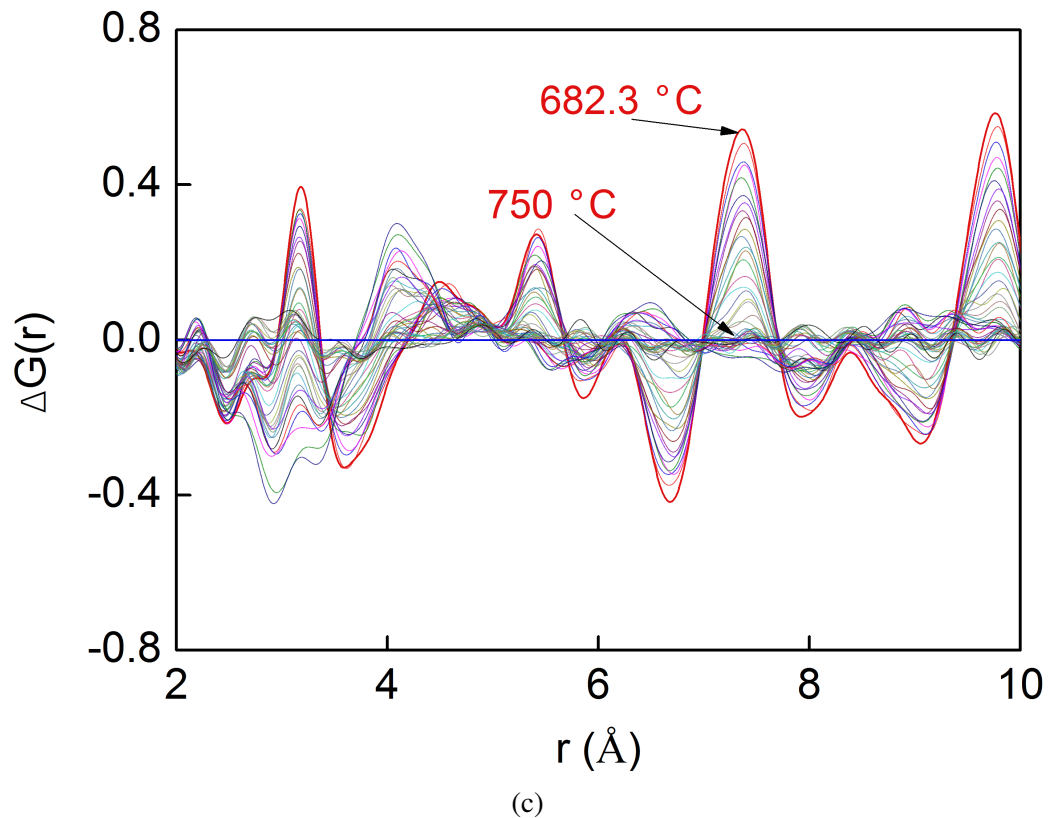
Fig. 7.5 $\Delta G(r)$ functions showing the difference between $G(r)$ at various temperatures and the one at 750 ° C ($\Delta G(r) = G(r) - G(r)_{750°C}$) during continuous heating at 1.5 K/s from (a) 50-467.4 ° C, (b) 467.2-682.3 ° C, and (c) 682.4-750 ° C.

467.3 °C, implying that the structure is relaxing as the temperature increases. The effect of the structure relaxation is to sharpen the PDF peaks without significantly shifting the positions [229] (Shown in Fig. 7.5a). Fig. 4.12 shows that during the heating, the peak shoulder of the main peaks, such as S2_P3 is increased in height and narrowed in width [229]. The initial changes in the structure below the crystallisation temperature are possibly due to local atomic stresses [248].

Fig. 4.16a presents that, as the temperature increased, the PDF peaks formed by most of the Zr-Zr pair (S1_P2, S2_P1, *etc*.) and Zr-Be pair (S4_P1) experienced dramatic changes in the temperature range from 459.2 to 467.3 °C in 6 s (shown in Fig. 7.5a). The peak intensity increased by 0.5 - 1.5, which implied a rapid structure reconfiguration in the short to medium range [228] to a more densely packed atomic structure in the long range is achieved during the crystallisation [229].

Fig. 4.16b shows that Zr-Cu atomic pair (S2_P2) and Zr-Zr pair fitted for Zr_2Cu (S2_HP1) were found to experience an earlier change at 270 °C. The peak intensities of these two peaks increased by 0.7. From 270 °C to melting temperature 720 °C, the peak intensity of these two peaks remains the same.

A dramatic increase of peak intensity for all PDF peaks occurred at two different temperature, 270 °C and 467.3 °C during heating. It suggests that, during the heating, part of the Zr-Zr (from Zr_2Cu) and all the Zr-Cu atomic pairs rapidly reconfigured to form the ordered structure Zr_2Cu at 270 °C, although there were no apparent diffraction peaks formed by Zr_2Cu that can be observed in diffraction spectra in Fig. 4.11. While most of the Zr-Zr and Zr-Be atomic pairs rapidly reconfigured to $ZrBe_2$ ordered structure at 467.3 °C, and also part of Zr-Zr pairs, *e.g*, S1_P1, S3_HP3, evolved to Zr_2Cu ordered structure.

It implied that most of Cu atoms reconfigured to the ordered structure of Zr_2Cu at 270 °C, while part of Zr atoms still existed in disordered structure and delayed to form Zr_2Cu until 467.3 °C, after then, they started to form a perfectly ordered crystalline structure of Zr_2Cu. In contrast, the Zr and Be atoms concurrently reconfigured and formed the ordered structure $ZrBe_2$ at 467.3 °C. The result is in contradiction to the fact reported by Van *et, al* [185] that $ZrBe_2$ (380 °C) is formed at nearly the same temperature with Zr_2Cu (385 °C) in an annealed Vit4 alloy.

In addition, more structure information was revealed by the analyse of peak position, it can be observed from Fig. 4.17 that, the peak position of Zr-Zr (SH_P1), Zr-Cu (S1_HP1) atomic pairs in the first atomic shell was getting closer when the temperature increase from 467.3 °C.

For the 2nd atomic shell, the peak position of Zr-Be pairs (S2_P1, S2_P3) was suddenly shifted from 5.00 Å to 4.90 Å, and from 5.85 Å to 5.75 Å, respectively at 467.3 °C. While the peak position of Zr-Cu pairs (S2_HP1) was shifted from 4.55 Å to 4.49 Å when the temperature increased from 100 to 270 °C.

For the 3rd atomic shell, the peak position of Zr-Zr atomic pairs ($ZrBe_2$, S3_HP2) was shifted from 7.20 to 7.35 Å, while that of Zr-Zr atomic pairs (Zr_2Cu, S3_HP2) experienced

a sudden shift from 7.55 Å to 7.45 Å at 467.3 °C, then it was shifted back to 7.70 Å as the temperature further increased.

7.4.2.3 Local atomic structure evolution during cooling

Section 4.2.2 present the atomic structural evolution of Vit 1 under three different average cooling rates, 14.7, 3.35, 0.79 K/s. The interesting phenomena found in the cooling processes are discussed in details in this section.

Fig. 7.6 shows $\Delta G(r)$ functions for the three different cooling rates. For 14.7 K/s, the peak shape does not change too much, however the height of the peaks increases with the decreasing temperature as the local ordering increases rapidly. For the case of 3.35 K/s, and 0.79 K/s, the crystallisation occurs from the super-cooled liquid. Fig. 7.6 shows the peak shape changes obviously, and the modulus of minima and maxima of $\Delta G(r)$ increased with the deceasing temperature dramatically.

In detail, for the case of 14.7 K/s, Fig. 4.23 shows that the glass formation occurred at a certain temperature, and the formed amorphous phase has a very similar PDF profile to the liquid phase [228]. Similarly, the analyses of the peak intensity of the PDFs give more quantitative information concerning glass formation, and Fig. 4.22 and 4.24 shows that the onset temperature of glass formation is 380 °C during the cooling process. However, Busch *et, al* reported that the onset temperature of glass formation T_g is around 410 °C [249]. The difference may be due to the fact that, T_g is measured by differential scanning calorimetry (DSC) [249, 250], however the T_g in our study is determined from a continuous cooling process. The same reason may be accounted for the difference of onset temperature of crystallisation T_x, which is 422 °C reported by Soubeyroux *et. al* [250].

Fig. 4.24 also shows that the maxima of all peaks increases (in the range of 0.5-1.0), when the temperature decreased from 380 °C to room temperature, indicating that the amorphous phase has a more densely packed atomic structure comparing to the liquid structure [228].

(a)

(b)
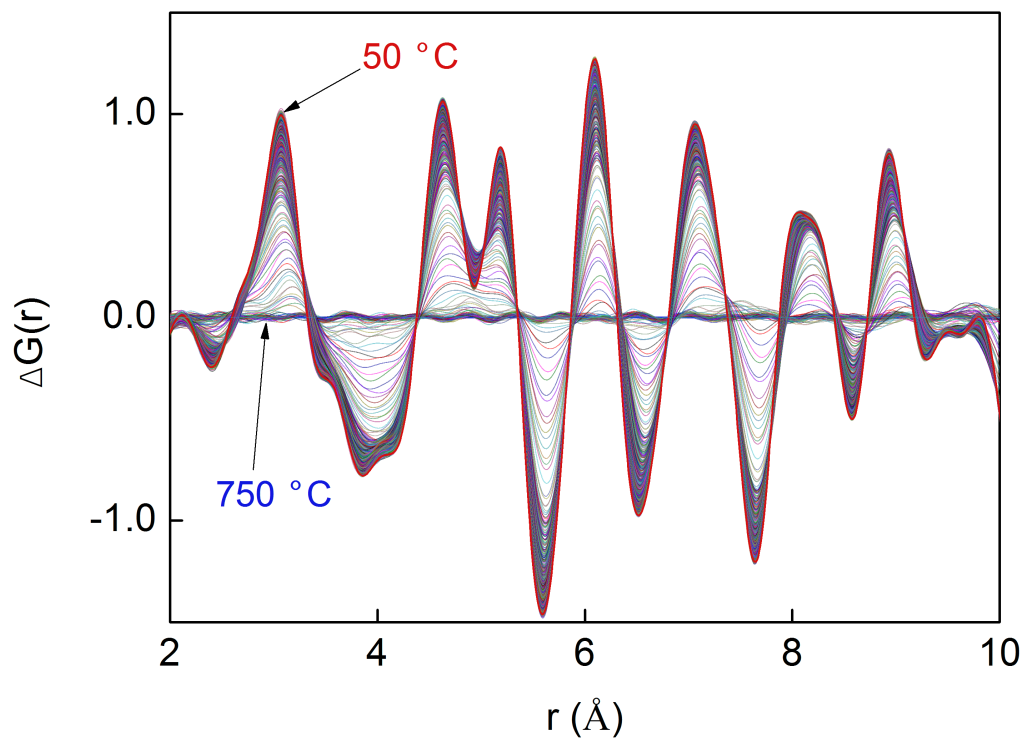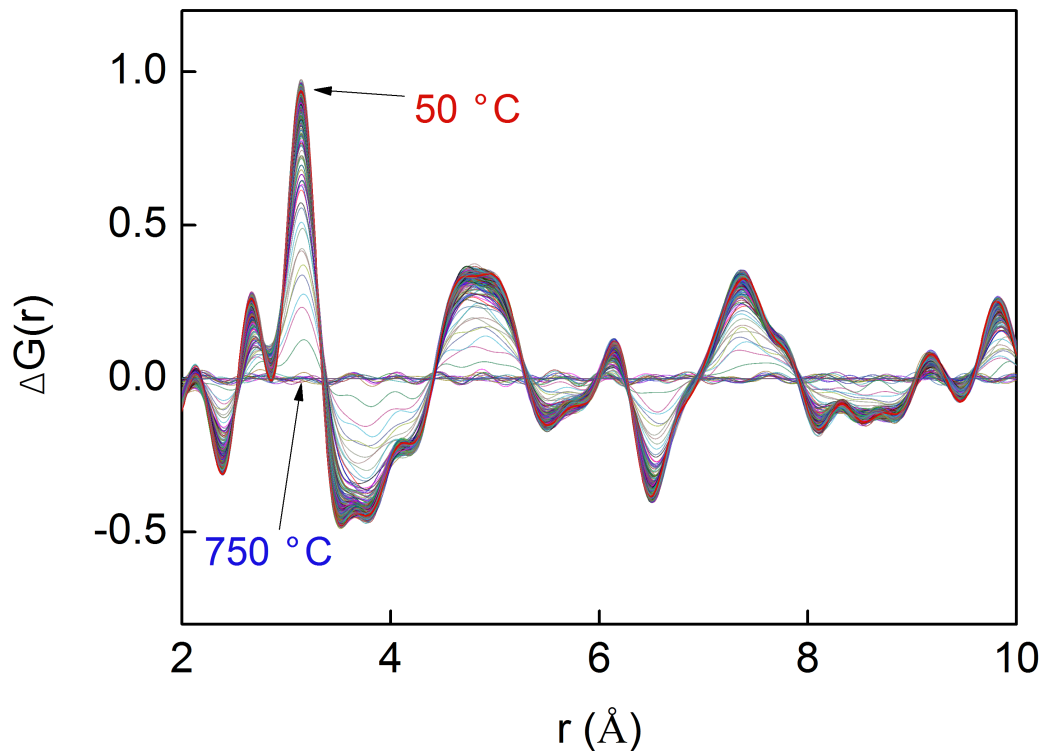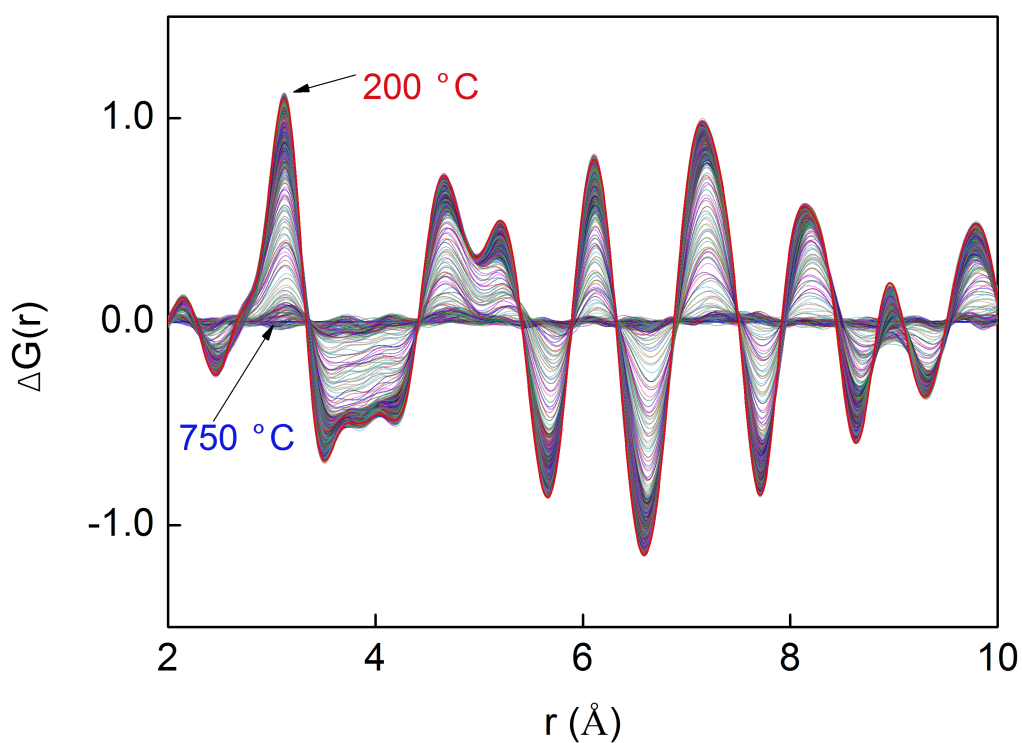
(c)

Fig. 7.6 $\Delta G(r)$ functions showing the difference between $G(r)$ at various temperatures and the one at 750 ° C ($\Delta G(r) = G(r) - G(r)_{750°C}$) during cooling from 750 to 50 °C (200 °C for (c)) at three different average cooling rates, (a) 14.7 K/s, (b) 3.35 K/s, and (c) 0.79 K/s.

However, as shown in Fig. 4.25, there is no obvious peak separation, although the peak position of some PDF peaks slightly shifted to either lower or higher r. This observation again implies that the atomic structure of amorphous phase is very similar to that of the liquid [228]. The structural rearrangements occurring during glass formation mainly involve atoms moving from interatomic distances in between the nearest atomic shells to those of the neighbouring coordination shells, which leads to the population of atomic clusters in each atomic shell and the increasing local atomic ordering [228].

In the case of 3.35 K/s, clear crystallisation events were observed as illustrated in Fig. 4.28, 4.29, 4.30. Fig. 4.31 gives more details about the evolution of PDF peak intensity with the decrease of temperature. Firstly, a rapid increase of PDF peak intensity was observed for all partial PDFs during solidification when temperature decreased from 627.3 °C to 503.7 °C, then the rate of increase slows down at the temperature below 503.7 °C. This

phenomenon indicates that the ordered crystalline structure is not stable just after the finish of solidification at 503.7 °C, and the atomic structure continues to reconfigure into a even more ordered structure during the cooling to room temperature.

It is interesting to find out that some PDF peaks (Fig. 4.31) disappeared during the crystallisation, such as S2_P1, S2_P3, S3_HP3. The possible reason is that these atomic pairs, *i.e.*, Zr-Zr ($ZrBe_2$, S2_P1), Zr-Be (S2_P3), and Zr-Zr (Zr_2Cu, S3_HP3) which were present in the liquid state, were reconfigured into a more stable ordered crystalline structure during the crystallisation. This argument can be further supported by the shift of PDF peaks shown in Fig. 4.32. For example, the peak position of Zr-Zr pairs ($ZrBe_2$, S2_P1) shifted from 4.90 Å to 4.80 Å when temperature reached 627.3 °C, which is closer to the peak position of Zr-Zr pairs (Zr_2Cu, S2_HP1); and the peak position of Zr-Be (S2_P3) shifted to 5.80 Å which was very close to the new position (6.10 Å) of Zr-Zr pairs ($ZrBe_2$, S2_HP2) at 600 °C. The above peak shift events imply that, during the crystallisation from the liquid, some atomic pairs undergo a structural reconfiguration to a new position to form ordered crystalline phase [248].

Crystallisation behaviour of metallic glasses largely depends on the processing conditions and history. Crystallisation directly from a supercooled liquid is very different from the crystallisation induced by annealing [240]. As presented in Fig. 4.9 and 4.26, the crystallisation occurred from the supercooled liquid is a rather slow process (21 s) comparing to that induced by heating (6 s), and it also happened in a relatively wide temperature range (from 627.3 °C to 473.1 °C) as in contrast to that from heating (from 467.4 °C to 482.3 °C).

The effect of an even slower cooling rate of 0.79 K/s on the structure changes was also studied. Although a very similar evolution of PDFs versus temperature were observed for both cooling cases, compared the maxima of PDF curves in Fig. 4.38 with those in Fig. 4.31, it is very clear that the maxima of all PDF peaks at 250-260 °C, for the case of 0.79 K/s are 0.5-1.0 higher than those of the 3.35 K/s case at the same temperature. For example, the peak intensity of S1_P1 ($G(r)_{max}$ = 3.6, at 260.7 °C) for the case of 0.79 K/s, is 0.6 higher than that ($G(r)_{max}$ = 3.0, at 249.4 °C) of 3.35 K/s case.

The higher peak intensity of PDFs represents a higher level of local ordering at atomic scale. The different local structures formed at two different cooling rates during solidification, may be due to fact the crystallisation from a supercooled liquid is preceded by phase separation with respect to Be and Zr [240, 241]. Therefore, the slower cooling rates allowed the atoms, *i.e*, Zr, Be in liquid state to have enough time to diffuse and to realise the phase separation, then an even higher level of local ordering in atomic scale is able to be formed.

7.5 Multi-scale structures of a bulk metallic glass composite

7.5.1 Structural transition across amorphous-crystalline interface

The amorphous structure in metallic glasses often consists of a certain type of short-range order (SRO, normally in the range of 0-5 Å) and medium range order (MRO, in the range of 5-10 Å) as in contrast to the long-rang order (LRO, in the range of > 10 Å) in crystalline phase [251, 252]. The amorphous matrix + crystalline structure (Fig. 5.1, 5.3) of DH3 is a perfect model structure for studying the transition from amorphous structure to crystalline structure from the aspects of SRO, MRO, and LRO. Hoffman [62] argued that the interface between a dendrite and the glass matrix of DH3 (ZrTi bulk metallic glass composite), is atomically sharp. However, a study of precipitation of nanosized quasicrysts in $Ti_{40}Zr_{29}Cu_8Ni_7Be_{16}$ BMG showed that the atomic structure gradually changes from the quasicrystalline to amorphous structure across the quasicrystal/amorphous interface, due to structural similarity between amorphous phase and quasicrystalline phase [253].

As described in section 2.3.2 and 2.3.3, X-ray total scattering based PDF is a standard and extensively used technique to evaluate the SRO in amorphous materials, however it is insensitive to the type of local ordering which is normally obvious in high resolution transmission electron micrographs. Recently several researchers reported that the PDF of local ordering of amorphous materials can be determined by integrating electron diffraction

patterns and Fourier transforming the resulted structure factors [252, 254]. However there are no reports on the PDF analyses of amorphous materials by image processing, *i.e*, the PDF is determined directly by the centroids of the atom positions extracted from the electron micrographs due to the difficulty of differentiating atoms.

In this work, an HRTEM image based 2D PDF method was proposed to characterise the local structure of DH3 at atomic scale. As presented in Fig. 5.8, $g(r)$ calculated from the processed HRTEM micrograph partly resembles that from the x-ray total scattering in terms of peak numbers and peak positions in short to medium r range. Fig. 5.8 shows that the PDF peaks at 5.0 Å and 7.5 Å is split into two sub-peaks, respectively. The peak separation is well captured by the 2D PDF from HRTEM and X-ray total scattering based PDF. A clear transition from the amorphous structure to crystalline structure is also revealed from template (0,1) to (2,1).

However, there are some discrepancies in the peak profile and peak intensity of $g(r)$, comparing to that from x-ray total scattering. For $g(r)$ obtained from HRTEM micrograph, the peak intensity of first atomic shell is about 1.5 for the amorphous phase, and 2.5 for the crystalline phase respectively; however for $g(r)$ from x-ray total scattering, the peak intensity is 4.5 for crystalline phase. These discrepancies are possibly due to the poor counting statistics in such a limited template size of 8×8nm for the calculation of $g(r)$, as illustrated in Fig. 5.6b.

Moreover compared to $g(r)$ from x-ray total scattering, the missing minor peaks for crystalline phase calculated from processed HRTEM micrograph, may be well explained by the fact that these "atoms" like particles involved in the calculation of $g(r)$ were predominantly extracted from a preferred lattice plane (110) due to specific sampling region.

Though some discrepancies exist for the 2D $g(r)$ obtained by image processing, the local structure of amorphous and crystalline phase at atomic scale, can be semi-quantitatively characterised, and it is especially useful for characterising structural changes within the interface region in nanometre scale, which is beyond the scope of x-ray total scattering analyses.

Auto correlation function is extensively used to characterise MRO in HRTEM images of metallic glasses. As revealed in Fig. 5.5b, MROs are often randomly distributed in the amorphous phase however, a clear transition of MRO is not evident in the interface region, where strongly and weakly correlated ACF patterns are randomly distributed in amorphous matrix.

Fast Fourier transform is able to provide the 2D structure information in the reciprocal space for the long r range. Fig. 5.4 revealed that the FFT patterns obtained by image processing are equivalent to the diffraction pattern, however in a local region of 6.4×6.4 nm. A amorphous-crystalline structure transition in long range can be clearly characterised by these FFT patterns.

7.5.2   Structural changes under thermal shock by electric currents

7.5.2.1   The thermal shock treatment

Applying high density electric currents into bulk metallic glasses can accelerate the diffusion and rearrangement of solute atoms over a short period of time [201, 197], and therefore promote nano-crystallisation. Johnson *et al* [255] and Liu *et al* [256] found that very rapid heat (up to 10^6 K/s) induced by high density electric currents can be used to heat BMGs into the supercooled liquid state without causing crystallisation; in this state, near net-shape shape thermoplastic processing can be applied. Johnson *et.al* [255] argued that most BMG systems have homogeneous and virtually temperature-independent electrical resistivities, so that passing a high density electric current pulse through the bulk samples can cause uniform volumetric Joule heating of the entire sample volume.

However no studies have been published concerning the influence of high density electric currents on the nano/microstructure evolution of BMGMCs, in which different phases have different electrical resistivities. In this work, a novel thermal shocked experiment was designed for such studies by using Gleeble thermomechanical simulator, which is capable

of rapidly heating samples at a heating rate of up to 10^4 K/s, using the electric resistance Joule heat generated when a high density electric current passing through the samples.

7.5.2.2   Multi-scale 3D structure characterisation

Almost all previous characterisation studies of these BMG composites have been performed on two dimensional (2D) sections using electron microscopy. Focused ion beam milling plus scanning electron microscopy (FIB-SEM) is a standard technique to generate 3D reconstructions through a series of sectioning and imaging [257]. However, FIB-SEM is practically limited to the sectioning of sub-micrometre structural features, and is therefore not suitable for studying whole dendrites in BMGMCs [62], which can be tens or hundreds of microns in length.

As a non-destructive method, X-ray micro-tomography is able to image the objects in μm to mm scale. As presented in 5.11, the 3D dendrites revealed by X-ray tomography are actually made of many interconnected and well-developed secondary arms, as highlighted by the single dendrite coloured in magenta (Fig.5.13a). However, when conventional 2D characterisation methods were previously used, these secondary dendrite arms were often identified as individual circular-shaped particles [258]. Each 3D dendrite actually consists of a few to a few tens of secondary arms, with an overall size of a few hundred μm.

Fig.5.12, and 5.14 show that the amorphous matrix was completely transformed into a highly interconnected 3D network of eutectic microstructure of Zr_2Cu and $ZrBe_2$ with a minor change of β-Zr dendritic inclusions, which is different from the amorphous matrix within the as-cast sample in Fig.5.11. The powerful combination of X-ray microtomography with FIB-SEM nanotomography allowed to characterise the 3D structure from nano- to micro- scale.

7.5.2.3 Thermal stabilities under thermal shock

Lee *et al* [187] studied the thermal stability of LM2A2 (a ZrTi based BMGMC) at low temperature (around 300°C in isothermal conditions), and found that the body centred cubic (BCC) β-Zr phase (the dendrites in the material) is unstable below 300°C because Zr tends to form the hexagonal close packed (HCP) crystal structure in low temperature. They also found that, the BCC β-Zr phase is stable at high temperatures (600°C), while the amorphous matrix crystallises at this temperature during isothermal heat treatment.

Fig. 5.16a-c, show that the new crystalline phases, $ZrBe_2$ and Zr_2Cu that were nucleated at the dendrite-amorphous matrix interface grew into the amorphous matrix until it was almost completely consumed (Fig. 5.9c). And as shown in Fig. 5.12, a little amount of primary β-Zr dendrites was dissolved and it turned into the intermetallic phases $ZrBe_2$ and Zr_2Cu, however most of the β-Zr remains stable. The fact that the amorphous matrix transformed into two other crystalline phases, *i.e*, $ZrBe_2$ and Zr_2Cu phases, in just 6 s of thermal shock processing indicates that the primary dendritic crystalline phase is more thermodynamically stable than the amorphous matrix [66]. In fact, the dendrites have electric resistivities (50 $\mu\Omega \cdot cm$) much lower than that of the amorphous matrix (250 $\mu\Omega \cdot cm$) [255]. Hence, there was less Joule heat generated in the crystalline phase.

7.5.2.4 Nucleation and growth of the newly formed intermetallics

Previous studies [199, 200] of isothermal annealing have found that quasicrystals nucleate (and then grow into nanocrystals) within the amorphous matrix. However, we have found that nucleation and growth occur predominantly at dendrite-matrix interface. Fig. 5.17 shows the typical microstructure of the transition region (marked by an oval on the rod sample in Fig. 3.14) between the as-cast and the thermally-shocked region for the 650 °C sample. It indicates that the majority of the new Zr_2Cu and $ZrBe_2$ crystalline phases, nucleated at the interface and grew together into the amorphous matrix in a form of eutectic growth [66]. The reason why nucleation events for the secondary crystalline phases occur

predominantly at the interface, can be well-explained by the fact that, the difference in electric resistivity between the two phases resulted in highly localised Ohmic dissipation across the dendrite-matrix interface [255].

Some of the Zr_2Cu and $ZrBe_2$ phases (Fig. 5.16) were also found to nucleate directly from the amorphous matrix and grow into the surroundings, similar to those found in most nano-crystallisation studies [201, 189, 202]. However, in this study, the evidence indicates that the dendrite-amorphous interface is the dominant nucleation site for the newly formed intermetallic phases.

7.5.2.5   Possibility of thermoplastic processing of BMGMCs using thermal shock

As presented in Fig. 5.15, the volume fraction of β-Zr in the thermal shocked sample (60.97%) was lower than that in the as-cast sample (69.21%) for the thermal shock at a preset temperature of 700 °C, because fast cooling after thermal shock resulted in more amorphous matrix; this confirms that fast heating using high density electric current followed by the relative fast cooling can retain the designed composite microstructure [256]. This opens the window for the possibility of using thermal-plasticity processing techniques to produce near net-shape BMGMC products without losing the originally designed composite microstructure.

Chapter 8

Conclusions and future work

8.1 Conclusions

A very comprehensive experimental and modelling research have been carried out to study the atomic structrue of the metallic glasses and composites, and their correlations with alloys compositions and processing conditions. The key conclusions of this thesis are:

- A binary vacancy phase-field crystal model and a ternary model have been developed and successfully used to interpret the atomic structure changes with composition for the binary alloys, CuZr and NiTi, and also the ternary alloys, CuZrAl and TiCuNi. As the concentration of Cu and Ti increases, the populations of Cu-Cu atomic pairs / Ti-Ti atomic pairs increase, which leads to increasing peak intensity of the first / second peak. The atomic size ratio significantly affects the peak positions and peak shape of PDFs for binary and ternary alloys. The peak separation of the first PDF peak for $Zr_{55}Cu_{40}Al_5$ is mainly due to the increasing population of Zr-Cu and Zr-Al pairs.

- An dedicated experimental apparatus were designed, made, and commissioned for the total scattering experiments using Synchrotron X-rays, which can be used to thoroughly acquire high-quality X-ray scattering data for real time studies of atomic structure using pair distribution functions.

- The crystallisation of Vit1 during heating is very different to those found during slow cooling. The crystallisation induced by heating is very rapid, and the crystalline structure is formed in 6 s, while that occurred in cooling is fairly slow ($\sim$ 21 s), and the atomic structure are largely determined by the cooling rates. During the crystallisation induced by heating at 1.5 K/s, Zr_2Cu is formed at 270 °C and $ZrBe_2$ is formed 467.4 °C. While Zr_2Cu and $ZrBe_2$ are formed together during the crystallisation induced by slow cooling.

- A novel 2D HRTEM image based PDF method was proposed to characterise the local structure transition within amorphous-crystalline interface at atomic level. The 2D PDFs, which are very sensitive to ordered and disordered structure, can provide an alternative approach to characterise the local ordering using HRTEM.

- The 3D nano and microstructures of the DH3 at different thermal shock conditions were studied and characterised using X-ray microtomography and FIB-SEM nanotomgraphy. It is found that the ductile β-Zr crystalline dendrites are interlocked 3D structures with complex morphology of a few hundreds of micrometres. They are not the "globular" particles of a few to tens of microns in length, as previously inferred from 2D imaging. The amorphous to crystalline transition at the interface under thermal shock by applying electric current is very different to that occurred in isothermal heating conditions. The large difference in electric resistivities between the amorphous matrix and the crystalline dendrites resulted in differential heating across the amorphous-crystalline interface, which led to the nucleation of new crystalline phases (Zr_2Cu and $ZrBe_2$) preferably at the interface, rather than within the amorphous matrix. They grew concurrently to form 3D eutectic network as revealed by using the FIB-SEM nanotomography.

8.2   Future work

It is interesting to study in-situ the atomic structure evolution of a ternary BMG (such as ZrCuAl) during heating and cooling, in which all the six partial PDFs can be completely resolved by real space refinement of the crystalline phases formed during crystallisation.

It is also interesting to study in-situ the growth of dendrites inside of BMGMCs (such as DH3) from semi-solid state using X-ray tomography, which may provide more insights on the real time evolution of 3D morphologies for dendrites.

It is important to establish a quantitative relation between the absolute atomic size and VPFC model parameter, $i.e$, q_i, and it therefore can simulate the effect of absolute atomic size for binary and ternary alloys. Also it is useful to extend the current 2D ternary VPFC model to a 3D multi-component model by introducing more two-body correlation or many body correlation terms into the PFC free energy, which can provide more insights on the real atomic configuration.

It is key to correlate the model parameters used in VPFC model to thermo-physical properties of real materials using molecular dynamics. Hence, the VPFC model can be used to interpret the true atomic structure changes for real materials.

References

[1] Takeshi Egami and Simon JL Billinge. *Underneath the Bragg peaks: structural analysis of complex materials*, volume 16. Newnes, 2012.

[2] Wikipedia. Delaunay triangulation. https://en.wikipedia.org/wiki/Delaunay_triangulation, 2015.

[3] D. Windt. Reflective x-ray optics: Technology - introduction. http://www.rxollc.com/technology/index.html, 2015.

[4] En.wikibooks.org. Basic physics of digital radiography/the source - wikibooks, open books for an open world. https://en.wikibooks.org/wiki/Basic_Physics_of_Digital_Radiography/The_Source, 2015.

[5] Arpansa.gov.au. Arpansa - x-rays. http://www.arpansa.gov.au/radiationprotection/basics/xrays.cfm, 2015.

[6] MJ Berger, JH Hubbell, SM Seltzer, J Chang, JS Coursey, R Sukumar, DS Zucker, and K Olsen. Xcom: Photon cross sections database. *NIST Standard reference database*, 8, 2013.

[7] Varley F Sears. Neutron scattering lengths and cross sections. *Neutron news*, 3(3):26–37, 1992.

[8] A Cecilia, E Hamann, C Haas, D Greiffenberg, A Danilewsky, D Haenscke, A Fauler, A Zwerger, G Buth, and P et al. Vagovic. Investigation of crystallographic and detection properties of CdTe at the ANKA synchrotron light source. *Journal of Instrumentation*, 6(10):P10016–P10016, 2011.

[9] D Arias and JP Abriata. Cu-Zr (copper-zirconium). *Journal of Phase Equilibria*, 11(5):452–459, 1990.

[10] P Nash, MF Singleton, and JL Murray. Al-Ni (aluminum-nickel). *Phase Diagrams of Binary Nickel Alloys*, 1:3–11, 1991.

[11] Joanne L Murray. Phase diagrams of binary titanium alloys. *ASM International, 1987*, page 354, 1987.

[12] Pak Yuen Chan, Nigel Goldenfeld, and Jon Dantzig. Molecular dynamics on diffusive time scales from the phase-field-crystal equation. *Physical Review E*, 79(3):035701, 2009.

[13] Joel Berry and Martin Grant. Modeling multiple time scales during glass formation with phase-field crystals. *Physical review letters*, 106(17):175702, 2011.

[14] Mark J Robbins, Andrew J Archer, Uwe Thiele, and Edgar Knobloch. Modeling the structure of liquids and crystals using one-and two-component modified phase-field crystal models. *Physical Review E*, 85(6):061408, 2012.

[15] William D Callister, David G Rethwisch, et al. *Materials science and engineering: an introduction*, volume 7. Wiley New York, 2007.

[16] Kurt Binder and Walter Kob. *Glassy materials and disordered solids: An introduction to their statistical mechanics*. World Scientific, 2011.

[17] W Klement and RH Willens. Non-crystalline structure in solidified gold–silicon alloys. 1960.

[18] AL Greer and E Ma. Bulk metallic glasses: at the cutting edge of metals research. *MRS bulletin*, 32(08):611–619, 2007.

[19] A Inoue, XM Wang, and W Zhang. Developments and applications of bulk metallic glasses. *Rev. Adv. Mater. Sci*, 18:1–9, 2008.

[20] C Suryanarayana and Akihisa Inoue. *Bulk metallic glasses*. CRC Press, 2010.

[21] Eugen Axinte. Metallic glasses from "alchemy" to pure science: present and future of design, processing and applications of glassy metals. *Materials & Design*, 35:518–556, 2012.

[22] Hagen Kleinert. *Gauge fields in condensed matter*, volume 2. World Scientific Singapore, 1989.

[23] Lesley E Smart and Elaine A Moore. *Solid state chemistry: an introduction*. CRC press, 2012.

[24] Peter Egelstaff. *An introduction to the liquid state*. Elsevier, 2012.

[25] Boris S Bokstein, David J Srolovitz, and Mikhail I Mendelev. *Thermodynamics and kinetics in materials science*. Oxford Univ. Press, UK, 2005.

[26] Richard LeSar. *Introduction to computational materials science: fundamentals to applications*. Cambridge University Press, 2013.

[27] Fabrizio Cleri and Vittorio Rosato. Tight-binding potentials for transition metals and alloys. *Physical Review B*, 48(1):22, 1993.

[28] Murray S Daw, Stephen M Foiles, and Michael I Baskes. The embedded-atom method: a review of theory and applications. *Materials Science Reports*, 9(7):251–310, 1993.

[29] Roman Frigg and Charlotte Werndl. Entropy-a guide for the perplexed. *Probabilities in physics*, 2011.

[30] Richard P Sear. Nucleation: theory and applications to protein solutions and colloidal suspensions. *Journal of Physics: Condensed Matter*, 19(3):033101, 2007.

[31] Paolo Nicolini, Diego Frezzato, and Riccardo Chelli. Exploiting configurational freezing in nonequilibrium monte carlo simulations. *Journal of Chemical Theory and Computation*, 7(3):582–593, 2011.

[32] Yang-Tse Cheng and William L Johnson. Disordered materials: a survey of amorphous solids. *Science*, 235(4792):997–1002, 1987.

[33] ZP Lu and CT Liu. Glass formation criterion for various glass-forming systems. *Physical review letters*, 91(11):115505, 2003.

[34] Li-ling Ooi. *Principles of X-ray Crystallography*. Oxford University Press, 2010.

[35] YQ Cheng and E Ma. Atomic-level structure and structure–property relationship in metallic glasses. *Progress in Materials Science*, 56(4):379–473, 2011.

[36] Keith James Laidler and H Gerischer. *The world of physical chemistry*, volume 3. Oxford University Press, 1995.

[37] Linus Pauling. *General chemistry*. Courier Corporation, 2014.

[38] Wikipedia. Molecular geometry — Wikipedia, the free encyclopedia. https://en.wikipedia.org/wiki/Molecular_geometry, 2015.

[39] Jun Ding, Sylvain Patinet, Michael L Falk, Yongqiang Cheng, and Evan Ma. Soft spots and their structural signature in a metallic glass. *Proceedings of the National Academy of Sciences*, 111(39):14052–14056, 2014.

[40] X Hui, HZ Fang, GL Chen, SL Shang, Y Wang, JY Qin, and ZK Liu. Atomic structure of Zr41.2Ti13.8Cu12.5Ni10Be22.5 bulk metallic glass alloy. *Acta Materialia*, 57(2):376–391, 2009.

[41] Simon JL Billinge. Pair distribution function technique: Principles and methods. In *Uniting Electron Crystallography and Powder Diffraction*, pages 183–193. Springer, 2012.

[42] Jerome Spanier and Keith B Oldham. *An atlas of functions*. Taylor & Francis/Hemisphere, 1987.

[43] Th Proffen, SJL Billinge, T Egami, and D Louca. Structural analysis of complex materials using the atomic pair distribution function—a practical guide. *Zeitschrift für Kristallographie/International journal for structural, physical, and chemical aspects of crystalline materials*, 218(2/2003):132–143, 2003.

[44] Ahmad Salah Masadeh. *Quantitative structure determination of nanostructured materials using the atomic pair distribution function analysis*. ProQuest, 2008.

[45] Jean-Louis Barrat and Jean-Pierre Hansen. *Basic concepts for simple and complex liquids*. Cambridge University Press, 2003.

[46] Alvaro Posada-Amarillas and Ignacio L Garzón. Microstructural analysis of simulated liquid and amorphous Ni. *Physical Review B*, 53(13):8363, 1996.

[47] John C Crocker and David G Grier. Methods of digital video microscopy for colloidal studies. *Journal of colloid and interface science*, 179(1):298–310, 1996.

[48] Takeshi Egami and Simon JL Billinge. *Underneath the Bragg peaks: structural analysis of complex materials*, volume 16. Elsevier, 2003.

[49] Franz Aurenhammer, Rolf Klein, Der-Tsai Lee, and Rolf Klein. *Voronoi diagrams and Delaunay triangulations*. World Scientific, 2013.

[50] Christopher Hammond. *The basics of crystallography and diffraction*. Oxford University Press, 2009.

[51] Arthur James Cochran Wilson. *Elements of X-ray Crystallography*. Addison-Wesley Reading, Massachusetts, 1970.

[52] RJ Hill and CJ Howard. Quantitative phase analysis from neutron powder diffraction data using the Rietveld method. *Journal of Applied Crystallography*, 20(6):467–474, 1987.

[53] Nature Graphics. ATOMIC SECRETS. http://naturegraphics.tumblr.com/post/75171119736/atomic-secrets-background-this-week-features-a, 2014.

[54] William D Callister and David G Rethwisch. *Fundamentals of materials science and engineering: an integrated approach*. John Wiley & Sons, 2012.

[55] Bertram Eugene Warren. *X-ray Diffraction*. Courier Corporation, 1969.

[56] Frank H Allen. The cambridge structural database: a quarter of a million crystal structures and rising. *Acta Crystallographica Section B: Structural Science*, 58(3):380–388, 2002.

[57] A Reza Yavari, JJ Lewandowski, and J Eckert. Mechanical properties of bulk metallic glasses. *Mrs Bulletin*, 32(08):635–638, 2007.

[58] WH Peter, RA Buchanan, CT Liu, PK Liaw, ML Morrison, JA Horton, CA Carmichael, and JL Wright. Localized corrosion behavior of a zirconium-based bulk metallic glass relative to its crystalline state. *Intermetallics*, 10(11):1157–1162, 2002.

[59] A Lindsay Greer. Metallic glasses. *Science*, 267(5206):1947, 1995.

[60] D Wang, Y Li, BB Sun, ML Sui, K Lu, and E Ma. Bulk metallic glass formation in the binary Cu–Zr system. *Applied Physics Letters*, 84(20):4029–4031, 2004.

[61] YQ Cheng, Al J Cao, HW Sheng, and E Ma. Local order influences initiation of plastic flow in metallic glass: Effects of alloy composition and sample cooling history. *Acta Materialia*, 56(18):5263–5275, 2008.

[62] Wen Sheng Lai, Qing Zhang, Bai Xin Liu, and Evan Ma. Structural stability and amorphization transition in the Ni–Ti system studied by molecular dynamics simulation with an n-body potential. *Journal of the Physical Society of Japan*, 69(9):2923–2937, 2000.

[63] N Gao and WS Lai. Relative stability of amorphous phase versus solid solution in the Ni–Ti system revealed by molecular dynamics simulations. *Journal of Physics: Condensed Matter*, 19(4):046213, 2007.

[64] HB Lou, XD Wang, F Xu, SQ Ding, QP Cao, K Hono, and JZ Jiang. 73 mm-diameter bulk metallic glass rod by copper mould casting. *Applied Physics Letters*, 99(5):051910, 2011.

[65] HS Chen. Thermodynamic considerations on the formation and stability of metallic glasses. *Acta Metallurgica*, 22(12):1505–1511, 1974.

[66] AJ Drehman, AL Greer, and D Turnbull. Bulk formation of a metallic glass: Pd40Ni40P20. *Applied Physics Letters*, 41(8):716–717, 1982.

[67] Akihisa Inoue, Tao Zhang, and Tsuyoshi Masumoto. Al–La–Ni amorphous alloys with a wide supercooled liquid region. *Materials Transactions, JIM*, 30(12):965–972, 1989.

[68] A Inoue, A Kato, Tao Zhang, SG Kim, and T Masumoto. Mg–Cu–Y amorphous alloys with high mechanical strengths produced by a metallic mold casting method. *Materials Transactions, JIM*, 32(7):609–616, 1991.

[69] Akihisa Inoue, Tao Zhang, and Tsuyoshi Masumoto. Zr–Al–Ni amorphous alloys with high glass transition temperature and significant supercooled liquid region. *Materials Transactions, JIM*, 31(3):177–183, 1990.

[70] Atakan Peker and William L Johnson. A highly processable metallic glass: Zr41.2Ti13.8Cu12.5Ni10.0Be22.5. *Applied Physics Letters*, 63(17):2342–2344, 1993.

[71] CP Kim, R Busch, A Masuhr, H Choi-Yim, and WL Johnson. Processing of carbon-fiber-reinforced Zr41.2Ti13.8Cu12.5Ni10.0Be22.5 bulk metallic glass composites. *Applied Physics Letters*, 79(10):1456–1458, 2001.

[72] H Choi-Yim and William L Johnson. Bulk metallic glass matrix composites. *Applied Physics Letters*, 71(26):3808–3810, 1997.

[73] X Hui, W Dong, GL Chen, and KF Yao. Formation, microstructure and properties of long-period order structure reinforced Mg-based bulk metallic glass composites. *Acta Materialia*, 55(3):907–920, 2007.

[74] Douglas C Hofmann, Jin-Yoo Suh, Aaron Wiest, Gang Duan, Mary-Laura Lind, Marios D Demetriou, and William L Johnson. Designing metallic glass matrix composites with high toughness and tensile ductility. *Nature*, 451(7182):1085–1089, 2008.

[75] William L Johnson. Bulk glass-forming metallic alloys: Science and technology. *MRS bulletin*, 24(10):42–56, 1999.

[76] CC Hays, CP Kim, WL Johnson, et al. Composite formed by precipitation of dendritic ductile intermetallic in metallic glass. *Phys Rev Lett*, 84:2901–2904, 2000.

[77] U Kühn, J Eckert, N Mattern, and L Schultz. ZrNbCuNiAl bulk metallic glass matrix composites containing dendritic bcc phase precipitates. *Applied physics letters*, 80(14):2478–2480, 2002.

[78] Douglas C Hofmann. Bulk metallic glasses and their composites: a brief history of diverging fields. *Journal of Materials*, 2013, 2013.

[79] M Ferry, KJ Laws, C White, DM Miskovic, KF Shamlaye, W Xu, and O Biletska. Recent developments in ductile bulk metallic glass composites. *MRS Communications*, 3(01):1–12, 2013.

[80] HW Sheng, WK Luo, FM Alamgir, JM Bai, and E Ma. Atomic packing and short-to-medium-range order in metallic glasses. *Nature*, 439(7075):419–425, 2006.

[81] John Desmond Bernal and John Leslie Finney. Random close-packed hard-sphere model. ii. geometry of random packing of hard spheres. *Discussions of the Faraday Society*, 43:62–69, 1967.

[82] Akihisa Inoue, Tao Zhang, Junji Saida, Mitsuhide Matsushita, Min Wei Chen, and Toshio Sakurai. Formation of icosahedral quasicrystalline phase in Zr–Al–Ni–Cu–M (M= Ag, Pd, Au or Pt) systems. *Materials Transactions, JIM*, 40(10):1181–1184, 1999.

[83] T Fujita, K Konno, W Zhang, V Kumar, M Matsuura, A Inoue, T Sakurai, and MW Chen. Atomic-scale heterogeneity of a multicomponent bulk metallic glass with excellent glass forming ability. *Physical review letters*, 103(7):075502, 2009.

[84] T Ichitsubo, E Matsubara, T Yamamoto, HS Chen, N Nishiyama, J Saida, and K Anazawa. Microstructure of fragile metallic glasses inferred from ultrasound-accelerated crystallization in Pd-based metallic glasses. *Physical review letters*, 95(24):245501, 2005.

[85] Jayanta Das, Mei Bo Tang, Ki Buem Kim, Ralf Theissmann, Falko Baier, Wei Hua Wang, and Jürgen Eckert. "work-hardenable" ductile bulk metallic glass. *Physical Review Letters*, 94(20):205501, 2005.

[86] Yan Hui Liu, Gang Wang, Ru Ju Wang, Ming Xiang Pan, Wei Hua Wang, et al. Super plastic bulk metallic glasses at room temperature. *science*, 315(5817):1385–1388, 2007.

[87] RL McGreevy and L Pusztai. Reverse monte carlo simulation: a new technique for the determination of disordered structures. *Molecular Simulation*, 1(6):359–367, 1988.

[88] Robert L McGreevy. Reverse monte carlo modelling. *Journal of Physics: Condensed Matter*, 13(46):R877, 2001.

[89] Yongmei M Jin and Armen G Khachaturyan. Atomic density function theory and modeling of microstructure evolution at the atomic scale. *Journal of applied physics*, 100(1):013519, 2006.

[90] Jens Als-Nielsen and Des McMorrow. *Elements of modern X-ray physics*. John Wiley & Sons, 2011.

[91] Stephen Jarvis Brent Reed. *Electron microprobe analysis and scanning electron microscopy in geology*. Cambridge University Press, 2005.

[92] George C Baldwin and Donald W Kerst. Origin of synchrotron radiation. *Physics Today*, 28(1):9–11, 2008.

[93] C Kunz. Introduction—properties of synchrotron radiation. In *Synchrotron Radiation*, pages 1–23. Springer, 1979.

[94] Paul L Hartman. Early experimental work on synchrotron radiation. *Synchrotron Radiation News*, 1(5):28–30, 1988.

[95] B Buras and S Tazari. European synchrotron radiation facility. *Report of the ESRP, c/o CERN*, 1985.

[96] APS User Portal. Advanced photon source. *Phys. Rev. Lett*, 92:237204, 2004.

[97] T Nakano, JK Ahn, H Ejiri, M Fujiwara, T Hotta, N Matsuoka, T Matsumura, T Mibe, M Nomachi, H Toki, et al. Experiment at SPring-8. *Nuclear Physics A*, 670(1):332–339, 2000.

[98] RP Walker. Progress with the diamond light source project. In *PAC*, volume 3, page 232, 2003.

[99] Lloyd Smith. Effects of wigglers and undulators on beam dynamics. *LBL ESG TECH Note-24*, 1986.

[100] Donald H Bilderback, Pascal Elleaume, and Edgar Weckert. Review of third and next generation synchrotron light sources. *Journal of Physics B: Atomic, molecular and optical physics*, 38(9):S773, 2005.

[101] Shyh-Yuan Lee. *Accelerator physics*, volume 491. World scientific Singapore, 1999.

[102] W Joho, M Munoz, and A Streun. The SLS booster synchrotron. *Nuclear Instruments and Methods in Physics Research Section A: Accelerators, Spectrometers, Detectors and Associated Equipment*, 562(1):1–11, 2006.

[103] Wikipedia. Synchrotron light source. https://en.wikipedia.org/wiki/Synchrotron_light_source, 2015.

[104] I Zanette, B Enders, M Dierolf, P Thibault, R Gradl, A Diaz, M Guizar-Sicairos, A Menzel, F Pfeiffer, and P Zaslansky. Ptychographic X-ray nanotomography quantifies mineral distributions in human dentine. *Scientific reports*, 5, 2015.

[105] Ian Peter Stephen Martin. *Short pulse x-ray generation in synchrotron radiation sources*. PhD thesis, University of Oxford, 2011.

[106] Alexandre Vabre, M Gmar, Delphine Lazaro, Samuel Legoupil, O Coutier, Antoine Dazin, WK Lee, and K Fezzaa. Synchrotron ultra-fast X-ray imaging of a cavitating flow in a Venturi profile. *Nuclear Instruments and Methods in Physics Research Section A: Accelerators, Spectrometers, Detectors and Associated Equipment*, 607(1):215–217, 2009.

[107] Anil Sethi. X-rays: Interaction with matter. *Encyclopedia of Medical Devices and Instrumentation*, 2006.

[108] J Anthony Seibert and John M Boone. X-ray imaging physics for nuclear medicine technologists. Part 2: X-ray interactions and image formation. *Journal of nuclear medicine technology*, 33(1):3–18, 2005.

[109] RH Pratt, Akiva Ron, and HK Tseng. Atomic photoelectric effect above 10 keV. *Reviews of Modern physics*, 45(2):273, 1973.

[110] Robley D Evans. X-ray and γ-ray interactions. *Radiation dosimetry*, 1:93–155, 1968.

[111] Stefan Hüfner. *Photoelectron spectroscopy: principles and applications*, volume 82. Springer Science & Business Media, 2013.

[112] M Morcrette, Y Chabre, G Vaughan, G Amatucci, J-B Leriche, S Patoux, C Masquelier, and JM Tarascon. In situ x-ray diffraction techniques as a powerful tool to study battery electrode materials. *Electrochimica acta*, 47(19):3137–3149, 2002.

[113] Peter J Chupas, Xiangyun Qiu, Jonathan C Hanson, Peter L Lee, Clare P Grey, and Simon JL Billinge. Rapid-acquisition pair distribution function (ra-pdf) analysis. *Journal of Applied Crystallography*, 36(6):1342–1347, 2003.

[114] Xiangyun Qiu, Jeroen W Thompson, and Simon JL Billinge. Pdfgetx2: a gui-driven program to obtain the pair distribution function from x-ray powder diffraction data. *Journal of Applied Crystallography*, 37(4):678–678, 2004.

[115] Pavol Juhás, Timur Davis, Christopher L Farrow, and Simon JL Billinge. Pdfgetx3: a rapid and highly automatable program for processing powder diffraction data into total scattering pair distribution functions. *Journal of Applied Crystallography*, 46(2):560–566, 2013.

[116] Simon JL Billinge and Christopher L Farrow. Towards a robust ad hoc data correction approach that yields reliable atomic pair distribution functions from powder diffraction data. *Journal of Physics: Condensed Matter*, 25(45):454202, 2013.

[117] LB McCusker, RB Von Dreele, DE Cox, D Louer, and P Scardi. Rietveld refinement guidelines. *Journal of Applied Crystallography*, 32(1):36–50, 1999.

[118] Th Proffen and SJL Billinge. PDFFIT, a program for full profile structural refinement of the atomic pair distribution function. *Journal of Applied Crystallography*, 32(3):572–575, 1999.

[119] CL Farrow, P Juhas, JW Liu, D Bryndin, ES Božin, J Bloch, Th Proffen, and SJL Billinge. PDFfit2 and PDFgui: computer programs for studying nanostructure in crystals. *Journal of Physics: Condensed Matter*, 19(33):335219, 2007.

[120] Simon JL Billinge. Real-space rietveld: full profile structural refinement of the atomic pair distribution function. In *Local Structure from Diffraction*, pages 137–156. Springer, 2002.

[121] George Edward Bacon. *Neutron diffraction 3 edition*. Clarendon Press, 1975.

[122] Stephen W Lovesey. *Theory of neutron scattering from condensed matter*. Clarendon Press, 1984.

[123] Gordon Leslie Squires. *Introduction to the theory of thermal neutron scattering*. Cambridge university press, 2012.

[124] Andrew Taylor, Mike Dunne, Steve Bennington, Stuart Ansell, Ian Gardner, Peter Norreys, Tim Broome, David Findlay, and Richard Nelmes. A route to the brightest possible neutron source? *Science*, 315(5815):1092–1095, 2007.

[125] Michael Follows. Research at ISIS. *Education in chEMistry*, 48(6):180, 2011.

[126] STFC. The layout of ISIS and its target stations. http://www.rsc.org/images/FEATURE_ISIS_pg181a_350_tcm18-209795.jpg.

[127] JS Fraser and GA Bartholomew. Spallation neutron sources. In *Neutron sources for basic physics and applications*. North-Holland, 1983.

[128] P Day, J Enderby, W Williams, and *et al*. Chapon, L. Scientific reviews: GEM: the general materials diffractometer at ISIS-multibank capabilities for studying crystalline and disordered materials. *Neutron News*, 15(1):19–23, 2004.

[129] Thomas Proffen, Katharine L Page, Sylvia E McLain, Bjørn Clausen, Timothy W Darling, James A TenCate, Seung-Yub Lee, and Ersan Ustundag. Atomic pair distribution function analysis of materials containing crystalline and amorphous phases. *Zeitschrift für Kristallographie*, 220(12/2005):1002–1008, 2005.

[130] David C Joy and James B Pawley. High-resolution scanning electron microscopy. *Ultramicroscopy*, 47(1):80–100, 1992.

[131] AL Cohen and MA Hayat. Principles and techniques of scanning electron microscopy. *Principles and Techniques of Scanning Electron Microscopy*, 1, 1974.

[132] Joseph Goldstein, Dale E Newbury, Patrick Echlin, David C Joy, Alton D Romig Jr, Charles E Lyman, Charles Fiori, and Eric Lifshin. *Scanning electron microscopy and X-ray microanalysis: a text for biologists, materials scientists, and geologists*. Springer Science & Business Media, 2012.

[133] Brent Fultz and James M Howe. *Transmission electron microscopy and diffractometry of materials*. Springer Science & Business Media, 2012.

[134] David B Williams and C Barry Carter. High-Resolution TEM. In *Transmission Electron Microscopy*, pages 483–509. Springer, 2009.

[135] E Hi Sondheimer. The mean free path of electrons in metals. *Advances in physics*, 1(1):1–42, 1952.

[136] George N Fursey. *Field emission in vacuum microelectronics*. Springer Science & Business Media, 2007.

[137] David B Williams and C Barry Carter. *The transmission electron microscope*. Springer, 1996.

[138] Errol J Wood. Applying fourier and associated transforms to pattern characterization in textiles. *Textile Research Journal*, 60(4):212–220, 1990.

[139] JM Liang and LJ Chen. Autocorrelation function analysis of phase formation in the initial stage of interfacial reactions of molybdenum thin films on (111) Si. *Applied physics letters*, 64(10):1224–1226, 1994.

[140] Guo-You Fan and JM Cowley. Auto-correlation analysis of high resolution electron micrographs of near-amorphous thin films. *Ultramicroscopy*, 17(4):345–355, 1985.

[141] AL Patterson. Zeit. f. *Krist*, 90:517, 1935.

[142] Young-Min Kim, Jong-Man Jeong, Jin-Gyu Kim, Youn-Joong Kim, and Young Soo Lim. Image processing of atomic resolution transmission electron microscope images. *Journal of the Korean Physical Society*, 48(2):250–255, 2006.

[143] MA Groeber, BK Haley, MD Uchic, DM Dimiduk, and S Ghosh. 3D reconstruction and characterization of polycrystalline microstructures using a FIB–SEM system. *Materials Characterization*, 57(4):259–273, 2006.

[144] John H Hubbell and Stephen M Seltzer. Tables of X-ray mass attenuation coefficients and mass energy-absorption coefficients 1 keV to 20 MeV for elements Z= 1 to 92 and 48 additional substances of dosimetric interest. Technical report, National Inst. of Standards and Technology-PL, Gaithersburg, MD (United States). Ionizing Radiation Div., 1995.

[145] Jiang Hsieh. Computed tomography: principles, design, artifacts, and recent advances. SPIE Bellingham, WA, 2009.

[146] Burton L Henke, Eric M Gullikson, and John C Davis. X-ray interactions: photoabsorption, scattering, transmission, and reflection at E= 50-30,000 eV, Z= 1-92. *Atomic data and nuclear data tables*, 54(2):181–342, 1993.

[147] Ulf Lundström, Daniel H Larsson, Anna Burvall, Per AC Takman, L Scott, H Brismar, and Hans M Hertz. X-ray phase contrast for CO2 microangiography. *Physics in medicine and biology*, 57(9):2603, 2012.

[148] A Snigirev, I Snigireva, V Kohn, S Kuznetsov, and I Schelokov. On the possibilities of x-ray phase contrast microimaging by coherent high-energy synchrotron radiation. *Review of Scientific Instruments*, 66(12):5486–5492, 1995.

[149] C Raven, A Snigirev, I Snigireva, P Spanne, A Souvorov, and V Kohn. Phase-contrast microtomography with coherent high-energy synchrotron X rays. *Applied physics letters*, 69(13):1826–1828, 1996.

[150] Sheridan C Mayo, Andrew W Stevenson, and Stephen W Wilkins. In-line phase-contrast x-ray imaging and tomography for materials science. *Materials*, 5(5):937–965, 2012.

[151] SW Wilkins, TE Gureyev, D Gao, A Pogany, and AW Stevenson. Phase-contrast imaging using polychromatic hard X-rays. *Nature*, 384(6607):335–338, 1996.

[152] Timm Weitkamp, Christoph Rau, Anatoly A Snigirev, Boris Benner, Til F Guenzler, Marion Kuhlmann, and Christian G Schroer. In-line phase contrast in synchrotron-radiation microradiography and tomography. In *International Symposium on Optical Science and Technology*, pages 92–102. International Society for Optics and Photonics, 2002.

[153] Carnegie Mellon University. X-ray computed tomography-X-ray Computed Tomography Facility - Carnegie Mellon University. http://www.cmu.edu/me/xctf/xrayct/index.html, 2015.

[154] Gabor T Herman. *Fundamentals of computerized tomography: image reconstruction from projections*. Springer Science & Business Media, 2009.

[155] A Ziegler, Th Köhler, and R Proksa. Noise and resolution in images reconstructed with FBP and OSC algorithms for CT. *Medical physics*, 34(2):585–598, 2007.

[156] Will J Schroeder, Bill Lorensen, and Ken Martin. *The visualization toolkit*. Kitware, 2004.

[157] Vincent Chabannes, Alexandre Ancel, Julien Jomier, and Christophe Prud'Homme. ANGIOTK: An Open Platform to reconstruct vessels from MRI images and simulate blood flows to ultimately provide Virtual Angiographies. In *Rencontre Inria Industrie Santé*, 2015.

[158] Andriy Fedorov, Reinhard Beichel, Jayashree Kalpathy-Cramer, Julien Finet, Jean-Christophe Fillion-Robin, Sonia Pujol, Christian Bauer, Dominique Jennings, Fiona Fennessy, Milan Sonka, et al. 3D Slicer as an image computing platform for the Quantitative Imaging Network. *Magnetic resonance imaging*, 30(9):1323–1341, 2012.

[159] José Baruchel, Jean-Yves Buffiere, and Eric Maire. X-ray tomography in material science. 2000.

[160] Christoph Rau, Ulrich Wagner, Zoran Pešić, and Alberto De Fanis. Coherent imaging at the Diamond beamline I13. *physica status solidi (a)*, 208(11):2522–2525, 2011.

[161] F Marone, C Hintermüller, S McDonald, R Abela, G Mikuljan, A Isenegger, and M Stampanoni. X-ray tomographic microscopy at tomcat. In *Journal of Physics: Conference Series*, volume 186, page 012042. IOP Publishing, 2009.

[162] Timm Weitkamp, Paul Tafforeau, Elodie Boller, Peter Cloetens, Jean-Paul Valade, Pascal Bernard, Françoise Peyrin, Wolfgang Ludwig, Lukas Helfen, and José Baruchel. Status and evolution of the ESRF beamline ID19. In *X-RAY OPTICS AND MICROANALYSIS: Proceedings of the 20th International Congress*, volume 1221, pages 33–38. AIP Publishing, 2010.

[163] Alain Karma and Wouter-Jan Rappel. Quantitative phase-field modeling of dendritic growth in two and three dimensions. *Physical review E*, 57(4):4323, 1998.

[164] Salih Ozen Unverdi and Grétar Tryggvason. A front-tracking method for viscous, incompressible, multi-fluid flows. *Journal of computational physics*, 100(1):25–37, 1992.

[165] Yu U Wang, YM Jin, AM Cuitino, and AG Khachaturyan. Nanoscale phase field microelasticity theory of dislocations: model and 3D simulations. *Acta Materialia*, 49(10):1847–1857, 2001.

[166] Dennis C Rapaport. *The art of molecular dynamics simulation*. Cambridge university press, 2004.

[167] X-P Tang, Ulrich Geyer, Ralf Busch, William L Johnson, and Yue Wu. Diffusion mechanisms in metallic supercooled liquids and glasses. *Nature*, 402(6758):160–162, 1999.

[168] TV Ramakrishnan and M_ Yussouff. First-principles order-parameter theory of freezing. *Physical Review B*, 19(5):2775, 1979.

[169] Yashwant Singh. Density-functional theory of freezing and properties of the ordered phase. *Physics Reports*, 207(6):351–444, 1991.

[170] KR Elder, Mark Katakowski, Mikko Haataja, and Martin Grant. Modeling elasticity in crystal growth. *Physical review letters*, 88(24):245701, 2002.

[171] KR Elder, Nikolas Provatas, Joel Berry, Peter Stefanovic, and Martin Grant. Phase-field crystal modeling and classical density functional theory of freezing. *Physical Review B*, 75(6):064107, 2007.

[172] Heike Emmerich, Hartmut Löwen, Raphael Wittkowski, Thomas Gruhn, Gyula I Tóth, György Tegze, and László Gránásy. Phase-field-crystal models for condensed matter dynamics on atomic length and diffusive time scales: an overview. *Advances in Physics*, 61(6):665–743, 2012.

[173] Sven van Teeffelen, Rainer Backofen, Axel Voigt, and Hartmut Löwen. Derivation of the phase-field-crystal model for colloidal solidification. *Physical Review E*, 79(5):051404, 2009.

[174] A Jaatinen, CV Achim, KR Elder, and T Ala-Nissila. Thermodynamics of bcc metals in phase-field-crystal models. *Physical Review E*, 80(3):031602, 2009.

[175] Joel Berry and Martin Grant. Phase-field-crystal modeling of glass-forming liquids: Spanning time scales during vitrification, aging, and deformation. *Physical Review E*, 89(6):062303, 2014.

[176] Tomoyuki Hirouchi, Tomohiro Takaki, and Yoshihiro Tomita. Development of numerical scheme for phase field crystal deformation simulation. *Computational Materials Science*, 44(4):1192–1197, 2009.

[177] Steven M Wise, Cheng Wang, and John S Lowengrub. An energy-stable and convergent finite-difference scheme for the phase field crystal equation. *SIAM Journal on Numerical Analysis*, 47(3):2269–2288, 2009.

[178] Mowei Cheng and James A Warren. An efficient algorithm for solving the phase field crystal model. *Journal of Computational Physics*, 227(12):6241–6248, 2008.

[179] LQ Chen and Jie Shen. Applications of semi-implicit fourier-spectral method to phase field equations. *Computer Physics Communications*, 108(2):147–158, 1998.

[180] Nikolas Provatas and Ken Elder. *Phase-field methods in materials science and engineering*. John Wiley & Sons, 2011.

[181] Matteo Frigo and Steven G Johnson. Fftw user's manual. *Massachusetts Institute of Technology*, 1999.

[182] Mark Basham, Jacob Filik, Michael T Wharmby, Peter CY Chang, Baha El Kassaby, Matthew Gerring, Jun Aishima, Karl Levik, Bill CA Pulford, Irakli Sikharulidze, et al. Data analysis workbench (dawn). *Journal of synchrotron radiation*, 22(3):0–0, 2015.

[183] BH Toby and T Egami. Accuracy of pair distribution function analysis applied to crystalline and non-crystalline materials. *Acta Crystallographica Section A: Foundations of Crystallography*, 48(3):336–346, 1992.

[184] Laura A Deschenes and Austin David A. Vanden BoutUniversity of Texas. Origin 6.0: Scientific data analysis and graphing software origin lab corporation (formerly microcal software, inc.). web site: www. originlab. com. commercial price: 595.academicprice: 446. *Journal of the American Chemical Society*, 122(39):9567–9568, 2000.

[185] Bertrand Van de Moortele, Thierry Epicier, JL Soubeyroux, and Jean-Marc Pelletier. Compositions of different phases appearing during devitrification of Zr46.75Ti8.25Cu7.5Ni10Be27.5 bulk metallic glass. *Philosophical magazine letters*, 84(4):245–256, 2004.

[186] JL Cheng, G Chen, C Fan, and Y Li. Glass formation, microstructure evolution and mechanical properties of zr 41.2 ti 13.8 cu 12.5 ni 10 be 22.5 and its surrounding alloys. *Acta Materialia*, 73:194–204, 2014.

[187] Seung-Yub Lee. *Deformation mechanisms of bulk metallic glass matrix composites*. PhD thesis, California Institute of Technology, 2005.

[188] Wei Hua Wang, Li Long Li, MX Pan, and Ru Ju Wang. Characteristics of the glass transition and supercooled liquid state of the Zr41Ti14Cu12.5Ni10Be22.5 bulk metallic glass. *Physical Review B*, 63(5):052204, 2001.

[189] J Schroers, R Busch, S Bossuyt, and WL Johnson. Crystallization behavior of the bulk metallic glass forming Zr41Ti14Cu12Ni10Be23 liquid. *Materials Science and Engineering: A*, 304:287–291, 2001.

[190] Michael D Abràmoff, Paulo J Magalhães, and Sunanda J Ram. Image processing with imagej. *Biophotonics international*, 11(7):36–42, 2004.

[191] Yongjiang Huang, Hongbo Fan, Dongjun Wang, Yu Sun, Fangyu Liu, Jun Shen, Jianfei Sun, and J Mi. The effect of cooling rate on the wear performance of a ZrCuAlAg bulk metallic glass. *Materials & Design*, 58:284–289, 2014.

[192] David San Martín, PEJ Rivera Diaz del Castillo, E Peekstok, and S Van Der Zwaag. A new etching route for revealing the austenite grain boundaries in an 11.4% cr precipitation hardening semi-austenitic stainless steel. *Materials characterization*, 58(5):455–460, 2007.

[193] H Hermann and M Ermrich. Microabsorption correction of X-ray intensities diffracted by multiphase powder specimens. *Powder diffraction*, 4(04):189–195, 1989.

[194] WG Williams, RM Ibberson, P Day, and JE Enderby. GEM–general materials diffractometer at ISIS. *Physica B: Condensed Matter*, 241:234–236, 1997.

[195] Brian H Toby. EXPGUI, a graphical user interface for GSAS. *Journal of applied crystallography*, 34(2):210–213, 2001.

[196] Allen C Larson and Robert B Von Dreele. Gsas. *General Structure Analysis System. LANSCE, MS-H805, Los Alamos, New Mexico*, 1994.

[197] Sheng-Bao Qiu and Ke-Fu Yao. Crystallization behavior of Zr41Ti14Cu12.5Ni10Be22.5 bulk metallic glass under the action of high-density pulsing current. *Journal of Non-Crystalline Solids*, 354(29):3520–3524, 2008.

[198] Birju Shah, Vasu Kumar Kakumanu, and Arvind K Bansal. Analytical techniques for quantification of amorphous/crystalline phases in pharmaceutical solids. *Journal of pharmaceutical sciences*, 95(8):1641–1665, 2006.

[199] FF Wu, ZF Zhang, SX Mao, A Peker, and J Eckert. Effect of annealing on the mechanical properties and fracture mechanisms of a Zr 56.2Ti13.8Nb5.0Cu6.9Ni5.6Be12.5 bulk-metallic-glass composite. *Physical Review B*, 75(13):134201, 2007.

[200] A Bracchi, Y-L Huang, M Seibt, S Schneider, and P Thiyagarajan. Decomposition and metastable phase formation in the bulk metallic glass matrix composite Zr56Ti14Nb5Cu7Ni6Be12. *Journal of applied physics*, 99(12):123519, 2006.

[201] Sheng-Bao Qiu and Ke-Fu Yao. Crystallization kinetics of Zr41Ti14Cu12.5Ni10Be22.5 bulk metallic glass in pulsing current pretreatment states. *Journal of Alloys and Compounds*, 475(1):L5–L8, 2009.

[202] U Kühn, J Eckert, N Mattern, and L Schultz. As-cast quasicrystalline phase in a Zr-based multicomponent bulk alloy. *Applied Physics Letters*, 77(20):3176–3178, 2000.

[203] Grzegorz Szamel. Mode-coupling theory and beyond: A diagrammatic approach. *Progress of Theoretical and Experimental Physics*, 2013(1):012J01, 2013.

[204] B.J Alder and T.E Wainwright. Studies in molecular dynamics. I. General method. *The Journal of Chemical Physics*, 31(2):459–466, 1959.

[205] David R Reichman and Patrick Charbonneau. Mode-coupling theory. *Journal of Statistical Mechanics: Theory and Experiment*, 2005(05):P05013, 2005.

[206] M Asta, C Beckermann, A Karma, W Kurz, R Napolitano, M Plapp, G Purdy, M Rappaz, and R Trivedi. Solidification microstructures and solid-state parallels: Recent developments, future directions. *Acta Materialia*, 57(4):941–971, 2009.

[207] R Evans. The nature of the liquid-vapour interface and other topics in the statistical mechanics of non-uniform, classical fluids. *Advances in Physics*, 28(2):143–200, 1979.

[208] Andrew J Archer, Mark J Robbins, Uwe Thiele, and Edgar Knobloch. Solidification fronts in supercooled liquids: How rapid fronts can lead to disordered glassy solids. *Physical Review E*, 86(3):031603, 2012.

[209] Joel Berry, KR Elder, and Martin Grant. Simulation of an atomistic dynamic field theory for monatomic liquids: Freezing and glass formation. *Physical Review E*, 77(6):061506, 2008.

[210] J Weber. Fluctuation dissipation theorem. *Physical Review*, 101(6):1620, 1956.

[211] Henry R Neave. On using the box-muller transformation with multiplicative congruential pseudo-random number generators. *Applied Statistics*, pages 92–97, 1973.

[212] Robert G Parr and Weitao Yang. *Density-functional theory of atoms and molecules*, volume 16. Oxford university press, 1989.

[213] György Tegze, Gurvinder Bansel, Gyula I Tóth, Tamás Pusztai, Zhongyun Fan, and László Gránásy. Advanced operator splitting-based semi-implicit spectral method to solve the binary phase-field crystal equations with variable coefficients. *Journal of Computational Physics*, 228(5):1612–1623, 2009.

[214] Joel M Berry. *Liquid-Solid Systems out of Equilibrium: Phase-Field Crystal Studies of Solidification, Melting, and Plasticity*. 2011.

[215] Ananth Grama. *Introduction to parallel computing*. Pearson Education, 2003.

[216] Z Guo, J Mi, and PS Grant. An implicit parallel multigrid computing scheme to solve coupled thermal-solute phase-field equations for dendrite evolution. *Journal of Computational Physics*, 231(4):1781–1796, 2012.

[217] Edgar Gabriel, Graham E Fagg, George Bosilca, Thara Angskun, Jack J Dongarra, Jeffrey M Squyres, Vishal Sahay, Prabhanjan Kambadur, Brian Barrett, Andrew Lumsdaine, et al. Open MPI: Goals, concept, and design of a next generation MPI implementation. In *Recent Advances in Parallel Virtual Machine and Message Passing Interface*, pages 97–104. Springer, 2004.

[218] Caroline A Schneider, Wayne S Rasband, and Kevin W Eliceiri. NIH Image to ImageJ: 25 years of image analysis. *Nature methods*, 9(7):671–675, 2012.

[219] Rana Rezakhaniha, Aristotelis Agianniotis, Jelle Tymen Christiaan Schrauwen, Alessandra Griffa, Daniel Sage, CVC Bouten, FN Van de Vosse, Michaël Unser, and Nikolaos Stergiopulos. Experimental investigation of collagen waviness and orientation in the arterial adventitia using confocal laser scanning microscopy. *Biomechanics and modeling in mechanobiology*, 11(3-4):461–473, 2012.

[220] Sow-Hsin Chen, John S Huang, and Piero Tartaglia. *Structure and dynamics of strongly interacting colloids and supramolecular aggregates in solution*. Kluwer Academic, 1992.

[221] Johannes Schindelin, Ignacio Arganda-Carreras, Erwin Frise, Verena Kaynig, Mark Longair, Tobias Pietzsch, Stephan Preibisch, Curtis Rueden, Stephan Saalfeld, Benjamin Schmid, et al. Fiji: an open-source platform for biological-image analysis. *Nature methods*, 9(7):676–682, 2012.

[222] Ryoichi Yamamoto and Akira Onuki. Dynamics of highly supercooled liquids: Heterogeneity, rheology, and diffusion. *Physical Review E*, 58(3):3515, 1998.

[223] KR Elder and Martin Grant. Modeling elastic and plastic deformations in nonequilibrium processing using phase field crystals. *Physical Review E*, 70(5):051605, 2004.

[224] PP Pal-Val, VD Natsik, and LN Pal-Val. Dynamic elastic moduli of niobium at low temperatures: their temperature dependence in the normal state, the influence of the superconducting transition, and dislocation effects. *Low Temperature Physics*, 32(2):169–185, 2006.

[225] J Garai and A Laugier. The temperature dependence of the isothermal bulk modulus at 1bar pressure. *Journal of applied physics*, 101(2):023514, 2007.

[226] N Mattern, A Schöps, U Kühn, J Acker, O Khvostikova, and J Eckert. Structural behavior of CuxZr100-x metallic glass (x= 35–70). *Journal of Non-Crystalline Solids*, 354(10):1054–1060, 2008.

[227] N Mattern, P Jóvári, I Kaban, S Gruner, A Elsner, V Kokotin, H Franz, B Beuneu, and J Eckert. Short-range order of Cu–Zr metallic glasses. *Journal of Alloys and Compounds*, 485(1):163–169, 2009.

[228] K Georgarakis, L Hennet, GA Evangelakis, J Antonowicz, GB Bokas, V Honkimaki, A Bytchkov, MW Chen, and AR Yavari. Probing the structure of a liquid metal during vitrification. *Acta Materialia*, 87:174–186, 2015.

[229] W Dmowski, C Fan, ML Morrison, PK Liaw, and T Egami. Structural changes in bulk metallic glass after annealing below the glass-transition temperature. *Materials Science and Engineering: A*, 471(1):125–129, 2007.

[230] K Georgarakis, AR Yavari, DV Louzguine-Luzgin, and G Vaughan. Crystallization and vitrification of a PdCuNiP metallic glass upon thermal and mechanical processes detected by synchrotron light X-ray radiation. In *4TH INTERNATIONAL SYMPOSIUM ON SLOW DYNAMICS IN COMPLEX SYSTEMS: Keep Going Tohoku*, volume 1518, pages 672–681. AIP Publishing, 2013.

[231] Thomas Kannengiesser, Sudarsanam Suresh Babu, Yu-ichi Komizo, and Antonio Ramirez. *In-situ Studies with Photons, Neutrons and Electrons Scattering II*. Springer, 2014.

[232] Stephen P Thompson, Julia E Parker, Julien Marchal, Jonathan Potter, Adrian Birt, Fajin Yuan, Richard D Fearn, Alistair R Lennie, Steven R Street, and Chiu C Tang. Fast X-ray powder diffraction on I11 at Diamond. *Journal of synchrotron radiation*, 18(4):637–648, 2011.

[233] SP Thompson, JE Parker, J Potter, TP Hill, A Birt, TM Cobb, F Yuan, and CC Tang. Beamline I11 at Diamond: A new instrument for high resolution powder diffraction. *Review of scientific instruments*, 80(7):075107, 2009.

[234] Julie L Fife, Michel Rappaz, Mattia Pistone, Tine Celcer, Gordan Mikuljan, and Marco Stampanoni. Development of a laser-based heating system for in situ synchrotron-based X-ray tomographic microscopy. *Journal of synchrotron radiation*, 19(3):352–358, 2012.

[235] Saul J Moorhouse, Nenad Vranješ, Andrew Jupe, Michael Drakopoulos, and Dermot O'Hare. The Oxford-Diamond In Situ Cell for studying chemical reactions using time-resolved X-ray diffraction. *Review of Scientific Instruments*, 83(8):084101, 2012.

[236] Dongyue Tan, Tung Lik Lee, Jia Chuan Khong, Thomas Connolley, Kamel Fezzaa, and Jiawei Mi. High-speed synchrotron X-ray imaging studies of the ultrasound shockwave and enhanced flow during metal solidification processes. *Metallurgical and Materials Transactions A*, pages 1–11, 2015.

[237] Jiawei Mi, Dongyue Tan, and Tung Lik Lee. In situ synchrotron X-ray study of ultrasound cavitation and its effect on solidification microstructures. *Metallurgical and Materials Transactions B*, pages 1–5, 2014.

[238] Theerapatt Manuwong, Wei Zhang, Peter Lobo Kazinczi, Andrew J Bodey, Christoph Rau, and Jiawei Mi. Solidification of Al alloys under electromagnetic pulses and characterization of the 3D microstructures using synchrotron X-ray tomography. *Metallurgical and Materials Transactions A*, 46(7):2908–2915, 2015.

[239] Theodore A Waniuk, Jan Schroers, and William L Johnson. Critical cooling rate and thermal stability of Zr–Ti–Cu–Ni–Be alloys. *Applied Physics Letters*, 78(9):1213–1215, 2001.

[240] Jan Schroers, Andreas Masuhr, William L Johnson, and Ralf Busch. Pronounced asymmetry in the crystallization behavior during constant heating and cooling of a bulk metallic glass-forming liquid. *Physical Review B*, 60(17):11855, 1999.

[241] J Schroers, R Busch, A Masuhr, and WL Johnson. Nucleation in undercooled Zr41Ti14Cu12Ni10Be23 melts. *Journal of non-crystalline solids*, 250:699–703, 1999.

[242] Theodore Waniuk, Jan Schroers, and William L Johnson. Timescales of crystallization and viscous flow of the bulk glass-forming Zr–Ti–Ni–Cu–Be alloys. *Physical Review B*, 67(18):184203, 2003.

[243] AR Yavari, A Le Moulec, A Inoue, P Rejmankova, A Kvick, et al. In situ crystallization of Zr55Cu30Al10Ni5 bulk glass forming from the glassy and undercooled liquid states using synchrotron radiation. *Journal of non-crystalline solids*, 247(1):31–34, 1999.

[244] JL Uriarte, T Zhang, S Deledda, G Vaughan, AR Yavari, A Inoue, and A Kvick. Real-time detection of metastable phases in Zr-based bulk glasses during fast heating in a synchrotron beam. *Journal of non-crystalline solids*, 287(1):197–200, 2001.

[245] Yan Li, Konstantinos Georgarakis, Shujie Pang, Chaoli Ma, Gavin Vaughan, Alain Reza Yavari, and Tao Zhang. Real time synchrotron radiation studies on metallic glass (Zr0.55Al0.1Ni0.05Cu0.3)99Y1 after cold rolling. *Intermetallics*, 17(4):231–234, 2009.

[246] K Georgarakis, AR Yavari, M Aljerf, DV Louzguine-Luzgin, M Stoica, G Vaughan, and A Inoue. On the atomic structure of Zr–Ni and Zr–Ni–Al metallic glasses. *Journal of Applied Physics*, 108(2):023514, 2010.

[247] Konstantinos Georgarakis, Dmitri V Louzguine-Luzgin, Jerzy Antonowicz, Gavin Vaughan, Alain R Yavari, Takeshi Egami, and Akihisa Inoue. Variations in atomic structural features of a supercooled Pd–Ni–Cu–P glass forming liquid during in situ vitrification. *Acta Materialia*, 59(2):708–716, 2011.

[248] D Srolovitz, T Egami, and V Vitek. Radial distribution function and structural relaxation in amorphous solids. *Physical Review B*, 24(12):6936, 1981.

[249] R Busch, A Masuhr, and WL Johnson. Thermodynamics and kinetics of Zr–Ti–Cu–Ni–Be bulk metallic glass forming liquids. *Materials Science and Engineering: A*, 304:97–102, 2001.

[250] JL Soubeyroux and N Claret. Crystallisation behaviour of bulk metallic glasses by in-situ neutron diffraction. *Applied Physics A*, 74(1):s1025–s1027, 2002.

[251] Stephen Richard Elliott. *Physics of amorphous materials*. Longman London; New York, 1983.

[252] Akihiko Hirata, Takuro Morino, Yoshihiko Hirotsu, Keiji Itoh, and Toshiharu Fukunaga. Local atomic structure analysis of Zr-Ni and Zr-Cu metallic glasses using electron diffraction. *Materials transactions*, 48(6):1299–1303, 2007.

[253] Yu Chan Kim, Jong Hyun Na, Jin Man Park, Do Hyang Kim, Jin Kyu Lee, and Won Tae Kim. Role of nanometer-scale quasicrystals in improving the mechanical behavior of Ti-based bulk metallic glasses. *Applied physics letters*, 83(15):3093–3095, 2003.

[254] Xiaoke Mu, Sridhar Neelamraju, Wilfried Sigle, Christoph T Koch, Nico Toto, J Christian Schön, Andreas Bach, Dieter Fischer, Martin Jansen, and Peter A van Aken. Evolution of order in amorphous-to-crystalline phase transformation of MgF2. *Applied Crystallography*, 46(4):1105–1116, 2013.

[255] William L Johnson, Georg Kaltenboeck, Marios D Demetriou, Joseph P Schramm, Xiao Liu, Konrad Samwer, C Paul Kim, and Douglas C Hofmann. Beating crystallization in glass-forming metals by millisecond heating and processing. *Science*, 332(6031):828–833, 2011.

[256] Xiao Liu, Marios D Demetriou, Georg Kaltenboeck, Joseph P Schramm, Glenn R Garrett, and William L Johnson. Description of millisecond Ohmic heating and forming of metallic glasses. *Acta Materialia*, 61(8):3060–3067, 2013.

[257] Wanqiang Xu, Rongkun Zheng, Kevin J Laws, Simon P Ringer, and Michael Ferry. In situ formation of crystalline flakes in Mg-based metallic glass composites by controlled inoculation. *Acta Materialia*, 59(20):7776–7786, 2011.

[258] Henry Kozachkov, Joanna Kolodziejska, William L Johnson, and Douglas C Hofmann. Effect of cooling rate on the volume fraction of B2 phases in a CuZrAlCo metallic glass matrix composite. *Intermetallics*, 39:89–93, 2013.

[259] EI Kazantsev. *Industrial Furnaces: Design and Calculation Reference Book*. Mir Publishers, 1977.

Appendix A

2D drawings of the custom parts of the experimental apparatus

In the appendix, in the beginning, the formula used to evaluate the heating power of the furnace [259], and also the selection of the heating wires are given. Then all the 2D drawings of the custom parts of the experimental apparatus for the in-situ PDF studies are attached. It includes, the assemble of the apparatus, key components, making of the heater, *etc*. The exact name of the components can be found in the table for each 2D drawings. All the dimension in the drawings are the real dimension for the manufacturing.

The calculation and selection of the electric resistance wires

1. To evaluate the total heating powder required.

$$A = \pi \cdot h \cdot d \tag{A.1}$$

where, A is the total area of the inner surface of the heating zone for the heater, m^2; h is the height of the heating zone, m; d is the inner diameter of the heating zone, m. Therefore, the theoretical heating powder needed is calculated,

$$P_{total} = P' \cdot A \tag{A.2}$$

where, P_{total} is the total heating powder required, kW; P' is the unit heating load in kW/m^2.

2. To determine the diameter of the electric resistance wires.

$$d_{wire} = 34.4 \times \sqrt[3]{\frac{P_{total}^2 \times \rho_t}{V_{heater}^2 \times \upsilon_{permitted}}} \tag{A.3}$$

where, d_{wire} is the diameter of the electric resistance wires, mm; ρ_t is the resistivity of electric resistance wires at operating temperature, $\Omega \cdot mm^2/m$. V_{heater} is the electric voltage used to power the electric resistance wires, Volt; $\upsilon_{permitted}$ is the permitted heating power load on surface of the heater, W/cm^2.

3. To determine the length of the electric resistance wires.

$$L_{wire} = \frac{V_{heater} \times A}{10^3 \times P_{total} \times \rho_t} \tag{A.4}$$

where, L_{wire} is the total length of the electric resistance wires, m.

4. To verify the calculated parameters for electric resistance wire.

$$\upsilon_{effective} = \frac{10^3 \times P_{total}}{\pi \times d_{wire} \times L_{wire}} \leq \upsilon_{permitted} \tag{A.5}$$

The parameters involved in the calculations are listed in Table. A.1, and also the units used in the calculation are included in the table, since not all the entries in the formula is in the International System of units.

where, $v_{effective}$ is the effective heating power load, W/cm^2.

Table A.1 Parameters used to design the electric resistance wires

h	d	P'	A	P_{total}	ρ_t	V_{heater}	$v_{permitted}$	d_{wire}	L_{wire}
0.12	0.18	20	0.0068	0.136	1.41	240	2.0	0.21	10.4
m	m	kW/m^2	m^2	kW/m^2	$\Omega \cdot mm^2/m$	Volts	W/cm^2	mm	m

$v_{permitted}$ and ρ_t can be determined from the properties of Kanthal wires

SECTION A-A
SCALE 1 : 2

∅25
∅6
50 20
∅4.50

∅18
∅15

120
20
∅34.50
∅9
200
120
120
15
10
6.50
∅16

∅0.98
82.03°
∅13
95
∅10
70
∅40
2.75
30
6.50
150
∅6
15.37

	NAME	SIGNATURE	DATE				
UNLESS OTHERWISE SPECIFIED: DIMENSIONS ARE IN MILLIMETERS SURFACE FINISH: TOLERANCES: LINEAR: ANGULAR:	FINISH:			DEBUR AND BREAK SHARP EDGES	DO NOT SCALE DRAWING	REVISION	
DRAWN					TITLE:		
CHK'D							
APPV'D							
MFG							
Q.A			MATERIAL:		DWG NO. **Furnace assembly**	A4	
			WEIGHT:		SCALE:1:5	SHEET 1 OF 1	

45.28°

Ø9.20

R1.50

Ø80.72

100

40

120

R21.18

120
100
40

UNLESS OTHERWISE SPECIFIED: DIMENSIONS ARE IN MILLIMETERS SURFACE FINISH: TOLERANCES: LINEAR: ANGULAR:	FINISH:			DEBUR AND BREAK SHARP EDGES	DO NOT SCALE DRAWING		REVISION

	NAME	SIGNATURE	DATE				TITLE:	
DRAWN								
CHK'D								
APPV'D								
MFG								
Q.A			MATERIAL:				DWG NO.	**front wall**	A4
			WEIGHT:				SCALE:1:2	SHEET 1 OF 1

SCALE 1 : 3

UNLESS OTHERWISE SPECIFIED: DIMENSIONS ARE IN MILLIMETERS SURFACE FINISH: TOLERANCES: LINEAR: ANGULAR:	FINISH:		DEBUR AND BREAK SHARP EDGES	DO NOT SCALE DRAWING	REVISION

	NAME	SIGNATURE	DATE			TITLE:	
DRAWN							
CHK'D							
APPV'D							
MFG							
Q.A			MATERIAL:			DWG NO.	furnace holder	A4
			WEIGHT:			SCALE:1:2	SHEET 1 OF 1

Ø6

Ø13.10

Ø6

Ø3.50

SCALE 2 : 1

23.50

25

30

6

20

34

Ø40

SCALE 2 : 1

	NAME	SIGNATURE	DATE			TITLE:		
UNLESS OTHERWISE SPECIFIED: DIMENSIONS ARE IN MILLIMETERS SURFACE FINISH: TOLERANCES: LINEAR: ANGULAR:	FINISH:				DEBUR AND BREAK SHARP EDGES	DO NOT SCALE DRAWING		REVISION
DRAWN								
CHK'D								
APPV'D								
MFG								
Q.A				MATERIAL:		DWG NO. **bottom bracket**		A4
				WEIGHT:		SCALE:1:1		SHEET 1 OF 1

⌀1.10

⌀3

⌀12

100

95

70

UNLESS OTHERWISE SPECIFIED:	FINISH:		DEBUR AND BREAK SHARP EDGES		DO NOT SCALE DRAWING	REVISION
DIMENSIONS ARE IN MILLIMETERS SURFACE FINISH: TOLERANCES: LINEAR: ANGULAR:						

	NAME	SIGNATURE	DATE			TITLE:		
DRAWN								
CHK'D								
APPV'D								
MFG								
Q.A				MATERIAL:		DWG NO.	Glass pin_tube	A4
				WEIGHT:		SCALE:1:1		SHEET 1 OF 1

UNLESS OTHERWISE SPECIFIED: DIMENSIONS ARE IN MILLIMETERS SURFACE FINISH: TOLERANCES: LINEAR: ANGULAR:	FINISH:			DEBUR AND BREAK SHARP EDGES		DO NOT SCALE DRAWING		REVISION	
	NAME	SIGNATURE	DATE			TITLE:			
DRAWN									
CHK'D									
APPV'D									
MFG									
Q.A				MATERIAL:		DWG NO.	sample holder base		A4
				WEIGHT:		SCALE:1:2		SHEET 1 OF 1	

ϕ14.50

ϕ25

ϕ6

SCALE 2 : 1

50

20

SCALE 2 : 1

UNLESS OTHERWISE SPECIFIED: DIMENSIONS ARE IN MILLIMETERS SURFACE FINISH: TOLERANCES: LINEAR: ANGULAR:		FINISH:			DEBUR AND BREAK SHARP EDGES		DO NOT SCALE DRAWING		REVISION	
	NAME	SIGNATURE	DATE				TITLE:			
DRAWN										
CHK'D										
APPV'D										
MFG										
Q.A				MATERIAL:			DWG NO.	top cover		A4
				WEIGHT:			SCALE:1:1		SHEET 1 OF 1	

47.50

⌀10.50

120

120

25

40

⌀9

35

37

39.50

	NAME	SIGNATURE	DATE				TITLE:		

UNLESS OTHERWISE SPECIFIED:
DIMENSIONS ARE IN MILLIMETERS
SURFACE FINISH:
TOLERANCES:
   LINEAR:
   ANGULAR:

FINISH:

DEBUR AND
BREAK SHARP
EDGES

DO NOT SCALE DRAWING

REVISION

DRAWN

CHK'D

APPV'D

MFG

Q.A

MATERIAL:

DWG NO.

Back wall

A4

WEIGHT:

SCALE:1:2

SHEET 1 OF 1

		NAME	SIGNATURE	DATE				TITLE:		
UNLESS OTHERWISE SPECIFIED: DIMENSIONS ARE IN MILLIMETERS SURFACE FINISH: TOLERANCES: LINEAR: ANGULAR:					FINISH:		DEBUR AND BREAK SHARP EDGES	DO NOT SCALE DRAWING		REVISION
DRAWN										
CHK'D										
APPV'D										
MFG										
Q.A					MATERIAL:			DWG NO.	side wall	A4
					WEIGHT:			SCALE:1:1		SHEET 1 OF 1

119

10

Ø 18   Ø 10

10   10

140

14

75   102   130

118

165   15

	NAME	SIGNATURE	DATE				TITLE:		
DRAWN									
CHK'D									
APPV'D									
MFG									
Q.A				MATERIAL:			DWG NO.	heater base	A4

UNLESS OTHERWISE SPECIFIED:
DIMENSIONS ARE IN MILLIMETERS
SURFACE FINISH:
TOLERANCES:
  LINEAR:
  ANGULAR:

FINISH:

DEBUR AND
BREAK SHARP
EDGES

DO NOT SCALE DRAWING   REVISION

WEIGHT: SCALE:1:5   SHEET 1 OF 1

⌀5

⌀18.50

⌀17

120

200

⌀34.50

		UNLESS OTHERWISE SPECIFIED:	FINISH:			DEBUR AND BREAK SHARP EDGES	DO NOT SCALE DRAWING	REVISION

UNLESS OTHERWISE SPECIFIED:
DIMENSIONS ARE IN MILLIMETERS
SURFACE FINISH:
TOLERANCES:
　LINEAR:
　ANGULAR:

FINISH:

DEBUR AND
BREAK SHARP
EDGES

DO NOT SCALE DRAWING

REVISION

	NAME	SIGNATURE	DATE				TITLE:
DRAWN							
CHK'D							
APPV'D							
MFG							
Q.A			MATERIAL:				DWG NO.

MATERIAL:

TITLE:

DWG NO.

heater making　A4

WEIGHT:

SCALE:1:5　　　SHEET 1 OF 1

⌀34.50

⌀18.50

90

17.25

120

60

⌀5

	NAME	SIGNATURE	DATE				TITLE:		
DRAWN									
CHK'D									
APPV'D									
MFG									
Q.A				MATERIAL:			DWG NO.	resistence heater	A4

UNLESS OTHERWISE SPECIFIED:
DIMENSIONS ARE IN MILLIMETERS
SURFACE FINISH:
TOLERANCES:
 LINEAR:
 ANGULAR:

FINISH:

DEBUR AND
BREAK SHARP
EDGES

DO NOT SCALE DRAWING   REVISION

WEIGHT:

SCALE:1:1   SHEET 1 OF 1